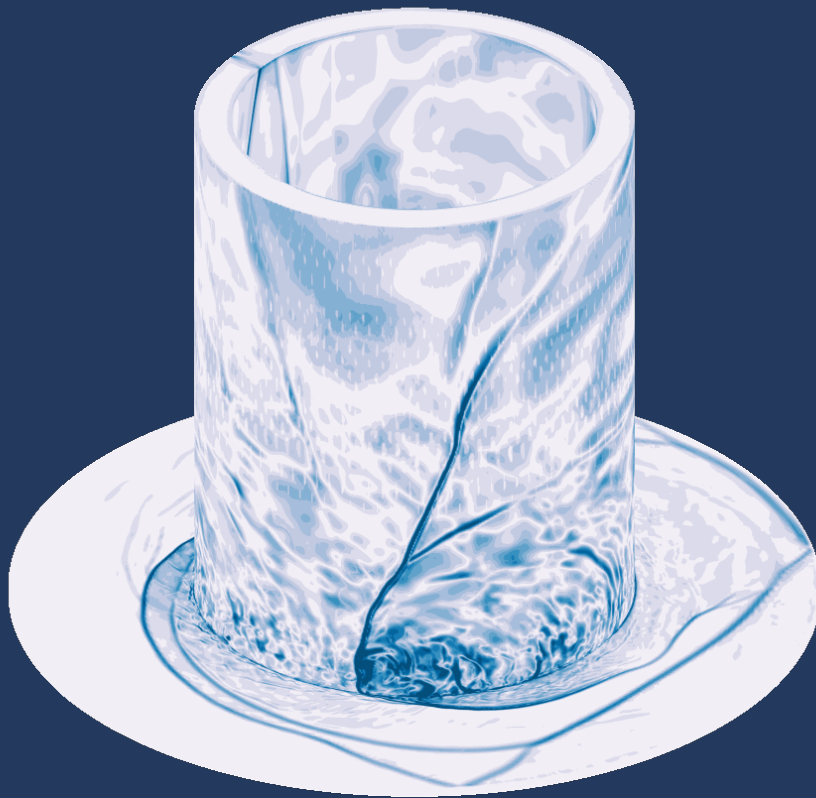# Numerical Simulation of Rotating Detonation Engines

Master of Science Thesis

Ignacio Serrano Martín-Sacristán

Numerical Simulation of Rotating Detonation Engines

Master of Science Thesis

Thesis report

by

Ignacio Serrano Martín-Sacristán

to obtain the degree of
Master of Science in Aerospace Engineering
at the Delft University of Technology
to be defended publicly on August 29, 2025 at 11:00

Thesis committee:

Supervisors:	Prof. Dr.-Ing. habil. Stefan Hickel
	Dr. rer. nat. Tim Horchler (DLR)
Chair:	Dr. ir. Ferdinand F.J. Schrijer
Examinor:	Dr. ir. Shobhit Jain
Place:	Faculty of Aerospace Engineering, Delft
Project Duration:	December, 2024 - August, 2025
Student number:	5925843

An electronic version of this thesis is available at `http://repository.tudelft.nl/`.

Faculty of Aerospace Engineering · Delft University of Technology

TUDelft

Delft
University of
Technology

Abstract

Rotating Detonation Engines (RDEs) are a type of pressure-gain combustion system based on detonation waves traveling around a cylindrical combustion chamber igniting the fresh gases. Compared to classical combustors, detonative combustion offers an increment in thermodynamic efficiency of the engine due to rapid heat release and lower entropy rise. The development of this technology could bring more compact and efficient combustors with applications to energy generation, aviation, and rocket propulsion.

The objective of the present work is to develop a robust set up to simulate an RDE employing the DLR TAU code to obtain physical solutions to investigate the flow field within the engine and its performance. The impact of different modeling decisions and their influence on the flow physics shall be addressed.

First, a set of 1D shock tube simulations have been conducted to evaluate the best solver parameters to capture detonation dynamics. Later, results of 2D simulations based on a test case from literature were performed and the modeling decisions were re-evaluated for this more realistic case. Lastly, two different 3D simulations have been performed and compared with the respective experimental results.

The results showed that a resolution of 200 μm was enough in 2D simulations to capture the main flow features. Moreover, the chosen chemical reaction mechanism was from Ó Conaire [1], and the upwind flux that performed the best was the AUSMDV [2] solver. Moreover, the time step employed was of the order of 10^{-8} seconds. Different inlet boundary conditions were studied, finding the Dirichlet type more suitable to uncouple injection and detonation dynamics. In addition, different ignition strategies were evaluated, proving that the strategies were successful and achieved a stable mode of operation.

This work presents a robust set up to perform 2D and 3D RDE simulations employing the DLR TAU code. It also provides many insights into the impact of different modeling decisions on the flow field and evolution of the engine performance.

Keywords: **rotating detonation engine**, **chemical reaction mechanism**, **hydrogen**, **mixing**, **DLR TAU**, **ignition**.

Preface

I would like to use this space to thank all the people that have made this work possible. First, I would like to thank my DLR supervisor, Dr. Tim Horchler. I am truly grateful for the opportunity to work with him at the Institute of Aerodynamics and Flow Technology DLR in Göttingen. For the time he has invested in our discussions, his guidance, his insight, his support, and his kindness. In general, I am very grateful to the people in the Spacecraft Department. I have felt welcomed and supported from the very first day, and it is thanks to the good environment within the office that I have been able to learn as much as I have.

I would also like to thank my TU Delft supervisor, Dr. Stefan Hickel. Not only for his guidance and support during the thesis, but also due to the technical level imparted in his courses at university. The acquired knowledge has been incredibly helpful when tackling the problem presented in this work.

I also would like to mention the other master students who have worked closely with me these months. Working along Sebas, Tobias, Federico, and Will have helped to push forward and to keep going. Thanks for making each day a little bit easier to navigate.

Lastly, but not less important, I would like to thank all my friends and family. Most of them in Spain, others scattered all around the world. Regardless of where they are, they have always supported me in my endeavors abroad. If I am here today, it is thanks to their love, as it is easier to survive a storm knowing that there are people waiting for you at the port.

Contents

Nomenclature

List of Abbreviations

AMR   Adaptative Mesh Refinement

AUSM Advection Upstream Splitting Method

CEA   Chemical Equilibrium with Applications

CFD   Computational Fluid Dynamics

CFL   Courant-Friedrichs-Levy

CJ   Chapman-Jouguet

DDT   Deflagration to Detonation Transition

DES   Detached Eddy Simulations

DLR   German Aerospace Center

DW   Detonation Wave

EARSM Explicit Algebraic Reynolds Stress Model

FDS   Flux-Difference Splitting

FVS   Flux-Vector Splitting

KNP   Kurganov-Noelle-Petrona

LES   Large Eddy Simulations

LS   Leading Shock

LUSGS Lower-Upper Symmetric Gauss-Seidel

M   Mach Stem

NIST   US National Institute of Standards and Technology

PC   Parasitic Combustion

PLIF   Planar Laser-Induced Fluorescence

PSD   Power Spectral Density

RANS Reynolds-Averaged Navier-Stokes

RDC   Rotating Detonation Combustor

RDE   Rotating Detonation Engine

T   Transverse Wave

TUB   Technische Universität Berlin

TUD   Delft University of Technology

URANS Unsteady Reynolds-Averaged Navier-Stokes

vN   von Neumann

WENO Weighted Essentially Non-Oscillatory

XLES   Extra-Large Eddy Simulations

ZND   Zel'dovich-von Neumann-Döring Theory

List of Symbols

α Detonation index parameter

Δ Combustion chamber width

Δt Physical time step

Δt^* Pseudo-time time step

Δt^ν Viscous time step

Δt^c Convective time step

$\dot{m}$ Mass flux

$\dot{m}^*$ Corrected mass flux

ϵ Normalized error

η_{comb} Combustion efficiency

η_{th} System thermal efficiency

γ Specific heat ratio

Γ_p Pressure marker threshold parameter

Γ_w Chemical heat release marker threshold parameter

κ Thermal conductivity

λ Detonation cell size

λ_ν^i Viscous terms eigenvalues

λ_c^i Convective terms eigenvalues

μ Dynamic viscosity

ν	Stoichiometric coefficient		h	Specific enthalpy
ω	Relaxation parameter		h_s	Species specific enthalpy
ϕ	Equivalence ratio		h_z	Fresh gases mixture height
ρ	Density		h_{det}	Detonation height
ρ_s	Species density		I_{det}	Detonation index
$\underline{\underline{F}}^{Eu}$	Inviscid or Euler fluxes matrix		I_{mix}	Mixture index
$\underline{\underline{F}}^{NS}$	Viscous Navier-Stokes fluxes matrix		k^b	Backward reaction coefficient
$\underline{\underline{I}}$	Identity matrix		k^f	Forward reaction coefficient
$\underline{\underline{P}}$	Viscous stress tensor		k_0^f	Forward reaction coefficient limit at high pressures
$\underline{f}$	Numerical flux		k_∞^f	Backward reaction coefficient limit at low pressures
$\underline{n}$	Normal vector			
$\underline{Q}$	Chemical source term		K^{eq}	Chemical equilibrium constant
$\underline{R}$	Residuals vector		L	Limiter function
$\underline{U}$	Convervative variables vector		L_{cc}	Combustion chamber length
$\underline{u}$	Velocity vector		M	Mach Number
ε	Nozzle area ratio		M_S	Species molar mass
ε'	Blockage factor		$M_{1/2}$	Mach Number at cell interface
A	Arrhenius equation constant		n	Arrhenius equation constant
a	Speed of sound		N_A	Avogadro Number
A_{eff}	Effective inlet area		n_S	Molar concentration of species
C	Species concentration		n_w	Number of detonation waves
c_p	Specific heat at constant pressure		p	Static pressure
c_V	Specific heat at constant volume		P_0	Total pressure
D	Diffusion coefficient		P_d	Detonation pressure
d_n	Outer combustion chamber diameter		P_m	Plenum pressure
E	Specific total energy		P_r	Reduced pressure
E_a	Reaction activation energy		p_{CJ}	Chapman-Jouguet pressure
e_S	Species internal energy		P_{cr}	Critical pressure
F	Correction function		P_{init}	Initial mixture pressure
f_w	Detonation frequency		p_{in}	Inner domain static pressure
g_i	Weighting functions		p_r	Inlet static pressure
			q	Chemical heat release
			Q_S	Partition function

R^0	Universal gas constant	u	Scalar 1D velocity
R_{cyl}	Cylindrical coordinates radius	$u_{1/2}$	Advection velocity at cell interface
s	Specific entropy	u_{CJ}	Chapman-Jouget velocity
s^0	Reservoir entropy	V	Volume
S_p	Pressure marker function	v	Specific volume
S_w	Chemical heat release marker function	V_D	Detonation Velocity
Sc	Schmidt Number	V_i	Specie diffusion velocity
T	Static temperature	W	Molecular weight
t	Physical time	w	Reaction rate
T_0	Total temperature	w_s	Species reaction rate
t_p	Detonation period time	w_{net}	Specific net work
t_r	Injection recovery time	Y	Mass fraction
T_{CJ}	Chapman-Jouguet temperature	Z	Mixture fraction
T_r	Inlet static temperature	Z_{st}	Stoichiometric mixture fraction

List of Figures

List of Tables

<div align="right">1</div>

Introduction

The aim of this M.Sc. thesis is to study the capabilities of the DLR TAU code [3] to simulate rotating detonation engines (RDEs) by simulating 2D and 3D cases from the literature, such as the experimental model tested at DLR Lampoldshausen [4], or the experiment from Bluenmer et al. [5]. The work has been conducted at the Institute of Aerodynamics and Flow Technology in Göttingen, in the Aerothermodynamics and Propulsion Technology group, in collaboration with Delft University of Technology (TUD). The two main areas of expertise of the group are the development of fluid dynamics simulation codes (CFD) for spacecraft applications, and the application of CFD methods for the design and analysis of re-entry flows, rocket combustion chambers, airbreathing propulsion systems, re-usable launch vehicles, and launcher aerothermodynamics.

1.1. Technological Problem

A rotating detonation engine (RDE) is a pressure-gain combustion system based on a detonation wave traveling around a cylindrical combustion chamber igniting the fresh gases, thus providing chemical heat release that sustains said detonation. A detonation is a combustion front moving at a supersonic speed. On the other hand, classical combustors are based on subsonic deflagration waves. Figure 1.1 shows a schematic of the working principle of an RDE. One, two, or more detonations travel around the combustion chamber, igniting the inlet gas mixture. Right after the detonation, the post-combustion products have high pressure and temperature, thus blocking the entrance of fresh gases. As the detonation moves, these hot gases expand downstream the combustion chamber and the pressure decreases, leading to the entrance to the fresh mixture into the chamber. The space between co-rotating detonations (l) and the detonation front height (h) depend mainly on the inlet conditions and mixture properties. Lastly, oblique shocks are induced in the expanding hot combustion products from the end of the detonation fronts. An RDE operating in a stable regime would be able to sustain the detonations traveling in the same direction without losing strength.

The development of RDEs has been going on for some decades now, with some of the foundational works from the sixties [7][8]. There have also been relevant works during the first decade of the 21st century [9]. Moreover, different types of pressure-gain engines such as pulse detonation engines (PDE) have been studied as well [10]. The main difference with respect to RDEs is the non-continous thrust capabilities. The detonation chamber has to be refilled after each detonation, limiting the frequency and thrust output due to mechanical limitations. On the other hand, although RDEs have variations, they are not a problem due to their high frequency [11].

In recent years, RDEs have been thoroughly investigated due to the improvement they offer compared to classical deflagration-based engines. Detonative combustion is characterized by a high increment of pressure at constant volume, which offers an increase in thermodynamic efficiency due to rapid heat release and lower entropy rise [12]. Moreover, this type of engine has a broad throttling range, and the possibility of having very compact designs compared to constant pressure combustors, which makes them especially interesting for space applications [13]. It is also relevant to mention that some studies have shown that there is no need for a convergent section of the nozzle to obtain high specific impulses for propulsive applications because of the expansion to Mach numbers over unity within the combustion chamber [14]. This helps to avoid dealing with a critical region in terms of heat loading [13].
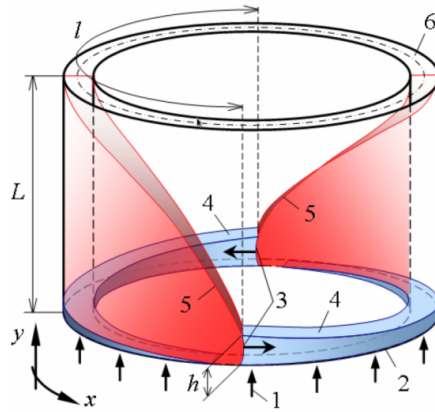
Figure 1.1: Schematic of an operating RDE. (1) Inlet gases, (2) Inlet boundary, (3) Detonation fronts, (4) Unburnt gases, (5) Oblique shocks, (6) Outlet boundary, (h) Detonation front height, (l) Space between successive fronts, (L) Combustor length [6].

There have also been many advances in the experimental field regarding RDEs: several experiments have been carried out at the Institute of Space Propulsion (DLR Lampoldhausen) in Germany to test design methodologies and investigate about the combustion dynamics of RDEs [4]. Moreover, other research groups have achieved flight demonstrations of RDEs, on board sounding rockets by a team at Warsaw University [15], and in space by a team from Nagoya University in collaboration with JAXA (see figure 1.2) [16]. However, there are still many challenges to overcome. The theoretical speed, at which the detonation waves should travel through fresh gases, is known as the Chapman-Jouguet (CJ) detonation velocity. Many authors have pointed out that the achieved speeds in both experiments and numerical simulations are below this value [14][6][17][18][19]. The mechanisms behind these losses are the incomplete mixing of the fresh gases before the detonation wave arrives, parasitic deflagration between the fresh incoming gases and the post-combustion products, wall friction, heat losses, and non-optimal chamber and nozzle geometries. There are currently many efforts into investigating how to mitigate and control these losses to improve RDE performance and increase the level of technological development [11].
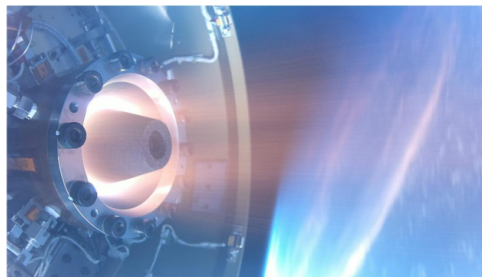
Figure 1.2: RDE operating in space [16].

Although the focus of this work is on cylindrical RDEs, different architectures and concepts have been proposed to enhance performance and aid in experimental data collection. Some authors have designed radial RDEs, where the detonation is sustained between two concentric disks [20]. This type of system has been integrated into turbomachinery for gas turbines (see figure 1.3a), with the objective of increasing efficiency and developing a compact combustor design [21]. In this regard, there have been many efforts in applying the RDE concept to a variety of applications such as aircraft ramjets (see figure 1.3b) [22], gas turbines, and power generation [11].

1.2. Objective and Research Questions

The objective of this thesis is to study the capabilities of the DLR TAU code to simulate 2D and 3D RDE simulations, defining a robust set up that can handle different cases. The designed set up shall be described in detail, considering the different modeling decisions taken, meshing strategies, ignition methods, and

(a) Radial RDE combined with a gas turbine [21].

(b) Rotating detonation ramjet concept [22].
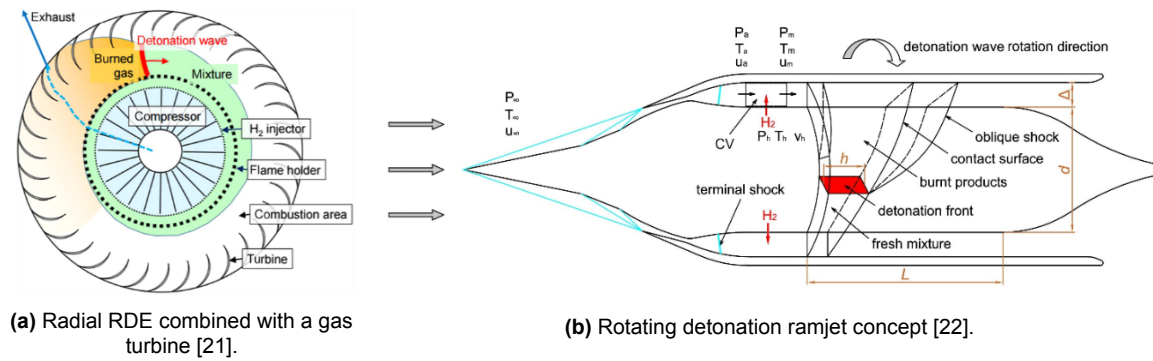
Figure 1.3: Schemes of different RDE concepts.

specified solver parameters. The following research questions shall be addressed regarding the set up definition:

- What is the best available chemical reaction mechanism for this application?
- What meshing strategy is suitable to adequately resolve the main flow features?
- What solver parameters are most suitable for this application?
- What inlet boundary condition is most suitable for this application?
- What is the most reliable ignition method to start the simulations?

When validating the set up with cases from the literature, the simulation results shall be in good agreement. Moreover, it shall be able to adapt to different cases and provide insight into the different flow features and engine performance of each case. The following research questions shall be answered regarding the results:

- To what extent are the main flow features represented in the TAU simulation?
- To what extent does the TAU simulation predict the results from the literature?
- To what extent is the set up stable and robust when running a different case?

The results shall also provide insight about the performance of RDEs and the challenges that these engines present. The formation of multiple competing detonation waves and the interaction between detonation and injection dynamics shall be addressed. The research questions that shall be answered regarding these points are as follows:

- To what extent are the injection and detonation dynamics coupled?
- To what extent is the mixing process during injection having an impact on the results?
- To what extent there is a correlation between the operating conditions and multiple wave formation?

1.3. Structure of the Report

First, chapter 2 presents a theoretical background to better understand the physics of RDEs internal flow and system performance. Afterwards, chapter 3 discusses the state of the art regarding RDEs numerical simulations. Subsequently, chapter 4 provides a detailed explanation of the solver employed to perform the simulations. Then, chapter 5 discusses the 1D and 2D simulations performed to validate the set up and gain insight into simple RDE cases. Chapter 6 shows the results for the Lampoldshausen experimental case employing a simplified 3D geometry, and Chapter 7 presents the results for a 3D case from the literature employing a more realistic 3D geometry. Finally, the conclusions are presented in chapter 8.

<div style="text-align: right; font-size: 3em;">2</div>

Theoretical Background

2.1. Combustion Waves Gas Dynamics

The most important feature within an RDE flow field is the detonation wave moving through the combustion chamber. To compute the properties before and after the shock, a mathematical model has to be defined. Although the flow within a real engine is very complex, the development of a simplified theoretical framework can help to establish relevant trends and identify important characteristics.

The Rankine-Hugoniot relations define the states of the fluid before and after a combustion wave, either a deflagration or a detonation. In the real world, these waves are usually very thin regions of space with very steep gradients, where the thermodynamic properties of the fluid change rapidly. Thus, in ideal flow problems (inviscid, no heat addition, no diffusion, and no chemical reactions) these elements are treated as discontinuities in the flow field [23].

Combustion wave

$$h_0, u_0, p_0, \rho_0 \qquad\qquad h_\infty, u_\infty, p_\infty, \rho_\infty$$
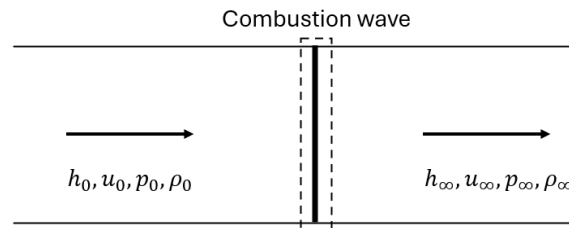
Figure 2.1: Schematic of a 1D combustion wave.

Figure 2.1 shows a simple scheme of a 1D combustion wave, which separates the two states of the gas, where subscript $_0$ indicates the equilibrium state far upstream the wave, and subscript ∞ indicates the equilibrium post-combustion state far downstream the wave. The reference system is defined so that the wave is stationary with respect to the surrounding gas. Since it is assumed to be a 1D problem, the flow properties change only in the x direction. The continuity, momentum, and energy equations are defined as:

$$\rho_0 u_0 = \rho_\infty u_\infty \equiv m \tag{2.1}$$

$$\rho_0 {u_0}^2 + p_0 = \rho_\infty {u_\infty}^2 + p_\infty \tag{2.2}$$

$$h_0 + \frac{u_0^2}{2} = h_\infty + \frac{u_\infty^2}{2} \tag{2.3}$$

where ρ is the density, u the velocity, m the mass flux density, p the static pressure, and h the enthalpy. The heat added to the flow due to chemical reactions is contained within the enthalpy term. As there are multiple species, the species conservation equations shall also be included:

<div style="text-align: center;">4</div>

$$\frac{d}{dx}[\rho Y_i(u + V_i)] = w_i \tag{2.4}$$

where V_i is the diffusion velocity of the species, and w_i the rate of reaction. Since the reactions are assumed to be confined within a fine reaction region where the combustion wave is, the reaction rates at both extremes of the domain shall be zero, which implies that $w_{i,0} = w_{i,\infty} = 0$ for $i = 1, ..., N$.

Lastly, the equation of state for an ideal gas case can be defined as:

$$p = \rho R^0 T \sum_{i=1}^{N} \frac{Y_i}{W_i} \tag{2.5}$$

where R^0 is the universal gas constant, and W_i is the species molecular weight.

Now that all the equations are defined, take equations 2.1 and 2.2 and combine them in one single expression such as:

$$\rho_\infty {v_\infty}^2 - \rho_0 {v_0}^2 = m^2 \left(\frac{1}{\rho_\infty} - \frac{1}{\rho_0}\right) \tag{2.6}$$

Equation 2.6 shows all the states within the domain that meet the continuity and momentum equations, and represents a straight line with a negative slope in a $p - (\frac{1}{\rho})$ diagram. This curve is the Rayleigh line.

Combining now equation 2.1 and 2.3, and employing equation 2.6 to eliminate the m^2 term, the following equation is obtained:

$$h_\infty - h_0 = \frac{1}{2} \left(\frac{1}{\rho_\infty} + \frac{1}{\rho_0}\right)(p_\infty - p_0) \tag{2.7}$$

Equation 2.7 is the Hugoniot curve, which relates the thermodynamic properties of the flow, and can be represented as a convex curve in a $p - (\frac{1}{\rho})$ diagram.

Now, the downstream properties of the flow can be computed. From the upstream variables, the thermodynamic properties and the composition can be fixed experimentally. However, the only parameter that cannot be controlled and is determined by other parameters is the propagation speed v_0. From the known upstream values, and after computing ρ_∞ and p_∞, the downstream temperature T_∞, chemical equilibrium composition $Y_{i,\infty}$, and enthalpy h_∞ can be computed. The graphic representation of this solution would be the intersection of the Rayleigh line with the Hugoniot curve in a $p - (\frac{1}{\rho})$ plane, starting the Rayleigh line at the point with upstream conditions.

The properties of the Rayleigh line and the Hugoniot curve define the possible solutions for the downstream properties. To analyze the different cases, let us define a simplified case. Assume an ideal gas mixture whose final equilibrium composition is the same for all points in the Hugoniot curve, so that the average molecular weight is kept the same ($\overline{W}$), and specific heat at constant pressure (c_p) is also constant. This assumption leads to the following simplification of the ideal gas state equation:

$$\frac{p_\infty}{\rho_\infty T_\infty} = \frac{p_0}{\rho_0 T_0} = \frac{R^0}{\overline{W}} \tag{2.8}$$

After performing some operations with the caloric equation of state and the expression for the heat of reaction of the mixture, employing the aforementioned simplifications, it can be demonstrated that the Hugoniot equation can be written as [23]:

$$\left(\frac{\gamma}{\gamma - 1}\right)\left(\frac{p_\infty}{\rho_\infty} - \frac{p_0}{\rho_0}\right) - \frac{1}{2}\left(\frac{1}{\rho_\infty} + \frac{1}{\rho_0}\right)(p_\infty - p_0) = q \tag{2.9}$$

Equations 2.9 and 2.6 completely define the solution for the simplified system. An example of the curves and possible different solutions is shown in figure 2.2. Consider a case with the initial state being $(1/\rho_0, p_0)$. It can be seen how the Hugoniot curve has two separate branches of solutions. Since the slope of the Rayleigh line is always negative, all the points in the upper-right part of the plot past the segmented lines cannot be a solution to the problem. The upper branch is the detonation branch, which is the region of interest for RDEs operation. The lower branch is the deflagration branch.
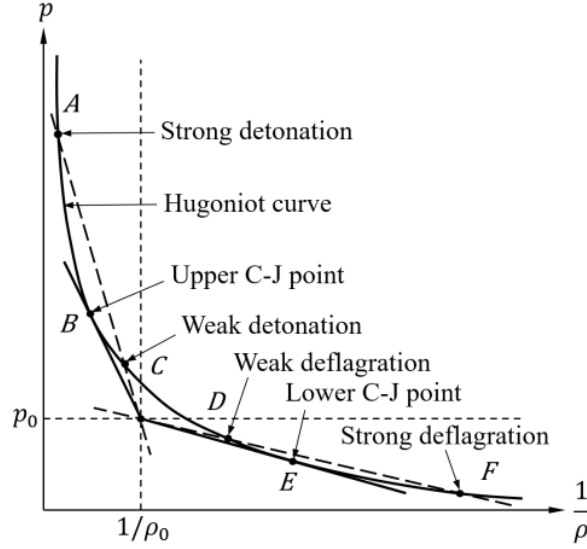
Figure 2.2: Schematic diagram of the Rayleigh and Hugoniot curves [23].

The differences between the branches can be directly seen on the plot. Strong detonations lead to a strong increment of pressure, while leading to a small variation in the specific volume (isochoric combustion). On the other hand, the deflagration waves lead to a very small pressure increase and a great change in specific volume. Deflagration are subsonic waves, while detonations are shocks traveling at supersonic speeds closely followed by a high chemical release region that sustains the traveling wave.

Focusing on the detonation branch, it can be seen how there is one Rayleigh line that, passing through $(1/\rho_0, p_0)$, is tangent to the Hugoniot line. The intersection point in such case is known as the upper Chapman-Jouguet (CJ) point, and the wave associated with said point is a Chapman-Jouguet detonation. Considering the definition of the slope of the Rayleigh line, this tangent point sets a limit to the minimum propagation velocity a detonation wave can have, thus meaning the lower limit for a stable running detonation. Higher values of the slope lead to two possible solutions, as seen in the figure, which can be divided into a strong and a weak shocks. The final state is determined by the experimental conditions. However, it has been proven experimentally that all detonations tend to move towards the Chapman-Jouguet point [23].

Regarding the deflagration branch, the tangent to the Hugoniot line defines the lower CJ point. In this case, due to the definition of the Rayleigh line, it defines the upper limit of a deflagration's propagation velocity. Lower values give two different solutions, however, experiments have shown that strong deflagrations do not occur, and most are nearly isobaric [23].

Based on the assumptions that heat capacity is constant, the gas mixture can be modeled as an ideal gas, and also assuming that $p_\infty \gg p_0$, the CJ velocity can be approximated as follows [24]:

$$u_{CJ} = \sqrt{2(\gamma^2 - 1)q_c} \tag{2.10}$$

where q_c is the heat release per unit mass flux, and is defined by the following expression:

$$q_c = c_p(T_\infty - T_0) + (h_\infty - h_0) \tag{2.11}$$

Equation 2.10 shows there is a direct relationship between the chemical heat release and the CJ velocity. The more exothermic the global set of reactions is, the faster the detonations will travel. It can be proved that at each CJ point the Mach number becomes unity. Moreover, along the Hugoniot line, the upper CJ point has local minimum entropy, while it is a local maximum at the lower CJ point.

The physical mechanism behind the transition from the initial state to the CJ point is different for strong and weak detonations. Shock tube experiments have shown that when a strong shock is originated, a rarefaction wave appears following the detonation. Their interaction weakens the detonation wave, shifting the fluid state towards the CJ point. When arriving at the CJ state, the postcombustion products become sonic with respect to the detonation, and the rarefaction wave can no longer influence the detonation, hence being a stable point. On the other hand, weak detonations show a monotonic increase of the pressure behind the detonation wave while propagating, moving the state of the fluid towards the CJ point [23].

Based on experimental results and CJ theory, a traveling detonation through a fresh mixture of reactants should achieve the Chapman-Jouguet velocity. In the case of RDEs, assuming curvature and wall friction have a negligible effect on the detonation propagation velocity, the detonation waves should achieve CJ velocity. Thus, CJ conditions serve as a reference for comparing the measured detonation velocity of an RDE and assessing losses.

2.2. Detonations

Let us consider a long enough tube filled with a combustible mixture. The mixture is ignited on one end, originating a deflagration wave traveling through the mixture. If the wave propagates for a long enough distance, it will transition into a planar detonation wave moving at speeds around the upper CJ point, as seen in the previous section. The transition from deflagration waves to detonation waves is a matter of current research [25]. Furthermore, detonation can also be generated by a strong shock passing through a combustible mixture, leading to the formation of a strong detonation if the pressure jump is high enough. Shocks can also ignite a mixture if the gases are preheated, without the need of very strong shocks. Once the detonation has been generated, it will tend to move at CJ velocity.

2.2.1. ZND Detonation Structure

A detonation wave can be described as a shock followed by deflagration. The shock heats the reactants, and they react fast enough so that the deflagration can follow the shock's pace. The first structure for detonations was proposed by Zel'dovich, von Neumann, and Döring [23]. This model is referred as the ZND wave structure. Figure 2.3 shows a schematic of the different regions and states that conform a detonation. Within the induction region the changes in the thermodynamic variables are small and the rates of the reactions are low. Then, the main chemical heat release occurs within the energy release region, shifting the properties of the flow towards the post-combution equilibrium values [26]. The model excludes weak detonations, however, it applies to most detonations seen in experiments. Later studies show that the structure is more complex, being a three-dimensional combination of traverse waves that, on average, form a planar moving wave [23].
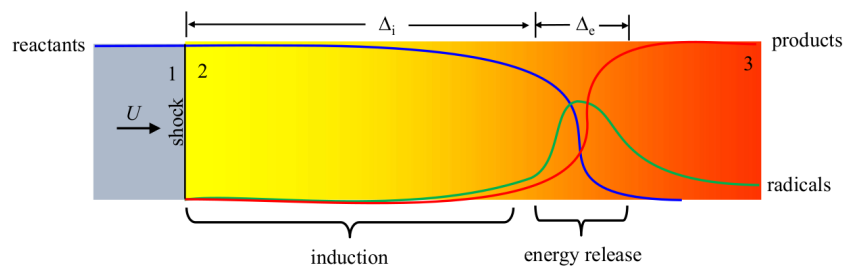
Figure 2.3: Schematic of the ZND detonation model showing the three different states (1, 2, 3) and the different reaction zones (induction and energy release) [26].

Simple analytical solutions for the shock wave structure can not be obtained with the continuum assumption equations unless the effective Prandtl number is $\frac{3}{4}$ [23]. The deflagration behind the shock is a high speed wave very different to standard subsonic deflagrations. In this case, viscosity, heat conduction,

and diffusion phenomena are negligible. The difference originates in the higher mass flow rate associated to detonations. Convective fluxes become orders of magnitude higher than transport fluxes, and the reaction rates are generally not high enough to compensate the difference. The chemical timescale determines the width of the reaction zone (energy release region in figure 2.3), but it is not tightly coupled to the speed of the detonation wave. Within the ZND structure, the shock is treated as a discontinuity, where the viscous and molecular transport interactions with the reaction region are negligible and do not alter significantly the structure of the wave. The wave is sustained not by molecular transport, but by compressible effects arising from the chemically reacting region. Exothermic recombination reactions create reaction products, which are expanded behind the shock creating a series of compression waves that sustain the shock [26].
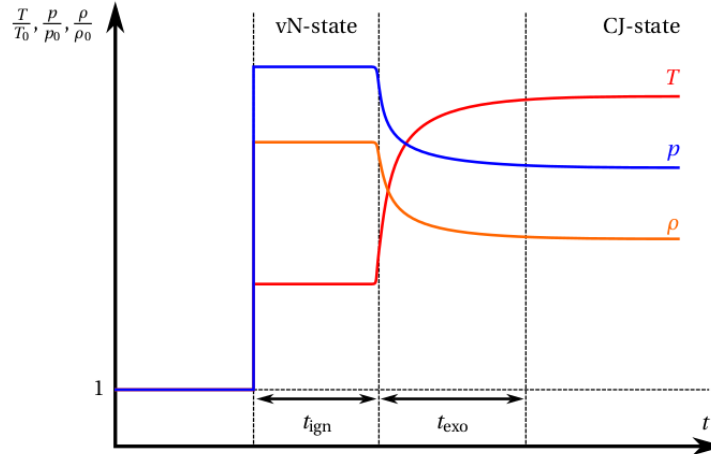
Figure 2.4: Schematic of the ZND detonation model showing the variation of different thermodynamic variables [25].

Figure 2.4 shows how the different thermodynamics variables change, having a decrease in static pressure due to the expansion of the combustion products, while increasing the temperature due to the chemical heat release. The plateau region where the variables remain constant is known as the von Neummann (vN) state, and the postcombustion state corresponds to the CJ state [25].

2.2.2. Three-dimensional Detonation Structures

Planar CJ waves do not exist since they are very unstable to pressure disturbances. The mechanisms that sustain these disturbances depend on how fast the heat is released, as well as on the detonation's characteristics [23]. Thus, detonations show a complex 3D structure. Figure 2.5 shows a simplified 2D scheme of a 3D detonation.

Figure 2.5 shows the standard rhomboid pattern of a 3D detonation outlined by the dashed lines. This pattern has been proven experimentally [27] and numerically [28]. The pattern represents the displacement of the triple points that constitute the shock front. Three shocks interact at those points, being local peaks of pressure, and they interact with each other while advancing. The transverse waves (T) stabilize the detonation front, and interact with the leading shock (LS) to produce the Mach stem (M). Taking a streamline in front of the detonation, a fluid particle has to cross both the LS and T waves to meet the particles that have crossed the M wave, which means that the M wave is the strongest. Since the velocity is subsonic after the M wave, the ignition time is shorter and the reaction front is closer to the Mach stem. The reaction region behind the LS wave is thicker as the flow is still supersonic, and behind the T wave there is no clear reaction region since the shock is not strong enough to ignite the mixture and the residence time is very low [25].

Let us consider a single cell: right after the collision and reflection of two triple points, a localized release of energy generates an M wave. The wave intensity decreases as it advances. For a regular pattern, when the shock arrives to the middle of the cell, a new reflection of triple points takes place, generating new M waves. Thus, the previous M wave becomes an LS wave until the detonation cell ends due to another collision of triple points [25]. This pattern keeps repeating itself as the detonation moves through a medium. The most relevant parameter that characterizes detonations is the detonation cell size λ. It depends on the gas mixture, and has an impact on the detonation behavior. The propagation of a self-sustained detonation
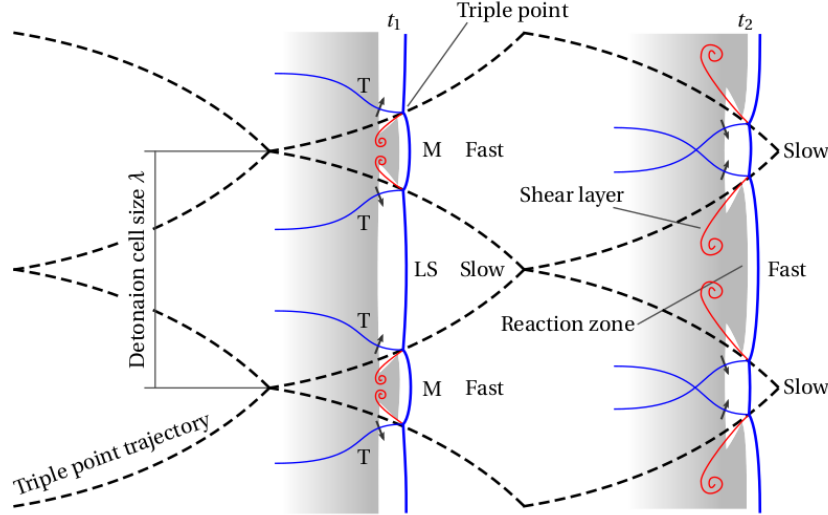
Figure 2.5: Schematic of the 3D structure of a detonation wave [25].

within a medium confined by two walls is determined by the ratio between the width of the channel and the detonation cell width. If the width is too small, the detonation will quench and fade away. Similarly, it also determines the minimum height of a combustible mixture boundary layer for a detonation through it without quenching [23].

The pattern presented in figure 2.5 is applicable for a regular case. The nature of said pattern depends on the gas mixture and the conditions it is subjected to. Moreover, although the detonation front is a combination of different shocks that move at different speeds, the velocity can be considered as the average speed of the shock front. This value is close to the 1D approximations given by CJ approach seen before [25].

2.3. Chemical Reaction Mechanisms

A chemical reaction mechanism is a set of chemical equations that describe the process of how reactants are transformed into products during the combustion process. It is relevant to properly capture this process since it determines the heat generated by the reaction, which determines the detonation properties. Moreover, depending on the number of reactions considered and the different species, important physical properties such as ignition delay times, flame speeds, and the variation of species concentration can be accurately predicted. This has a high impact on the final results, since not all mechanisms are applicable to every set of conditions. For certain applications, while one mechanism could predict a sustained reaction, a different mechanism could predict the extinction of the flame. The applicability range of a mechanism and its degree of precision depend on the reliability of the experimental data used to define its parameters. Therefore, it is important to evaluate the different options available before running any simulations, to ensure an adequate mechanism is employed.

As seen in the previous section, each new species included is modelled by a conservation equation (see equation 2.4) including a source term for the rate of reaction w_i. This term is computed by the law of mass action in the following manner [29]:

$$w_i = W_i(\nu_i'' - \nu_i') \left(k^f \prod_{n=1}^{ns} C_n^{\nu_n'} - k^b \prod_{n=1}^{ns} C_n^{\nu_n''} \right) \tag{2.12}$$

where W_i is the molecular weight, ν_i'' and ν_i' are the stoichiometric coefficients of the products and reactants respectively, k^f and k^b are the rate of reaction coefficients for the forward and backward reactions respectively, and C_n is the species concentration. The forward rate coefficient is computed employing the Arrhenius equation [30]:

$$k^f = AT^n \exp\left(\frac{-E_a}{RT}\right) \tag{2.13}$$

where A and n are reaction constants, and E_a is the reaction activation energy. All these parameters are provided by the chemical reaction mechanism for each of the reactions. They are obtained from analytical results and fitting of experimental data. Some authors also state the level of uncertainty of the parameters [31][1][32]. To compute the backward reaction rate some authors employ the equilibrium constant (K^{eq}) to save computational time [30]. The expression is as follows:

$$k^b = \frac{k^f}{K^{eq}} \tag{2.14}$$

Equation 2.13 shows a clear dependency of the reaction rate on temperature. However, some reaction rates are also dependent on pressure. To introduce this dependency, the forward reaction rates at high (k^f_∞) and low pressure (k^f_0) limits are defined. They are computed employing equation 2.13 substituting their specific constant values. Then, the rate constant at any pressure can be computed as follows [33]:

$$k^f_p = k^f_\infty \left(\frac{P_r}{1 + P_r}\right) F(T, P_r) \tag{2.15}$$

where P_r is the reduced pressure, and F a correction function that can take different forms depending if the Lindemann's or the Troe's approach are chosen [30][33].

The reduced pressure P_r is defined as:

$$P_r = \frac{k^f_0 [M]}{k^f_\infty} \tag{2.16}$$

where $[M]$ is the mixture's concentration, or the concentration of a third-body specie that has an influence on the kinetics of the reaction.

2.3.1. H_2-O_2 Reaction Mechanisms

Evans et al. [34] proposed a 12-species 25-reaction chemical reaction mechanism for computing supersonic hydrogen flames. In this case, it is important to properly compute the ignition delay time, since it can determine whether the flame is stable or it will extinguish. Hence, reactions that control the concentration of radicals such as H, O, and OH, which help sustaining the flame, are very important. Moreover, the different reaction paths considered help to better predict the ignition phenomena due to the presence of different sinks and sources of the radicals. For instance, Evans et al. [34] added to a previous chemical reaction mechanism reactions which considered HO_2 molecules, which become important at low temperature ignition processes. Furthermore, the presence of NO and NO_2 in the air make the mixture more sensitive to ignition at low temperatures.

Jachimowski [31] developed a chemical reaction mechanism tailored to hydrogen-air combustion for scramjet applications. The reaction constants are set to properly adapt the results to shock-tube ignition delay results, as well as burning velocity data. It is a 12-species and 33-reaction mechanism. Moreover, it is not pressure dependent, but has different third-body efficiencies for different species. The author states that the ignition delay times and burning velocities are very sensitive to the following reactions:

$$H + O_2 \rightarrow OH + O \tag{2.17}$$
$$H + O_2 + M \rightarrow HO_2 + M \tag{2.18}$$
$$H + OH + M \rightarrow HO_2 + M \tag{2.19}$$
$$H + HO_2 \rightarrow OH + OH \tag{2.20}$$

Here M is a third-body molecule. It can be seen from the equations above that HO_2 chemistry is very relevant to the reaction mechanism. Reaction 2.18 is the main source of HO_2, and reaction 2.20 is the primary chain-branching reaction, which sustains the combustion due to OH radicals being very reactive. Both reactions are exothermic.

If the production and consumption of HO_2 is not properly modeled, not enough chain-branching reactions would take place, and the ignition process would not be captured and early extinction could occur. However, it is important to mention that not all reactions and paths are equally relevant in every case. If the residence time within a region is very low, third-body reactions can be considered to be frozen. Jachimowski et al. [31] studied the flow within scramjets employing their reaction mechanism. Results showed that for Mach 8 the overall reaction rate is controlled by the propagation, recombination, and consumption of HO_2. On the other hand, when going up to Mach 25 the overall reaction rate is mainly controlled by the recombination process.

Different authors have employed the Jachimowski mechanism to conduct studies on combustion processes. Gaffney et al. [29] employed a reduced version of the mechanism only considering the first 7 reactions. It did not consider HO_2 chemistry. The objective of the work was to study how temperature fluctuations influence the combustion process in a mixing layer employing an assumed PDF method to model the interaction. Instead of computing the production terms from the average temperature, this approach computes the mean production terms in the following fashion:

$$\overline{w_i} = \int_0^\infty \int_0^\infty w_i P(T) dT dC_n \tag{2.21}$$

where $P(T)$ is the probability density function that models the temperature fluctuations, and C_n is the species concentration. This approach allows to better predict local ignition processes and non-linear phenomena associated with the fluctuations.

Gerlinger et al. [35] employed a reduced version of the Jachimowski mechanism to study the influence of turbulence in combustion processes. The new mechanism excludes the nitrogen reactions, but considers the presence of diatomic nitrogen N_2. It has a total of 9 species and 19 reactions. The authors studied the influence of turbulence employing a presumed pdf approach. It had an important impact on the ignition delay time due to the fluctuations in temperature and species concentration. Therefore, even if an accurate chemical reaction mechanism is employed, other mathematical modeling decisions such as turbulence treatment can impact the results. Moreover, finite-rate chemistry modeling tends to cause the system of equations to become numerically stiff. Gerlinger et al. employed an implicit time integration method to deal with the wide range of time- and length-scales present in the flow and ensure stability of the simulation. Hence, when introducing detailed chemical reaction mechanisms special care has to be taken regarding numerical stability.

Ó Conaire et al. [1] improved the mechanism from Mueller et al. [36] employing new experimental data. The experimental data expanded the mechanism for higher pressure and temperature ranges. It resulted in a 9-species and 19-reaction mechanism. After performing a sensitivity analysis, the most sensitive reactions are the following:

$$H + O_2 \rightarrow OH + O \tag{2.22}$$
$$O + H_2 \rightarrow H + OH \tag{2.23}$$
$$OH + H_2 \rightarrow H + H_2O \tag{2.24}$$
$$O + H_2O \rightarrow OH + OH \tag{2.25}$$
$$H + OH + M \rightarrow H_2O + M \tag{2.26}$$
$$H + O_2 + M \rightarrow HO_2 + M \tag{2.27}$$
$$HO_2 + H \rightarrow H_2 + O_2 \tag{2.28}$$
$$HO_2 + H \rightarrow OH + OH \tag{2.29}$$
$$H_2O_2 + H \rightarrow H_2 + HO_2 \tag{2.30}$$
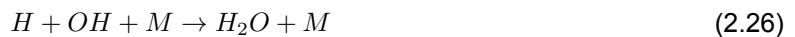
Ignition delay is mostly influenced by reaction 2.27, and to a lesser extent by reactions 2.22 and 2.30. This is in agreement with the Jachimowski scheme reactions mentioned above, which stated the relevance of HO_2 chemistry in ignition processes. Moreover, reaction 2.22 is the most relevant reaction when modeling freely propagating flames and flame speeds. This is because it is a chain-branching reaction that sustains the flame. Reaction 2.24 also showed some influence in flame speed calculations, which is explained due to the fast chemistry of the OH radical. Furthermore, high-pressure experiments data show how the third-body reactions gain relevance in very high pressure environments, changing the main reaction paths. The Ó Conaire mechanism was defined employing a wider set of data than Jachimowski, hence the constants are different. Nevertheless, they only differ in reactions for the production and consumption of H_2O_2 and HO_2.

Hong et al. [32] proposed an improved 9-species 20-reaction mechanism. It expanded the experimental data employed by previous authors to determine the constants. When directly compared with the Ó Conaire mechanism, it proved to match better the experimental results. Moreover, compared to the Jachimowski mechanism, it considers an extra reaction regarding the consumption of H_2O_2. Hong et al. stated that the current mechanisms can properly predict chain-branching reactions to accurately compute ignition delay times. However, there are still relatively large uncertainties when it comes to HO_2 and H_2O_2 dominated systems. Furthermore, authors such as Ó Conaire suggested that reactions $H + HO_2 \rightarrow H_2O + O$ and $H + HO_2 \rightarrow OH + OH$ were kinetically similar, hence only added the latter to their mechanisms. It was found in sensitivity analysis that they have different signs on their influence on the laminar flame speed, so both reactions were added to the Hong et al. mechanism. Additionally, the chain-initiation reaction $H_2 + O_2 \rightarrow OH + OH$ was found to be very unlikely, thus, it was removed. Another reaction left out of the mechanism is $O + OH + M \rightarrow HO_2 + M$. Although it has an impact on lean high-pressure flames, the uncertainties associated to its rate constants are too high to provide accurate enough results. On the other hand, some relevant reactions have been included in the mechanism regardless of the uncertainty associated. $H + O_2 \rightarrow OH + O$ is one of the most important reactions in combustion and has been thoroughly studied. However, it still has a high uncertainty due to the lack of data for the reaction rates of $H + HO_2 \rightarrow H_2 + O_2$. Certain reactions also have high errors associated due to the lack of experimental data in high-pressure environments. Reaction $H_2O_2 + M \rightarrow 2OH + M$ is the main kinetic feature in spark ignition and liquid-fueled diesel engines. It is the dominant chain-branching reaction which controls the thermal decomposition of H_2O_2. Although the associated error is not negligible, it was added to the mechanism. Reactions which strongly vary with temperature also have high uncertainty associated. $OH + HO_2 \rightarrow H_2O + O_2$ is one example. Lastly, reactions $H + HO_2 \rightarrow 2OH$ and $H + HO_2 \rightarrow H_2 + O_2$ have been proven to be critical in modeling the species time-histories in flow reactor studies, and in flame speeds calculations. Even though there is a lack of experimental data to reduce the uncertainty, they were included in the mechanism.

As mentioned before, very detailed reaction mechanisms can lead to high computational costs and numerical stiffness. Therefore, some efforts have been invested into reducing the size of the mechanisms while keeping a good accuracy. Boivin [37] proposed different reduced chemical kinetics mechanisms obtained from a baseline 12-reaction scheme. As stated by the author, the baseline chemical mechanism has all the required reactions to accurately predict premixed and non-premixed flames, autoignition, and detonation under conditions of interest. Reactions such as $HO_2 + H \rightarrow H_2O + O$ and $HO_2 + H \rightarrow OH + O$ are eliminated since they were unimportant in many conditions compared to other HO_2 reactions. On the other hand, to properly compute high-pressure deflagrations and autoignition, and detonations, it is important to retain the following reactions:

$$HO_2 + HO_2 \rightarrow H_2O_2 + O_2 \tag{2.31}$$
$$H_2O_2 + M \rightarrow 2OH + M \tag{2.32}$$
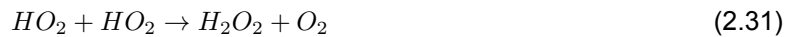
As mentioned by Hong et al., H_2O_2 becomes relevant at high pressures due to production from HO_2 when the concentration is high enough. It is also relevant in low temperature regions at atmospheric pressure. After evaluating the relevance of all the reactions within the mechanism, Boivin performs a steady-state approximation for intermediate species to obtain different reduced reaction mechanisms. The global rates of the new set of equations are a linear combination of the reaction rates of the baseline mechanism, the

temperature, and the concentration of the relevant species. The algebraic system of equations is then solved instead of the extra species transport equations to obtain the results.

Lastly, table 2.1 presents a brief summary of the reaction mechanisms commented in this section.

Table 2.1: Summary of H_2-O_2 reaction mechanisms.

Name	No. Species-Reactions	Pressure Dependent	Ref.
Evans	12-35	No	[34]
Jachimowski	12-33	No	[31]
Gaffney	6-7	No	[29]
Gerlinger	9-19	No	[35]
Ó Conaire	9-19	Yes	[1]
Hong	9-20	Yes	[32]
Boivin (Baseline)	9-12	Yes	[37]

2.4. RDE Theory

2.4.1. Thermodynamic Cycle Analysis

Thermodynamic cycle analysis provides a simple way of estimating the maximum expected thermal efficiency of a system. Thermal efficiency is defined as the ratio between the net work done (w) and the added heat (q_c), which in an RDE is by combustion.

$$\eta_{th} = \frac{w_{net}}{q_c}$$

(2.33)

Conventional deflagration-based combustors are studied employing the ideal Brayton-Joule thermodynamic cycle. Since this is an ideal cycle, expansions are isentropic, and the heat addition process is considered isochoric (constant volume). As seen above in figure 2.2, the change in pressure through a deflagration wave is negligible. Hence, it can be approximated as a constant-volume process due to the small change in density.

On the other hand, different ideal cycles have been proposed to study pressure-gain combustor processes, such as the Humphrey and the Fickett-Jacobs cycles. However, it has been suggested by different authors that the Fickett-Jacobs cycle is a better approximation of the detonative combustion process within a pressure-gain combustor due to including the CJ detonation condition [38][12].
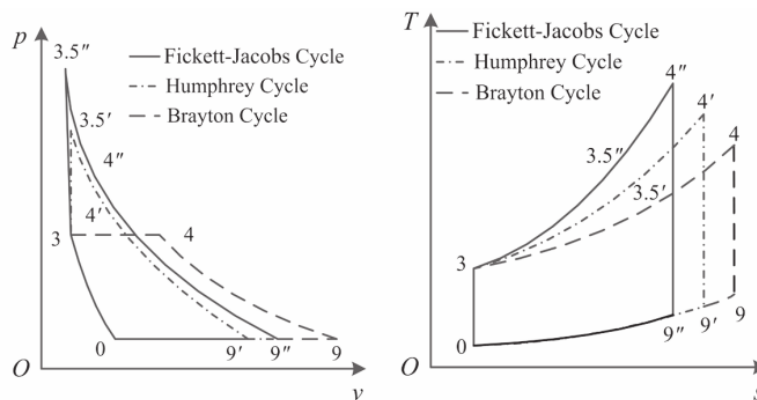
Figure 2.6: Comparison between the ideal Brayton, Humphrey and Fickett-Jacobs cycles [38].

Figure 2.6 shows a direct comparison of the three cycles on a $p-v$ and a $T-s$ diagram. It can be seen how the pressure peak of the Fickett-Jacobs is the highest of the three, while also having the lowest maximum entropy. Hence, this implies that the highest efficiency is achieved with a pressure-gain engine,

which is one of the main motivations to pursue the development of this type of technology. Moreover, this cycle allows to set an upper bound on the maximum thermal efficiency that can be achieved by an RDE [38][39].

Let us compute the thermal efficiency assuming a thermally and calorically perfect gas and a constant γ to compute the detonation process. The expression to compute the thermal efficiency is as follows [38]:

$$\eta_{th} = 1 - \frac{c_p T_0}{q_c} \left[\frac{1}{M_{CJ}^2} \left(\frac{1 + \gamma M_{CJ}^2}{1 + \gamma} \right)^{(\gamma+1)/\gamma} - 1 \right] \tag{2.34}$$

where the Mach number M_{CJ} is computed from the CJ ideal detonation velocity. This expression shows that the higher this value is, the higher the efficiency. Moreover, the higher the combustion heat release, the higher the CJ detonation velocity. Therefore, a high combustion heat release will lead to a high thermal efficiency. Higher M_{CJ} is related to a stronger detonation. This causes a stronger expansion of the postcombustion gases, which leads to a further reduction of the temperature when arriving to state 9 in figure 2.6, and thus less heat is exchanged during 9-0 isobaric process, increasing the thermal efficiency [38].

However, the application of this type of ideal analysis is limited to the definition of an upper bound. Since it does not consider complex phenomena within the RDE flow field and combustion processes, it can not provide a good estimate of a realistic engine performance.

2.4.2. RDE Operation

RDEs are characterized by the design of the injection system, the combustion chamber conditions and geometry, and the exit conditions. There is a strong coupling between the different elements. These complex interactions define the performance of the engine and are not captured by the idealized model of the previous section. Before defining any new models, let us describe the different processes involved in the operation of an RDE and how they interact with each other.

Figure 2.7 shows schematically the main features of an RDE, as well as offering a detailed view of the injector geometry and of the flow field near the detonation wave. First, the fresh gases enter the combustion chamber through the injectors. It can be seen in the figure how there is a mixing region below the detonation. The mixing process is key to sustain a stable detonation [9]. Ideally, the shock front should meet both fuel and oxidizer perfectly mixed at a molecular level. Theoretically, this could be obtained by injecting fuel and oxidizer already premixed. Some authors have pointed out that this approach leads to unstable modes of operation and flashback problems within the injectors [18][19]. Thus, different injection approaches have been studied, to assess the impact on engine performance and to evaluate the most efficient method [40]. Results showed that the length-diameter ratio of the injection ports determined the stability of the detonations. Moreover, Schwer et al. [41] showed with his numerical results that the measured thrust can show an oscillatory behavior when increasing the length-diameter ratio of the injection ports.

The pressure waves also propagate upstream the injectors, arriving to the plenum. The interaction between the detonation and the injectors is a subject of study since it causes pressure oscillations that affect the mixing process and hence influence the combustion process [39]. This interaction can lead to low-frequency periodic unstable detonation waves within the combustion chamber [40]. Moreover, inefficient mixing leads to detonation fronts being broader, and it is also linked to propagation velocities lower than the CJ velocity. If the reactants are not properly mixed, concentration gradients will be present within the flow. This can lead to complex detonation front structures and uneven heat loading on the inner and outer walls of the combustion chamber [28]. These concentration gradients change the propagation characteristics of the detonations, and can cause a separation between the leading shock and the reaction behind, causing the detonation to vanish [39].

As it can be seen in the unwrapped flow field view of figure 2.7, the fresh mixture of gases entering the chamber can suffer from autoignition (B) due to high pressures and temperatures, or mix within recirculation zones (R) caused by the interaction of the fresh gases with the moving detonation. Due to the high local pressure after the detonation has passed, there is a recovery time before the new fresh gases can enter the combustion chamber. Since fuel and oxidizer do not have the same density, and the total pressure in
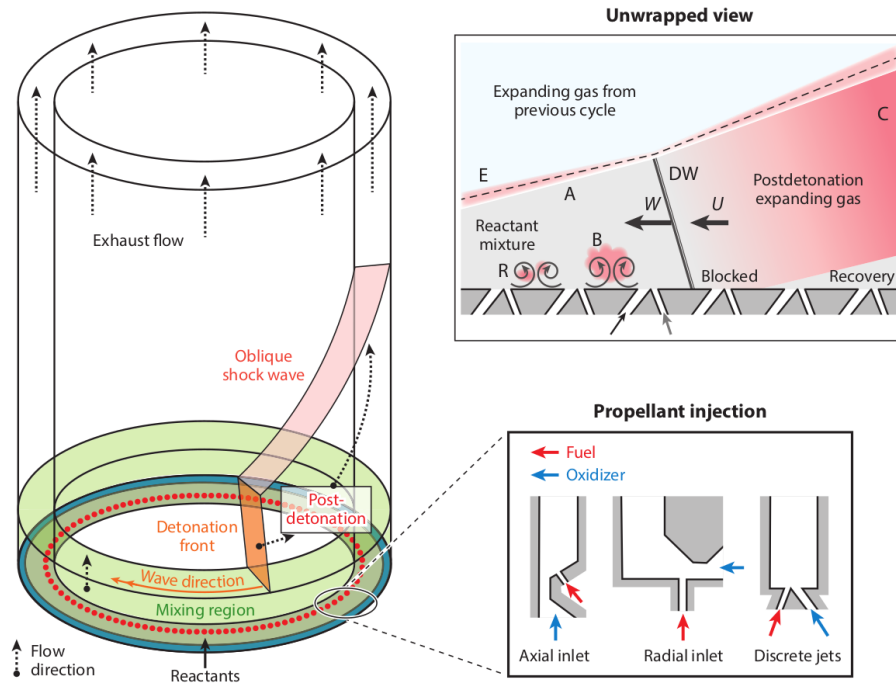
Figure 2.7: Scheme of the main features of an RDE with different injection configurations. A simplified image of the flow field is also shown, outlining the main elements: fresh gases (A), autoignition of injected gases (B), postcombustion gases expansion with low pressure commensal combustion (C), contact region between fresh gases and postcombustion gases from the previous cycle (E), and recirculation region due to injection recovery (R). U is the induction velocity and W the detonation wave (DW) velocity [11].

their plena and interaction with pressure oscillations can be different, the recovery times can differ as well. This leads to a stratification of the mixture and alters the local equivalence ratio [11]. This coupling between the detonation dynamics, the inlet mass flow and the equivalence ratio determines the combustion mode, and whether it will be stable or unstable [39].

Frolov et al. [42][43] performed a series of 3D URANS simulations of RDEs. The results showed that more than one detonation wave of different intensity can coexist within the combustion chamber. Moreover, Yao et al. [44] showed with his numerical simulations that multiple detonations of the same strength can coexist as well (see figure 2.8). Other studies evaluated the effects of changing the number of injectors and oxidizer mass flow rate for a fixed fuel mass flow rate on the detonation dynamics. It was shown that depending on the mass flow and local mixing efficiency the combustion mode changed between single-wave mode, alternating single- and double-wave modes, and double-wave mode [45]. As the oxidizer mass flow increased, only the single-wave mode occurred, which is also the behavior seen in the experiments performed by Frolov et al. [46]. However, other authors have found that increasing the oxidizer mass flow rate can lead to multiple detonations due to combustion instabilities. Furthermore, if the fuel mass flow is lowered, double-wave collisions will take place within the combustor. In fuel rich conditions single-wave mode is dominant, and as conditions become leaner, double-wave mode becomes more dominant [39].

The injection pressure has an influence in detonation dynamics since it is linked to the mass flow. Wu et al. [47] evaluated the influence of this parameter on the combustion process. The results indicate that the detonation front tends to become unstable as the total pressure increases. It can lead to a periodic oscillation of the detonation's intensity, changing from a weak to a strong state at a fixed frequency resulting from the interaction between the injection and the detonation dynamics. On the other hand, a minimum critical total pressure is required to sustain a stable detonation [11]. If the total pressure is too low, the mass flow will not be high enough to sustain the traveling detonation.

The ignition process also plays a relevant role and is connected to the combustion mode within the engine. It determines the initial energy provided to the flow to start the detonation. There are two types of
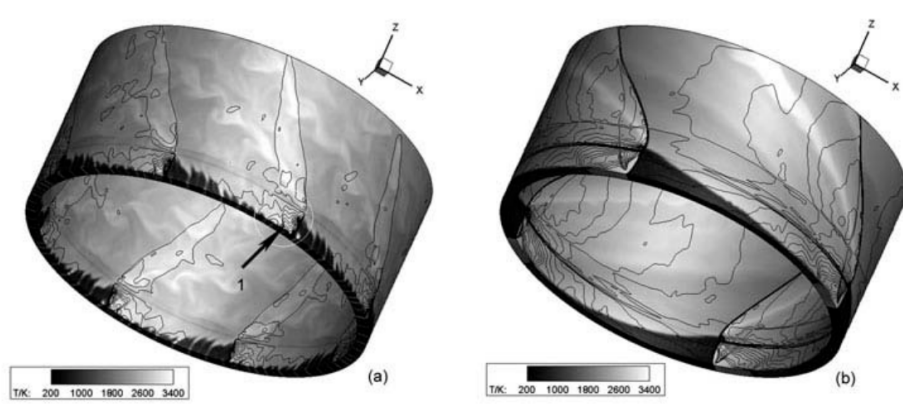
Figure 2.8: 3D simulation results of multiple detonations propagating showing static temperature (colored) and pressure (isolines) for two different cases [44].

ignition methods: direct methods where enough energy is provided to the flow to generate a detonation, or indirect methods where a small amount of energy is employed to ignite a deflagration wave that will suffer a deflagration-to-detonation transition (DDT) [25] along a pre-detonation tube. It has been proven in the literature that the ignition process does not have a relevant influence on the propagation velocity of the detonations. However, the transition from the ignition process to a stable detonation is not well understood. Moreover, there is yet not a complete control of the detonation's propagating direction after ignition [39].

Lastly, the outflow of the expanded gases can have an influence on the combustion mode within the combustion chamber. Pressure waves can be reflected at the nozzle throat due to abrupt changes in geometry or regime transition. The transition from subsonic to supersonic flow at the throat can cause the partial reflection of pressure waves back to the combustion chamber. This can lead to changes in the combustion mode, potentially hindering detonation stability and engine performance [48].

2.4.3. Wave Multiplicity Model

RDEs are a complex dynamic system where each element interacts with all others. There is no analytical theory that can predict the equilibrium point of the engine [11]. This section presents a simple model proposed by Wolański et al. [49] that aims to find the minimum mass flow required to sustain the stable propagation of a certain number of detonations for a combustion chamber with a defined geometry and fixed operating conditions.

The equation that relates the number of detonations (n_w) to the mass flow and combustion chamber geometry was proposed by Wolański et al. [49] and then corrected by Connolly-Boutin et al. [50]. The equation is as follows:

$$n_w = \frac{\dot{m}}{\rho V_D h_z \Delta} \tag{2.35}$$

where V_D is the detonation propagation velocity, ρ is the density of the reactant mixture, h_z is the height of the fresh reactant layer, and Δ is the width of the combustion chamber.

The model identifies three basic criteria to ensure the stable propagation of a detonation:

- The wave number shall be at least unity, and close to an integer [49].

- The width of the combustion chamber shall be big enough to fit 2.5 to 3 detonation cell widths (λ) [9].

- The aspect ratio of the filling height with respect to the combustion chamber width shall be high enough so that the fresh layer of gases is robust against perturbations. It can be expressed as: $h_z > K_L \Delta$, where $K_L \approx 5$.

The injection velocity is assumed to be constant and always positive, so it does not account for back-propagation. There is no mixing layer since the reactants enter the chamber perfectly mixed, and there is no recovery time for the injection process. Moreover, detonations are assumed to be homogeneous, moving at a constant velocity, and equidistant of each other.

A correction to the equation was proposed by Hermannsson [51] to account for the time recovery of the injector after a detonation has passed. The corrected mass flow rate can be expressed as:

$$\dot{m}^* = \rho v_{inj} A_{eff} \tag{2.36}$$

where v_{inj} is the injection velocity and A_{eff} is the effective area of injection. This quantity is expressed as follows.

$$A_{eff} = d_n \pi \Delta (1 - \varepsilon') \tag{2.37}$$

where d_n is the outer diameter of the combustion chamber, and ε' is the fraction of the input area blocked by the pressure increase caused by the detonation.

Including this term in equation 2.35 leaves the following expression:

$$n_w = \frac{\dot{m}}{\rho V_D h_z \Delta} (1 - \varepsilon') \tag{2.38}$$

The two variables in equation 2.38 that have to be defined in order to close the model are the filling height h_z and the blockage factor ε'. A scaling law for the filling height was proposed by Bykovskii et al. [9]:

$$h_z \in [7\lambda, 17\lambda] \tag{2.39}$$

This equation introduces a non-negligible uncertainty into the model. Not only due to the variable scaling factor, but also because of the detonation cell width λ. As seen previously in this chapter, this quantity depends on the gas mixture and its conditions. There is no analytical theory that can predict the cell width, thus, experimental data is often employed. Hermannsson [51] used the data from the GALCIT database of the Explosion Dynamics Laboratory at the California Institute of Technology [52] and obtained the following expression for the detonation cell width for a H_2-O_2 mixture.

$$\lambda = 148.32 P_{init}^{-1.006} \tag{2.40}$$

where P_{init} is the initial pressure of the mixture before the detonation.

Connolly-Boutin et al. [50] also performed the same curve fitting procedure for other mixtures such as H_2-Air and C_2H_4-O_2-N_2. In their work they also considered different equivalence ratios.

On the other hand, the blockage effects depend on the detonation characteristics and their interaction with the injection conditions. Goto et al. [53] showed that the effective injection area is proportional to the ratio of the plenum pressure to the combustion chamber pressure ($\varepsilon' \propto P_m/P_c$), known as injector stiffness. Hermannsson [51] defines the blocked area fraction as follows:

$$\varepsilon' = \frac{t_r}{t_p} \tag{2.41}$$

where t_r is the total recovery time of injection, and t_p is the detonation period. This quantity is defined as the time difference between detonations from a fixed point of view on the injector plane in the combustion chamber. It can be defined as:

$$t_p = \frac{d_n \pi}{n_w V_D} \tag{2.42}$$

Since equation 2.42 only depends on combustion chamber geometry and detonation characteristics, the recovery time shall be dependent on the pressure ratio of the plenum and the combustion chamber to agree with the results from Goto et al. [53]. This is what Celebi et al. [54] identified, proposing an equation fitted with empirical data of the recovery time of an injector after a detonation wave. This equation closes the proposed model and allows to approximate the number of detonation waves for a given mass flow, chamber geometry, and operating conditions employing equation 2.38.

2.4.4. Flow Field Characteristics

Section 2.4.2 explained the operation of an RDE, showing the complex interactions between the different elements. The modeling of this type of engine is complicated, and only simplified analytical approaches have been developed to try to predict the equilibrium point of operation, as seen in section 2.4.3. Apart from performing experiments, another approach to studying and predicting engine performance is through numerical simulations. However, it is not trivial to set up a simulation that can properly resolve the flow field within an RDE due to the range of length and time scales involved. This section aims to cover the different flow features and scales present in the flow field.

Figure 2.9 shows an example of an unwrapped RDE flow field [6]. The images on the left show an instantaneous snapshot in time of the results, while the images on the right show an average of the flow field values over several detonation periods. Comparison clearly shows the unsteadiness of the flow field. Images a) and c) show how the detonation wave is inhomogeneous. Turbulent mixing of the fresh reactants sustains the traveling detonation wave. Due to turbulent mixing, the detonation front encounters different local equivalence ratios at each point, having different properties along the front. As commented in section 2.4.2, this mixing process couples the detonation properties with the injection dynamics. However, these processes can be identified as large- or small-scale controlled [11].
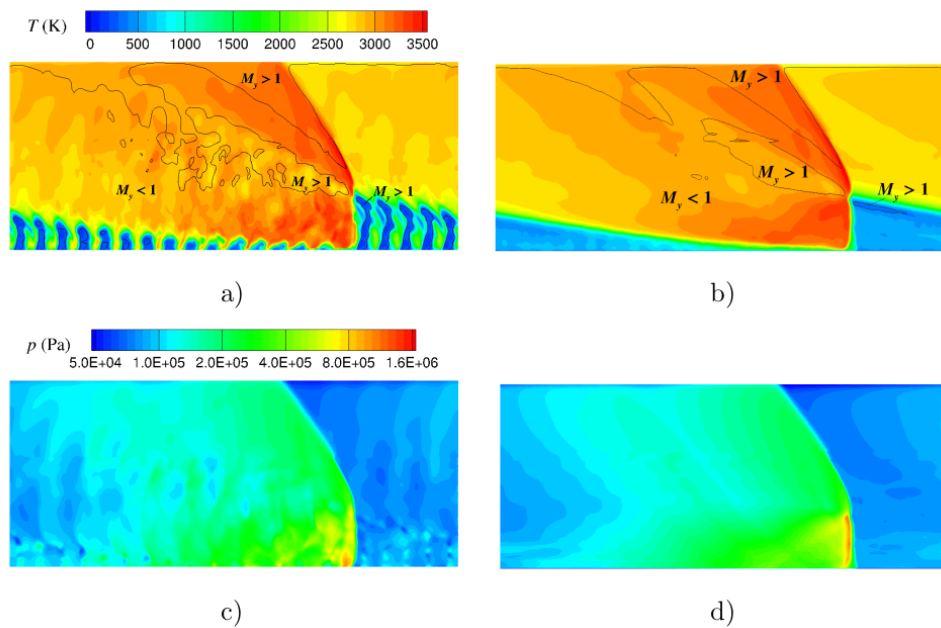
Figure 2.9: Unwrapped 3D RDE simulation flow field. Left: instantaneous values. Right: averaged values [6].

Large-scale controlled processes are defined as the phenomena whose time scale is proportional to the mode of operation (number of detonations and their properties). The mode of operation is defined by the detonation period (see equation 2.42). Thus, injector dynamics is a large-scale controlled process since injector recovery time is proportional to the detonation period. Moreover, reactant mixing and post-combustion gases entrainment into the fresh layer are a large-scale controlled process as well. Although the physical length-scale of the turbulent structures is very small, for the mode of operation to be stable, the mixing processes has to be fast enough to sustain the traveling detonation [49].

On the other hand, the small-scale controlled processes are the phenomena that determine the

detonation's structure. These include the collision of triple points, merging and motion of transverse shocks, and the generation of multiple waves. Although there is a dependence of these processes on the large-scale mixing process, it is still not clear which of the processes are the main drivers towards the equilibrium operation point [11]. Some authors [50][55] have conducted numerical studies to understand the impact of small-scale processes on the flow field characteristics. As commented before, the structure of the detonation depends on the state of the fresh mixture of gases.

In this coupling between the small- and the large-scales there is a third factor which also determines the mode of operation: nonideal phenomena. The nonidealities present in an RDE flow field are: inhomogeneous mixing, secondary combustion due to deflagration, and multiple competing waves. These phenomena hinder engine performance, however, they could also improve the operability [11].

As mentioned before, the design and positioning of the injectors plays an important role in RDE operation. Concentration gradients within the combustion chamber alter the structure of the detonation front and its characteristics. It can lead to localized heat loading on certain regions. Stratification and uneven mixing leads to thicker detonation waves and reduces their propagation velocity. Moreover, turbulent eddies merging and decay is influenced by sidewalls [11]. Figure 2.9 a) clearly shows how the inlet reactants are not completely mixed within the fresh gases layer. Furthermore, it can be seen in figure 2.10 how the inlet gases get mixed with the postcombustion gases all throughout the fresh gases layer.
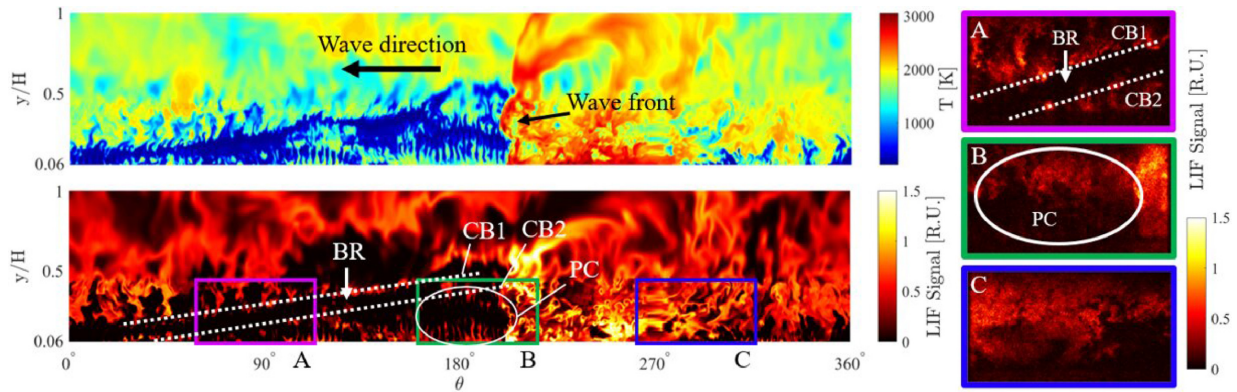
Figure 2.10: Left: Unwrapped RDE flow field showing (Top) temperature flow field from a high-fidelty simulation and (Bottom) computed OH-PLIF. Right: OH-PLIF images from an experiment [56].

Secondary combustion refers to deflagration fronts in low-pressure regions which consume the reactants [57]. This combustion phenomena does not support the running detonation, while changing the thermodynamic state of the gases encountering the detonation wave. These processes weaken the shock and thus have an influence on detonation characteristics. There are two types of deflagration fronts described by the authors Chacon [58], and Sato et al. [56] depending on where they are with respect to the detonation. Upstream the detonation it is known as parasitic combustion (PC), and downstream deflagration is named commensal combustion. Secondary combustion occurs due to turbulence and unsteady injection. When post-combustion gases get in contact with fresh reactants, local autoignition processes can take place. Figure 2.10 shows how there are combustion processes apart from the detonation wave in the bottom left and right images. Parasitic combustion (PC) upstream the detonation can be found in the first and second contact regions (CB1 and CB2 respectively), and closer to the injection ports (see image B). Commensal combustion CB1 occurs due to the mixing of postcombustion gases with fresh gases. On the other hand, commensal combustion CB2 depends on the injection process and flow recirculation between the interior of the fresh gases layer and the expanding gases. This is the same reason why there is PC within the fresh gases layer. The region between CB1 and CB2 is the buffer layer (BR). It results from stratification and different injection recovery times. Furthermore, image C shows an example of commensal combustion. It is also important to mention that secondary combustion also has an impact on the efficiency of the engine, since constant-pressure combustion is less efficient than constant-volume combustion (see section 2.4.1).

The prediction of how many waves will be created is still a matter of research [9][58]. The mechanisms and interactions between the splitting and merging between the different shocks are not fully understood, nor how the propagation direction is determined. Some studies suggest that the final steady state is

determined by the initial energy provided at ignition, and not the ignition method itself [11]. As mentioned in the previous section, some authors suggest that the refill height (h_z) is the main parameter that determines how many waves will be formed, for a minimum mass flow and plenum pressure. Moreover, the mode of operation and number of waves is determined by the mass flow rate, equivalence ratio, and injector plenum total pressure (see section 2.4.2).

In addition to the main detonation waves, another type of pressure wave, known as secondary waves, is observed in both experiments and simulations during the operation of RDE combustion chambers. Secondary waves are pressure waves too weak to be considered detonations. It has been seen experimentally that there are two stable cases [58]: multiple secondary waves moving at the acoustic speed of the postcombustion gases counter to the detonation wave, or a single detonation wave traveling in opposite direction to the detonation at a similar speed. Figure 2.11 shows the time evolution in an RDC where a detonation (label 1) and different secondary waves (labels 2 and 3) can be seen. The intensity of the detonation changes throughout the images as it collides with the different secondary waves. It can also be seen how wave number 2 disappears after a collision with detonation 1 and later appears again. Although it may seem as a chaotic behavior, Fourier analysis of the data showed that it is a stable mode of operation [59]. Furthermore, the link between the formation of secondary waves and performance is not fully understood. Some authors suggest that the impact on wave speed is minimal after seen that the average speed of the detonation over some periods is very similar. However, it could be influencing injector recovery time and fresh gases thermodynamic state [11].
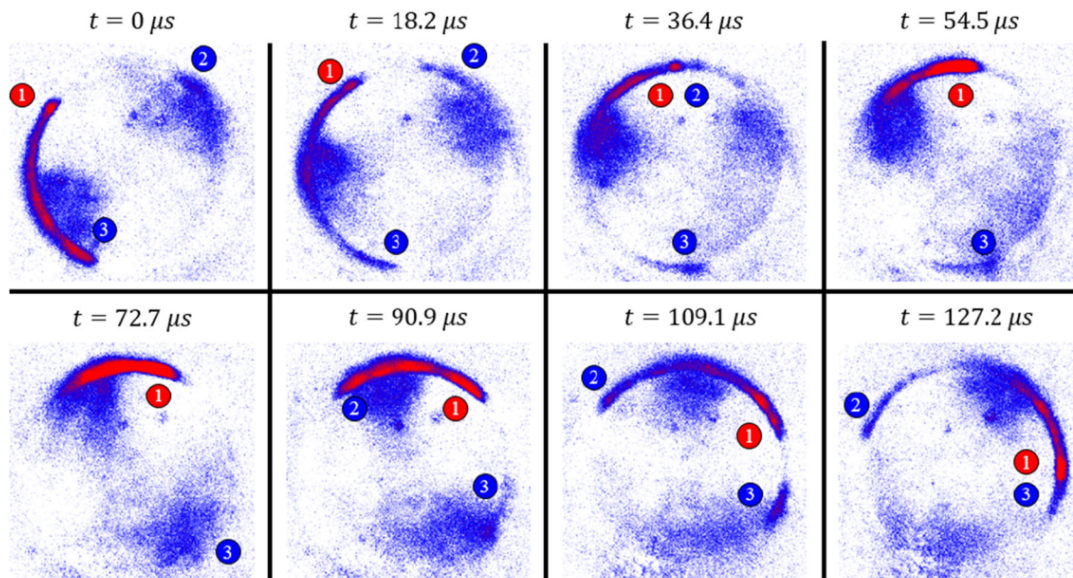
Figure 2.11: OH* chemiluminescence images of the time evolution of an RDC showing the detonation wave (red) and the secondary waves (blue) [59]

To properly compute an RDE performance and its flow field employing numerical techniques, many different aspects have to be taken into account. The detonation wave introduces a wide range of time and length scales, from the operation mode to the small cellular structure. Moreover, the chemical reactions make the simulation stiffer and more prone to instabilities [35]. It has also been seen that turbulent processes play a mayor role, hence, turbulence modeling has an impact on the results. This also adds a layer of complexity in terms of computational cost. The mesh design is not only influenced by the resolution of small turbulent structures, but also has an impact on the formation secondary shocks and detonation characteristics. If it is not fine enough, simulations can lead to nonphysical results and differ from experimental observation [60]. In addition, since simulation time is limited, it is difficult to determine whether the solution is still in a transient phase or if it has arrived to a steady solution. It is also relevant to consider the influence of the numerical methods that model detonation collision and merging, since this phenomena play a relevant role in the final equilibrium state [11].

2.4.5. Future Technological Challenges

The physics behind the different elements of an RDE and their coupling are not fully understood. The injection dynamics interaction with the detonations and multiple wave formation is still a subject of research. The impact of secondary waves on performance is thought to be negligible. However, further investigations are required. The complex behavior of the shock fronts (collisions, splitting, merging, and reflections) not only determine the combustion mode, but can also lead to instabilities in the injection process. A technology to control this processes and prevent back-propagation upstream the injectors is also required. Moreover, further research is required to understand the role of nonidealities in the operational mode of RDEs. Lastly, there are still challenges to overcome regarding simulations. RDEs involve a wide range of physical and time scales, which increases the computational cost and the complexity of the simulations. Insightful solutions require set ups that can handle a variety of phenomena within the flow field.

Moreover, detailed simulations resolving the detonation structure are required to obtain comparable results to the experiments with the numerical methods. Turbulence modeling also requires further understanding to apply tailored models for these applications.

<div style="text-align: right">3</div>

State of the Art in RDE Simulations

This section presents the main trends in the literature regarding RDE simulations. RDE simulations are inherently complex due to the underlying flow physics and operational characteristics. Given that the objective of this work is to establish a robust and stable setup, it is crucial to examine the various modeling approaches employed by different authors in the literature.

3.1. Canonical Flows

Canonical flows are a specific type of simulation employed to better understand the physical processes within RDEs. They differ from the other simulations this chapter will be describing as they do not simulate operating RDEs. They focus on certain processes such as injector design, detonation characteristics [61], or deflagration-to-detonation transition (DDT) [62]. The geometry can be 1D, 2D, or 3D depending on the application and the objective. Gaillard et al. [63] performed a numerical optimization of an injector design for RDEs. They computed the mixing efficiency with a 3D model of an RDE engine. The flow was considered chemically frozen, and they employed an LES approach to model turbulence. This work was later applied to RDE simulations [18]. Moreover, Weiss et al. [64] performed 3D simulations of a section of an RDE employing a RANS model. They studied the influence of different mass flows on the mixing efficiency of the reactants. Furthermore, certain canonical flows can serve as benchmark simulations to validate chemical reaction mechanisms or different numerical schemes for detonation applications. Prakash et al. [57] performed a series of canonical flow simulations to validate their setup and study detonation propagation across different non-premixed mixtures. Figure 3.1 shows the results for a 2D simulation of a shock tube to study the detonation cell size of a certain reactant mixture. This work has been later employed as validation of their set up for RDE simulations [28][55]. In addition, Melguizo-Gavilanes et al. [65] performed experiments and numerical simulations of curved combustion chambers. The objective was to characterize the detonation dynamics and their structure as a function of curved geometry and initial pressure.

3.2. Simulation Domain and Boundary Conditions

RDE simulations can be divided into two categories depending on the geometry of the domain: 2D and 3D simulations. 2D simulations do not consider the effect of curvature and combustor geometry on RDE operation. They also lack realistic modeling of turbulent mixing of the reactants or the entrainment of postcombustion gases into the inlet gases layer [11]. However, they offer a cheaper option while providing insight into the main flow features.

3.2.1. 2D Domains

Zhdan et al. [14] performed a 2D calculation of an H_2-O_2 mixture to study the main features of the flow. Other early numerical works conducted to understand the physics of RDEs and the stability of the numerical simulations were done by Hishida et al. [66] and Schwer et al. [41]. These works further investigated the viability of RDEs to provide steady thrust under different operating conditions and the characteristics of the fresh gases layer interface. Figure 3.2 shows the temperature flow field from the simulations performed by Schwer et al. [41]. It can be seen how the main flow features commented in Chapter 2 are present. Li et al. [17] focused their study on the contact surface instabilities and the underlying physical mechanisms
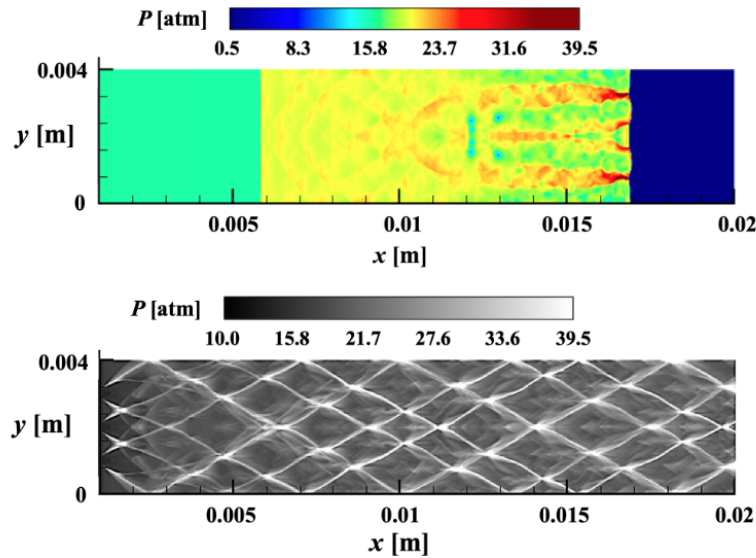
Figure 3.1: Pressure contours of a detonation front advancing through a tube filled with premixed H_2-Air. (Top) Instantaneous pressure contours. (Bottom) Maximum pressure history [57]

behind the unstable behavior. Paxson [67] performed a simulation in a reference frame relative to the detonation. He studied the influence of different injection conditions. Moreover, recent works focus on simulating different mixtures. Fujii et al. [68] studied the differences between premixed and non-premixed C_2H_4-O_2 mixtures. Fang et al. [69] studied the viability of ammonia-hydrogen-air mixtures, and Wang et al. [70] the effect of employing solid particles to enhance combustion. Furthermore, Deng et al. [71] employed 2D simulations to study how to control the operation mode of the engine. In addition, a recent work from Cheng et al. [72] presented an improved code based on OpenFOAM [73] for RDE applications called BYCFoam.
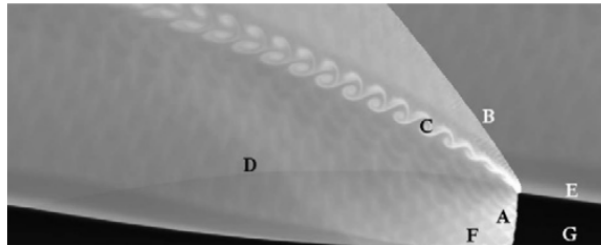
Figure 3.2: Temperature from a 2D simulation showing the main flow features from an RDE: (A) detonation wave, (B) oblique shock, (C) slip line, (D) secondary shock, (E) contact discontinuity, (F) blocked inlet, and (G) fresh reactants
[41]

Regarding boundary conditions, consider the domain in figure 3.2. The side walls are defined as periodic boundary conditions. The outlet boundary condition is usually defined as a mixed subsonic-supersonic outlet. If the Mach number is over unity, all variables are extrapolated from the domain. On the other hand, if it is below one the pressure will be prescribed at the exit pressure and the rest of the variables will be computed [17][71][69]. The inlet boundary can be defined in different ways. Some authors prescribe total pressure and temperature in the plenum and compute the inlet as an isentropic expansion depending on the domain values [14][17][69]. Deng et al. [71] specifies a mass flow rate and the static temperature. Moreover, most authors treat the inlet gases as premixed. Nevertheless, Fujii et al. [68] defines for one of the simulations individual ports for the reactants.

3.2.2. 3D Domains
3D geometries offer the possibility to study in further detail the effects of geometry on the RDE operation. As seen in Chapter 2, the width of the combustion chamber has an impact on the detonation characteristics,

as well as the curvature. However, some 3D simulations are performed with unwrapped combustion chambers to focus on the coupling between detonation dynamics and injection recovery [74][6]. Injector design also plays a relevant role in RDE operation due to the impact of mixing efficiency. Hellard et al. [75][76] conducted simulations of one injector element of a full-sized combustion chamber to save computational costs and evaluated mixing efficiency employing an LES approach. Athmanathan et al. [77] studied the impact of stratification on a full-scale RDE, and compared it with experimental results. On the other hand, early works focused on the study of stable RDE operation [42][43]. Wu et al. [47] investigated the impact on stability of the total injection pressure and the number of detonation waves. Yao et al. [44][78] continued their work and performed more detailed simulations. They also investigated the transition between different modes of operation. Sato et al. [56][79] investigated about the mixing efficiency and impact of different mass flows on the RDE stability for an axial injector design. Moreover, Prakash et al. [28][55] performed high-fidelity simulations employing a tailored solver based on OpenFOAM, UMdetFOAM. Their objective was to evaluate the stability of methane-oxygen RDEs and their detonation dynamics. Hellard et al. [19] proposed a new injector geometry for RDEs employing a methane-oxygen mixture. They achieved the highest detonation wave propagation relative to the theoretical CJ velocity (close to 90% of the theoretical value). Pal et al. [80] conducted a detailed simulation of an RDE employing adaptive mesh refinement and an LES approach. Results showed that optimal RDE operation is a trade-off between wave speed, number of detonation waves and achievable heat release.

Boundary conditions for 3D geometries share many similarities with the conditions seen for 2D geometries. Wu et al. [47] defined the inlet as finite number of nozzles injecting a premixed reactant mixture. The mass flux is dependent on the ratio between the plenum pressure and the pressure at the inlet boundary, being artificially blocked when backflow would occur. Similarly, Frolov et al. [42][43] prescribed at the inlet total pressure, temperature, turbulence characteristics and species concentration. Other works, such as Pal et al. [80], define at the injector inlets the experimental mass flow values. Hellard et al. [75][76][81][82][19] prescribed at the injectors inlets mass flux and total temperature values. Regarding wall boundary conditions, Wu et al. [47] did not consider viscous effects and defined the walls as adiabatic and non-catalytic. Moreover, Hellard et al. [19] applied no-slip boundary conditions on the walls since results showed that the losses due to skin friction were negligible. On the other hand, most authors apply no-slip, adiabatic, non-catalytic for the side walls [28][83]. To save computational costs, Pal et al. [80] applied a law-of-the-wall boundary condition for velocity. Lastly, outlet boundary treatment is the same as for the 2D cases, being adequate for subsonic, supersonic, and dynamically changing outflow.

From the literature findings it can be concluded that the most critical boundary condition to RDE performance is the inlet boundary. The modeling of the injection and its coupling with detonation dynamics has a strong impact on the flow field. Modeling the injectors and assuming a premixed inlet leads to less realistic results. On the other hand, solving the injector flow can provide more accurate results compared to the experiments.

3.3. Mesh and Numerical Schemes

Chapter 2 showed the wide range of scales within an RDE flow field. The smallest length scale corresponds to the induction region behind the shock within the detonation wave, which is of the order of 10 μm for H_2-O_2 mixtures [11]. Ideally, the detonation wave should be fully resolved in the simulation, however, due to computational costs it is not possible. Thus, the mesh has to be coarse enough to be viable, but fine enough to capture the relevant detonation dynamics. Moreover, the numerical methods employed also play an important role in the simulations. They introduce numerical errors and can have an impact on the flow physics.

3.3.1. 2D Domains

In their early work, Zhdan et al. [14] employed a finite differences scheme on a grid of 80x100 nodes. The system of equations was integrated with a Godunov-Kolgan 2nd-order method. Later works applied a finite volumes approach. Regarding the mesh resolution, due to computational capacity limitations ,Schwer et al. [41] employed a resolution of 2000 μm. Later works reduced the resolution by a factor of 10. A resolution of 200 μm was found to be fine enough to properly reproduce the detonation dynamics [66] [17][22]. Other authors such as Fujii et al. [68] employed finer meshes with non-uniform sizer ranging from 10 to 100 μm, and Deng et al. [71] employing a mesh with a resolution from 100 to 500 μm. More recent advancements apply adaptive mesh refinement (AMR) techniques to RDE simulations, as presented in Cheng et al. [72]

work.

Regarding the numerical modeling, most authors use TVD Runge-Kutta schemes for time integration. Either 2nd-order [67][71] or higher orders [66][17]. Fujii et al. [68] employed a tailored multi-timescale integration scheme to deal with chemically reaction flows. Other authors have employed 2nd-order implicit methods [22][69][72]. Most authors apply 2nd-order MUSCL schemes for the convective terms with different slope limiters such as Van Albada [66][71], or Van Leer [22]. To compute the fluxes different schemes have been implemented in the literature, such as HLLE [66], Kurganov-Noelle-Petrona (KNP) [22], HLLC, AUSMPW+ [71], and AUSM+M. Cheng et al. [72] compared the different schemes available and obtained the best results with the AUSM+M scheme. Other authors such as Li et al. [17] employed a 5th-order Weighted Essentially Non-Oscillatory (WENO) scheme. It is interesting to note that no author makes special emphasis on specific shock treatment for stability purposes.

3.3.2. 3D Domains

Frolov et al. [42][43] employed a semi-implicit method for pressure-linked equations (SIMPLE) combined with a semi-implicit Monte Carlo method for notional particles. The mesh size was adjusted to fit 10 particles per cell based on their particle-based approach. As in the 2D cases, most authors employ solvers based on finite volumes methods. The finest mesh size was employed by Gaillard et al. [6], being 50 μm for the mixing region. Hellard et al. employed a mesh of 100 μm for the mixing region [75][76][81][82][19]. Moreover, Prakash and Sato et al. research group employed 200 μm [28][55][56][79][83]. Downstream the mixing region the meshes are coarsened until reaching a resolution of 800 to 1000 μm. On the other hand, Pal et al. [84][80] employed adaptive mesh refinement reaching a minimum resolution of 200 μm.

The numerical models employed are very similar that the ones seen for the 2D cases. Wu [47] and Yao et al. [44][78] employed a 5th-order monotonicity-preserving WENO scheme for spatial discretization and 3rd-order Runge-Kutta for time integration. Prakash and Sato et al. [55][83] research group employ the solver UMdetFOAM. To discretize the fluxes at the cell faces it uses the HLLC scheme, and for 2nd-order spatial discretization MUSCL scheme is employed. Moreover, diffusion terms are discretized employing the KNP scheme. A 2nd-order Runge-Kutta method is employed for time integration. A very similar approach is employed by Gaillard and Hellard et al. [6][19] research group. They employed the CEDRE code for their simulations. The convective fluxes are computed with the HLLC scheme as well, and the space discretization is achieved with the MUSCL scheme. A central-difference scheme is employed for the viscous terms, and an implicit time integration scheme is employed. Lastly, Pal et al. [80] employed a commercial code (CONVERGE [85]) to perform the calculations.

3.4. Combustion Modeling

Combustion modeling is a key step in RDE simulations. Detonation dynamics depend on how the chemistry is resolved since the shock is sustained by the chemical reactions of the mixture. The stability and mode of operation are dependent on these modeling decisions. It is also important to note that it determines the detonation cell size, which is linked to the engine performance [9].

3.4.1. 2D Domains

Early works from Zhdan et al. [14] and Schwer et al. [41] employ simplified chemical reaction mechanisms due to computational limitations. They separate the detonation into two regions, one defined by an approximated induction time, and another region where the heat release occurs. Hishida et al. [66] implemented the Korobeinikov-Levin model, which computes the chemical source terms based on two progress variables. Paxon et al. [67] defined the chemical source terms as a step function. Heat release would only take place past certain temperature threshold, and the reaction rate was constant. Later works implemented detailed chemical reaction mechanisms validated with canonical flows for this applications [68][17][71][69]. However, there is no preferred chemical reaction mechanism tailored for RDE applications.

3.4.2. 3D Domains

Wu et al. [47] and Yao et al. [44] employed a one-step chemical reaction model to model H_2-O_2 reaction. A similar approach was taken by Frolov et al. [42][43]. They also employed a Particle Method (PM) to account for turbulence-chemistry interaction. The rest of the authors employ chemical reaction mechanisms validated in previous works, or in canonical flow simulations. Prakash et al. [55] and Sato et al. [56]

employed the FFCMy-12 reaction mechanism with 12 species and 38 reactions to model methane-oxygen reaction. For an H_2-O_2 reaction, Sato et al. [83] employed a chemical reaction mechanism from Mueller et al. [36] with 9 species and 19 reactions. Gaillard et al. [6] and Hellard et al. [81] employed a skeletal mechanism for hydrogen-oxygen reaction validated previously by their research group. Furthermore, Hellard et al. [19] employed a skeletal reaction mechanism for methane-oxygen combustion developed for rocket combustion [86]. Lastly, Pal et al. [84][80] also employed different reaction mechanisms validated by previous works.

3.5. Turbulence Modeling

Turbulence enhances mixing of the reactants, which helps sustaining the detonation wave. However, secondary combustion losses due to deflagration is also partially caused by turbulence. It is clear that turbulent mixing plays a mayor role in RDE performance and mode of operation. However, there is still not a validated turbulence modeling approach for RDEs [11].

Prakash et al. [55] and Sato et al. [83] employed their high-fidelity code UMdetFOAM to solve the Navier-Stokes equations. Moreover, Pal et al. [84] employed a URANS approach for their simulation. They tested the standard k-ϵ, realizable k-ϵ, and k-ω models. Results showed that detonation velocity variations were negligible, so they employed the realizable k-ϵ. Similarly, Frolov et al. [42][43] employed a URANS approach with the standard k-ϵ model. In later works, Pal et al. [80] employed an LES approach with the Dynamic Smagorinsky model. In a similar fashion, Gaillard et al. [6] and Hellard et al. [19] research group have employed an LES approach with the Smagorinsky model for their simulations.

To this date, no author has modeled turbulence-chemistry interactions for an RDE simulation. Gaffney et al. [29] and Gerlinger et al. [35] presented in their works a presumed PDF approach to model the effects of turbulent fluctuations on chemical reactions. This approach could be considered in the future for RDE simulations.

3.6. Simulation Initialization

The method employed to initialize the simulation can have an impact on the numerical stability since it can lead to problems due to high gradients. Moreover, different methods can lead to different times before reaching a stable mode of operation. As mentioned in Chapter 2, some authors suggest that the equilibrium point only depends on the total energy provided to the flow, while others support the idea that it is only determined by the operation conditions.

For 2D domains, two strategies are most commonly found in the literature. The first option is to artificially place a detonation wave in the domain based on analytical values from CJ theory or an initial guess [66][67][68]. The second option is to define a small region with artificially high pressure and temperature [41][17][22][69], or to add energy by changing the energy source terms [14].
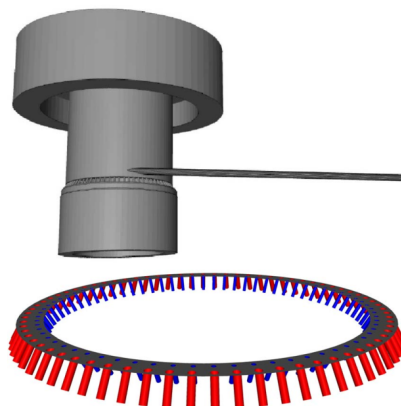
Figure 3.3: (Top) RDE simulation domain with a pre-detonator tube and (Bottom) the injector elements distribution showing fuel (blue) and oxidizer (red) tubes [80]

The strategies followed for 3D domains are very similar to the ones employed for the 2D geometries.

Frolov et al. [42][43] artificially ignited the mixture to start the simulation. Other authors such as Wu et al. [47], Yao et al. [44], and Hellard et al. [75] have employed theoretical values from CJ theory as a first guess of the detonation wave. Similarly, Prakash et al. [55] and Sato et al. [83] initialized the simulation employing an ideal ZND detonation wave. Other strategy employed to enhance stability and save computational costs is to start from an interpolated 2D solution projected into the 3D domain [6][19]. Lastly, Pal et al. [84][80] started their simulations employing a pre-detonation tube (see figure 3.3). It is important to mention that this methods requires a series of steps to ensure stability of the simulation.

Methodology

4.1. The DLR TAU Code

The framework employed for this work has been the DLR TAU-code [3]. It can perform CFD simulations of both viscous and inviscid flows, being applicable to complex geometries in regimes from subsonic to hypersonic velocities [87]. It can be applied to structured and hybrid unstructured grids, having also specific modules to apply grid deformation. It accepts different types of volume elements: hexahedrons, prisms, tetrahedrons, and pyramids. For a better resolution of boundary layer flows, hexahedrons and prisms are employed, while tetrahedrons fill the rest of the computational domain to better adapt to complex geometries. Lastly, pyramids serve as a connection between elements with quadrilateral and triangular faces.

TAU can perform parallel computations employing a grid-partitioning algorithm. It separates the mesh into a number of domains before starting the simulation. The partitioning details can be specified by the user, but it can automatically perform a load balancing computation based on edge- and point weights. This takes place before starting a simulation if the settings have been changed, and when the mesh has suffered any alterations.

The standard solver employs an edge-based dual-cell approach based on a vertex-centered scheme. Before numerically solving the equations, the preprocessing module computes the dual grid from the given primary grid. The newly generated control volumes are centered at the points of the primary grid. The data is stored in an edge-based fashion, making the solver independent of the primary grid elements. The information of the new edges is defined by normal vectors, which define the size and orientation of the faces; the coordinates of the grid nodes, and the volume of the cells. The grid connectivity is defined by the connection of two nodes on different faces of the dual grid to the associated edge of the primary grid. Moreover, an agglomeration approach is employed when applying multi-grid techniques. Starting from a fine-grid, the cells are fused to obtain coarser grids.

To compute the inviscid terms of the equations two options are available in TAU: a second-order central scheme or different upwind schemes based on linear reconstruction, which combined with a MUSCL-type gradient reconstruction, achieves second-order spatial accuracy. Viscous terms are computed with second-order central schemes unless specified.

Regarding time integration, TAU offers several explicit Runge-Kutta schemes, as well as an implicit factorization scheme Lower-Upper Symmetric Gauss-Seidel (LUSGS). To help with convergence speed, multi-grid and residual smoothing algorithms are implemented. Furthermore, a Jameson-type dual time-stepping approach [88] is implemented for a time-accurate solution of simulations with wide ranges of characteristic times.

TAU also offers turbulence modeling capabilities. The RANS turbulence models available include eddy viscosity models, as well as one- and two-equation models. The standard model is the Spalart-Allmaras model [89] due to its robustness and accurate results for a wide range of applications. Other implemented eddy-viscosity models are Wilcox k-ω [90] and Menter-SST [91]. Furthermore, nonlinear explicit algebraic Reynold Stress models (EARSM) are available as well. Lastly, TAU can perform Detached Eddy Simulations (DES) in combination with the Spalart-Allmaras or the Menter-SST models.

A more detailed description of TAU applications, auxiliary tools, algorithms, and capabilities can be found in the work of Schwamborn et al. [92].

4.2. Governing Equations

The Navier-Stokes equations for a mixture of compressible ideal reacting gases in thermal equilibrium can be written in integral form as follows [3]:

$$\frac{\partial}{\partial t} \int_V \underline{U} dV + \int_S \underline{\underline{F}}^{Eu} \underline{n} dS = \int_S \underline{\underline{F}}^{NS} \underline{n} dS + \int_V \underline{Q} dV \tag{4.1}$$

where $\underline{U}$ is the vector of conservative variables defined as:

$$\underline{U} = (\rho_s, \ \rho\underline{u}^T, \ \rho E)^T \tag{4.2}$$

where ρ_s is the density of the different species, ρ the mixture density, $\underline{u}$ the velocity vector, and E the specific total energy. Moreover, $\underline{\underline{F}}^{Eu}$ is the matrix of inviscid or Euler fluxes, which is defined as follows:

$$\underline{\underline{F}}^{Eu} = \begin{pmatrix} \rho_s \underline{u}^T \\ \rho \underline{u}\,\underline{u}^T \\ \rho E \underline{u}^T \end{pmatrix} + \begin{pmatrix} 0 \\ \rho\underline{\underline{I}} \\ p\underline{u}^T \end{pmatrix} \tag{4.3}$$

where $\underline{\underline{I}}$ is the identity matrix and p the pressure.

The third term $\underline{\underline{F}}^{NS}$, is the matrix of viscous or Navier-Stokes fluxes. This matrix reads as follows:

$$\underline{\underline{F}}^{NS} = \begin{pmatrix} \left(\frac{\mu}{Sc}\right)\underline{\nabla}^T \frac{\rho_s}{\rho} \\ \underline{\underline{P}} \\ \kappa\underline{\nabla}^T T + \left(\frac{\mu}{Sc}\right)\sum_s h_s \underline{\nabla}^T \frac{\rho_s}{\rho} + (\underline{\underline{P}}\,\underline{u})^T \end{pmatrix} \tag{4.4}$$

where μ is the dynamic viscosity, Sc is the Schmidt number, which is defined as the ratio of the viscous diffusion rate by the molecular diffusion rate. κ is the thermal conductivity, T is the temperature, h_s is the specific static enthalpy of each species S, and $\underline{\underline{P}}$ is the viscous stress tensor, which is defined as follows:

$$\underline{\underline{P}} = \mu(\underline{\nabla}\,\underline{u}^T + (\underline{\nabla}\,\underline{u}^T)^T) - \frac{2}{3}\mu(\underline{\nabla}^T \underline{u})\underline{\underline{I}} \tag{4.5}$$

From the first element of the viscous matrix in equation 4.4, it can be seen that the diffusion flux $\rho_s \underline{u}_s^d$ of species S, is modeled employing Fick's law. The diffusion coefficient is an average and constant for all the different species. The Fick's law, and following the term in equation 4.4, is as follows:

$$\rho_s \underline{u}_s^d = -\rho D \underline{\nabla}\left(\frac{\rho_s}{\rho}\right) = \left(\frac{\mu}{Sc}\right)\underline{\nabla}^T \frac{\rho_s}{\rho} \tag{4.6}$$

where D is the diffusion coefficient.

Lastly, the source term $\underline{Q}$ contains the chemical sources terms ω_s of the different species S:

$$\underline{Q} = (\omega_s, \ 0, \ 0)^T \tag{4.7}$$

The chemical source term is computed employing the law of mass action by the summation of all the considered chemical reactions in the chemical reaction mechanism, as seen in section 2.3, in equation 2.12. This term determines the rate of production and destruction of the different species, which combined with the transport equations for each species, closes the system of equations to solve.

4.3. Thermodynamic Properties

As seen in section 2.3, to compute the chemical source term from the law of mass action, both the forward and backward reaction rates are required. The forward reaction rate is computed employing a modified Arrhenius law defined as follows [3]:

$$k_r^f = a_r^f \left(\frac{T}{1K} \right)^{b_r^f} \exp \left(-\frac{c_r^f}{T} \right) \tag{4.8}$$

where a_r^f, b_r^f, and c_r^f are constants of the forward reaction.

To compute the backward reaction rate, the same approach as seen in equation 2.14 is employed. The equilibrium constant K_r^{eq} is used to calculate the backward reaction rate since $k_r^b = k_r^f / K_r^{eq}$. The equilibrium constant is computed from the Gibbs free energy ($G^s = H^s - TS^s$) and other thermodynamics quantities as follows [30]:

$$\ln(K_r^{eq}) = \sum_s \nu_r^s \ln \left(\frac{p_{ref}}{R^0 T} \right) - \frac{1}{R^0 T} \sum_s \nu_r^s G^s \tag{4.9}$$

where $\nu_r^s = \nu_n'' - \nu_n'$ (see equation 2.12), $p_{ref} = 1 \times 10^5$ Pa is a reference value, and R^0 is the universal gas constant.

In this work, the thermodynamics variables are computed from a set of tabulated values that define: c_p, $H - H_0$, and $\Phi = -G/T = -(H - H_0 - TS)/T$, as functions of temperature T. These values are defined for each of the species. All the constants required for the computation of the thermodynamic properties are taken from the Computational Chemistry and Benchmark Database of the US National Institute of Standards and Technology (NIST) [93], and from the data published by Gurvich [94].

Once all the thermodynamic properties for the different species have been computed, the mixture properties are calculated as the mass fraction average:

$$\psi = \sum_S Y_S \psi_S \tag{4.10}$$

4.4. Laminar Transport Coefficients

The laminar viscosity coefficient of each species S is calculated by fitting the Blottner curve [95] defined as:

$$\mu_S = 1 \frac{Ns}{m^2} \exp(C_S) T^{A_S \ln(T) + B_S} \tag{4.11}$$

by employing a quadratic fit of the logarithm of the laminar viscosity ($\ln(\mu_S)$) with respect to the logarithm of the temperature ($\ln(T)$) using data from the CEA software [96]:

$$\ln(\mu_S) = A_S \ln^2(T) + B_S \ln(T) + C_S \tag{4.12}$$

where the coefficients A_S, B_S, and C_S are known as the Blottner coefficients. Tabulated results of these coefficients for a relevant TAU application can be found in Karl [3].

Once the laminar viscosity is defined for each of the species, Wilke's rule [97] is employed to compute the laminar viscosity of the gas mixture. This model is applicable to gas mixtures with no ionisation [98]. The expression is as follows:

$$\mu = \sum_S \frac{n_S \mu_S}{\sum_s n_S \Phi_{S,s}} \; ; \text{where } \Phi_{S,s} = \frac{1}{\sqrt{8}} \left(1 + \frac{M_S}{M_s} \right)^{-\frac{1}{2}} \left[1 + \left(\frac{\mu_S}{\mu_s} \right)^{\frac{1}{2}} \left(\frac{M_s}{M_S} \right)^{\frac{1}{4}} \right]^2 \tag{4.13}$$

where n_S is the molar concentration of species S, and M_S is the molar mass of species S.

Regarding the thermal conductivity, each specie specific value is computed employing the Eucken correction [99] in the modified version of Hirschfelder [100]. The expression is as follows:

$$k_S = \mu_S \left(\frac{5}{2}(C_V)_S^t + \frac{(C_V)_S^{rot} + (C_V)_S^{vib} + (C_V)_S^e}{Sc} \right) \tag{4.14}$$

where the superscripts t, rot, vib, and e refer to the different contributions coming from the translational, rotational, vibrational, and electronic energy modes, respectively.

Lastly, the gas mixture heat conductivity is computed employing the rule of Zipperer and Herning [101], leading to the following expression:

$$k = \sum_S \frac{n_S k_S}{\Phi_S} \; ; \text{where } \Phi_S = \sum_s n_s \sqrt{\frac{M_s}{M_S}} \tag{4.15}$$

4.5. Numerical Methods

The spatial discretization employed in TAU is based on a cell-vertex approach, as it can be seen in figure 4.1. The primary grid can be composed of tetrahedra, prisms, hexahedra or pyramids. Afterwards, the dual grid is generated in the preprocessing step around the vertices of the primary grid. The variables are stored at the cell vertices, and the fluxes are computed on the dual grid faces when considering a finite volumes approach.
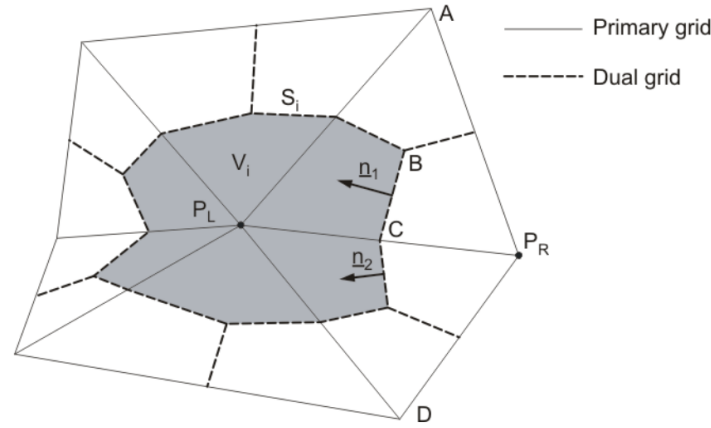
Figure 4.1: Schematic of the cell-vertex discretization employed in TAU showing the relationship between the primray and the dual grids [3].

Figure 4.1 shows the dual cell of volume V_{in} and surface S_i defined by the normal vectors of its faces $\underline{n}_j$ around vertex P_L. The faces of the dual cell are always associated with two adjacent points of the primary grid. For example, in figure 4.1, points P_L and P_R are associated to their respective dual face by a normal vector which is a linear combination of the normal vectors of the dual faces between those points. This normal vector is defined as:

$$\underline{n} = \underline{n}_1 + \underline{n}_2 \tag{4.16}$$

The boundaries that define the dual cells around the vertices are computed by connecting the centers of the primary cells with the centers of the faces of the primary grid. In the case of figure 4.1, it can be seen how point B (primary grid cell center) is connected to point C (primary grid face center) to form one of the boundaries of the dual cell. For a 2D case, the coordinates of the primary cell centers are computed as follows [3]:

$$\underline{B} = \frac{g_1 \underline{P}_L + g_2 \underline{A} + g_3 \underline{P}_R}{g_1 + g_2 + g_3} \tag{4.17}$$

where the functions g_i are weighting functions that determine the relevance of one point compared to the adjacent ones based on the following expression, for example, for the first weighting function:

$$g_1 = (\overline{P_L P_R})^2 + (\overline{P_L A})^2 \tag{4.18}$$

Now, take the conservation equations from 4.1 and write them in a discretized form after applying a finite volumes scheme for one control volume V with faces i. The system of equations is as follows:

$$V \frac{dU}{dt} + \sum_i \underline{\underline{F}}_i^{Eu} \underline{n}_i = \sum_i \underline{\underline{F}}_i^{NS} \underline{n}_i + V \underline{Q} \tag{4.19}$$

Once discretized, the system of equations can be rearranged as follows:

$$\frac{dU}{dt} = -\underline{R} \, ; \text{ where } \underline{R} = \frac{1}{V} \left(\sum_i \underline{\underline{F}}_i^{Eu} \underline{n}_i - \sum_i \underline{\underline{F}}_i^{NS} \underline{n}_i - V \underline{Q} \right) \tag{4.20}$$

where $\underline{R}$ is the residuals vector.

The numerical approximation of the inviscid flux term $\underline{\underline{F}}_i^{Eu} \underline{n}_i$ can be computed by either different upwind or a central scheme, with different dissipation approaches, available in TAU. Section 4.6 provides a more detailed explanation of some of the upwind fluxes available in TAU and relevant to this work.

In order to have a second-order approximation of the solution, a piecewise linear distribution is employed to extrapolate the quantities on both sides of the dual faces (ϕ_L, ϕ_R). The expression is as follows:

$$\phi_L^{face} = \phi_L^{node} + \frac{1}{2} L \underline{\nabla} \phi_L (\underline{P}_R - \underline{P}_L) \tag{4.21}$$

$$\phi_R^{face} = \phi_R^{node} + \frac{1}{2} L \underline{\nabla} \phi_R (\underline{P}_L - \underline{P}_R) \tag{4.22}$$

where L is a limiter function that prevents overshooting due to flow discontinuities. In the regions where the grid is unstructured, the Barth-Jespersen limiter [102] is applied.

As seen in equations 4.21 and 4.22, the flow variables gradients ($\underline{\nabla}\phi$) are required to perform the piecewise linear reconstruction. Hence, a least-squares fitting approach was implemented. A second-order Taylor expansion is employed to approximate the values of the variables at the vertices. The gradients in said Taylor expansion are defined in such a way that the approximation corresponds to the optimum of a least-squares fit to the values stored at each cell vertex. A more in depth description of the algorithm can be found in Anderson [103] and Haselbacher [104]. On the other hand, in structured regions with high aspect ratio cells the gradients are computed along the grid boundaries since they undergo small changes in direction. A second order finite difference approach with a van Leer limiter [105] is employed to compute the gradients.

Considering now the viscous flux term $\underline{\underline{F}}_i^{NS} \underline{n}_i$ on face i, it is computed by applying a central scheme to the equations defined in 4.4. To achieve this, both the flow variables values ϕ and their respective gradients $\underline{\nabla}\phi$ are required. These quantities are approximated as follows:

$$\phi^{face} = \frac{1}{2} (\phi_L + \phi_R) \, ; \quad \underline{\nabla}\phi^{face} = \frac{1}{2} (\underline{\nabla}\phi_L + \underline{\nabla}\phi_R) \tag{4.23}$$

To keep the second-order accuracy of the gradient reconstruction for the viscous fluxes in unstructured regions, a correction is applied. The correction expression is the following [3]:

$$\underline{\nabla}\phi^{face,corrected} = \underline{\nabla}\phi^{face} - \left(\frac{\underline{\nabla}\phi^{face} \underline{\Delta x}_{LR}}{|\underline{\Delta x}_{LR}|} + \frac{\phi_L + \phi_R}{|\underline{\Delta x}_{LR}|} \right) \frac{\underline{\Delta x}_{LR}}{|\underline{\Delta x}_{LR}|} \tag{4.24}$$

where the term $\underline{\Delta x}_{LR}$ is the vector that defines the distance between the two vertices on the sides of the face for which the gradient is being computed. The idea behind this correction is to keep the components normal to the face while applying a correction to the components tangential to the distance vector $\underline{\Delta x}_{LR}$.

Once the different terms in equation 4.20 are defined, it can be solved in an iterative fashion. First, temporal discretization with a 3-stage Runge Kutta scheme [106] was employed. Consider the solution to a steady-state problem for which the solution would be achieved when $\underline{R} = 0$ as the time derivative would turn to zero. If the time discretization is performed on a pseudo-time t^*, the 3-stage Runge Kutta scheme is defined as follows:

$$\underline{U}^1 = \underline{U}^n - 0.15\Delta t^* \underline{R}\left(\underline{U}^n\right) \tag{4.25}$$

$$\underline{U}^2 = \underline{U}^n - 0.5\Delta t^* \underline{R}\left(\underline{U}^1\right) \tag{4.26}$$

$$\underline{U}^{n+1} = \underline{U}^n - 1.0\Delta t^* \underline{R}\left(\underline{U}^2\right) \tag{4.27}$$

This scheme allows to compute the jump from step n to step $n + 1$ in the pseudo-time t^* frame.

The chemical source terms in equation 4.19 are exponentially dependent on the temperature, hence they can lead to a numerical stiffness problem. Therefore, they are treated with a point implicit approach described by Sheffer [107]. This approach rescales the characteristic time of the reactions to a magnitude comparable to the convective terms characteristic times.

To accurately resolve equation 4.19 in time, a dual time-stepping approach described by Jameson [88] was employed. The physical time domain $(0, t)$ is divided into physical time steps Δt. Then, a second order backward differencing scheme is applied. The discretized equation is as follows:

$$\frac{3\underline{U}^{n+1}}{2\Delta t} - \frac{2\underline{U}^n}{\Delta t} + \frac{\underline{U}^{n-1}}{2\Delta t} = -\underline{R}\left(\underline{U}^{n+1}\right) \tag{4.28}$$

When solutions n and $n - 1$ are known, the solution at time step $n + 1$ can be found interpreting it as the solution of a steady-state problem by rewriting equation 4.28 as the following equation:

$$\frac{d\underline{U}^*}{dt^*} = -\underline{R}\left(\underline{U}^*\right) - \frac{3\underline{U}^*}{2\Delta t} + \frac{2\underline{U}^n}{\Delta t} - \frac{\underline{U}^{n-1}}{2\Delta t} = -\underline{R}^{dual}\left(\underline{U}^*\right) \tag{4.29}$$

Equation 4.29 is solved employing the aforementioned 3-stage Runge Kutta scheme. To find the solution for time $t + \Delta t$, the solution is iterated over the pseudo-time t^*. These iterations are called inner iterations. All techniques used in TAU to enhance the convergence of the residuals for steady-state problems are applied in this step. TAU also allows to define Cauchy-Convergence criteria based on flow-integral parameters such as, for example, the lift or the drag coefficients [30]. Furthermore, the number of inner iterations can also be manually set to a maximum number.

Another technique implemented to improve the convergence rate is the smoothing of the residuals as follows:

$$\underline{R}^{smoothed} = (1 - \omega)\underline{R} + \frac{\omega}{\sum_{adj.\ cells}|\underline{n}_i|} \sum_{adj.\ cells}\left(\underline{R}_i|\underline{n}_i|\right) \tag{4.30}$$

where ω is a relaxation parameter fixed to a value of 0.2. The idea is to take as the smoothed residuals the weighted sum of the residuals of a cell, and the contributions from the residuals of the adjacent cells based on their respective face surface ($|\underline{n}_i|$) with respect to the total cell surface.

To further enhance the convergence of the inner iterations, a local time stepping approach is employed. The pseudo-time step Δt^* is computed for each cell based on the minimum between the convective and the viscous time steps:

$$\Delta t^* = \min\left(\Delta t^c, \Delta t^\nu\right) \tag{4.31}$$

where superscripts c and ν refer to the convective and viscous time steps respectively.

Both time steps are computed by considering the convective and viscous eigenvalues at each face i of the cell. The expressions are as follows:

$$\Delta t^c = CFL \cdot 2V \left(\sum_i \lambda_c^i \right)^{-1} \tag{4.32}$$

$$\Delta t^\nu = CFL \cdot \frac{V^2}{2} \left(\sum_i \lambda_\nu^i \right)^{-1} \tag{4.33}$$

where V is the cell volume, and CFL refers to the Courant-Friedrichs-Levy number.

The maximum convective eigenvalue is defined as:

$$\lambda_c^i = \underline{u}_i \underline{n}_i + a_i |\underline{n}_i| \tag{4.34}$$

where a_i is the speed of sound at face i.

On the other hand, the convective eigenvalue in equation 4.33 is computed as follows:

$$\lambda_\nu^i = (\lambda_{\nu 1}^i + \lambda_{\nu 2}^i)|\underline{n}_i| \tag{4.35}$$

where the eigenvalue $\lambda_{\nu 1}^i$ reflects the contribution from the viscous momentum transport, and $\lambda_{\nu 2}^i$ the contribution from the heat conductivity. The contribution from species diffusion $\lambda_{\nu 3}^i$ is not considered since $\lambda_{\nu 3}^i < \lambda_{\nu 2}^i$.

4.6. Upwind Fluxes

TAU offers a wide variety of upwind fluxes. However, in this work only the Advection Upstream Splitting Method (AUSM) family of fluxes employed in the simulations will be discussed. These fluxes are applied mainly to solve the compressible Euler and Navier-Stokes equations for high-speed and shock-dominated flows such as detonation waves, supersonic jets, and blast waves. This family of upwind fluxes was first introduced by Liou and Steffen [108] as a way to find a trade-off between stability and numerical diffusion inherent to flux-vector splitting techniques.

Employing a finite volume approach to solve a set of equations, and after an explicit time integration of a simple 1D advection equation, the system of equations can be written as follows:

$$\underline{u}_j^{n+1} - \underline{u}_j^n + \frac{\Delta t}{\Delta x} \left[\underline{f}(x_{j+1/2}, t_n) - \underline{f}(x_{j-1/2}, t_n) \right] = 0 \tag{4.36}$$

where $\underline{u}_j^n$ is the cell-average of the variables at time step t_n, and $\underline{f}$ is the numerical flux evaluated at the cell faces. To compute the numerical flux, Godunov first proposed treating it as a Riemann problem considering the cell averages at each side of the cell face as the initial value pair $(\underline{u}_L, \underline{u}_R)$. For complex cases, the exact solution of the Riemann problem is not known, and different approximations have been proposed. A widely known approximation is the Roe splitting [109]. It assumes the flux to be a contribution of perturbations coming from both sides depending on the propagation direction of the characteristics. This approach is known as flux difference splitting (FDS). The drawback from this approximation is that it does not make a difference between stationary and expansion shocks, hence violating the entropy condition in certain cases. Later variations corrected this issue.

Another common approximation of the fluxes is the flux-vector splitting (FVS) method, being the van Leer [110] two flux-vector splitting a well known example. It is based on the idea of approximating the flux by computing the upwind contributions of the states from both sides of the cell face. The van Leer implementation is algorithmically simple, can be applied to complex fluid problems, satisfies the entropy

condition, and is robust for a wide variety of cases. Hänel [111] developed an improved version of this flux approximation to preserve the total enthalpy. Nevertheless, these FVS methods suffer from high numerical diffusion, leading to less accurate results.

The aim of the AUSM fluxes is to combine the positive attributes from FDS and FVS methods while eliminating their drawbacks [112]. Moreover, the scheme does not have matrix operations nor differentiation of the fluxes. Hence, it is efficient and smoother than other relevant flux approximations such as the aforementioned Roe splitting [108]. The core idea is to treat the convection (mass, momentum, and energy conservation terms), and the acoustic waves as two physically different processes. The numerical flux is therefore divided into the convection term $\underline{f}^{(c)}$ and the pressure term $\underline{f}^{(p)}$.

$$\underline{f} = \underline{f}^{(c)} + \underline{f}^{(p)} = \rho u (1 \ u \ H)^T + (0 \ p \ 0)^T \tag{4.37}$$

Considering the discretization of equation 4.36, the convective term at the cell interface is defined as [108]:

$$\underline{f}^{(c)}_{1/2} = u_{1/2} \begin{pmatrix} \rho \\ \rho u \\ \rho H \end{pmatrix}_{L/R} \quad \text{where } (\bullet)_{L/R} = \begin{cases} (\bullet)_L & \text{if } u_{1/2} \geq 0 \\ (\bullet)_R & \text{otherwise} \end{cases} \tag{4.38}$$

The definition of the advection velocity $u_{1/2}$ has a larger impact on the flux approximation. The choice taken for the AUSM flux was to represent the advection velocity as a combination of wave speeds traveling to the interface from both sides [108]:

$$u_{1/2} = a_{L/R} M_{1/2} \quad \text{where } M_{1/2} = M_L^+ + M_R^- \tag{4.39}$$

The Mach number at the interface $M_{1/2}$ is computed by considering the contributions from the waves coming to the interface from both sides. The definition of the split Mach numbers $M^\pm$ also has an influence on the flux performance. Liuo and Steffen [108] employed the van Leer splitting [110]. The split Mach number function is expressed as a polynomial expansion of the characteristic speeds $(M \pm 1)$. This AUSM flux with the van Leer splitting is available in TAU under the name AUSM_Van_Leer.

The pressure term of the flux is computed by considering the contributions from the acoustic waves coming to the interface from both sides. The expression is similar to the one seen in equation 4.39 for the interface Mach number $M_{1/2}$. It is as follows:

$$p_{1/2} = p_L^+ + p_R^- \tag{4.40}$$

The split pressure functions $p^\pm$ are computed employing a polynomial expansion in terms of the characteristics speeds $(M \pm 1)$. Different behaviors of the flux can be seen depending on the order of said polynomials [108].

Substituting equations 4.38, 4.39, and 4.40 into equation 4.37, gives the following expression for the numerical flux:

$$\begin{pmatrix} \rho u \\ \rho u^2 + p \\ \rho u H \end{pmatrix}_{1/2} = M_{1/2} \frac{1}{2} \left[\begin{pmatrix} \rho a \\ \rho a u \\ \rho a H \end{pmatrix}_L + \begin{pmatrix} \rho a \\ \rho a u \\ \rho a H \end{pmatrix}_R \right] - \frac{1}{2} |M_{1/2} \Delta_{1/2} \begin{pmatrix} \rho a \\ \rho a u \\ \rho a H \end{pmatrix} + \begin{pmatrix} 0 \\ p_L^+ + p_R^- \\ 0 \end{pmatrix} \tag{4.41}$$

where $\Delta_{1/2}\{\bullet\} = \{\bullet\}_R - \{\bullet\}_L$. The first term of the flux is a Mach-weighted average of the states at the sides of the interface, the second term is a dissipation term, and the third term is the pressure flux.

This family of fluxes saw some improvements in later versions. The AUSMDV developed by Wada and Liou [2] proposed some ideas that would be employed in some later iterations: they introduced a common

interface speed of sound $a_{1/2}$, they introduced a pressure diffusion term in the mas flux definition to improve the performance of the method for non-grid-aligned discontinuities, and they included a sonic-point fix to handle better sonic transitions. The problem with this flux was that it was prone to suffer from the so called Carbuncle response, or oscillations after strong shocks [113]. This flux is also available in TAU under the same name.

The pressure diffusion term added to the AUSMDV flux prevented the overshoot at shock waves. This problem was caused by the flux differencing term [2]. However, the addition of this extra diffusion term is what caused the Carbuncle response of the flux, thus being removed in the later iteration of the flux family, AUSM+ [114], named in TAU as AUSMP. The AUSMP scheme is capable of capturing both stationary contact discontinuities and stationary shocks exactly. Compared to the baseline AUSM splitting Mach and pressure functions, more general and accurate higher order functions are employed. This scheme is able to achieve higher levels of accuracy while avoiding the post-shock overshooting problem [114].

When employing the AUSMP upwind flux to solve low Mach number problems where $u \ll a$, numerical dissipation is severely increased, leading to large numerical errors. Moreover, convergence is either very slow or stalls. To solve these problems, a rescaling of the speed of sound is required. Also, to ensure stability, a coupling between the velocity and the pressure fluxes is included. The updated flux is the AUSM+-up [115][116], named in TAU as AUSMPUP. This flux included pressure and velocity diffusion terms in both the mass flux and the pressure terms. Although the pressure diffusion term led to Carbuncle phenomena, it was seen that it was required to properly capture non-grid aligned shocks [113]. Even if the AUSMPUP flux has not been employed in later simulations, it is interesting to see how new fluxes adapt to provide robust and accurate results for a wider range of cases.

Other authors have developed tailored fluxes based on the AUSM family ideas. Kim et al. [117] developed the AUSMPW flux for hypersonic re-entry applications. The idea is to employ pressure-weighted functions to avoid the Carbuncle response of the AUSMDV flux and the oscillations near the wall and after strong shocks of the AUSM+ flux. The split Mach number and pressure functions of AUSMPW are the same as those for AUSMP. The difference comes when computing the mass flux at the interface to determine the upwind approximation, since it is thought that the Carbuncle response and oscillatory behavior from AUSMDV and AUSMP respectively stem from this step. The AUSMPW flux includes pressure-weighted functions that consider the effect of the pressure on both sides of the interface depending on the local Mach number. Later versions of this flux such as AUSMPW+ [118] introduced a new way of computing the numerical speed of sound to improve the accuracy and efficiency of the calculations. This flux is available in TAU as the AUSMPWP flux. Moreover, the flux was updated to provide better results for multi-dimensional compressible flows, being named M-AUSMPW+ [119]. Improvements to this family of upwind fluxes is still a current research topic.

4.7. Boundary Conditions

Boundary conditions play a critical role in defining the physical behavior of the computed flow. The appropriate choice directly influences the results, having an impact on their convergence and accuracy. TAU offers a wide variety of boundary conditions. However, in this section, only the relevant boundary conditions for the conducted simulations are presented.

4.7.1. Non-viscous and Viscous Walls

The non-viscous wall boundary condition is named in TAU as Euler wall. It imposes a restriction on the mass flux through the boundary such that it is zero. Thus, the normal velocity component is also zero. Moreover, it assumes the flow to be non-viscous, hence not considering shear stresses and not imposing any restrictions on the tangential velocity. There is also no heat flux information defined at the boundary.

On the other hand, a viscous wall boundary condition can be defined. The difference with respect to the Euler wall boundary is the consideration of the shear stresses and the restriction on the tangential velocity component. TAU gives the possibility to implement transition models from laminar to turbulent boundary layers. Furthermore, laminar or turbulent options alone can be defined. Lastly, the wall heat flux or temperature-reservoir boundary condition can be defined. This condition calculates the heat flux through the wall as a function of the wall thickness, the heat conductivity, and the difference between the flow temperature and a prescribed reservoir temperature. However, in this work only adiabatic walls have been considered.

4.7.2. Dirichlet-type
The Dirichlet-type boundary condition fixes the values of the variables at the boundary. It can be defined as an inlet or an outlet. It allows the user to specify the species mass fractions, density, temperature, velocity vector, or to prescribe a mass flux. Furthermore, instead of the values, it can be defined to set the variables which then are employed to compute the fluxes by solving a Riemann problem at the respective boundary. Strictly, it can only be used in supersonic flows ($M > 1$) since it sets all incoming characteristic lines.

4.7.3. Reservoir-pressure Inflow
The reservoir-pressure inflow boundary condition was designed to model the inlet boundary for nozzle flows. The user can define the total temperature, pressure, or density. Furthermore, the velocity is assumed to be zero within the reservoir. Moreover, the species mass fractions can be specified as well. The variables in the first cells of the domain are computed as follows. The velocity in the first cell is taken, and considering this value and the total properties of the reservoir, the thermodynamic state at the inlet is computed as the expansion from the reservoir conditions that provide the velocity field at the first cell of the domain. Later changes to this boundary condition added the option to prevent backflow, avoiding stability problems. Moreover, to avoid chemical reactions prior to entering the computational domain, a frozen composition switch was added. The baseline boundary condition computes the chemical equilibrium composition already in the reservoir, thus changing the inlet properties of the flow.

4.7.4. Exit-pressure Outflow
The exit-pressure outflow boundary condition is defined by an external pressure defined by the user. This boundary condition handles both supersonic and subsonic outlets, even within the same wall. When the inner domain Mach number is over unity, the boundary variables are computed from the inner domain values since the flow is supersonic and it is not affected by the outside pressure. On the other hand, when the flow is subsonic, the flow variables are computed by considering this external pressure when computing the fluxes at the wall boundary.

4.7.5. Farfield
The farfield boundary condition can be applied to both inlets and outlets. It can compute the convective fluxes in two different ways: either employing an approximate Riemann method, or an AUSM scheme augmented by the method of Whitfield. This boundary condition can handle both supersonic and subsonic regimes. The computation of the variables vary depending on the regime. For example, for the subsonic case, the pressure in the inner domain is the same as the defined exit pressure.

4.7.6. Periodic
The periodic boundary condition in TAU connects two planes and imposes the same values for the variables. It works for both translational and angular periodicity. However, it requires the meshes to be at least 1 cell wide. This has to be taken into account when employing it for 2D cases, since it has a non-negligible impact on the convergence and the results of the simulation.

4.7.7. Symmetry Plane
The symmetry plane boundary condition imposes a restriction on the normal to the wall velocity component and gradients, being both zero. It assumes that there is no flux through the boundary.

4.7.8. Pressure-driven Inflow
The boundary condition presented in this section is not included in TAU. However, very similar concepts have been extensively employed in the literature for 2D RDE simulations. Therefore, the algorithm to implement the boundary condition in TAU has been designed based on the structure of the reservoir-pressure inflow boundary.

The reservoir-pressure inflow computes the variables at the inlet according to the velocity field. Thus, it could be said that the expansion of the variables depends on the pressure gradient. The idea behind the pressure-driven boundary condition is to expand the mixture depending on the pressure in the inner domain.

First, the user defines the total gas properties and the species mass fractions. These information allows to compute the complete thermodynamic state of the reservoir mixture. In order to compute the variables at the domain inlet, the following assumptions are made: the chemical composition remains frozen during the expansion, and the expansion is isentropic. Then, the critical pressure can be computed as:

$$P_{cr} = P_0 \left(\frac{2}{\gamma + 1} \right)^{\frac{\gamma}{\gamma - 1}} \tag{4.42}$$

where P_0 is the reservoir total pressure and γ the specific heat coefficient of the mixture. Now, considering the inner domain pressure p_{in}, the critical pressure P_{cr}, and the total reservoir pressure P_0, the expansion regime can be determined. If the inner domain pressure is higher than the total reservoir pressure ($p_{in} > P_0$), then the boundary is treated as a wall to prevent backflow. If the inner domain pressure is higher than the critical pressure ($p_{in} > P_{cr}$) the expansion is subsonic, and otherwise is supersonic. Now, for each case, the expansion can be computed based on the value of the static pressure of the inner domain and the reservoir total pressure.

Due to the available thermodynamic solver tools in TAU, it is not possible to compute the complete thermodynamic state from the static pressure and the entropy. Therefore, a secant iterative method employing the static temperature is implemented. Since the secant method requires two points, two initial seeds are defined:

$$T^0 = T_0 \left(\frac{p_{in}}{P_0} \right)^{\frac{\gamma - 1}{\gamma}} \tag{4.43}$$

$$T^1 = 1.01 \cdot T^0 \tag{4.44}$$

where p_r is the inner domain static pressure and T_0 is the reservoir total temperature. For each temperature T^n, an associated entropy s^n is computed, and the method iterates until convergence. The convergence criteria is defined as the difference between the computed entropy at each step s^n, and the reservoir entropy s^0 such that: $|s^n - s_0| < 10^{-10}$.

Once the method has converged, the static pressure, temperature and entropy at the inlet are known, and the full thermodynamic state can be computed, as well as the inlet velocity. The boundary condition's algorithm (algorithm 1) can be seen below.

Algorithm 1: Determine inlet variables

Init: Y^0, P_0, T_0, p_{in}
Result: p_r, T_r, u_r, h_r

Compute the reservoir thermodynamic state (s_0, h_0)
Compute the critical pressure P_{cr}

if $p_{in} > P_0$ **then**

> *Blocked state*
> *The boundary is treated as a wall*
> ***Exit the function***

end
if *($p_{in} < P_0$) and ($p_{in} > P_{cr}$)* **then**

> *Subsonic regime*
> *Set the static pressure at the inlet*
> $p_r \leftarrow p_{in}$

end
if *($p_{in} < P_0$) and ($p_{in} < P_{cr}$)* **then**

> *Supersonic regime*
> *Set the static pressure at the inlet*
> $p_r \leftarrow P_{cr}$

end

Compute the initial seeds for the secant method: (T^0, T^1)
$s^0 \leftarrow f(T^0, p_r, Y^0)$
$s^1 \leftarrow f(T^1, p_r, Y^0)$

while $|s^n - s_0| > 1e - 10$ **do**

> $T^n \leftarrow g(s_0, s^0, s^1, T^0, T^1)$
> $s^n \leftarrow f(T^n, p_r, Y^0)$
>
> **if** *Convergence achieved* **then**
>
> > $T_r \leftarrow T^n$
> > $s_r \leftarrow s^n$
> >
> > ***Exit the function***
>
> **end**
>
> $T^0 \leftarrow T^1$
> $T^1 \leftarrow T^n$

end

Compute the complete thermodynamic state at the inlet

Preliminary RDE Characteristics Simulations

Before running the full 3D experimental case simulations, the employed set up has to be defined. In order to do this, a series of simulations have been conducted to study TAU capabilities to model RDEs physical phenomena.

5.1. 1D Shock Tube Simulations

The detonation wave is the main flow feature within the RDE flow field. To ensure it is properly resolved, a series of 1D shock tube simulations have been conducted to evaluate the most suitable parameters to capture this phenomenon.

The domain of the simulation can be seen in figure 5.1. The length of the tube is 500 mm, with a height of 1 mm. The tube is filled with a stoichiometric mixture of H_2-O_2 at ambient conditions (1 bar, 300 K). To ignite the mixture and generate a detonation, a hot spot is defined on the left side of the domain, where the origin of the coordinate system is considered to be. Within this region, the pressure is set to 15 bar and the temperature to 3000 K. After the ignition, the detonation will move towards the right side of the domain, in the positive x direction.

The Euler equations considering chemical reactions are solved. Moreover, the top and bottom boundaries of the domain are defined as inviscid, adiabatic walls. The right- and left-side boundaries are defined as a pressure-outlet boundary conditions with a prescribed ambient pressure of 1 bar. Furthermore, a third-order Runge-Kutta scheme is employed for time integration, as well as a dual-time-stepping approach.
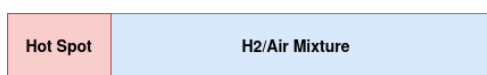
Figure 5.1: Schematic of the detonation tube and simulation initialization.

The mesh size found to be the best trade-off between computational cost and quality of the results was between 100 and 200 μm (see Appendix B), which is in line with the mesh sizes found in the literature. Regarding spatial discretization, the AUSMP upwind scheme was found to provide good results. Moreover, it was found that large time steps were stable thanks to the dual time-stepping strategy implemented in the solver. However, to obtain physically correct solutions at a reasonable computational cost, a time step of order 10^{-8} s was found to be the best option.

In this work, a set of simulations have been conducted to compare the behavior of different chemical reaction mechanisms. The mesh resolution is 100 μm. Moreover, the time step has been set to 10^{-9} s. Since the computational cost of the simulations is very low, a small time step can be used. Thus, the uncertainty introduced by larger time steps is reduced and it is easier to compare between different chemical reaction mechanisms. Furthermore, a more in-depth study of the different available upwind flux discretization schemes has been conducted after determining the most suitable chemical reaction mechanism.

5.1.1. Comparison Between Different Chemical Reaction Mechanisms

Figure 5.2 shows the evolution of the static pressure along the tube for different time steps. It can be seen how the detonation wave is confined to a very thin region of space. The mixture undergoes a sudden increment of the static pressure when the detonation arrives. Right downstream the detonation the value is the Chapman-Jouguet state. The reference values of the CJ state for the employed mixture were obtained from CEA [96]. After the detonation has passed, the mixture evolves from the CJ state towards equilibrium, and the pressure decreases according to the outflow condition set on the left-side boundary. All the different chemical reaction mechanisms show the same behavior regarding the static pressure evolution along the tube.
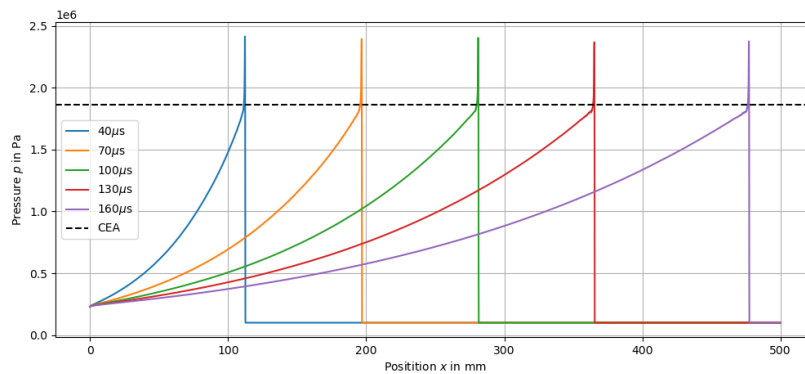
Figure 5.2: Static pressure along the shock tube for different points in time for the Ó Conaire [1] mechanism.

To compare the detonation properties of the chemical reaction mechanisms a closer look at the detonation waves is shown in figures 5.3 and 5.4. These figures are centered at the maximum static pressure since each mechanism has a different detonation velocity. For the same snapshot in time, each detonation wave is in a different point of the tube. The centering allows for a direct comparison of the shape and characteristics of the detonation waves.

When comparing the structure of the detonation from the ZND theory in figure 2.4 with the results in figure 5.3, it is clear that the resolution of the simulation is not enough to capture all the details of the detonation wave. The induction region is not clearly defined, not being able to see the region of constant temperature and pressure. However, the region of chemical heat release and the subsequent transition to the CJ state are better captured. This proves that this resolution is good enough to capture the main detonation characteristics relevant to RDE simulation.

Looking at figure 5.3a, it can be seen how all mechanisms behave similarly and according to detonation theory. However, there is a clear difference between the pressure and non-pressure dependent mechanisms. Gaffney has the highest pressure peak and slowest transition to the CJ state. This is probably due to the fact that it does not consider H_2O_2 and HO_2 chemistry. These two species paths become more relevant at high pressures. They are also related to the production and reaction of OH radicals. These radicals generally present fast chemical rates and very exothermic reactions. Not considering these reaction is what leads to Gaffney showing a slower temperature evolution compared to the other mechanisms (see figure 5.3b). On the other hand, Gerlinger has a more similar behavior compared to the other mechanisms since it considers the same chemical paths. Nevertheless, the difference comes from the fact that is not pressure dependent. At high pressures third body reactions become more predominant, thus influencing the primary chemical path. From figure 5.3 not much differences can be appreciated between Ó Conaire, Hong (Stf) and Boivin mechanisms. Hong has some reactions different to Ó Conaire and Boivin, mainly influencing ignition processes. This is why Hong shows a slower static pressure and temperature increment than the other mechanisms.

Figure 5.4 shows the evolution of hydrogen mass fraction and normalized heat release around the detonation wave. It can be seen how Gaffney has the highest hydrogen mass fraction, which can be explained by the fact that it does not consider H_2O_2 and HO_2 chemistry. Gerlinger shows a low value of the hydrogen mass fraction compared to the pressure-dependent mechanisms due to not considering the

(a) Static pressure.

(b) Static temperature.

Figure 5.3: 1D shock tube results comparison of static pressure and temperature for different chemical reaction mechanisms at $t = 100\ \mu$s centered at the maximum static pressure.

effect of pressure on the predominant chemical path. On the other hand, the differences between the pressure dependent mechanisms stem from the different included reactions and the constants defined, determining the rate of production and consumption of hydrogen.

Regarding figure 5.4b, although the resolution of the detonation wave is not fine enough, the heat release shows how the main detonation physics are captured. As defined by detonation theory, the induction region before the chemical heat release is where radicals are being produced, presenting endothermic reactions and therefore a negative heat release. Afterwards, the chemical heat release occurs, presenting exothermic reactions and achieving a maximum. These two regions can be distinguished in figure 5.4b. The differences seen in the normalized heat release for the different reaction mechanisms stem from the different dominant chemical paths and the levels of production of OH radicals. It is important to note that all mechanisms present the endothermic and exothermic reactions at the same point in space. This is due to not having enough mesh resolution to solve the detonation structure and the small chemical time scales of these processes, rather than matching results between the mechanisms. It can be seen how then each mechanisms evolves at a different rate towards the CJ state.

Since the origin in figure 5.4 is fixed where the static pressure is maximum, it shows how the peak in chemical heat release occurs right before the pressure peak, and similar to the hydrogen mass fraction peak. At this point, as seen in figure 5.3b, the temperature is still rising towards, the CJ state. ZND theory states that pressure should stay constant at its maximum right before the chemical heat release. The difference in the results probably caused by insufficient mesh resolution. Furthermore, the pressure peak right after the chemical heat release could also be related to the production of intermediate species and radicals in chain-branching reactions. As these species are consumed and the chemical heat release decreases, the pressure undergoes a decrease as well.

A key parameter related to detonation waves is the detonation wave speed. To compute the velocity at which the detonation is moving, at least two solutions at different times are required. The detonation velocity is computed by dividing the distance between the pressure peaks by the time difference between the two solutions. However, depending on how you choose the two solutions, different values of the detonation speed can be obtained due to accumulated errors. The mesh resolution, time step, and computer round-off are the main sources of error. In order to minimize the influence of these uncertainties, different solutions at different times have been compared to extract the minimum mean error of the detonation velocity.

Figure 5.5 shows the results of the mean error of the detonation velocity for the different chemical reaction mechanisms. It is important to note that for all mechanisms comparing two solutions too close in time leads to higher errors. This is because of the order of magnitude of the time difference being around $O(10^{-5})$ and the uncertainty coming from the mesh resolution. On the other hand, there seems to be an error increment when comparing two solutions very far apart, probably due to the uncertainty in the mesh

(a) Hydrogen mass fraction.

(b) Normalized heat release ($\|q\|_{mech} = (q/q_{max})_{mech}$).

Figure 5.4: 1D shock tube results comparison of hydrogen mass fraction and normalized heat release for different chemical reaction mechanisms at $t = 100 \ \mu$s centered at the maximum static pressure.

resolution and changes to the detonation properties along the tube. It can be seen how a minimum can be found for time differences of order $O(10^{-4})$ seconds.

As expected, Gaffney presents the highest error since it does not consider all the relevant species for H_2-O_2 chemistry. On the other hand, Gerlinger offers the lowest error. The difference with Ó Conaire could be explained by the fact that the latter used different reactions relevant to ignition delay, as well as having the influence of third-body reactions. Moreover, it could be argued that Hong (Stf) presents an error higher than Ó Conaire and Gerlinger due to adding an extra reaction for H_2O_2, altering the dominant chemical path and influencing the produced radicals.
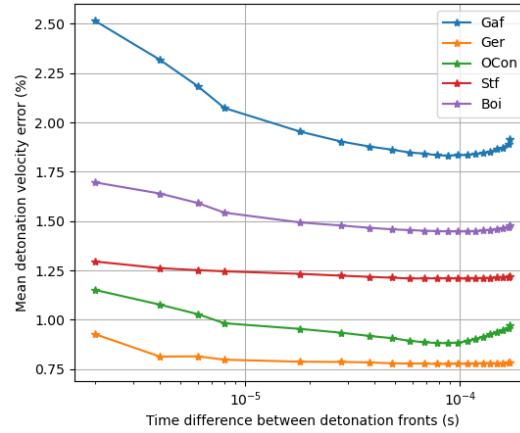
Figure 5.5: Mean error compared to CEA [96] values of the computed detonation velocity with respect to the time difference of the solutions employed to compute it for different chemical reaction mechanisms.

Table 5.1 shows a summary of all relevant results obtained for each chemical reaction mechanism and compared to CEA [96] values. The CJ state for the different mechanisms was obtained based on the normalized heat release. The shock is followed by a region of high chemical heat release. Right downstream said region, the CJ state is achieved. Therefore, to determine when this state was achieved for each case, algorithm 2 was employed.

In order to compare the different reaction mechanisms, different variables have to be taken into account: CJ temperature, CJ pressure, and detonation velocity. Each different quantity has a different order of

magnitude and an associated error with respect to the CEA result. Therefore, to determine which reaction mechanism is better, the three quantities are taken into consideration to determine a global normalized error (ϵ).

First, the absolute relative error ε of each quantity ψ with respect to the CEA result is calculated for each case i:

$$\varepsilon_{\psi,i} = \left| \frac{\psi_i - \psi_{CEA}}{\psi_{CEA}} \right| \cdot 100 \tag{5.1}$$

Once the absolute relative error is computed, a normalized relative error $\|\varepsilon_{\psi,i}\|$ is calculated for each case as follows:

$$\|\varepsilon_{\psi,i}\| = \frac{\varepsilon_{\psi_i}}{\varepsilon_{\psi_{max}}} \tag{5.2}$$

where $\varepsilon_{\psi_{max}}$ is the maximum absolute relative error among the different cases being compared.

Lastly, the global normalized error quantity can be computed for each case as an average of the different normalized relative errors:

$$\epsilon_i = \frac{1}{3} \left(\|\varepsilon_{T,i}\| + \|\varepsilon_{p,i}\| + \|\varepsilon_{U_D,i}\| \right) \tag{5.3}$$

Table 5.1 shows the values of the normalized global error for each case. It can be seen that Gaffney and Boivin offer the highest errors. This is expected since they are the simplest mechanisms, not being able to fully capture all the relevant processes. Then, Gerlinger and Hong are very similar, being the pressure-dependent mechanism slightly better. Lastly, Ó Conaire offers the best result, being the error of all the variables around 1% compared to CEA values. It is concluded that this is the best available chemical reaction mechanism.

Table 5.1: Results comparison of the Chapman-Jouguet state between 1D shock tube simulations for different chemical reaction mechanisms and CEA results for a stoichimetric mixture of H_2-O_2 in ambient conditions: 1 bar and 300 K.

Model	T_{CJ} (K)	p_{CJ} (MPa)	u_{CJ} (m/s)	ϵ (-)	Reference
CEA	3673.3	1.864	2834.9	-	[96]
Gaffney	3653.7	1.795	2782.9	0.9974	[29]
Gerlinger	3660.5	1.803	2812.8	0.6506	[35]
Ó Conaire	3665.7	1.842	2809.9	0.3979	[1]
Hong (Stf)	3660.9	1.818	2800.6	0.6493	[32]
Boivin	3655.2	1.794	2793.8	0.9043	[37]

5.1.2. Comparison Between Different Upwind Fluxes Discretization

In this section a comparison between different available upwind flux discretization schemes is conducted. The simulations employed the same set-up as in the previous section. The Ó Conaire reaction mechanism was chosen.

Figure 5.6a shows the static pressure and figure 5.6b the temperature profiles for different upwind fluxes at the same simulation time. The profiles are centered at the pressure peak. It can be seen that the fastest response comes from the AUSMDV flux, while the slowest is seen in the van Leer. This could be explained by the fact that the van Leer flux has a larger numerical dissipation, thus the slower response seen in both pressure and temperature profiles. On the other hand, the AUSMDV is specifically designed for accurate shock capturing, thus being the fastest of the four. AUSMP and AUSMPWP employ the same splitting Mach and pressure functions and compute the mass flux at the interface in the same fashion. The
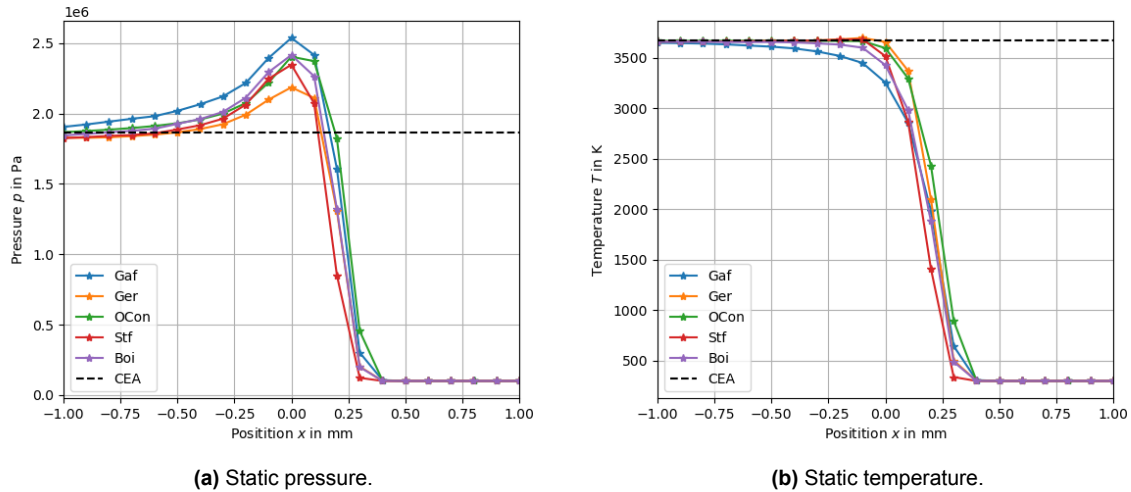
(a) Static pressure.

(b) Static temperature.
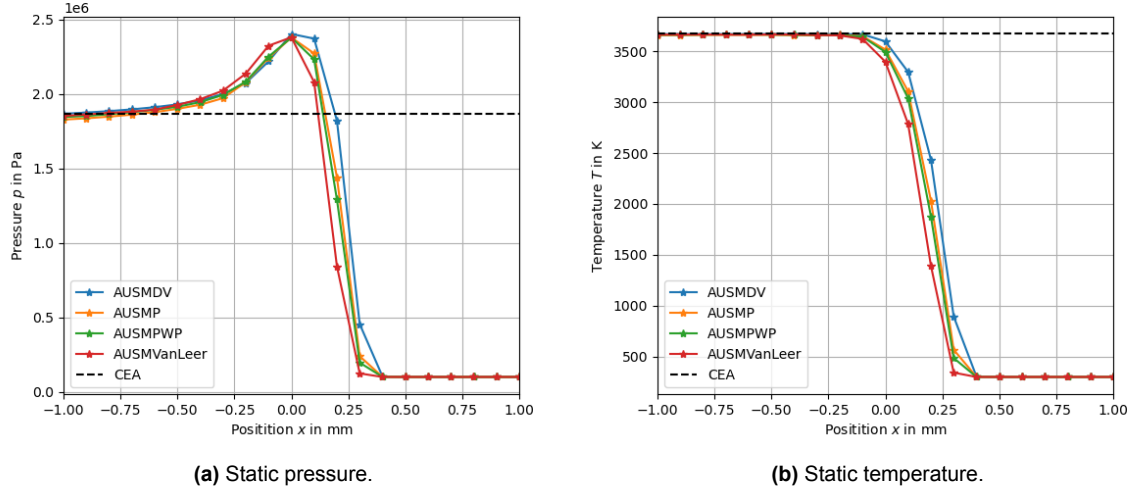
Figure 5.6: 1D shock tube results comparison of static pressure and temperature for different upwind discretization schemes at $t = 100$ μs centered at the maximum static pressure.

main difference between the two can be seen close to walls, hence having a very similar behavior for this 1D shock case.

Figure 5.7a shows the hydrogen mass fraction for the different fluxes. It is interesting to note that, as seen for the pressure and temperature profiles, the AUSMDV shows the fastest response. In this case, AUSMP and AUSMPWP differ more, being AUSMPWP slower reaching the peak. This could be due to the pressure-weighting functions having an influence on the local pressure and thus on the chemical paths.

Regarding the normalized heat release in figure 5.7, it can be seen how AUSMDV is the only flux to show clear oscillations. As seen in the literature review, this could be due to the tendency of AUSMDV to accept an oscillatory behavior in the vicinity of shocks compared to the other fluxes. However, as seen in figure 5.4b, these oscillations also depend on the chemical reaction mechanism. Therefore, the flux does not generate the oscillations, but rather fails to dampen them. On the other hand, the van Leer flux fails to predict the endothermic region due to the high numerical dissipation. Lastly, AUSMP and AUSMPWP capture properly the endothermic region before the chemical heat release thanks to their better handling of the pressure overshoots.

(a) Hydrogen mass fraction.

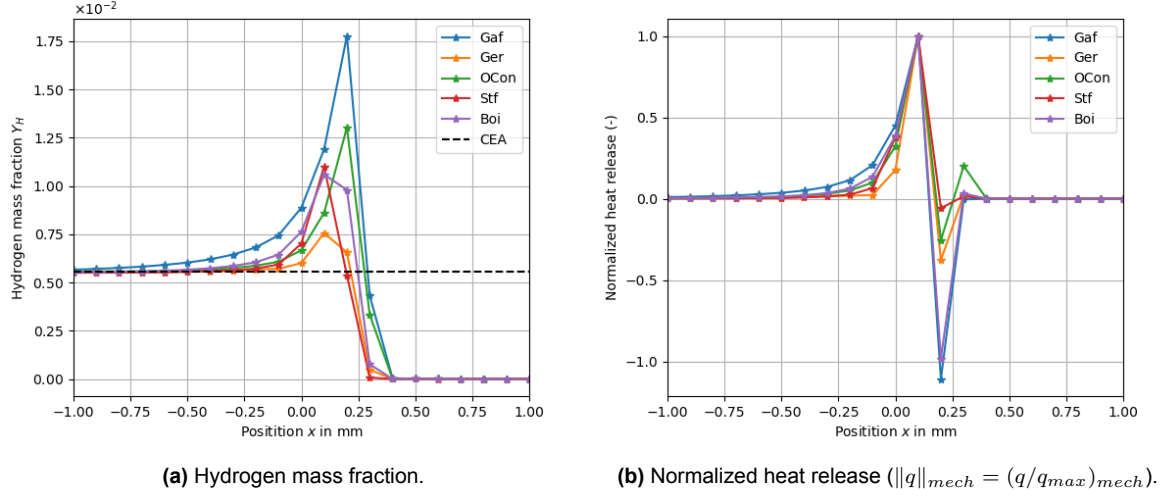**(b)** Normalized heat release ($\|q\|_{mech} = (q/q_{max})_{mech}$).
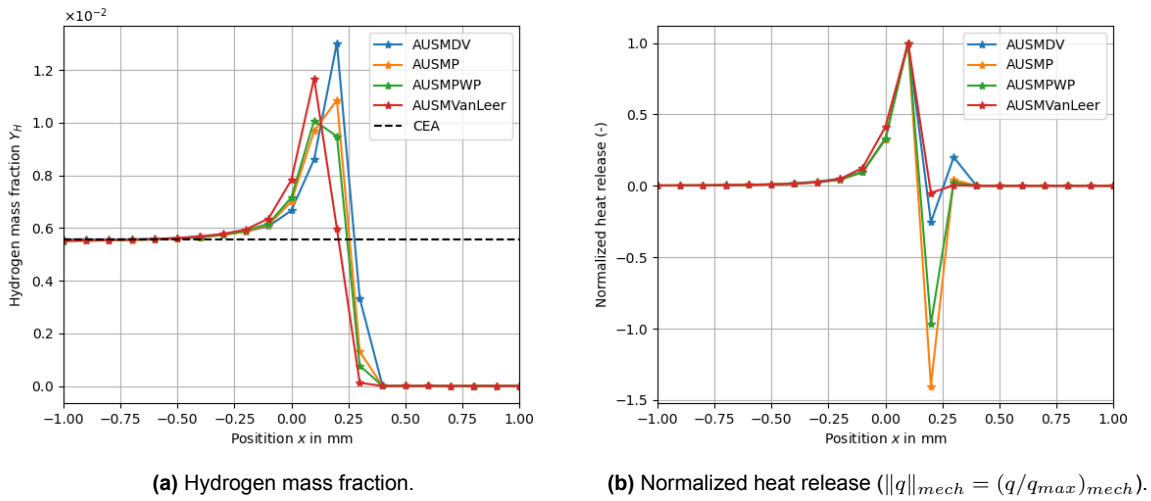
Figure 5.7: 1D shock tube results comparison of hydrogen mass fraction and normalized heat release for different upwind discretization schemes at $t = 100$ μs centered at the maximum static pressure.

Figure 5.8 shows the mean detonation velocity error for the different cases and for a range of different time differences. Although all the fluxes offer a low error (< 2.5%) it is clear that for this purpose the AUSMDV flux provides the best result. As mentioned above, the flux is tailored for shock capturing, having the fastest response, hence providing the fastest detonation velocity. On the other hand, AUSMP and AUSMPWP show a very similar behavior due to having the same definition of the splitting functions. The lower detonation velocity stems from the difference in the upwind flux and pressure-weighting functions compared to the AUSMDV flux. They are more robust and do not accept an oscillatory response, but dampen the solution as a results. The van Leer flux lies in between, although closer to AUSMP and AUSMPWP.
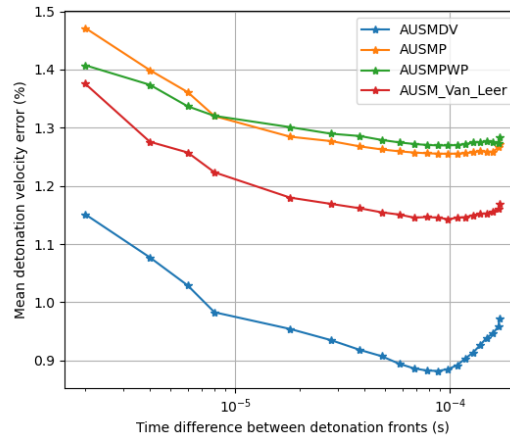
Figure 5.8: Mean error compared to CEA [96] values of the computed detonation velocity with respect to the time difference of the solutions employed to compute it for different upwind discretization schemes.

Lastly, table 5.2 shows the CJ state results and the detonation velocity for each case, employing the same normalized error described in equation 5.3. It can be seen how the best option in this case is the AUSMDV flux followed by the van Leer flux. For this specific case, the shock capturing ability of the AUSMDV flux makes it perform better than the more robust AUSMP and AUSMPWP fluxes. Considering this outcome, the AUSMDV flux will be employed as the baseline method. However, it is important to remember that the other fluxes could be more suited for different applications.

Table 5.2: Results comparison of the Chapman-Jouguet state between 1D shock tube simulations for different upwind discretization schemes and CEA results for a stoichimetric mixture of H_2-O_2 in ambient conditions: 1 bar and 300 K.

Model	T_{CJ} (K)	p_{CJ} (MPa)	u_{CJ} (m/s)	ϵ (-)	Reference
CEA	3673.3	1.864	2834.9	-	[96]
AUSMDV	3665.7	1.842	2809.9	0.4933	[2]
AUSMP	3656.0	1.798	2799.3	0.9962	[114]
AUSMPWP	3657.5	1.804	2798.9	0.9443	[118]
AUSM van Leer	3663.1	1.844	2802.5	0.6008	[111]

5.2. 2D Simulations of Sheng et al. Literature Case

Once the set up has been tested for 1D detonation simulations, it is important to evaluate it for 2D cases as well. This is due to the physical complexity associated with detonation dynamics. The structure of the detonation wave changes drastically when going from 1D to 2D. Therefore, the baseline case from Sheng et al. [120] has been reproduced employing the tools available in TAU.

A schematic of the domain with the ignition strategy employed can be seen in figure 5.9. The domain size is 120x40 mm. It is initially filled with diatomic nitrogen (N_2) since it is an inert gas, to avoid numerical

instabilities and chemical reactions. The static pressure of the inert gas is 1 bar and its static temperature is 300 K. In the lower left corner, the mixture of fresh gases consisting of diatomic hydrogen (H_2) and air in stoichiometric proportions is ignited by prescribing a static pressure of 15.75 bar and a static temperature of 2942 K. These values correspond to the CEA [96] values for a detonation of a H_2-Air mixture in stoichiometric conditions for an initial pressure of 1 bar and a temperature of 300 K. These values for static pressure and temperature are prescribed for the rectangular fresh mixture region right next to the hot spot. The dimensions of the hot spot are 5x5 mm and the rectangular fresh mixture region has dimensions 50x5 mm.
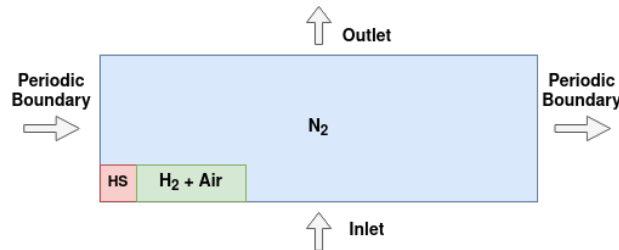
Figure 5.9: Schematic of the 2D domain and ignition strategy.

Once the mixture is ignited, a detonation wave will be generated, consuming the fresh reactants and moving towards the positive x-direction. The fresh mixture enters the domain from the lower boundary. The baseline inlet boundary condition employed for the simulations is a Dirichlet type. However, a more in-depth discussion on the impact of these choice on the results will be presented later. The post-combustion gases exit the domain through the upper boundary. The upper boundary is defined as an exit-pressure outlet, with a prescribe static pressure of 1 bar. On the sides, a periodic boundary condition has been defined.

The Euler equations considering chemical reactions are solved. The time step chosen for the simulations is $2 \cdot 10^{-8}$ s, with a CFL of 0.2 for the entire domain, and 0.1 for regions with large pressure gradients. For time integration, a third-order Runge-Kutta scheme is employed, combined with a dual-time step approach. The baseline chemical reaction mechanism employed for the simulations has been the Ó Conaire [1] mechanism. Moreover, the baseline upwind flux used has been the AUSMDV. Later in this section, the impact of different chemical reaction mechanisms and upwind fluxes will be evaluated. Lastly, the mesh resolution employed for the simulations is 200 μm. Nevertheless, the impact of mesh refinement on the results will be addressed as well.

Regarding the results shown in this section, all the flow field snapshots shown have been taken at time $t = 4.82 \times 10^{-4}$ seconds. Taking these results always at the same time allow to compare possible differences in the transient state that lead to different solutions at the same physical time.

5.2.1. Influence of the Inlet Boundary Condition
The choice of the inlet boundary condition plays a major role in the simulation results. As seen in chapter 2, the injection dynamics of an RDE are tightly coupled with the detonation dynamics, thus having an impact on the engine performance. The inlet boundary aims to model this injection process and its interaction with the flow field in the combustion chamber. Nevertheless, since it is a 2D simulation, the degree of accuracy with respect to experimental results is limited. Turbulent mixing effects are not present in this case, and the injected mixture is already premixed, rather than having a mixing process. Therefore, the solution obtained by a 2D simulation is an idealized approximation of a 3D case. In this work, two inlet boundaries have been evaluated: the reservoir-pressure inflow, and a Dirichlet type boundary condition.

The inlet gases enter the domain from a reservoir with a total temperature of 360 K and a total pressure of 5 bar, as described in Sheng et al. [120]. To define the reservoir-pressure inflow, these two quantities are set in the boundary condition definition, as well as the mass fractions for an H_2-Air stoichiometric mixture. The composition is assumed to be frozen, thus no chemical reactions occur until the mixture enters the domain. Moreover, backflow is prevented by treating the boundary as a wall when the inner domain pressure is higher than the reservoir total pressure. This inlet boundary condition could be physically interpreted as a set of convergent nozzles which expand the mixture from the reservoir depending on the velocity field seen in the simulation domain.

On the other hand, the physical interpretation of the Dirichlet boundary condition is different. Since

the flow variables are prescribed at the inlet, this boundary condition is interpreted as a fixed sonic inlet injecting the stoichiometric mixture into the domain. The sonic injection is a design choice from Sheng et al. [120]. The values prescribed at the inlet are the velocity, static temperature and the density, as well as the mass fractions. Therefore, the isentropic expansion from reservoir conditions to sonic conditions has to be computed. To do so, the area ratio expression for a convergent nozzle assuming isentropic quasi-1D flow is employed [121]:

$$\frac{A}{A^*} = \varepsilon = \frac{\Gamma(\gamma)}{\left(\frac{p_r}{P_0}\right)^{\frac{1}{\gamma}} \sqrt{\frac{2\gamma}{\gamma-1} \left[1 - \left(\frac{p_r}{P_0}\right)^{\frac{\gamma-1}{\gamma}}\right]}}; \quad \text{where } \Gamma(\gamma) = \left(\frac{2}{\gamma+1}\right)^{\frac{\gamma+1}{2(\gamma-1)}} \tag{5.4}$$

where γ is the specific heat ratio computed from the reservoir mixture mass fractions, p_r is the static pressure prescribed at the boundary, and P_0 is the reservoir total pressure. Since the mixture is being expanded to sonic conditions, the area ratio is unity ($\varepsilon = 1$).

Equation 5.4 is solved in an iterative fashion to obtain the nozzle pressure ratio for the supersonic branch solution. Starting from an initial pressure ratio of zero $\left(\left.\frac{p_r}{P_0}\right|_0 = 0\right)$, equation 5.4 is rearranged in the following manner to solve for the pressure ratio:

$$\left.\frac{p_r}{P_0}\right|_{n+1} = \left(\frac{\Gamma(\gamma)}{\varepsilon\sqrt{\frac{2\gamma}{\gamma-1}\left[1 - \left(\left.\frac{p_r}{P_0}\right|_n\right)^{\frac{\gamma-1}{\gamma}}\right]}}\right)^{\gamma} \tag{5.5}$$

The convergence criteria employed is as follows:

$$\left\| \left.\frac{p_r}{P_0}\right|_{n+1} - \left.\frac{p_r}{P_0}\right|_n \right\| < 10^{-12} \tag{5.6}$$

Once the iterative process has converged and the pressure ratio is found, the other inlet variables can be computed employing the isentropic expansion expressions and the equation of state, as shown below:

$$T_r = T_0 \left(\frac{p_r}{P_0}\right)^{\frac{\gamma-1}{\gamma}} ; \quad u_r = M\sqrt{\gamma R T_r} ; \quad \rho_r = \frac{p_r}{R T_r} \tag{5.7}$$

where R is the mixture gas constant, and M is the Mach number, which is equal to unity as it is a sonic expansion. Once all the static inlet variables have been computed, the Dirichlet boundary condition is fully defined.

Figure 5.10 shows the static pressure along the combustion chamber for the two different boundary conditions compared to Sheng et al. [120] results. It can be seen how the detonation waves for both simulations are behind Sheng et al. wave. This implies that the predicted detonation velocity is lower than in the literature case. Moreover, when comparing the shape of the pressure profile, it is clear that the reservoir inlet underpredicts the maximum pressure. It also shows a different behavior of the expansion after the pressure peak. On the other hand, the Dirichlet boundary condition has a very similar maximum pressure and expansion process after the pressure wave compared to Sheng et al. The inlet boundary condition employed by Sheng et al. is the same pressure-driven boundary condition described in section 4.7.8. This boundary condition behaves as the Dirichlet boundary condition when in sonic conditions, but it adapts the injection variables depending on the inner domain static pressure. On the other hand, the reservoir-pressure boundary condition is driven by the velocity field, thus having different results compared to the other two cases. It could be said that the Dirichlet boundary condition is an idealized case of the pressure-driven boundary, since it assumes the injection is always sonic and it is not affected by the detonation dynamics.
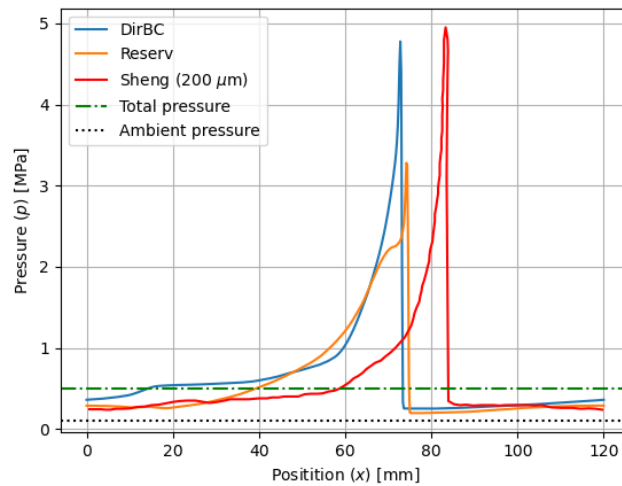
Figure 5.10: Static pressure comparison between the Dirichlet boundary condition (DirBC), the reservoir-pressure inlet (reserv), and Sheng et al. [120] results for its baseline case with a resolution of $200 \ \mu$m along the combustion chamber at a height $z = 10$ mm.

Regarding the detonation velocity, the differences between the simulations and the literature probably stem from the TAU limitations when simulating 2D geometries with periodic boundary conditions. As this feature is not implemented in TAU, a 3D simulation of a 1-cell-wide mesh is being solved instead, thus having an impact on the results. However, the difference in detonation velocity between the two inlet boundary conditions is negligible. Figure 5.11a shows the static pressure measured at a probe located at $[60,2]$ mm within the combustion chamber for both inlet boundaries. It can be seen that the Dirichlet boundary condition (Dir) records a higher maximum pressure compared to the reservoir-pressure (Reserv) inlet, as seen in the previous figure. On the other hand, the pressure peaks in both cases are located on top of each other, thus indicating that the detonation velocity in both cases is very similar. Lastly, it can be seen how the expansion after the wave is different for both cases, being more abrupt for the reservoir-pressure case.
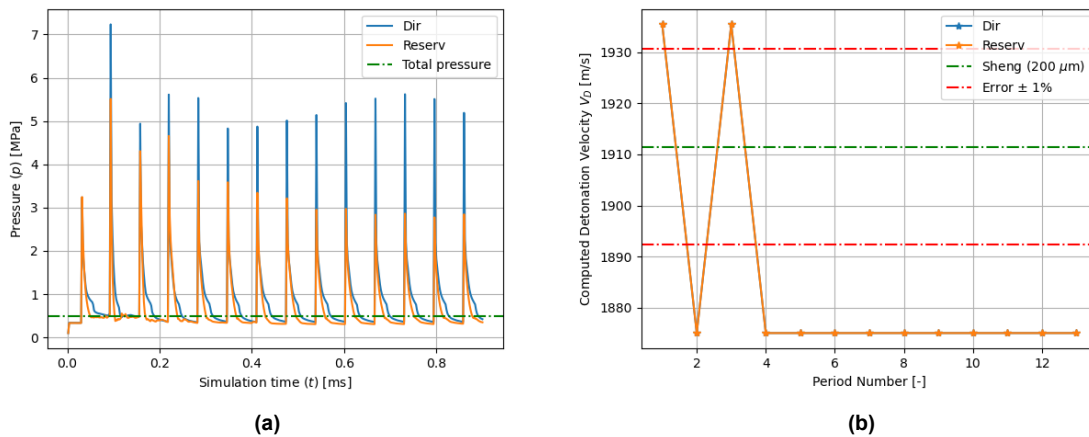
Figure 5.11: a) Static pressure measured at a probe located in $[60,2]$ mm during the simulation time, and b) computed detonation velocity based on the time between pressure peaks of the measured pressure at the probe for the Dirichlet inlet (Dir) and the reservoir-pressure inlet (Reserv) boundaries.

Figure 5.11 shows the detonation velocity computed by taking the time difference between pressure peaks in figure 5.11a. It is clear that both inlet boundaries have the same detonation velocity. It is

also interesting to note how in the first and third periods the velocity is higher, and then converges into the final velocity. This could be due to the initial transient state, when the detonation is still varying in strength and height. Moreover, due to the finite number of measurements taken during the simulation time, and the error associated with this method of computing the detonation velocity, slight differences in the detonation velocity are not captured. In order to ensure this method is reliable, another way of computing the detonation velocity was implemented. Instead of measuring the detonation period around the combustion chamber, the velocity was computed by taking the space and time difference between two pressure waves of consecutive measurement, tracking the movement of the detonation. As the time step between samples is of order $O(10^{-6})$ seconds, the errors associated with each computed velocity are quite high. However, when taking the mean of the values, a good detonation velocity approximation is found. The results are shown in table 5.3. As it can be seen, the wave tracker method shows a slightly higher detonation velocity of the reservoir-pressure inlet boundary, as seen in figure 5.10. Nevertheless, both detonation velocities are very similar and are within 1.5% error when compared to Sheng's result.

Table 5.3: Detonation velocity for the different inlet boundaries computed with different methods: period measurement (Period), and wave tracker (Tracker); and compared to the result of Sheng et al. [120] for a resolution of $200 \ \mu$m.

Method	Dirichlet [m/s]	Reservoir [m/s]	Sheng [m/s]
Period	1884.31	1884.31	1911.52
Tracker	1884.41	1887.52	-

The differences between the two inlets are also visible in the flow field. Figure 5.12 shows the static temperature flow field for the Dirichlet inlet (figure5.12a) and the reservoir-pressure inlet (figure 5.12b) for a certain instant in time. Both cases show the same range of temperatures and typical structures of a 2D RDE flow field. The detonation front moving towards a triangular-like shaped mixture of fresh gases, an oblique shock emanating from the end of the detonation wave, and a slip-line between the expanded post-combustion gases behind the detonation and the gases from the previous period. The main difference when looking at these features is the oscillations present in the reservoir-pressure inlet case. The mixture of fresh gases seen in figure 5.12b has a parabolic shape compared to the fresh gases seen in figure 5.12a. This is because the inlet variables depend on the velocity field, and are thus affected by the detonation dynamics, when employing the reservoir-pressure inlet. The Dirichlet boundary condition shows an ideal triangular shape as the injection velocity is independent of the flow field within the combustion chamber. It is also interesting to note the difference in the slip line behind the oblique shock. While the reservoir-pressure inlet case (figure 5.12b) shows clear instabilities that resemble Kelvin-Helmholtz instabilities, the Dirichlet type inlet (figure 5.12a) does not show the same oscillatory behavior.

(a)   **(b)**
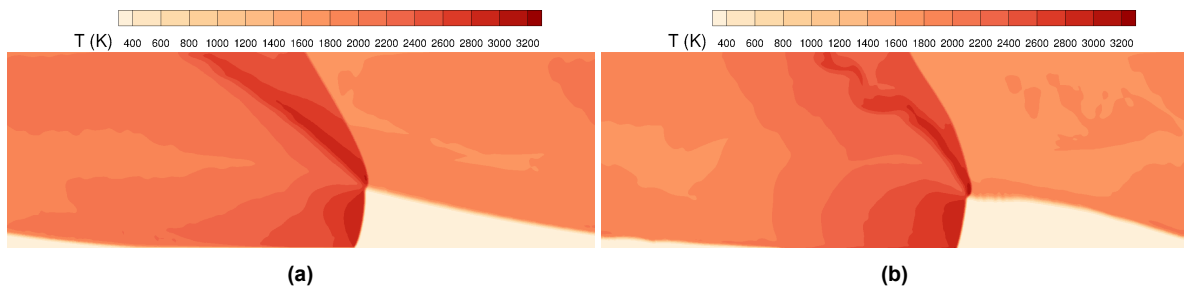
Figure 5.12: Static temperature flow field for the Dirichlet inlet (a) and the reservoir-pressure inlet (b).

Figure 5.13 shows the normalized pressure gradient flow field, as well as the normalized heat release colored in red. It can be seen how, for both cases, the detonation wave is the region with the highest chemical heat release, and can be easily differentiated from other pressure waves.

The normalized pressure gradient is defined as follows:

$$|\nabla p\| = 1 - \exp\left(-50 \frac{|\nabla p|}{|\nabla p|_{max}}\right) \tag{5.8}$$

where $|\nabla p|_{max}$ is the maximum pressure gradient module throughout the full simulation time.

The normalized heat release at a time step n, $\|q^n\|$, is defined as the ratio between the heat release at that time step q^n divided by the maximum heat release throughout the full simulation time q_{max}. The idea behind this quantity is to qualitatively distinguish between pressure waves and detonation waves, since it clearly depicts where the highest chemical heat release is taking place. On the other hand, the normalized pressure gradient informs about the regions in the domain where shocks and expansions are present. Both cases in figure 5.13 have the detonation wave followed by two expansion fans emanating from the detonation's ends. However, as seen in figure 5.12, the differences are found in the oscillatory behavior of the reservoir-pressure inlet (figure 5.13b). It can be seen how, for this case, the post-combustion gases suffer a stronger expansion right after the detonation wave. Then, the expansion becomes weaker again in an intermittent fashion. This is shown by the horizontal dashed line that separates the post-combustion gases from the flow behind the oblique shock, close to the center of the domain in the vertical z direction. On the other hand, the Dirichlet boundary (figure 5.13a) has a clear line that separates the post-combustion gases from the gases after the oblique shock.

(a)   **(b)**
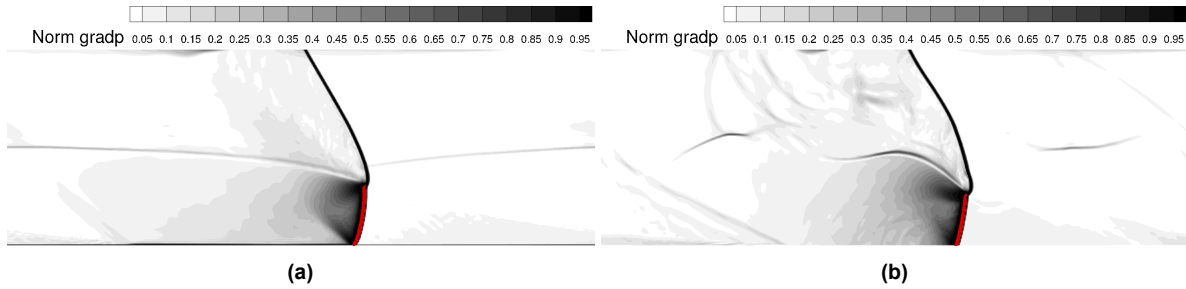
Figure 5.13: Normalized pressure gradient flow field for the Dirichlet inlet (a) and the reservoir-pressure inlet (b) showing the normalized heat release region colored in red.

Some differences can also be identified when looking at the Mach number flow field in figure 5.14. As seen in the normalized pressure gradient flow field, the Dirichlet inlet (see figure 5.14a) has a continuous horizontal expansion region emanating from the same point as the oblique shock, and fading away before the detonation wave arrives. This same region in the reservoir-pressure inlet (see figure 5.14b) is not continuous, having an expansion pocket in front of the incoming detonation wave and a small subsonic pocket after it. Moreover, right after the detonation and after the oblique wave, the expansion is much stronger, having larger regions of high Mach number. It is important to mention that, in both cases, the outlet Mach number in the entire exit boundary is above unity.

(a)   **(b)**
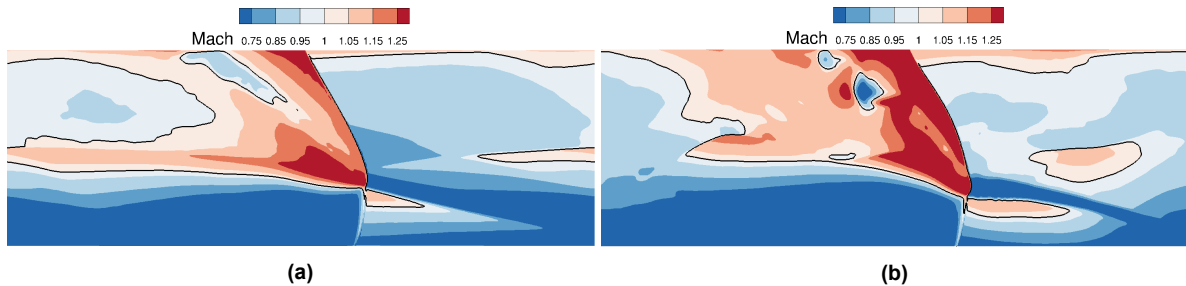
Figure 5.14: Mach number flow field for the Dirichlet inlet (a) and the reservoir-pressure inlet (b) outlining Mach unity with a black line.

Another indicator of the differences in the oscillatory behavior of the two inlets can be seen in figure 5.15a. It shows the detonation height as a function of the simulation time. This quantity is tightly coupled with the injection dynamics and their interaction with the detonation dynamics. Both simulations have a transient regime until they reach a more stable state, approximately after 0.3 ms. After that, they oscillate around the same value with a decreasing amplitude. To compute the detonation height for every time step, the normalized heat release field was employed. Taking a constant z line, the maximum normalized heat release drops several orders of magnitude when the detonation ends. Therefore, the detonation height

can be determined by looking at when the chemical heat release suffers an abrupt decrement.

When comparing the detonation height signals of both cases, it can be seen how the Dirichlet inlet (Dir) and the reservoir-pressure inlet (Reserv) follow the same low-frequency oscillations. On top of that, the reservoir-pressure inlet shows high-frequency oscillations. This can be proven by taking the power spectral density (PSD) of the signal as seen in figure 5.15b. At around 8000 Hz, both Dirichlet and reservoir-pressure inlets have a peak of similar magnitude. However, towards higher frequencies, the PSD for the Dirichlet case drops, while the reservoir-pressure inlet shows more peaks. This proves the coupling of the injection and the detonation dynamics in the reservoir-pressure case. The Dirichlet boundary only has the oscillations associated with the periodicity of the detonation wave running around the combustion chamber.

(a)   (b)
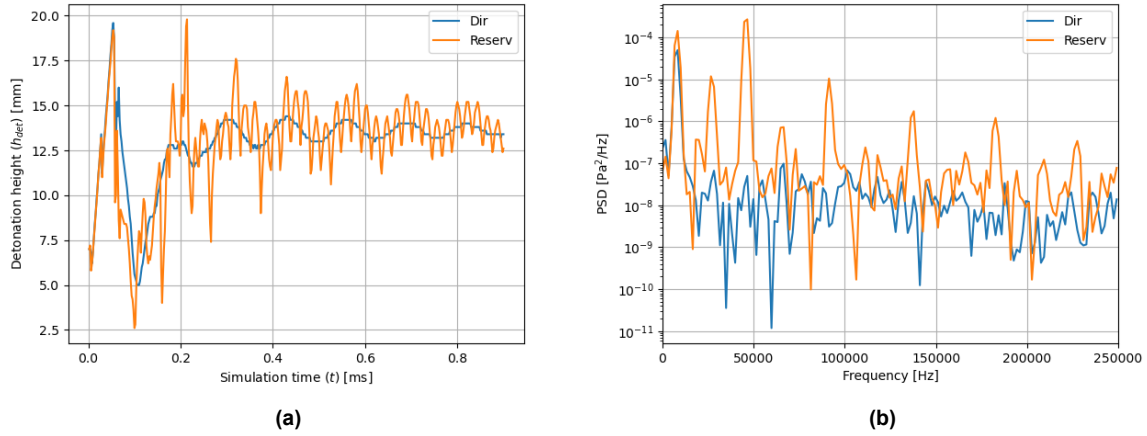
Figure 5.15: Detonation height as a function of simulation time (a) and Power Spectral Density [PSD] of the detonation height signal (b) for both Dirichlet (Dir) and reservoir-pressure (Reserv) inlet boundary conditions.

The differences seen in the flow field and the detonation height also have an impact on the outlet variables. Figure 5.16a shows the average outlet static pressure as a function of the simulation time. It can be seen how the pressure, on average, is higher for the Dirichlet (Dir) case. Moreover, the reservoir-pressure inlet (Reserv) shows again this high-frequency oscillations. On the other hand, the standard deviation of the outlet static pressure shows that it is higher for the reservoir-pressure case. This implies that the range of values at the outlet for the reservoir-pressure inlet is higher. This behavior could be a consequence of the coupling between the injection process and the detonation wave.

(a)   (b)
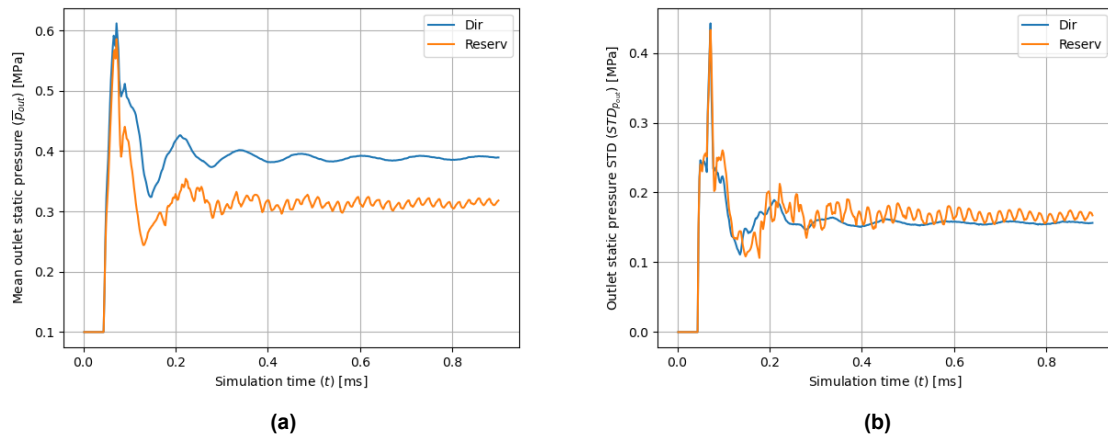
Figure 5.16: Mean outlet static pressure (a) and standard deviation of the outlet static pressure (b) for both Dirichlet (Dir) and reservoir-pressure (Reserv) inlet boundary conditions as a function of the simulation time.

In addition, the difference in the value of the outlet pressure could also be a consequence of the well- or ill-posedness of the problem. When defining the inlet as a Dirichlet boundary, the characteristic lines emanating from the boundary are prescribed, but it does not consider characteristics coming from the inside of the domain, as in a subsonic case. Therefore, the problem is ill-posed for the Dirichlet boundary condition when the inlet is subsonic and there is a prescribed outlet pressure. This could lead to errors in the results for some cases.

Figure 5.17 shows the mean outlet static temperature (figure 5.17a) and the standard deviation of the outlet static temperature (figure 5.17b). The trends are identical to those seen in the static pressure plots (see figure 5.16). On average, the outlet static temperature is higher in the Dirichlet case (Dir) while the standard deviation is lower. Moreover, the reservoir-pressure inlet presents these high-frequency oscillations in the signals.
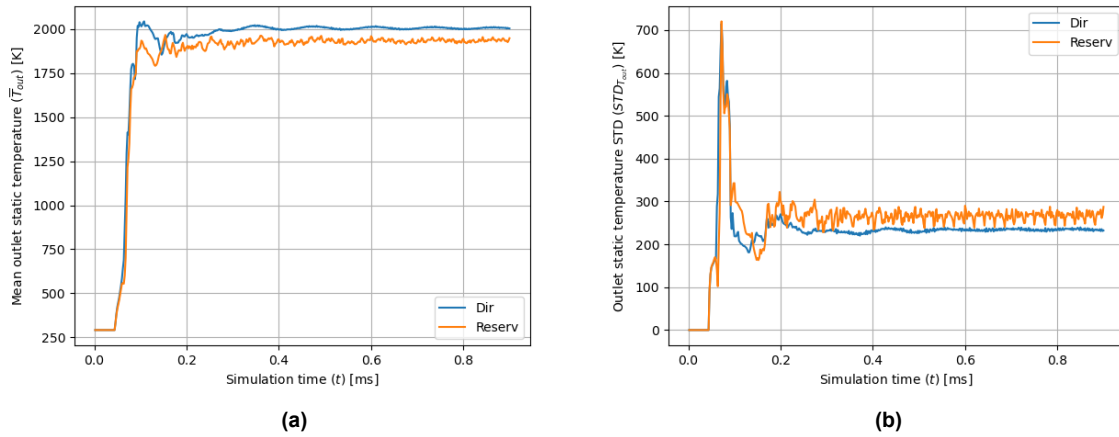
Figure 5.17: Mean outlet static temperature (a) and standard deviation of the outlet static temperature (b) for both Dirichlet (Dir) and reservoir-pressure (Reserv) inlet boundary conditions as a function of the simulation time.
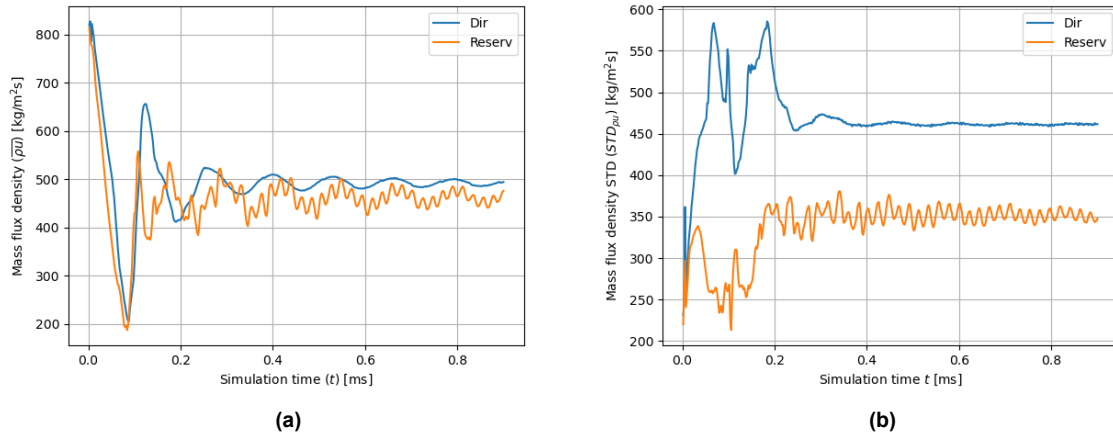
Figure 5.18: Mean mass flux density (a) and standard deviation of the mass flux density (b) for both Dirichlet (Dir) and reservoir-pressure (Reserv) inlet boundary conditions as a function of the simulation time.

Lastly, figures 5.18a and 5.18 show the mean mass flux density and its standard deviation, respectively. The trends are not the same as for the static pressure and temperature. The average mass flux density (figure 5.18a) shows again how the Dirichlet inlet case (Dir) has a higher average, while not presenting the high-frequency oscillations of the reservoir-inlet case (Reserv). On the other hand, the standard deviation (figure 5.18b) clearly shows how the variation is higher in the Dirichlet inlet case. This is probably due to the constant inlet velocity and the assumption that the inlet is always choked and sonic. The injection is

never fully blocked, thus having a great difference between the high pressure region around the detonation wave, and the rest of the domain.

This section shows how the reservoir-pressure inlet can model the interaction between injection and detonation dynamics, capturing these high-frequency oscillations that can also be seen in the results of Sheng et al. [120]. It can also predict with a good degree of accuracy the detonation velocity, a seen in table 5.3. However, it fails to properly compute the detonation wave properties as it underpredicts the maximum pressure (see figure 5.10). It is also important to mention that the expansion from the reservoir state is not controlled by the pressure field within the combustion chamber, but rather by the velocity field. On the other hand, the Dirichlet boundary condition offers a more idealized solution which does not model the interaction between the detonation wave and the injection. Nevertheless, the overall detonation properties are computed with accuracy. Therefore, the Dirichlet boundary condition has been employed for the rest of the 2D simulations conducted.

5.2.2. Influence of the Ignition Methodology

An important step when setting up RDE simulations is the ignition method to generate the detonation wave. The objective of this section is to evaluate whether a different ignition procedure can lead to different results.
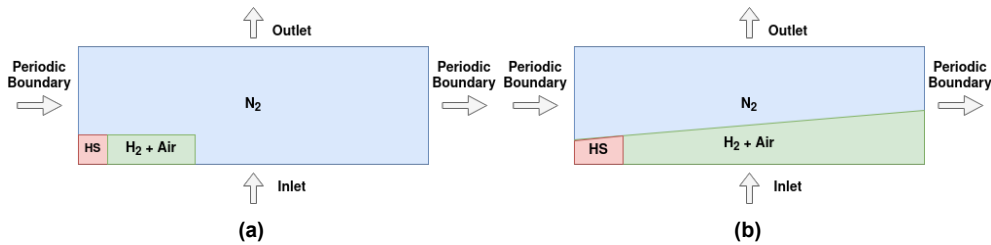
Figure 5.19: (a) Schematic of the rectangular ignition strategy and (b) schematic of the oblique ignition strategy.

The oblique ignition strategy employed as a comparison with respect to the baseline method is shown in figure 5.19b. The oblique mixture of fresh gases is set to ensure the propagation of a stable detonation. Moreover, the hot pocket region is defined to have the same area as in the rectangular ignition method, with exactly the same pressure and temperature. This is done to ensure that the same amount of energy is artificially added to the domain. In addition, a third ignition strategy has been evaluated to study the impact of different levels of energy added to the simulation. In this case, the rectangular scheme shown in figure 5.19a is employed, but the hot pocket dimensions are doubled compared to the baseline case, thus being $10x10$ mm size.
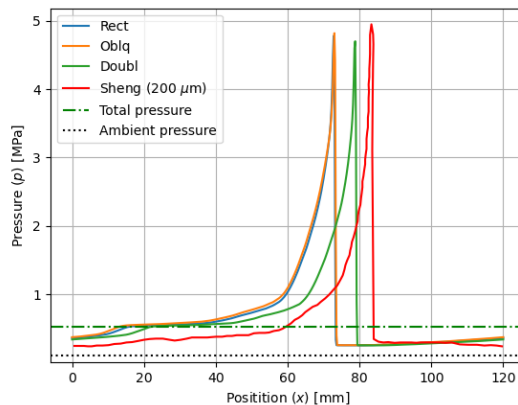
Figure 5.20: Static pressure comparison between the rectangular ignition strategy (Rect), the oblique ignition strategy (Oblq), the double-energy rectangular ignition strategy (Doubl), and Sheng et al. [120] results for its baseline case with a resolution of $200\ \mu$m along the combustion chamber at a height $z = 10$ mm.

For the oblique ignition case, the boundary conditions on the sides are set to Euler walls until the initial detonation wave is in the middle of the domain. This is done to prevent the hot pocket consuming the fresh reactants in both directions, generating two counter rotating detonation waves that cancel out each other when colliding. The set up employed is the same as described at the beginning of this chapter, and the Dirichlet boundary condition is employed at the inlet. Moreover, during the first iterations of the simulation, the dual-time stepping technique is turned off. The lowest local time step is employed for the entire domain. This is done due to the artificially high gradients and associated numerical stiffness of the problem. After some iterations have passed, the dual-time stepping approach is used again.

Figure 5.20 shows the static pressure profile along the combustion chamber at a height of $z = 10$ mm. It can be seen how there are no differences between the rectangular and the oblique ignition methods. The shape of the wave, as well as the maximum pressure are the same. Moreover, they are at the same position, which implies that they have the same detonation speed. On the other hand, the double-energy rectangular case wave is ahead and closer to the Sheng et al. results. This implies a higher detonation velocity. Moreover, the pressure peak is also very similar, as well a the wave shape.

(a)

(b)
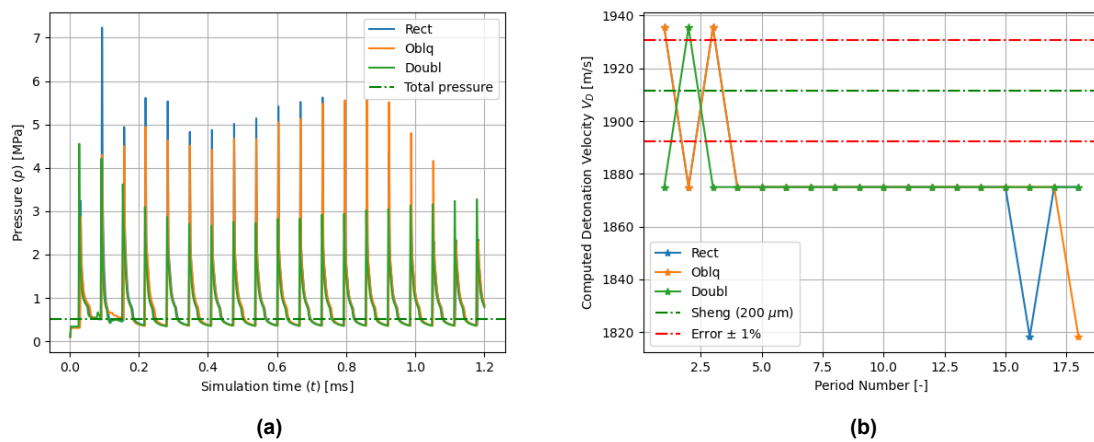
Figure 5.21: a) Static pressure measured at a probe located in $[60,2]$ mm during the simulation time, and b) computed detonation velocity based on the time between pressure peaks of the measured pressure at the probe for the rectangular ignition (Rect), the oblique ignition (Oblq) and the double-energy rectangular ignition (Doubl) strategies.

Figure 5.21a shows the static pressure measured at the combustion chamber mid span throughout the simulation time. The baseline rectangular and oblique ignition methods present very similar pressure peak values throughout the entire simulation time, having both a drop in this value after $t = 1$ ms. On the other hand, the double-energy rectangular case after around $t = 0.4$ ms does not suffer from large variations on the pressure peak value.

On the other hand, figure 5.21b shows the computed detonation velocity from the difference in time of the pressure peaks from the pressure plot. The three cases show a very similar detonation velocity results. It is interesting to note how the detonation velocity decreases for the baseline rectangular and oblique ignition methods at the same point in time as their peak pressure values decrease, as seen in figure 5.21a, while the double-energy rectangular case values remain constant.

Table 5.4: Detonation velocity for the different ignition methodologies computed with different methods: period measurement (Period), and wave tracker (Tracker); and compared to the result of Sheng et al. [120] for a resolution of 200 μm.

Method	Rectangular [m/s]	Oblique [m/s]	Double [m/s]	Sheng [m/s]
Period	1878.56	1878.56	1878.36	1911.52
Tracker	1881.80	1881.96	1885.80	-

The detonation velocity was not only computed employing the pressure log, but also the pressure wave tracker mentioned in the previous section. Table 5.4 shows the results for the detonation velocity computed with both methods. From the results it can be concluded that the period method tends to provide lower detonation velocities compared to the tracker. In addition, it can be seen how the detonation velocity is not influenced by changing the ignition strategy. Even if the hot pocket dimensions are doubled, the difference in the detonation velocity based on the tracker method results between the rectangular and double-energy cases is of 0.21%.

Figure 5.22 shows the static temperature flow fields for the different ignition strategies. It is clear that once the simulation stabilizes after some periods, the results are close to being identical. The same can be said for the normalized pressure gradient flow fields shown in figure 5.23 and the Mach number flow fields from figure 5.24. They share the same features with no clear differences.
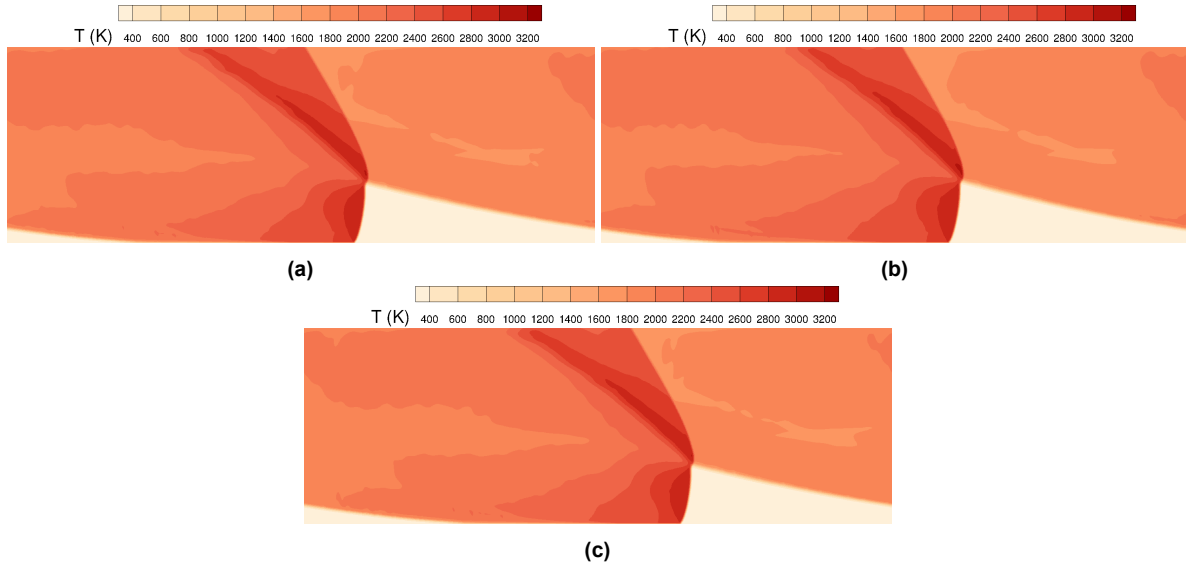
Figure 5.22: Static temperature flow field for the rectangular ignition strategy (a), the oblique ignition strategy (b) and double-energy rectangular strategy (c).
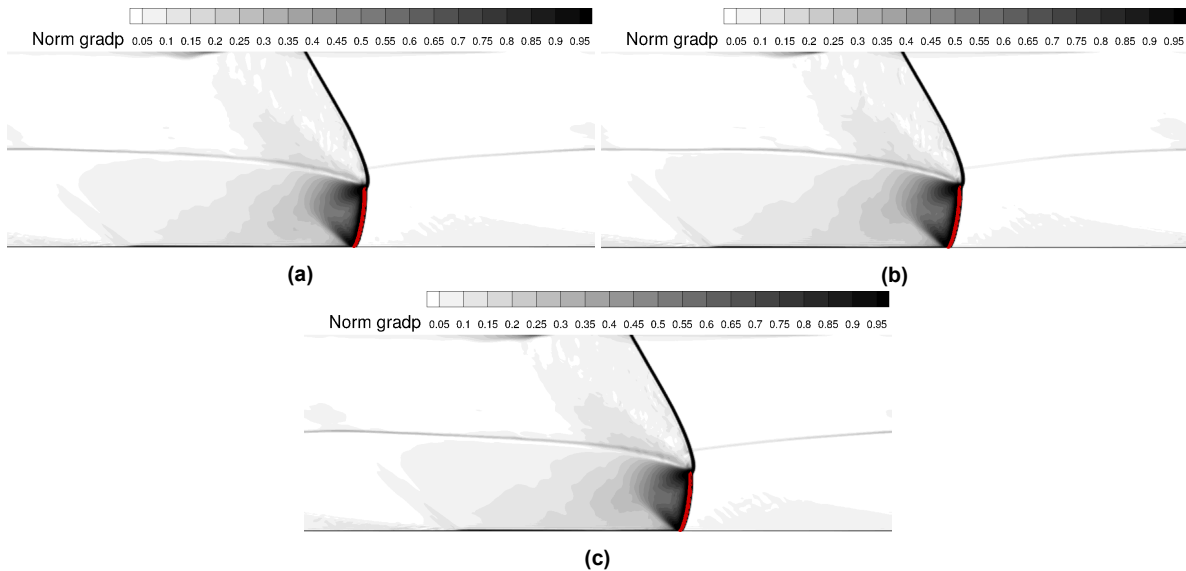
Figure 5.23: Normalized pressure gradient flow field for the rectangular ignition strategy (a), the oblique ignition strategy (b) and double-energy rectangular strategy (c) showing the normalized heat release region colored in red.
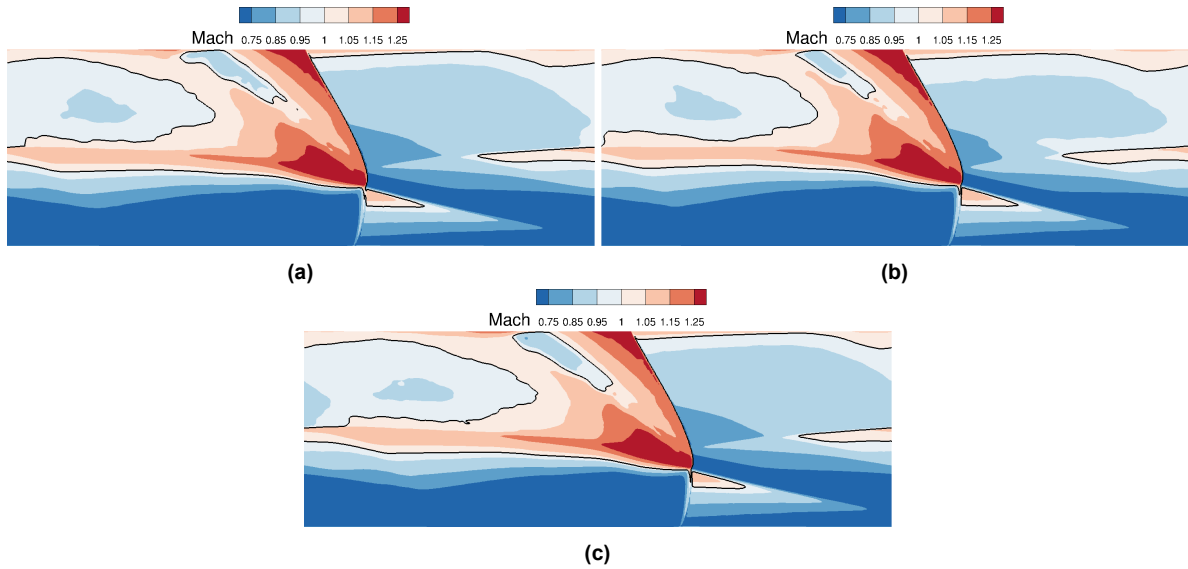
Figure 5.24: Mach number flow field for the rectangular ignition strategy (a), the oblique ignition strategy (b) and double-energy rectangular strategy (c) outlining Mach unity with a black line.
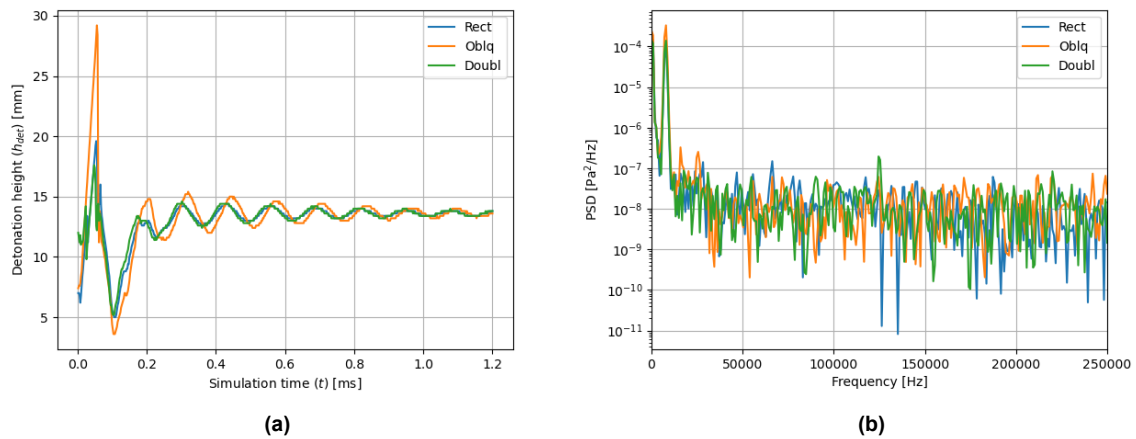
Figure 5.25: Detonation height as a function of simulation time (a) and Power Spectral Density [PSD] of the detonation height signal (b) for both rectangular (Rect), oblique (Oblq) and double-energy rectangular (Doubl) ignition strategies.

When comparing the detonation wave height and shape in the normalized pressure gradient flow fields (see figure 5.23), it seems like there are no differences. However, figure 5.25a clearly shows how there is a difference in the detonation height when comparing the rectangular and the oblique approaches. The oblique ignition detonation height seems to have the same frequency of variation associated to the periodicity of the solution, while presenting a higher amplitude and a phase shift. It is also important to mention that this initial higher amplitude is damped as the simulation progresses, becoming more similar to the rectangular case. This oscillatory behavior is probably related to the initial disposition of the fresh gases which force the initial detonation wave to grow higher than the inlet conditions could generate. After this initial very high detonation height and the sudden drop, the dampened oscillatory behavior occurs. On the other hand, it can be seen how the double-energy case is identical to the baseline results. This implies that the evolution of the detonation height is coupled to the injection of the fresh gases rather than the amount of energy introduced into the system.

On the other hand, figure 5.25b shows how the three cases share the same frequency peak at low frequencies, directly related to the detonation velocity. Nevertheless, the oblique case has a small frequency peak in the low frequencies, which is not seen in the rectangular ignition case. It is probably related to the

dampened oscillatory behavior of the oblique strategy.

Figure 5.26a shows the mean outlet static pressure. As in figure 5.25a, the results for the baseline and double-energy case are identical. On the other hand, the oblique ignition case has a small phase shift at the beginning, but the results tend to the same values as the other two cases as time progresses. The same behavior can be seen in the outlet static pressure standard deviation in figure 5.26b.
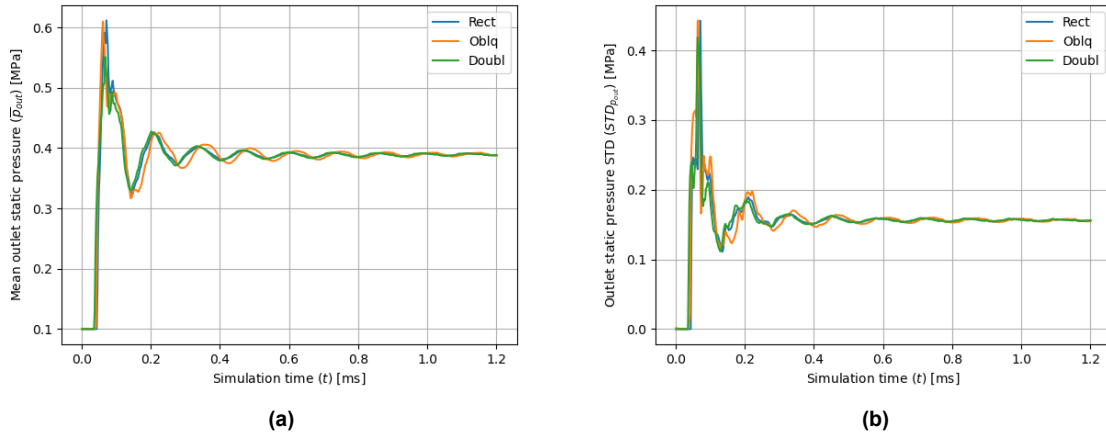
Figure 5.26: Mean outlet static pressure (a) and standard deviation of the outlet static pressure (b) for the rectangular (Rect), oblique (Oblq) and double-energy rectangular (Doubl) ignition strategies as a function of the simulation time.

Similar differences during the early unsteady stages of the simulation can be seen in figure 5.27, when comparing the mean outlet static temperature and the outlet temperature standard deviation. In this case the oblique ignition strategy has some differences in the beginning, but disappear very soon in the simulation time.

The mean mass flux density in figure 5.28 shows the same trend. The oblique case has a small phase shift and different amplitude compared to the rectangular cases. On the other hand, the baseline and double-energy strategies share the exact same results. Moreover, as the simulation time advances the results converge to the same result, also for the mass flux density standard deviation in figure 5.27b.
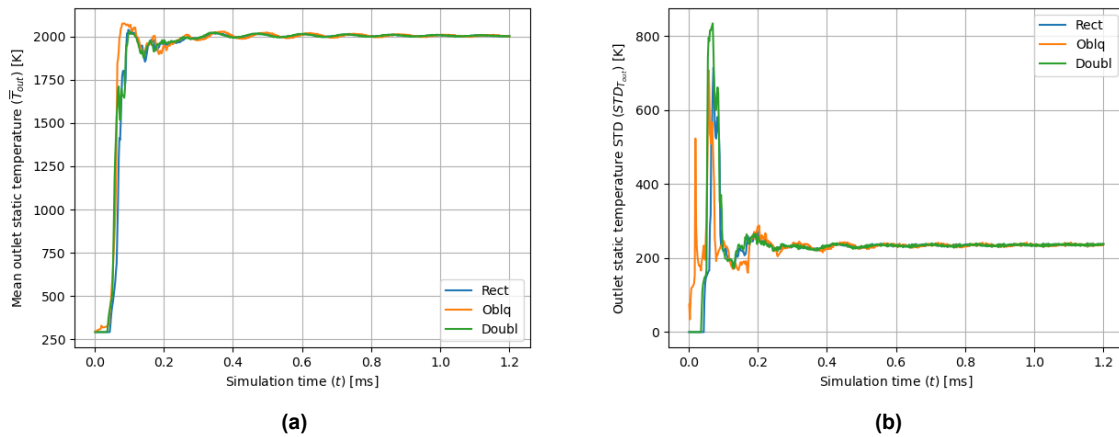
Figure 5.27: Mean outlet static temperature (a) and standard deviation of the outlet static temperature (b) for the rectangular (Rect), oblique (Oblq) and double-energy rectangular (Doubl) ignition strategies as a function of the simulation time.

The results presented in this section allow to conclude that the ignition strategy does not impact the final results. Although the oblique ignition has a different behavior in the early stages of the simulation, it
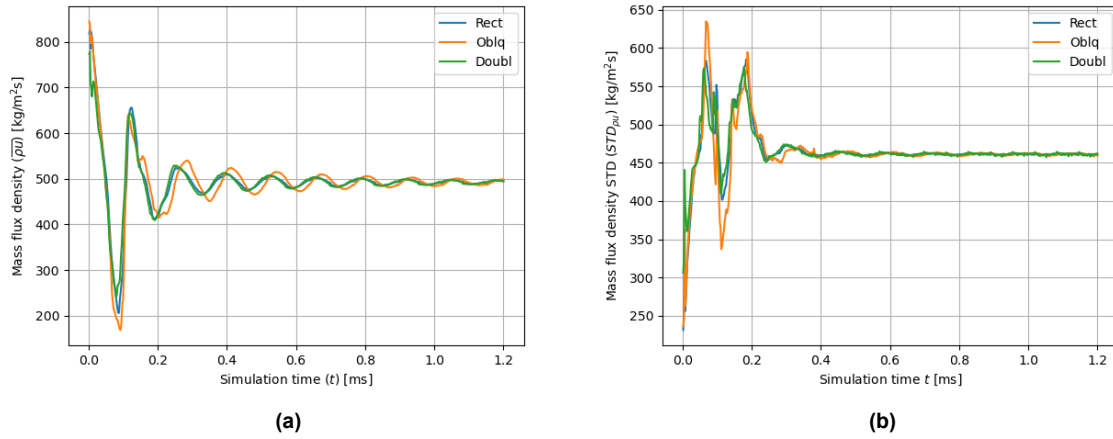
Figure 5.28: Mean mass flux density (a) and standard deviation of the mass flux density (b) for the rectangular (Rect), oblique (Oblq) and double-energy (Doubl) ignition strategies as a function of the simulation time.

converges to the same results as the rectangular strategy. Moreover, the double-energy strategy achieves a slightly higher detonation velocity, but the overall behavior is the same as the baseline case. Nevertheless, it is important to mention that these results assume that the injection and the detonation dynamics are decoupled. Thus, maybe these interactions could lead to different results, or to longer convergence times until the same values are achieved. Lastly, the rectangular ignition strategy will be employed for the 2D simulations. It shows less of an oscillatory behavior, converging faster to the results, it does not require a change of the side walls boundary conditions, and it is the same strategy as the one employed in the paper from the literature used as reference, being then a better comparison of the results.

5.2.3. Influence of Different Chemical Reaction Mechanisms

As seen in the 1D results section, the chemical reaction mechanism has a non-negligible impact on the results due to the non-equilibrium phenomena. It has a direct influence on the thermodynamic state of the mixture within the expansion after the detonation, determining the pressure, temperature, and detonation velocity depending on the reaction mechanism properties. In this section, only three mechanisms have been considered: Ó Conaire [1], Hong [32], and Gerlinger [35]. The simulation set up is exactly the same as that described for the rectangular ignition method, and the inlet boundary condition has been defined as a Dirichlet type.
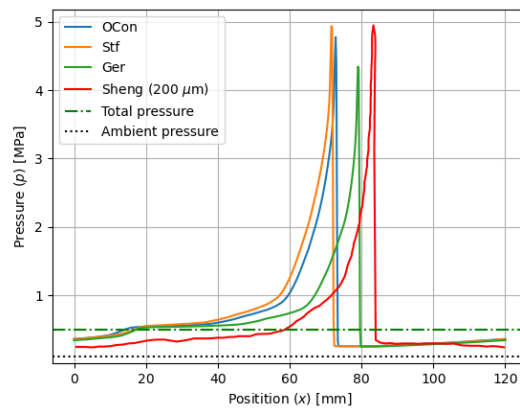
Figure 5.29: Static pressure comparison between the chemical reaction mechanisms from Ó Conaire (OCon), Hong (Stf), and Gerlinger (Ger), and Sheng et al. [120] results for its baseline case with a resolution of $200\ \mu$m along the combustion chamber at a height $z = 10$ mm.

Figure 5.29 shows a comparison of the static pressure along the combustion chamber at a height of $z = 10$ mm for the different chemical reaction mechanisms and Sheng et al. results. As seen in table 5.1 for the 1D results, the Gerlinger (Ger) mechanism shows the fastest detonation velocity, while underpredicting the pressure. On the other hand, Hong (Stf) and Ó Conaire (OCon) offer similar results, the latter showing a slightly higher detonation velocity. In this case, it can be seen how Hong's maximum pressure matches better the maximum pressure from the Sheng et al. case. It is also important to mention that all the three different mechanisms show very similar results after the detonation wave, from position $x = 40$ mm towards $x = 0$ mm, and have the same detonation wave shape.

Figure 5.30a shows the static pressure as a function of the simulation time measured at the mid span of the combustion chamber. It can be seen how the pressure peaks for both Ó Conaire and Hong match, since they have a very similar detonation velocities. On the other hand, Gerlinger pressure peaks are slightly behind the other two due to a higher detonation velocity. It is important to note how Ó Conaire results show a higher pressure throughout the entire simulation time, being Hong results the lowest and Gerlinger varying. The pressure measurements have errors associated due to the finite number of measurements, the frequency at which data is gathered, and the width of the detonation waves. However, since the sampling conditions are the same for the three cases, it could be said that the Ó Conaire mechanism provides a more consistent maximum pressure, while being close to the results from the literature. Regarding the shape of the pressure peaks, it is clear that there are no relevant differences between the three cases. This implies that the chemical reaction mechanisms have an influence on the detonation wave properties, but behave very similarly upstream and downstream the wave.

(a)   (b)
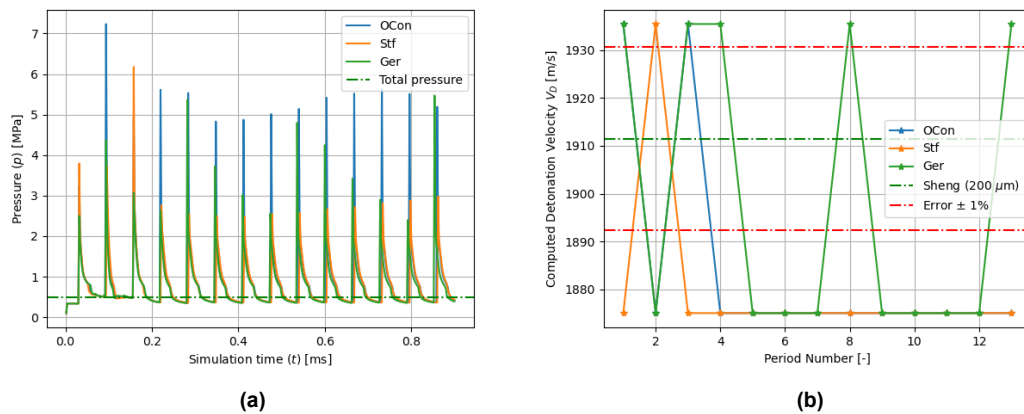
Figure 5.30: a) Static pressure measured at a probe located in $[60,2]$ mm during the simulation time, and b) computed detonation velocity based on the time between pressure peaks of the measured pressure at the probe for the different chemical reaction mechanisms: Ó Conaire (OCon), Hong (Stf), and Gerlinger (Ger).

Figure 5.30b shows the detonation velocity per period for each chemical reaction mechanism. It is clear that there are some differences between each case, being Gerlinger the one that shows velocity variations while Hong and Ó Conaire have already converged. It is interesting to note that when employing the period method to compute the detonation velocity, the different chemical reaction mechanisms have the same highest and lowest velocity values. This is probably because of the errors associated with the way of computing the velocity, as well as the similarity of the results. Table 5.5 shows the results for the detonation velocity for each chemical reaction mechanism computed with the period and tracker methods. As expected, the highest velocity is achieved by the Gerlinger mechanism, followed by Ó Conaire and Hong mechanisms. Moreover, all results have less than 2% error when compared to Sheng results.

Figure 5.31 shows the static temperature flow fields for the Hong reaction mechanism (see figure 5.31a) and the Gerlinger reaction mechanism (see figure 5.31b). When compared to the Ó Conaire results (see figure 5.22) it can be seen that the flow fields are very similar. They share the same features and there are no clear differences.

On the other hand, when looking at the normalized pressure gradient flow field from Gerlinger in figure 5.32b, it can be seen how there is a difference in the morphology of the horizontal expansion line compared

Table 5.5: Detonation velocity for the different chemical reaction mechanisms computed with different methods: period measurement (Period), and wave tracker (Tracker); and compared to the result of Sheng et al. [120] for a resolution of $200\ \mu$m.

Case	Period [m/s]	Tracker [m/s]	Reference
Ó Conaire (OCon)	1884.31	1884.41	[1]
Hong (Stf)	1879.65	1882.85	[32]
Gerlinger (Ger)	1898.48	1897.99	[35]
Sheng	1911.52	-	[120]

to Hong and Ó Conaire results. The difference is small, as it does not influence the temperature nor the Mach number (see figure 5.33). Nevertheless, it shows how after the detonation and the oblique shock, in high-pressure regions, the non-pressure dependent mechanism behaves differently, having this expansion line further downstream towards the outlet of the combustion chamber.
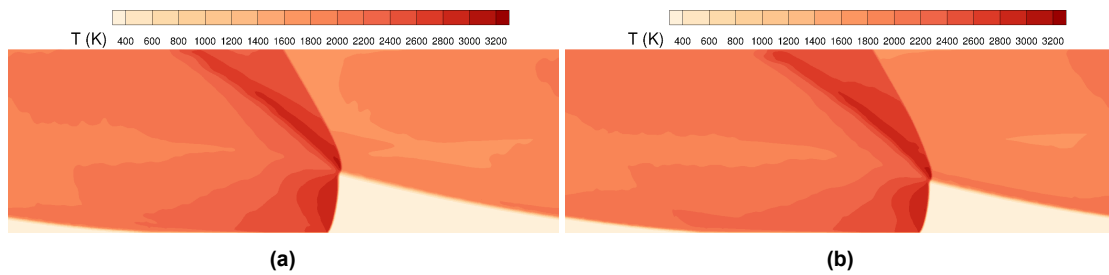
Figure 5.31: Static temperature flow field for Hong (Stf) reaction mechanism (a) and Gerlinger (Ger) reaction mechanism (b).
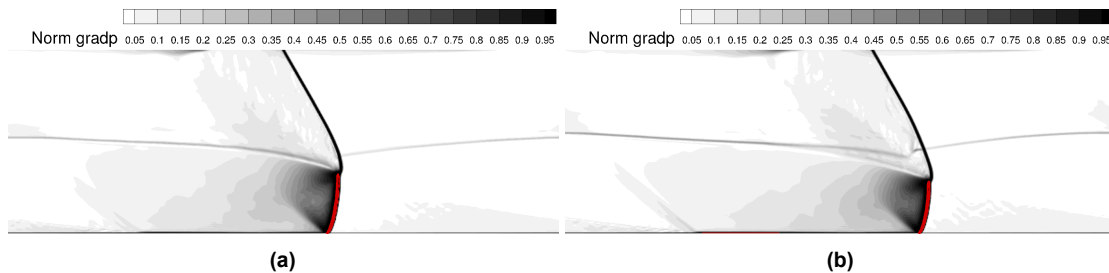
Figure 5.32: Normalized pressure gradient flow field for Hong (Stf) reaction mechanism (a) and Gerlinger (Ger) reaction mechanism (b).
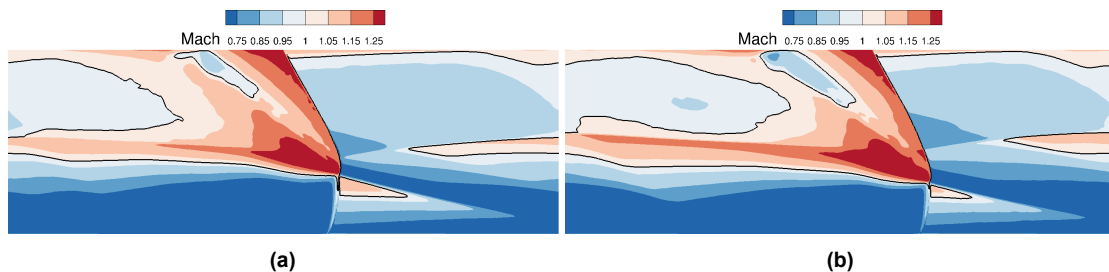
Figure 5.33: Static temperature flow field for Hong (Stf) reaction mechanism (a) and Gerlinger (Ger) reaction mechanism (b).

Regarding the detonation height, figure 5.34a shows how it varies with respect to the simulation time. It is interesting to see how the three reaction mechanisms behave in a very similar fashion during the

early stages of the simulation, and how they all converge to the same oscillatory behavior at the same time, around $t = 0.3$ ms. The maximum detonation height is very similar for the three cases, being slightly higher for the Hong case. On the other hand, the Gerlinger case shows the highest amplitude of the oscillations. As Gerlinger is pressure independent and models better the ignition processes, it is also more sensitive to changes in the detonation properties. Hence, the difference when compared to the other models. Moreover, Ó Conaire lies in between Hong and Gerlinger. The differences with the Hong reaction mechanism are related to HO_2 and H_2O_2 chemical paths, making the latter less sensitive to these variations.

Figure 5.34b shows a PSD of the detonation height signal. The three mechanisms have the peak at very similar frequencies, being Gerlinger the highest. This implies that the chemical reaction mechanism does not have a strong impact on the main frequency, which is related to the detonation velocity. In addition, it does not introduce any new oscillatory behavior in the flow field.

(a) **(b)**
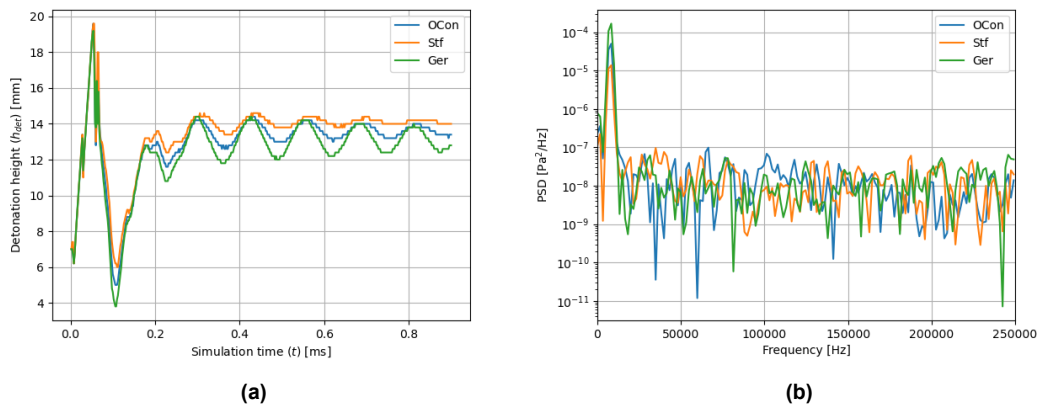
Figure 5.34: Detonation height as a function of simulation time (a) and Power Spectral Density [PSD] of the detonation height signal (b) for different chemical reaction mechanisms: Ó Conaire (OCon), Hong (Stf), and Gerlinger (Ger).

Looking at the outlet variables, the results show the same trends as before in the detonation height signal, since they are linked. Figure 5.35a shows the mean outlet static pressure for the three different reaction mechanisms. Again, the Gerlinger results show the highest amplitude. However, it is important to note that the results are very close to each other. The same behavior can be seen when looking at the standard deviation of the outlet pressure in figure 5.35b. It shows how the different reaction mechanisms do not have a large impact on the outlet variables, considering that the three mechanisms presented share the same main chemical reaction paths.

(a) **(b)**
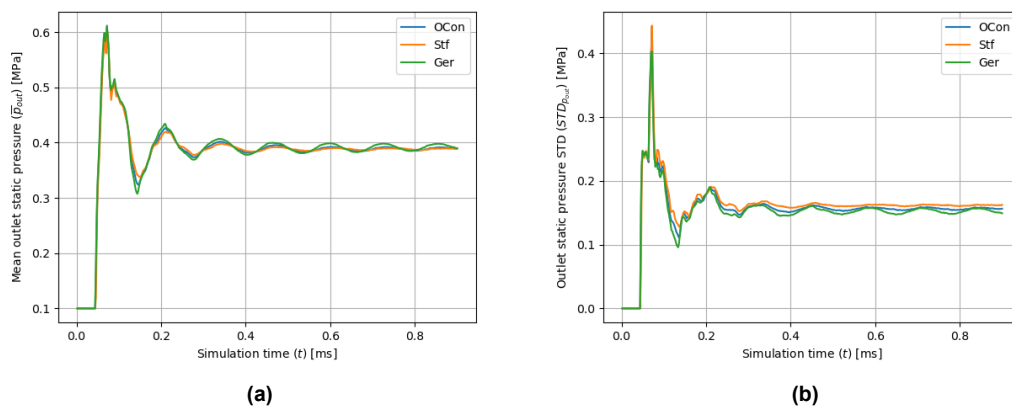
Figure 5.35: Mean outlet static pressure (a) and standard deviation of the outlet static pressure (b) for different chemical reaction mechanisms: Ó Conaire (OCon), Hong (Stf), and Gerlinger (Ger), as a function of the simulation time.
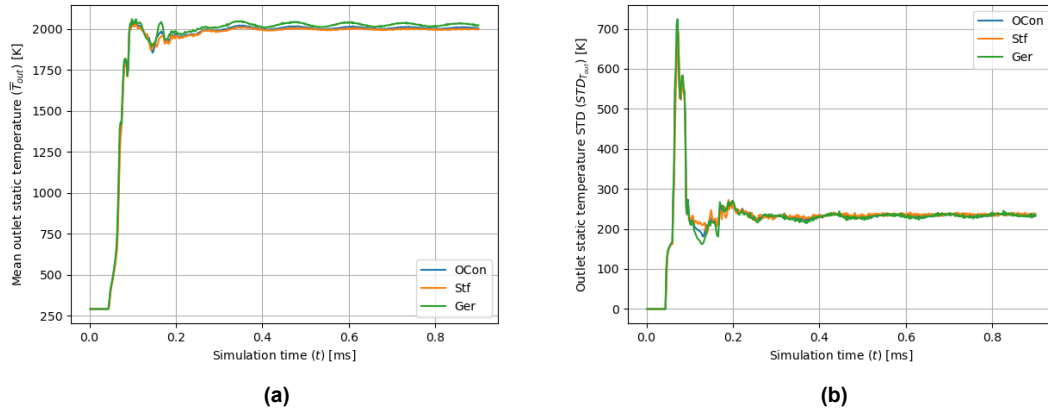
Figure 5.36: Mean outlet static temperature (a) and standard deviation of the outlet static temperature (b) for different chemical reaction mechanisms: Ó Conaire (OCon), Hong (Stf), and Gerlinger (Ger), as a function of the simulation time.
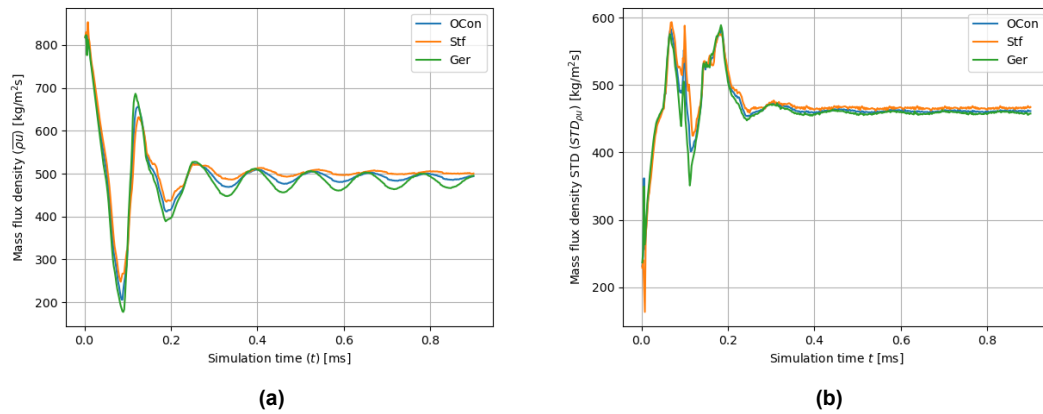
Figure 5.37: Mean mass flux density (a) and standard deviation of the mass flux density (b) for different chemical reaction mechanisms: Ó Conaire (OCon), Hong (Stf), and Gerlinger (Ger), as a function of the simulation time.

In addition, figures 5.36 and 5.37 show the outlet static temperature and mass flux density means and standard deviations. The trends shown are the same as already discussed for the detonation height and the static pressure.

It can be concluded from the results shown in this section that the reaction mechanism has an impact on the detonation velocity and the flow field oscillations. As long as they consider the same chemical species, even if the chemical paths or the reactions are not exactly the same, the averaged results at the combustion chamber outlet are very similar, as well as their standard deviation. Gerlinger proved to have the fastest detonation velocity, while also being most sensitive to oscillations. On the other hand, the Hong mechanism is the slowest. To properly conclude which one is the best option, experimental data would be required. Moreover, it is important to mention that these simulations assume that the injection is decoupled from the detonation wave dynamics.

5.2.4. Influence of Different Upwind Fluxes

In this section, the impact of employing different upwind fluxes will be evaluated. Section 5.1.2 compared the different results for a 1D case. It is interesting to evaluate their behavior in a more realistic RDE case considering an extra dimension compared to the canonical 1D shock tube simulations. The set up employed for the simulations is the same as the one described at the beginning of the section, employing the rectangular ignition strategy, the Dirichlet inlet boundary, and the Ó Conaire reaction mechanism.

Figure 5.38 shows a comparison between the different upwind fluxes and the Sheng case of the static pressure along the combustion chamber at a height of $z = 10$ mm. It can be seen how all different fluxes are behind Sheng's wave, while being very close to each other. However, AUSMDV and AUSMP waves are behind AUSMPWP and AUSM van Leer. Moreover, AUSMP seems to underpredict the maximum pressure, while AUSM van Leer predicts a maximum pressure higher than Sheng results. Moreover, it is interesting to note that downstream the detonation wave, the AUSMP flux matches better with Sheng results, while the other fluxes show a slightly higher pressure than AUSMP and Sheng.
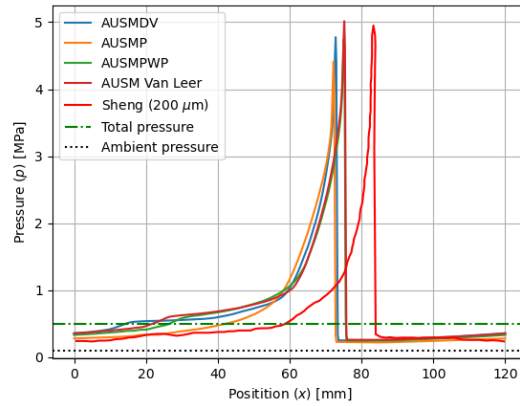
Figure 5.38: Static pressure comparison between the upwind fluxes AUSMDV, AUSMP, AUSMPWP, and AUSM van Leer, and Sheng et al. [120] results for its baseline case with a resolution of 200 μm along the combustion chamber at a height $z = 10$ mm.

Figure 5.39a shows the static pressure measured at the mid span of the combustion chamber during the simulation time. It can be seen how the AUSM van Leer flux has a large variation of the maximum pressure peak throughout the entire simulated time. The AUSMP and AUSMPWP fluxes also seem to have a strong increment after $t = 0.6$ ms. This is probably due to periodic oscillations and errors associated with the measurements taken. On the other hand, the pressure peaks for the AUSMDV flux are more numerically stable. It is important to note that all the peaks from the different fluxes coincide with each other, meaning that they have very similar detonation velocities.

(a)   **(b)**
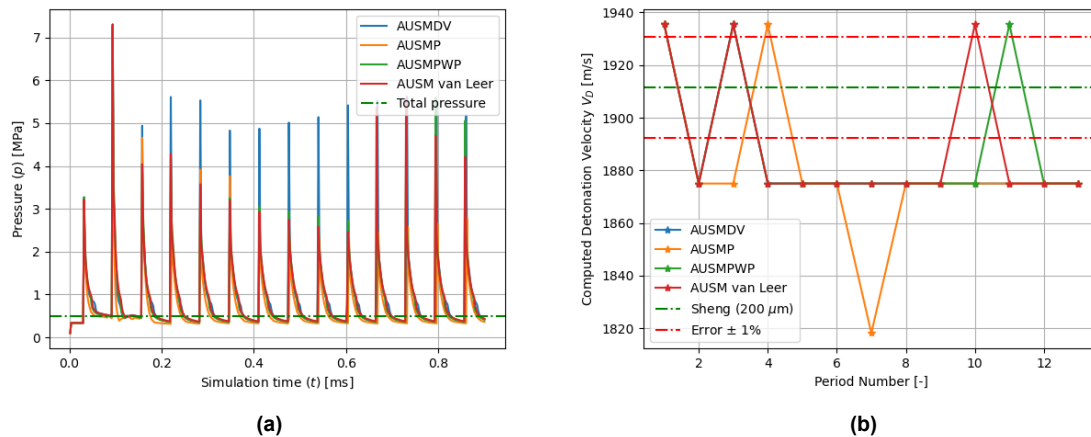
Figure 5.39: a) Static pressure measured at a probe located in $[60, 2]$ mm during the simulation time, and b) computed detonation velocity based on the time between pressure peaks of the measured pressure at the probe for the different upwind fluxes AUSMDV, AUSMP, AUSMPWP, and AUSM van Leer.

Figure 5.39b shows the velocity computed with the period method for the different fluxes. The AUSMP flux shows the lowest detonation velocity, while both AUSMPWP and AUSM van Leer fluxes show variations

towards higher detonation velocities at later periods. More detailed detonation velocity results can be seen in table 5.6. As seen in figure 5.38, AUSMP has the lowest detonation velocity, while AUSM van Leer and AUSMPWP have very similar and higher velocities. Nevertheless, the difference in detonation velocity between the AUSMP and AUSM van Leer is lower than 0.5%, and all of them have an error below 2% when compared to Sheng's results.

Table 5.6: Detonation velocity for the different upwind fluxes computed with different methods: period measurement (Period), and wave tracker (Tracker); and compared to the result of Sheng et al. [120] for a resolution of 200 μm.

Case	Period [m/s]	Tracker [m/s]
AUSMDV	1884.31	1884.41
AUSMP	1879.93	1882.85
AUSMPWP	1888.96	1889.31
AUSM van Leer	1888.95	1889.97
Sheng	1911.52	-

Figure 5.40 shows a comparison of the static temperature flow field for the four different evaluated fluxes. The only difference that can be appreciated between the different figures is the flow right after the oblique shock. For the AUSMPWP and AUSM van Leer fluxes, the temperature after the oblique shock is lower, and the slip line region seems to be thinner and defined. As the AUSMDV and AUSMP cases have regions with higher temperature after the shock, it could imply that in those cases the oblique shock is stronger. This could be why both AUSMPWP and AUSM van Leer have a higher, and similar, detonation velocity.
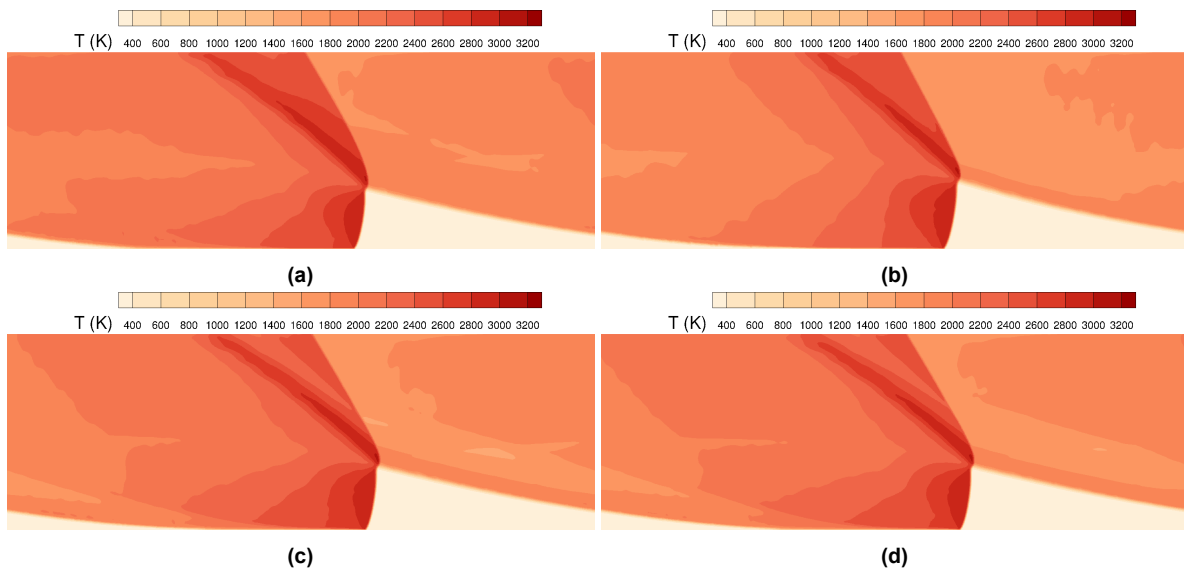
Figure 5.40: Static temperature flow field for AUSMDV (a), AUSMP (b), AUSMPWP (c), and AUSM van Leer (d) upwind fluxes.

Figure 5.41 shows the normalized pressure gradient flow field for the different fluxes. The flow fields do not seem to have very different features, however, when looking at the normalized heat release there is a clear difference: for the AUSMPWP and AUSM van Leer cases, the heat release region is not only concentrated where the detonation is, but also at the inlet boundary along the region where the pressure is still very high and there is no inlet of new gases. Since the Dirichlet boundary condition is used, the inlet is not fully blocked. Therefore, reactions between the fresh inlet mixture and the post-combustion gases can take place. In the case of AUSMPWP and AUSM van Leer, the heat release in that region is of the same order as the heat release in the detonation wave. This is not expected, since the combustion

occurring in that region, if any, should be deflagration, which has orders of magnitude lower heat release than detonation waves. The reason to why this occurs is still unknown.
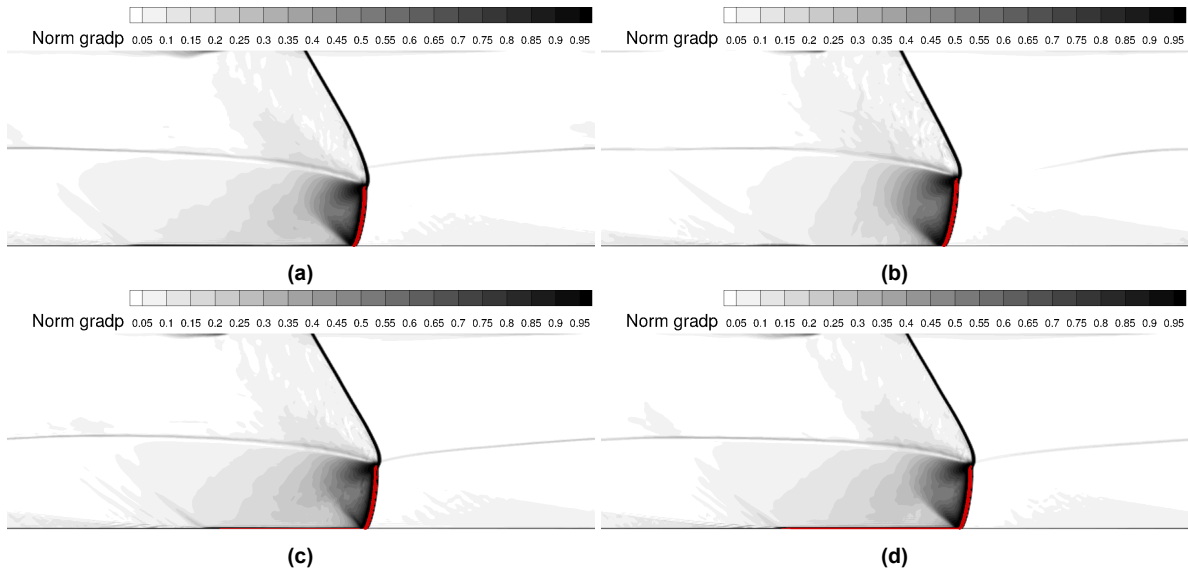
Figure 5.41: Normalized pressure gradient flow field for AUSMDV (a), AUSMP (b), AUSMPWP (c), and AUSM van Leer (d) upwind fluxes.

Figure 5.42c shows the Mach number flow field for the four different fluxes. The differences between the results are very small, and they all share the same features. In the AUSMPWP and AUSM van Leer cases, the expansion of the gases from the lower to the upper half of the combustion chamber is not as strong and defined as for the AUSMDV and AUSMP cases. Moreover, the Mach number after the oblique shock also varies, as well as the distribution after it. It is also important to note that these figures are only a snapshot in time, thus, the structures and features seen can change.
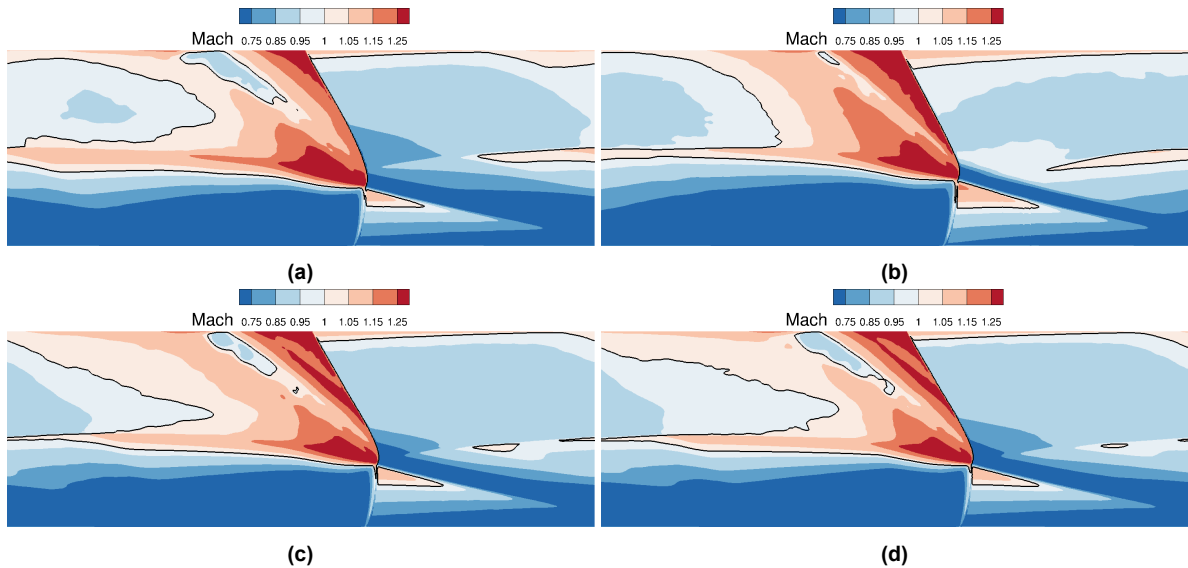
Figure 5.42: Mach number flow field for AUSMDV (a), AUSMP (b), AUSMPWP (c), and AUSM van Leer (d) upwind fluxes.

Figure 5.43a shows the detonation height for the different fluxes throughout the simulation time. It can be seen how the AUSMP flux has a consistently higher height, while also introducing oscillations of higher frequencies (see figure 5.43b) during the early stages of the simulation. On the other hand, both AUSMPWP and AUSM van Leer fluxes show the lowest amplitude oscillations. In the case of the AUSM

van Leer, it is probably due to its higher numerical diffusion, which helps damping these oscillations. On the other hand, the AUSMPWP flux dampened behavior is linked with the pressure-weighting functions it employs to compute the mass flux through the cell boundaries.

Regarding the PSD results from figure 5.43b, it is clear that the only flux introducing clear oscillations at higher frequencies is the AUSMP flux. Moreover, all the fluxes share the same peak at a low frequency linked to the detonation wave period.

(a)   (b)

Figure 5.43: Detonation height as a function of simulation time (a) and Power Spectral Density [PSD] of the detonation height signal (b) for different upwind fluxes: AUSMDV, AUSMP, AUSMPWP, and AUSM van Leer.

Figure 5.44a shows the mean outlet static pressure for the different evaluated fluxes. It can be seen how the AUSMP flux has the lowest values, while the AUSMPWP and AUSMDV fluxes share similar results, and the AUSM van Leer flux is slightly higher than the rest. As when compared to Sheng results (see figure 5.38), the AUSM van Leer flux seems to overpredict the static pressure. The AUSMDV and AUSMPWP results are lower probably due to the presence of the pressure diffusion terms when computing the mass flux, which prevent overshoots after strong shocks.

On the other hand, figure 5.44b shows the standard deviation of the outlet pressure. The results are very similar for all the different fluxes, being AUSMPWP and AUSM van Leer slightly higher.

(a)   (b)

Figure 5.44: Mean outlet static pressure (a) and standard deviation of the outlet static pressure (b) for different upwind fluxes: AUSMDV, AUSMP, AUSMPWP, and AUSM van Leer, as a function of the simulation time.

The mean outlet static pressure is shown in figure 5.45a. The AUSMP flux shows again the lowest values. However, the AUSMDV flux has the highest mean outlet temperature while suffering from small

amplitude oscillations. Moreover, figure 5.45b shows that the highest standard deviation occurs for tor the AUSMP case. It is also important to note that these variations are of order 250 K, which is roughly around 10% of the mean outlet temperature. Hence, the temperature standard deviation is low.

(a)   (b)
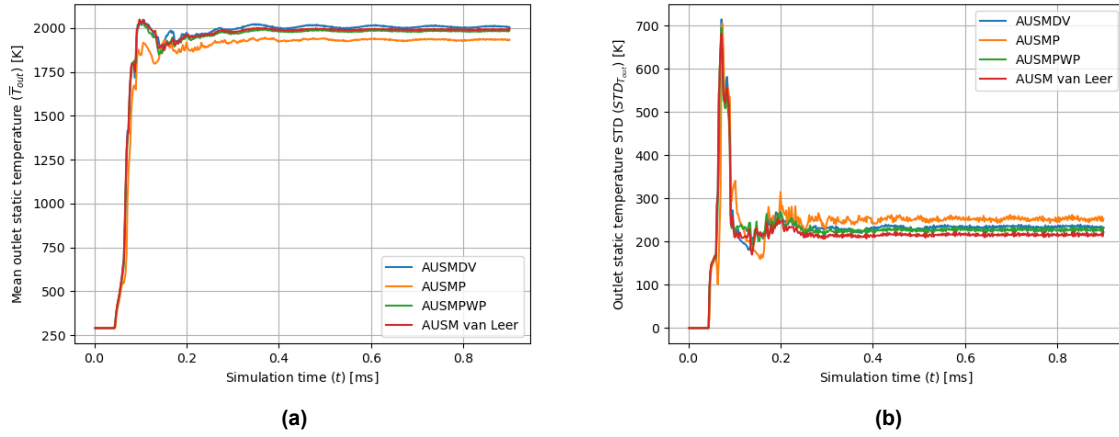
Figure 5.45: Mean outlet static temperature (a) and standard deviation of the outlet static temperature (b) for different upwind fluxes: AUSMDV, AUSMP, AUSMPWP, and AUSM van Leer, as a function of the simulation time.

Figure 5.46a shows the mean mass flux density for the different upwind fluxes. It can be seen that the AUSMP and AUSMDV fluxes are more prone to having an oscillatory behavior than the AUSM van Leer and AUSMPWP fluxes. Moreover, it is interesting to note that the AUSMPWP flux has the lowest mass flux density, while having slightly higher detonation velocity than AUSMDV and AUSMP fluxes. This could be due to the interaction of the AUSMPWP flux with the Dirichlet inlet, and this interaction affecting only the inlet mass flux density but not the detonation properties.

On the other hand, the standard deviation of the mass flux density seen in figure 5.46b shows that the AUSMPWP flux has the lowest variation of the four cases. However, all four fluxes have similar values, and only the AUSMP flux shows oscillations.

(a)   (b)
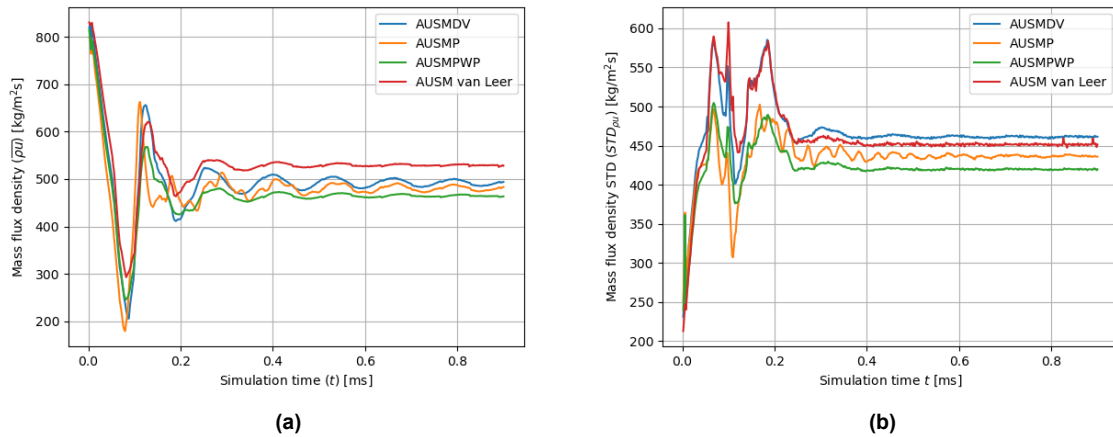
Figure 5.46: Mean mass flux density (a) and standard deviation of the mass flux density (b) for different upwind fluxes: AUSMDV, AUSMP, AUSMPWP, and AUSM van Leer, as a function of the simulation time.

The results discussed in this section show that the behavior of the fluxes is not exactly the same for 1D and 2D simulations. while the AUSM van Leer flux offers the highest detonation velocity, it overpredicts the maximum pressure and an unexpectedly high heat release at the inlet. On the other hand, the AUSMP flux suffers from high frequency oscillations while underpredicting the maximum pressure and having a

lower detonation velocity. The AUSMDV and AUSMPWP fluxes do not suffer from these problems and, in general, show similar results. However, the AUSMPWP flux also shows a strangely high heat release at some inlet regions. Nevertheless, the results for the different fluxes are relatively similar and the errors are generally low. The AUSMDV flux has been employed as the baseline flux for the upcoming simulations. It is also important to note that these results have been obtained assuming a decoupling between the injection and the detonation wave.

5.2.5. Influence of Mesh Refinement

So far all the simulation results presented have been obtained for a resolution of 200 μm. In this section, those results are compared with a simulation employing a 100 μm mesh resolution. The set up is as described in the beginning of the section. The rectangular ignition strategy was employed, the Ó Conaire reaction mechanism was chosen, the upwind flux is the AUSMDV, and the Dirichlet type boundary is defined at the inlet.
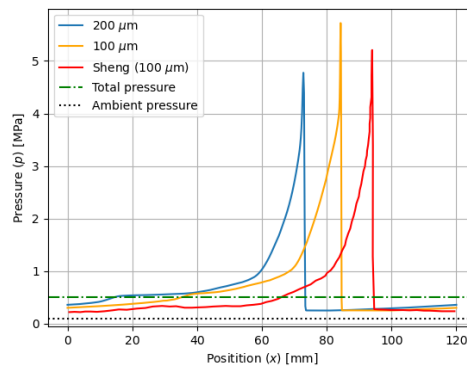
Figure 5.47: Static pressure comparison between two mesh resolutions: 200 and 100 μm, and Sheng et al. [120] results for its baseline case with a resolution of 100 μm along the combustion chamber at a height $z = 10$ mm.

Figure 5.47 shows the static pressure along the combustion chamber for the two mesh resolutions and compares it with the Sheng results for a resolution of 100 μm. It can be seen how detonation velocity increases with mesh resolution. The obtained results still show lower detonation speed compared to Sheng's result. However, there is a clear improvement. It is interesting to note that the resolution does not affect the shape of the detonation wave itself. Moreover, the higher resolution solution gives a higher maximum pressure, but still close to the literature's result.
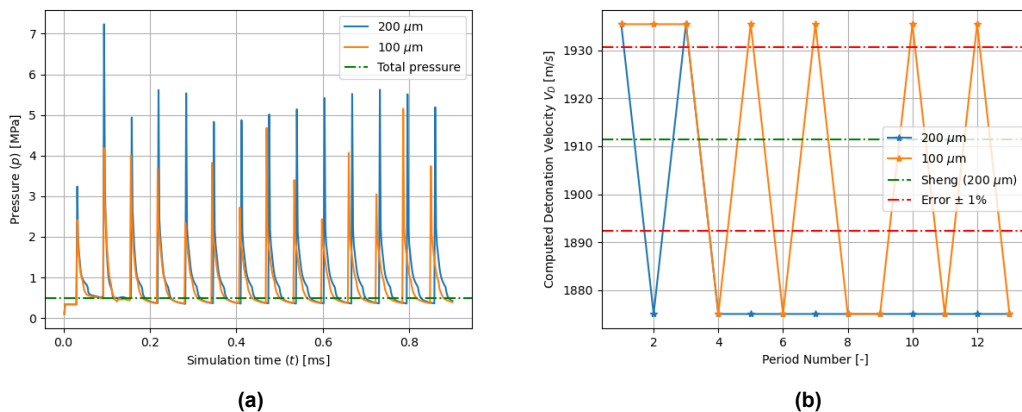
Figure 5.48: a) Static pressure measured at a probe located in [60,2] mm during the simulation time, and b) computed detonation velocity based on the time between pressure peaks of the measured pressure at the probe for two different mesh resolutions: 200 and 100 μm.

Figure 5.48a shows the pressure measured at the middle of the combustion chamber for both mesh resolutions. It is clear that, as the simulation time progresses, the pressure peaks of the $100\ \mu$m resolution come before. It consistently predicts a higher detonation velocity. On the other hand, the measured maximum pressure is higher for lower mesh resolution. This is probably related to where the measurement is taken in the combustion chamber and the samlping frequency.

Regarding figure 5.48b, it shows how the detonation velocity measured for the $100\ \mu$m mesh resolution is higher, on average, than the one measured for the lower resolution mesh. This is expected since the error associated with the spatial discretization decreases as the mesh resolution increases. Moreover, the detonation position can be better approximated, allowing a more precise computation of the detonation velocity.

Table 5.7: Detonation velocity for different mesh resolutions computed with different methods: period measurement (Period), and wave tracker (Tracker); and compared to the result of Sheng et al. [120] for a resolution of $100\ \mu$m.

Method	$200\ \mu$m [m/s]	$100\ \mu$m [m/s]	Sheng [m/s]
Period	1884.31	1907.56	1933.37
Tracker	1884.41	1908.24	-

Table 5.7 shows the computed detonation velocity for the two mesh resolutions and the Sheng et al. detonation velocity for its $100\ \mu$m mesh. It can be seen how, as the resolution increased, the detonation velocity results improved. Compared to the literature, the $100\ \mu$m case has less than 1.5% error.

When comparing the flow fields in figures 5.49, 5.50, and 5.51 it can be seen that the features are the same, but have a higher definition and less diffusion in the $100\ \mu$m case. Moreover, at the end of the slip line in the temperature flow field (see figure 5.49b) small vortices can be seen. That feature, due to higher diffusion, is not captured in the $200\ \mu$m case. This slip line vortical structures can also be seen in the Mach number flow field with more detail when compared to the lower resolution case (see figure 5.51b). It is also interesting to mention how the detonation is thinner in the $100\ \mu$m case, as well as the oblique shock and the expansion fans behind it.
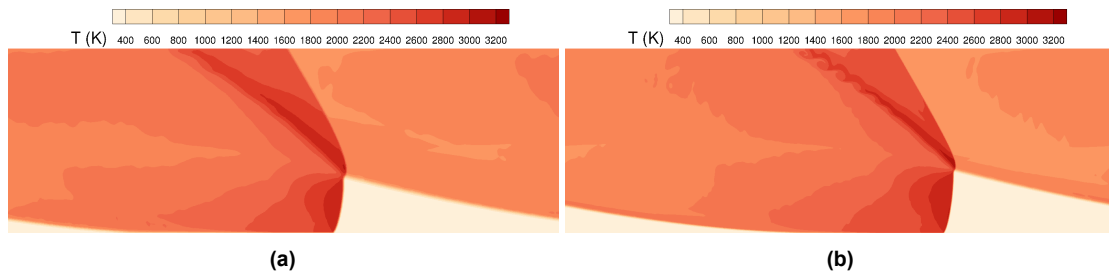
Figure 5.49: Static temperature flow field for $200\ \mu$m (a) and $100\ \mu$m (b) mesh resolutions.
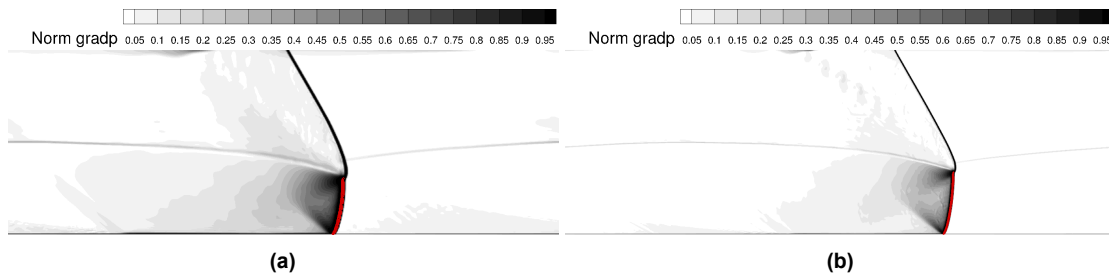
Figure 5.50: Normalized pressure gradient flow field for $200\ \mu$m (a) and $100\ \mu$m (b) mesh resolutions.
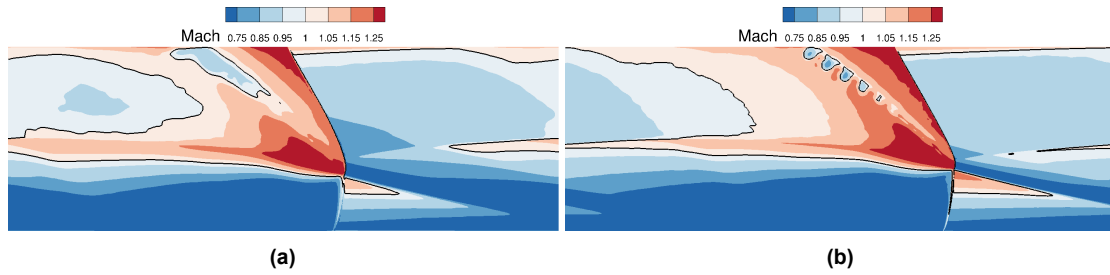
Figure 5.51: Mach number flow field for 200 μm (a) and 100 μm (b) mesh resolutions.
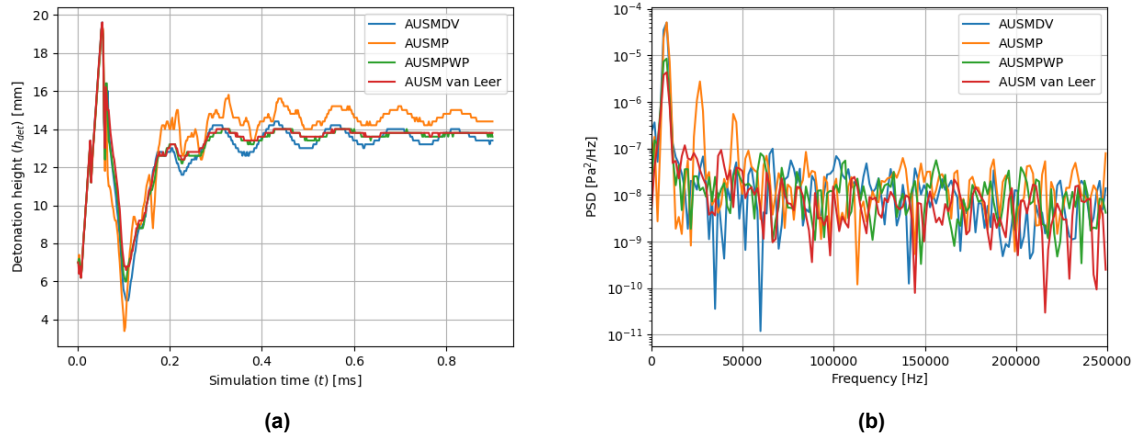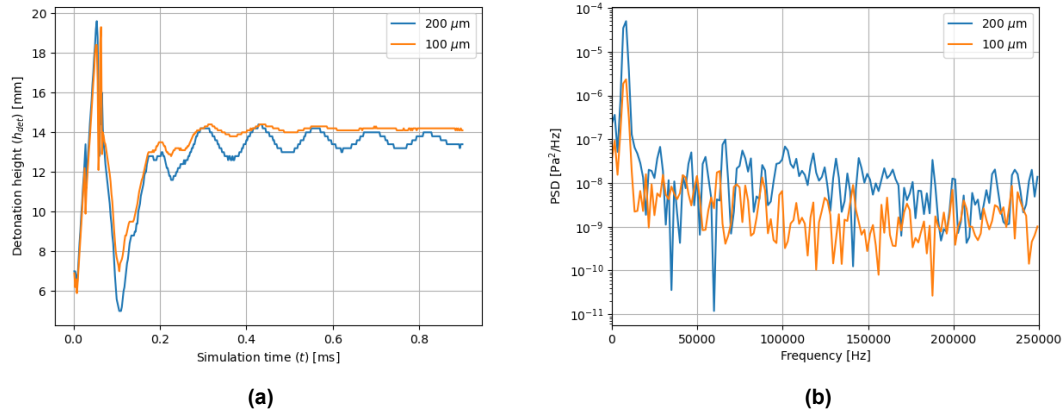

Figure 5.52: Detonation height as a function of simulation time (a) and Power Spectral Density [PSD] of the detonation height signal (b) for different mesh resolutions: 200 and 100 μm.

Figure 5.52a shows the detonation height for the two mesh resolutions. It can be seen how, as the resolution increased, the detonation height increased and experienced less oscillations. This is related to the lower diffusion and accuracy of the results. Moreover, even if the oscillations are dampened in the 200 μm case, it can be seen that the final detonation height value is lower due to the higher associated error. On the other hand, figure 5.52b shows the PSD results for both cases. As expected, the maximum value is from the 200 μm case. Still, both cases have the peak at the same frequency.
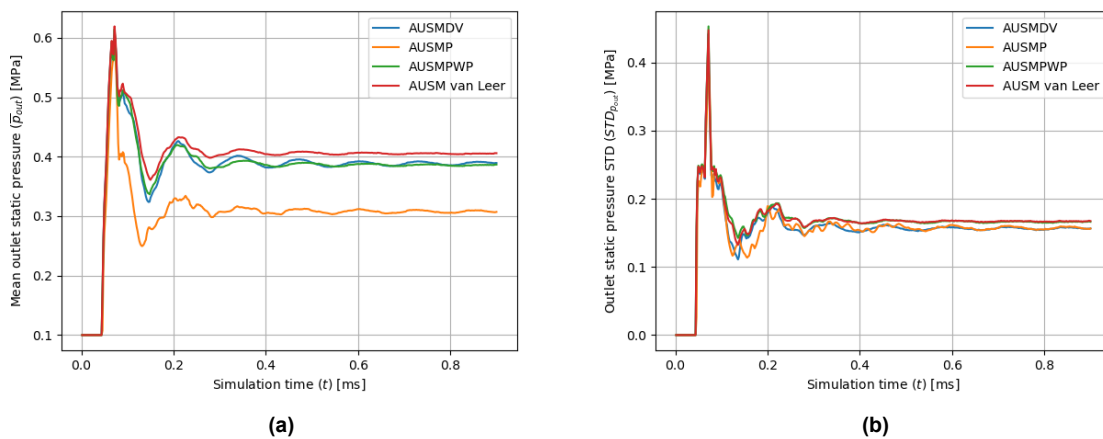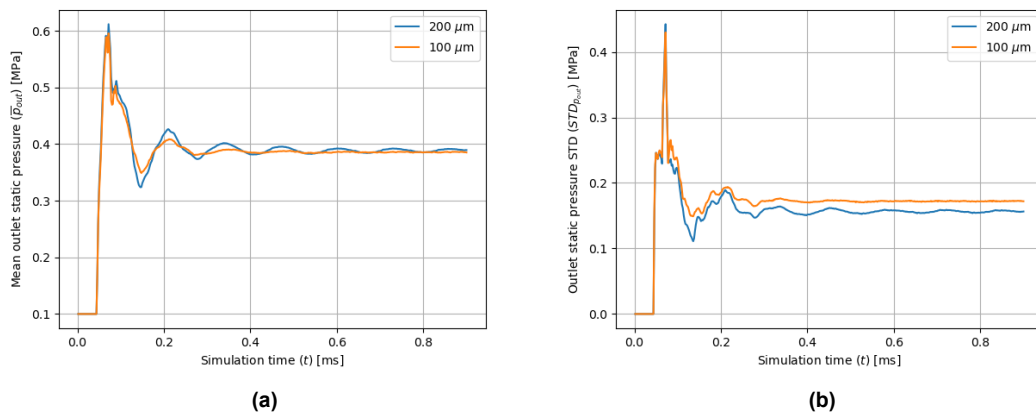

Figure 5.53: Mean outlet static pressure (a) and standard deviation of the outlet static pressure (b) for different mesh resolutions: 200 and 100 μm, as a function of the simulation time.

The mean outlet static pressure can be seen in figure 5.53a. It is interesting to see how the higher

resolution simulation dampens the oscillations, but still converges to the same value as the coarser mesh. The only difference can be seen in the standard deviation in figure 5.53b. The finer mesh has a slightly higher variation than the coarser case. This difference is probably related to the better resolution of the oblique shock and gas expansion behind the detonation.

On the other hand, when comparing the results from the mean outlet static temperature in figure 5.54a and its standard deviation in figure 5.54b, it is clear that the results are very similar in both cases. The mean temperature is slightly lower in the $100\ \mu$m case, which is probably related to the lower error during the gas expansion.
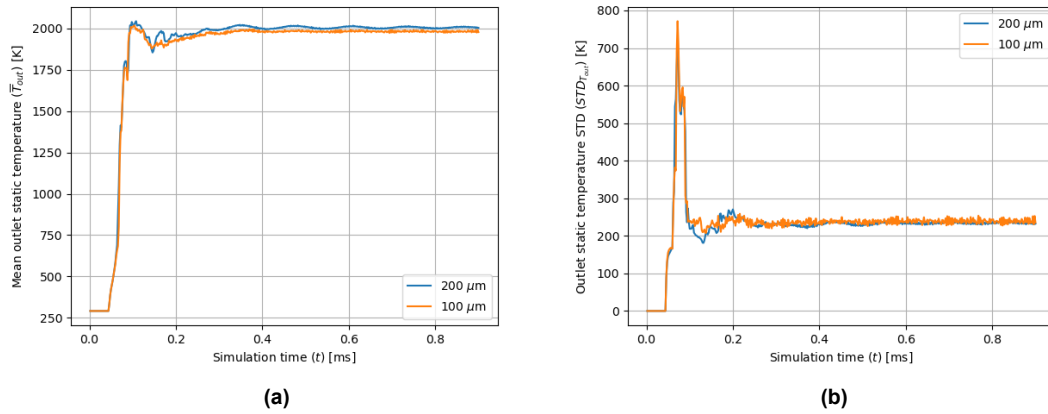
Figure 5.54: Mean outlet static temperature (a) and standard deviation of the outlet static temperature (b) for different mesh resolutions: 200 and $100\ \mu$m, as a function of the simulation time.

A bigger difference can be seen when comparing the mass flux density in figure 5.55a. As the resolution increases and the spatial error decreases, the mean mass flux density that enters the domain increases, as well as not suffering from any oscillations. Moreover, the standard deviation is clearly lower, which is related to the lower amplitude detonation height oscillations. This higher difference in the mass flux density is probably related to the higher accuracy when solving the detonation structures, shocks, and expansion processes. The velocity results are more accurate, thus leading to these differences.
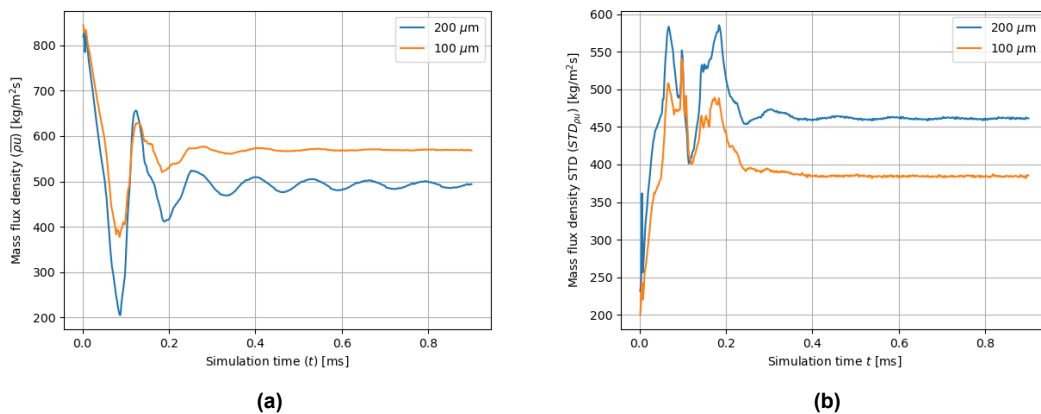
Figure 5.55: Mean mass flux density (a) and standard deviation of the mass flux density (b) for different mesh resolutions: 200 and $100\ \mu$m, as a function of the simulation time.

The results discussed in this section show how the mesh resolution can have an influence on the results. Not only on the variables values, but also on their dynamic behavior. However, it is important to mention the severe increment in the computational costs of the simulations when increasing the resolution

from 200 μm to 100 μm. The simulation time, for exactly the same set up and settings, was multiplied by 4. Therefore, there has to be a trade-off between the accuracy of the results and the computational costs that can be assumed. A coarser mesh still captures the main features of the simplified 2D RDE flow field, offering accurate enough results to study the flow field and to use the solution to ignite a 3D case.

6

DLR Lampoldshausen RDE Experimental Case

This chapter presents the results of the simulation of the experiment conducted at the DLR Institute of Space Propulsion experimental campaign [4]. First, a brief introduction to the experimental setting is given. Afterwards, the simulation set up and results are discussed.

6.1. Experiment Description

A technical drawing of the tested RDE at DLR Institute of Space Propulsion is shown in figure 6.1a. The combustor has a modular design to facilitate the interchangeability of the different parts of the engine. It was initially designed to test hydrogen-oxygen mixtures, with the possibility to vary the inlet mass flow, the reactant mixture, their temperature, and considering the use of cryogenic propellants in the future. The engine has 72 pairs of impinging jet injectors, with a combustion chamber length of 50 mm, a width of 4.5 mm, and an outer diameter of 68 mm. To ignite the mixture, a spark-plug was employed. Later experiments substituted the ignition system for a pre-detonator tube [4].

Figure 6.1b shows an image of one of the tests. The engine was tested in the M3 test bench, specifically in the M3.1 test position. This test bench has been employed for the development of cryogenic rocket propulsion systems. During the testing, oxidizer to fuel ratios close to stoichiometric conditions were used, but on the fuel-rich side to protect the hardware (6.8-8) [4]. The total mass flow rate injected ranged from 28 to 44 g/s. Moreover, the tests duration was about 0.7 ms due to heat flux limitations.

To measure the pressure oscillations within the combustion chamber, three different piezoelectric pressure sensors were installed to measure the dominant frequency. In addition, high-speed cameras were employed to study the flow field inside the combustion chamber looking through the outlet. No optical filter was applied. To post-process the high-speed imaging data, Dynamic Mode Decomposition (DMD) was chosen to study the flow dynamics. With this method the dominant periodic dynamics can be identified. However, non-linear and non-periodic effects such as secondary waves may not be captured [4].

1. Manifold
2. Injector Plate
3. Measurement Ring
4. Ignition Ring
5. Aerospike Cowl
6. Aerospike Nozzle
7. Core Extension
8. Core

(a)　　　　　　　　　　　　　　　　(b)
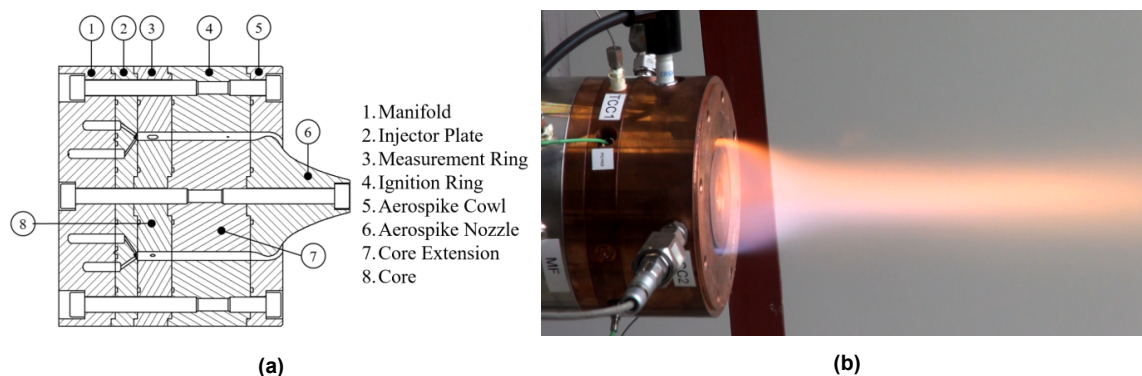
Figure 6.1: (a) Technical drawing of the mid-section of the experimental RDE and (b) hot-fire test side view of the RDE at test bench M3, from Armbruster et al. [4].

Results show how for a mass flow of 28 g/s a stable mode of three co-rotating waves is achieved. As the mass flow increases to 44 g/s, the mode of operation changes to five co-rotating waves. The measured detonation wave speeds are 1800 m/s for the 3-waves case and 1600 m/s for the 5-waves case. Compared to the theoretical CJ speed, the results obtained are in a range of 0.53 to 0.65. This implies that the identified detonations are weak [4].

Future tests will focus on obtaining stronger detonation waves by improving injector design, the ignition method, and increasing the total mass flux [4].

6.2. Simulation Set Up

To reduce the complexity of the simulation, the combustion chamber geometry has been changed. The cylindrical combustion chamber was flattened to avoid curvature effects. TA 3D view of the geometry can be seen in figure 6.2a. In addition, pressure sensors and the spark-plug were not included in the 3D model.

(a) 3D view.
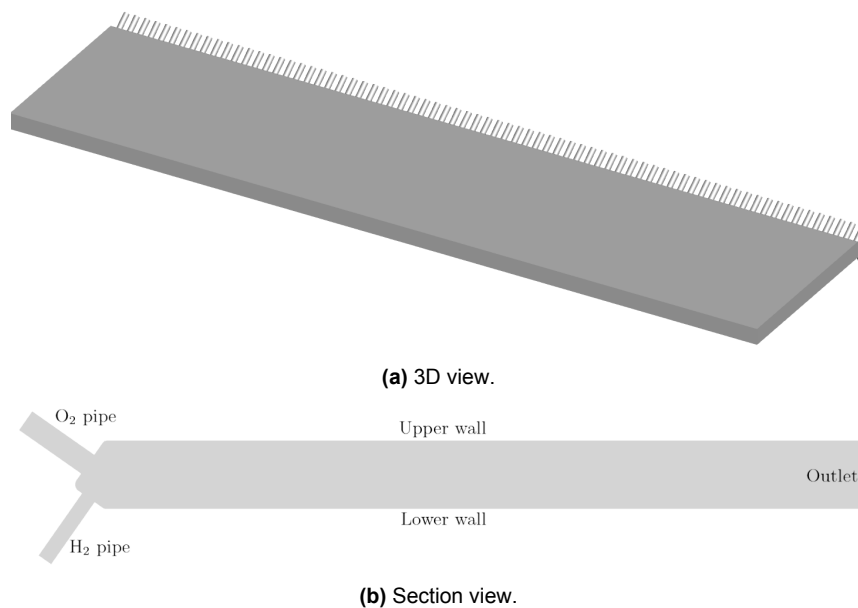
(b) Section view.

Figure 6.2: Simulation domain geometry based on the experiment from Armbruster et al. [4].

Figure 6.2b shows a section view of the simulation domain. The O_2 pipe has a diameter of 1.5 mm and a length of 9.8 mm. On the other hand, the H_2 pipe has a diameter of 1.0 mm and a length of 10.2 mm. The injector pipes are inclined so that the two impinging jets mix at the center of the combustion chamber. Moreover, the total length of the extended combustion chamber is 213.6 mm, which corresponds to the cylindrical combustion chamber with an outer diameter of 68 mm. Table 6.1 shows all the geometry parameters that define the simulation domain.

Regarding the boundary conditions, the pipe inlets are defined as reservoir-pressure inflow boundary conditions. The total temperature is set to 295 K, and the total pressure to 2.5 bar for both fuel and oxidizer. The reservoir conditions and injector geometry are designed to have choked flow at the pipe exit in nominal operation conditions, achieving a total mass flux of 44 g/s. If perfect mixing of the reactants is assumed, the equivalence ratio of the simulation is unity ($\phi = 1$). The outlet is defined as an exit-pressure outflow with an ambient static pressure of 1 bar. Moreover, the walls are defined as viscous, adiabatic, turbulent walls. Lastly, the sides of the domain are defined as periodic boundary conditions.

The Navier-Stokes equations are solved employing the Spalart-Allmaras (SA) RANS model [89]. For time integration, a 3rd-order Runge-Kutta scheme is employed combined with a dual-time stepping approach. The time step size employed is 10^{-8} s, with a global CFL of 0.2, and 0.1 in regions with high pressure gradients. The AUSMDV upwind flux [2] has been employed, as well as a 1st-order spatial discretization approach at shocks for enhanced stability. In addition, the Ó Conaire [1] chemical reaction mechanism has been employed to model the finite rate chemistry.

Table 6.1: Lampoldshausen experiment [4] simulation domain geometry parameters.

Name	Dimensions	Value
Number of injector pairs	-	72
Oxidizer pipe diameter	mm	1.5
Oxidizer pipe length	mm	9.8
Oxidizer pipe inclination	deg	35
Fuel pipe diameter	mm	1.5
Fuel pipe length	mm	10.2
Fuel pipe inclination	deg	55
Combustion chamber height	mm	50
Combustion chamber width	mm	4.5
Combustion chamber length	mm	213.6

Lastly, all the results snapshots shown in section 6.4 have been taken at time $t = 0.891$ ms.

6.2.1. Mesh Definition

The mesh employed for the simulations is shown in figure 6.3. It is divided into three different refinement zones. The region closer to the injectors is where the mixing of the reactants takes place. This process is key to the engine performance and it is an unsteady process where different concentration gradients are present. Moreover, there is also the interaction with the detonation wave in this region, hence having high temperature and pressure gradients as well. Thus, the finest mesh is found close to the injectors, being the largest length scale 120 μm. Downstream after this region, the mesh is coarsened, since the main detonation processes are expected to occur on the fine mesh region near the injectors. The largest length scale in this region is set to 250 μm. Lastly, the last half of the combustion chamber is the coarsest mesh, being the largest length scale set to 1000 μm. However, it can be seen how, due to stretching from smaller cells at the walls, the size of the inner cells is still limited.
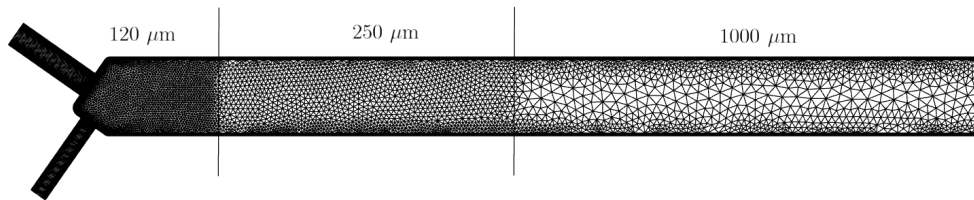
Figure 6.3: Simulation domain mesh side view.

The first layer thickness is set to 10 μm, which proved to be sufficient to achieve a y+ around 1 over the entire domain in previous cold flow simulations (see Appendix B). Lastly, the mesh has a total number of 21.2 million points.

6.3. Ignition Strategy

In order to ignite the reactants, the experimental set up employed a built-in spark plug. However, the approach taken in the simulation has been different in order to simplify the ignition process. A similar strategy to the one shown for the 2D cases has been employed.

Figure 6.4 shows a schematic of the ignition strategy. First, a cold flow solution has been obtained to resolve the mixing jets coming from the inlet pipes. Afterwards, a hot spot with a prescribed temperature and pressure is included into the domain. As it can be seen in figure 6.4, the hot spot is not touching the inlet boundary. This was done to not overwrite the variables in the region where the two reactant jets collide with each other, to enhance the numerical stability of the simulation. Moreover, as the hot spot is defined over a converged cold flow solution, the first detonation propagates in the upward direction

(looking at figure 6.4) consuming the fresh reactants.
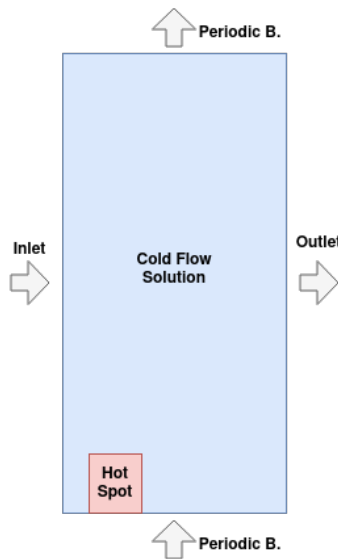
Figure 6.4: Lampoldshausen experiment simulation ignition scheme.

When defining the hot spot, the static pressure, static temperature, density, and partial density of the different species are artificially set. The specified pressure and temperature within the hot spot are 18.65 bar and 3673 K respectively. These values were obtained from CEA [96] for a H_2-O_2 stoichiometric mixture at 1 bar and 295 K. The mass fractions of the reactants in the region are set to $Y_{H_2} = 0.1119$ and $Y_{H_2} = 0.8881$, and the density is computed by employing the equation of state.

To avoid the generation of counter-rotating detonations from the start, the periodic boundary conditions are set to Euler walls until the detonation wave has reached the mid-span of the combustion chamber. In addition, to ensure the numerical stability of the simulation, the dual-time stepping technique is turned off during the first iterations and the dominant time step is the chemical time step, being the most restrictive one. This has an impact in convergence speed. Once the detonation has developed and has reached the mid-span of the combustion chamber, the solver settings are defined as shown in section 6.2.

6.4. Simulation Results

Figure 6.5a shows the static pressure measured within the combustion chamber at the mid-span, at a height of 2 mm. It is directly compared with the outlet pressure measured at the mid-span and the mean outlet pressure, as well as the total reservoir pressure. Compared to the pressure measurement plots seen in the previous chapter for the 2D cases (e.g. see figure 5.30a), the signal is noisier and has high frequency oscillations. There are pressure peaks clearly above the total reservoir pressure, which could be associated with the measured detonation waves. However, it is not easy to identify a clear period or detonation structure by just looking at this pressure plot. Moreover, the value of the peaks varies in time. This is related to the unsteady nature of an RDE flow field, as well as the errors associated with the measurements. On the other hand, it is clear that along the combustion chamber the post-combustion gases are expanded, decreasing the pressure with respect to the one in the combustion chamber. It is also interesting to note that the amplitude of the oscillations is much lower at the exit.

Figure 6.5b shows the standard deviation of the outlet static pressure. First, it shows how the amplitude of the pressure variations at the outlet is not very high. In addition, it allows to identify when the simulation reaches what could be considered a stable mode of operation. Soon after $t = 0.5$ ms, the outlet pressure STD appears to oscillate around a certain value.
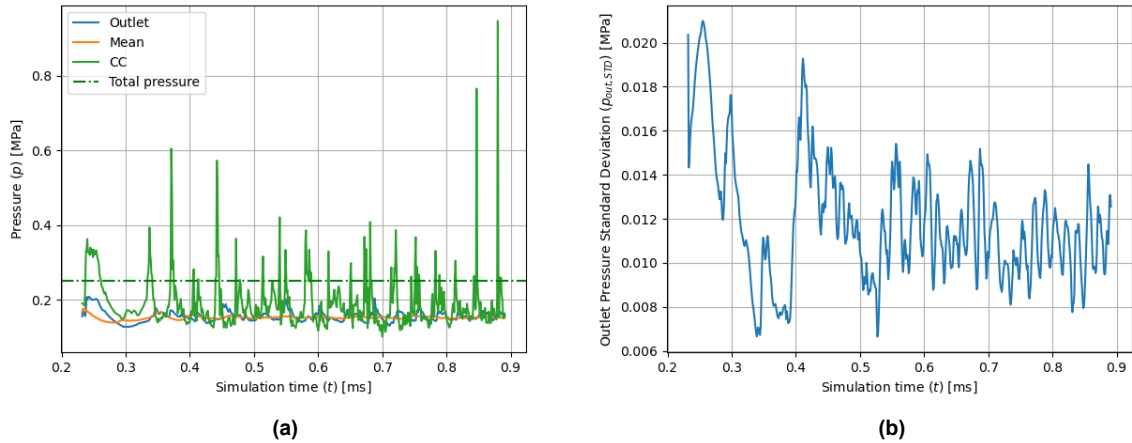
Figure 6.5: a) Static pressure measured at a probe located in the mid-span of the combustion chamber at a height of 2 mm during the simulation time compared with outlet, reservoir, and mean exit pressure. b) Standard deviation of the outlet static pressure measured at the mid-span of the combustion chamber during the simulation time.

Figure 6.6a shows the measurement of the static temperature at the mid-span of the combustion chamber, at a height of 2 mm. It is compared to the instantaneous outlet static temperature and mean outlet static temperature. As with the static pressure measurement from figure 6.5a, it is not easy to define a clear detonation structure from the signal. It is clear that there are high frequency variations present. Moreover, the range of values is very high, going from 500 up to 3000 K. This is a clear indicator of the inhomogeneous mixing process taking place near the injector pipes. There are fast temperature variations within this range due to the probe encountering pockets of detonation and fresh reactants. It can be seen how at the outlet, after the reactants have been burnt and far away from the mixing region, the temperature oscillations are very small in comparison.

Figure 6.6b shows the standard deviation of the outlet static temperature. Considering that the outlet temperature is, on average, around 3000 K, the temperature variations are very small. Moreover, this results allow to give confirm when the stable mode of operation starts. It is clear that the temperature oscillations become regular after $t = 0.5$ ms, as seen in the outlet pressure STD in figure 6.5b.
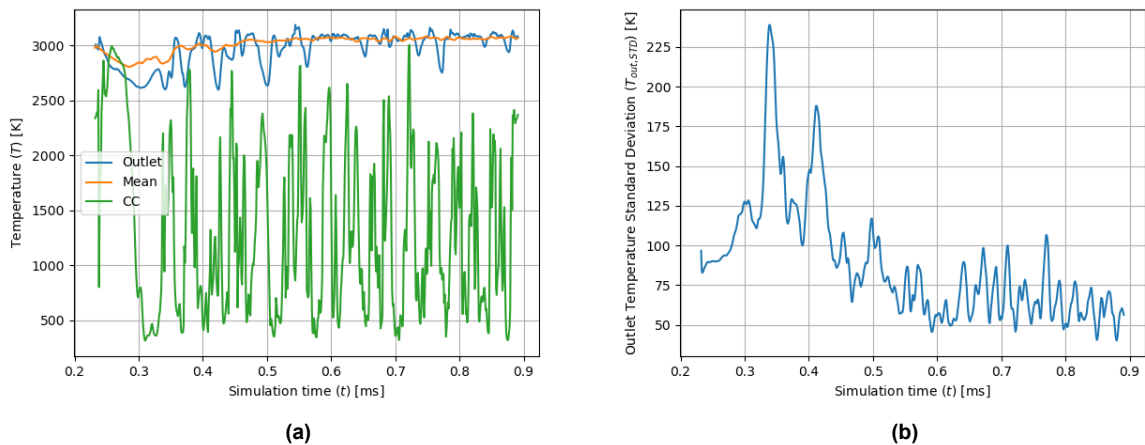
Figure 6.6: a) Static temperature measured at a probe located in the mid-span of the combustion chamber at a height of 2 mm during the simulation time compared with outlet and mean exit temperature. b) Standard deviation of the outlet static temperature measured at the mid-span of the combustion chamber during the simulation time.

The high frequency oscillations seen in both static pressure (figure 6.5a) and temperature (figure 6.6a)

measurements can be better understood when looking at the field snapshots in figure 6.7.

Figure 6.7a shows the temperature field at the mid-width of the combustion chamber. When compared to the results of the 2D simulations (e.g. see figure 5.49) the are several differences: First, the fresh reactant layer does not have a clear boundary. It can be seen that there is a mixing region with pockets of unburnt (low temperature) and burnt (higher temperature) gases right next to each other. This inhomogeneity extends further downstream, but less pronounced as the reactants are burnt. It is important to note that from this flow field, the detonation position is difficult to determine since there are no clear detonation fronts. However, some inflow regions have a blockage effect, which can be identified by the height of the fresh reactant gases.

Regarding the Mach number field shown in figure 6.7b, it can be seen how there are no strong expansions nor sudden changes in Mach number regions. Most of the flow field at the mid-width of the combustion chamber is subsonic. This is in agreement with the results from the experiment conducted by Armbruster et al. [4], where it is stated that the Mach number at the outlet of the combustor is mostly subsonic. This confirms that there are no clearly visible strong shocks in the flow field.

To better identify the pressure waves, the normalized pressure gradient flow field is shown in figure 6.7c. This quantity is defined as follows:

$$\|\nabla p\|^n = 1 - \exp\left(-\chi_p \frac{|\nabla p|^n}{|\nabla p|_{max}^n}\right) \tag{6.1}$$

where the superscript n indicates the time step, $|\nabla p|_{max}^n$ is the maximum pressure gradient within the domain at time step n, and χ_p is a scaling parameter set to 100.
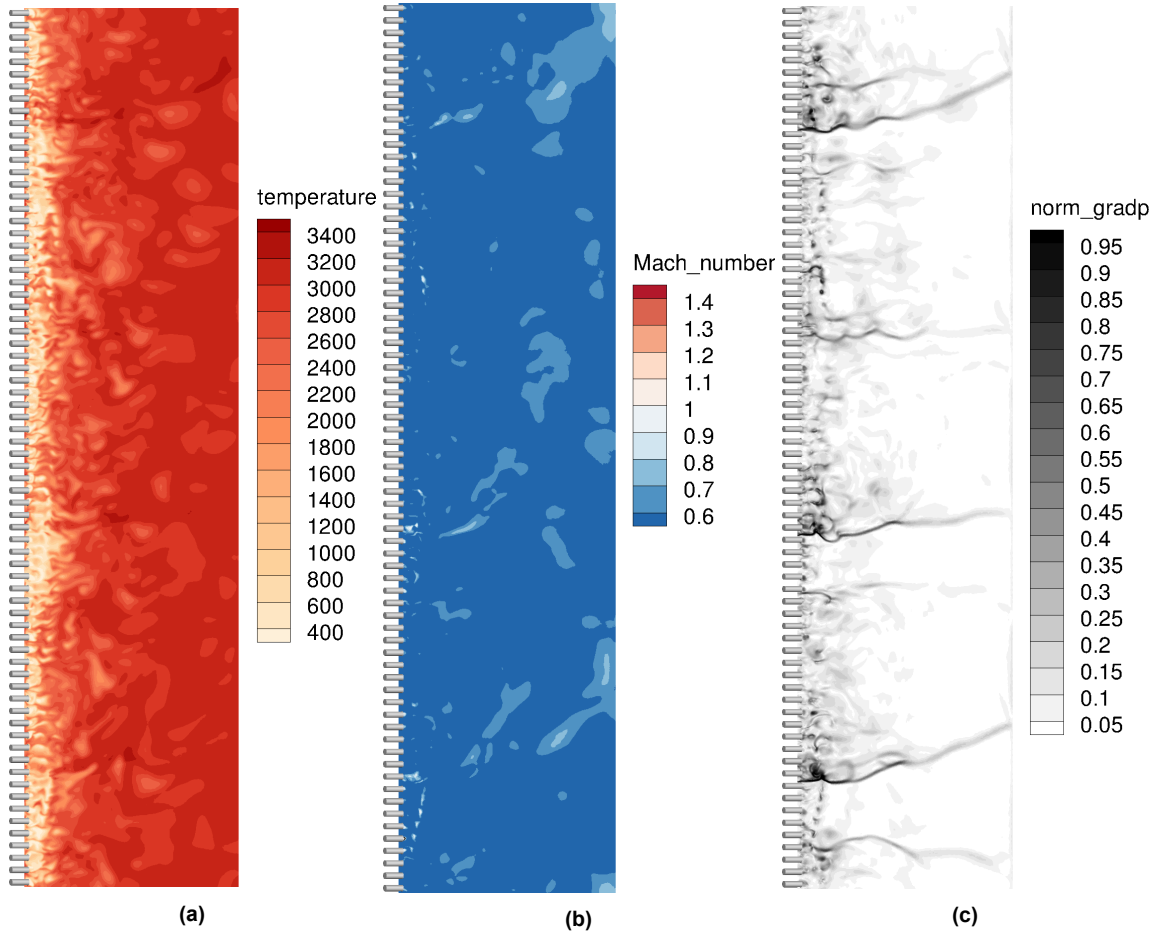
Figure 6.7: Flow field snapshots at the mid-width of the combustion chamber: a) static temperature (K), b) normalized pressure gradient (-), and c) Mach number (-).

The normalized pressure gradient field shows how the pressure front is not as clearly defined as for the 2D cases (e.g. see figure 5.50). There are four pressure waves spatially distributed over the combustion chamber. Starting from the top in figure 6.7c, the second pressure wave looks weaker than the other three. Moreover, the fronts are wrinkled and do not have homogeneous strength. The oblique shocks are also weak and show the same irregularities as the wave fronts. In addition, there are some smaller pressure waves visible within the combustion chamber. For example, the pressure wave seen at the top, slightly above the first strong pressure wave, and at the bottom of the combustion chamber. These could be identified as secondary waves, which arise due to the unsteadiness of the flow field and the interaction between the injection and the detonation dynamics.

Compared to a pressure wave, which is well visualized by the normalized pressure gradient, detonation waves are always accompanied by a chemical heat release region. Therefore, a detonation index parameter (I_{det}) has been defined to locate the detonation waves. The idea of using this parameter to determine the position of the detonation waves was presented by Strempfl et al. [122]. This quantity is defined as follows:

$$I_{det} = S_w \cdot S_p \tag{6.2}$$

where the two terms S_w and S_p have been changed in this work to make use of the normalized heat release and the normalized pressure gradient field definitions. These two variables are defined by the following expressions:

$$S_w = \frac{1}{2} \left(1 + \tanh\left[\alpha(\|q\|^n - \Gamma_w)\right]\right) \tag{6.3}$$

$$S_p = \frac{1}{2} \left(1 + \tanh\left[\alpha(\|\nabla p\|^n - \Gamma_p)\right]\right) \tag{6.4}$$

The parameter α is defined as $\alpha = 1000$, so that the hyperbolic tangent acts as a step function. Moreover, Γ_w and Γ_p are the parameter thresholds that determine what is considered a detonation. Term S_w depends on the normalized heat release at that time step ($\|q\|^n$). As this quantity is defined as the ratio with respect to the highest chemical heat release, any point which is two orders of magnitude lower than the maximum, which is assumed to be the detonation within the flow field, is considered to be deflagration. Therefore, the parameter Γ_w is defined as $\Gamma_w = 10^{-2}$. On the other hand, the second term S_p depends on the normalized pressure gradient at that time step ($\|\nabla p\|^n$). A detonation will be considered as long as this value is above 0.4, hence the threshold parameter can be defined as $\Gamma_p = 0.4$. The detonation index parameter (I_{det}) allows to detect detonation waves by considering both the pressure wave and the chemical heat release regions.

Another helpful quantity to better understand the unsteady mixing process is the mixing index I_{mix} proposed by Strempfl et al. [122] defined as:

$$I_{mix} = \frac{Y_{H_2} Y_{O_2}}{Z_{st} Y_{H_2}^0 Y_{O_2}^0 (1 - Z_{st})} \tag{6.5}$$

where Z_{st} is the stoichiometric mixture fraction, which for an H_2-O_2 mixture is 0.1119, and Y_k^0 are the mass fractions in the fuel and oxidizer jet streams. In this case, both are unity.

The mixing index provides information on the mixture rich and lean regions. Compared to the mixture fraction, it is not only helpful to determine the shape of the inlet gases, but also to identify the stoichiometric region of the inlet gases, since it is located where the index is unity.

Figure 6.8a shows the detonation index described in equation 6.2. It can be seen how, as mentioned before, the detonation fronts are small and not clearly defined. The three strong pressure waves identified in figure 6.7c have a higher value of the detonation index associated, while the weaker one has a very low values and small regions of the detonation index. This result further proofs that the detonations present in this simulation are rather weak.

On the other hand, figure 6.8b shows how the fresh layer of reactants is far from stoichiometric. There are some fresh mixture rich pockets close to the injectors, as well as pockets with very low values of the

mixing index. It can be said that the weakness of the detonations is caused by the mixing efficiency of the injectors. The detonation wave does not encounter a layer of fresh reactants, but rather a inhomogeneous mixture of gases. This leads to weaker detonations as it has an impact in the combustion process.
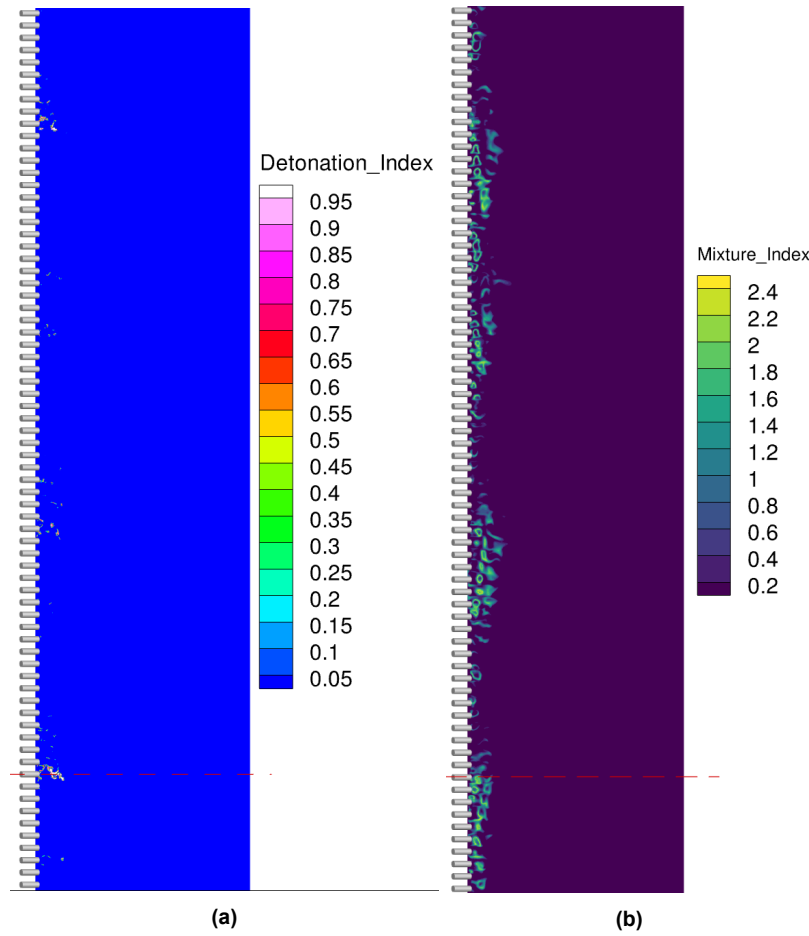
Figure 6.8: Flow field at the mid-width of the combustion chamber: a) detonation index, and b) mixing index.

Let us now take a section of the combustion chamber right at the position of a detonation wave, as illustrated by the red dashed lines in figure 6.8. Figure 6.9a shows the detonation index at that location. It can be clearly seen how the detonation front is irregular and does not cover the entire combustion chamber width. Moreover, the irregular shape and presence of pockets below and at the border of the fresh reactants jets shows the influence of turbulent mixing.

Figure 6.9b shows the mixing index at the same spot. Due to the consumption of the reactants, the regions where the detonation index is high, the mixing index is the lowest. It can be seen how there are still unburned gases closer to the lower wall and above the detonation region, as well as in between the reactants jet streams. The mixing index is higher at the lower wall due to the impinging jet design. The oxygen jet pushes the inlet reactants towards the lower wall. This is another example of the influence of turbulent mixing, creating pockets of unburnt reactants as the detonation wave goes by, leading to weaker detonation waves. However, downstream the combustion chamber, the mixing index is very low, which implies that most of the fuels are being burnt.

To quantify the burnt fuel within the combustion chamber with respect to the inlet fuel, the following combustion efficiency has been employed:

$$\eta_{comb} = 1 - \frac{Y_{H_2}^{out}}{Y_{H_2}^{in}}, \quad \text{where } Y_{H_2}^{out} = \frac{1}{A} \int_{out} Y_{H2} \, dA \tag{6.6}$$

(a)

(b)
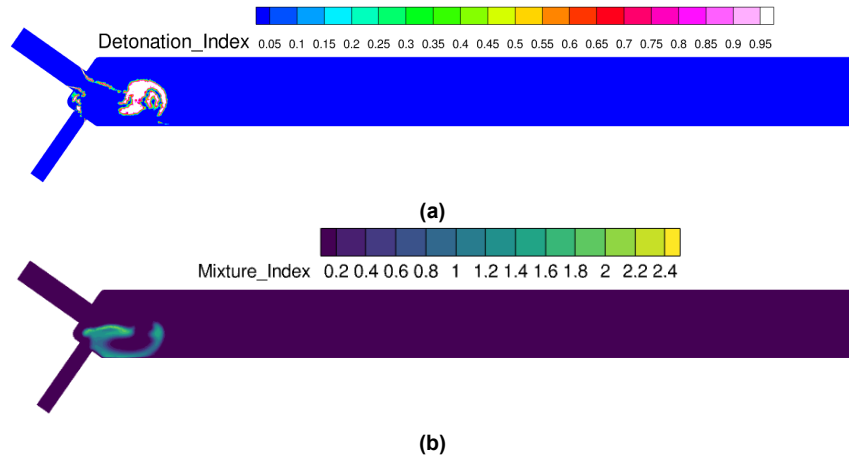
Figure 6.9: Combustion chamber section flow field taken at the red dashed line of the combustion chamber in figure 6.8: a) detonation index, and b) mixing index.

where the inlet mass fraction is defined as the stoichiometric mass fraction for hydrogen $Y_{H_2}^{in} = 0.1119$.

The results for the combustion efficiency can be seen in figure 6.10a. It shows a value close to 0.99 or above. This implies that most of the hydrogen has been burnt by the combustor exit. However, this quantity does not provide information about how it was burnt (deflagration or detonation).

Figure 6.10b shows the average maximum normalized heat release along the combustion chamber height for the simulation time. It can be seen how, on average, the maximum normalized heat release is found at a height of 3.03 mm. After this peak, the heat release quickly decreases. However, it does not approach zero until reaching 40 mm downstream within the combustion chamber. This results combined with the fact that the detonation waves are weak, leads to the conclusion that there is a non-negligible percentage of the fresh reactants being consumed by deflagration. Moreover, figure 6.10b provides an estimate of the average height of the detonations, which is at most 10 mm.

(a)

(b)
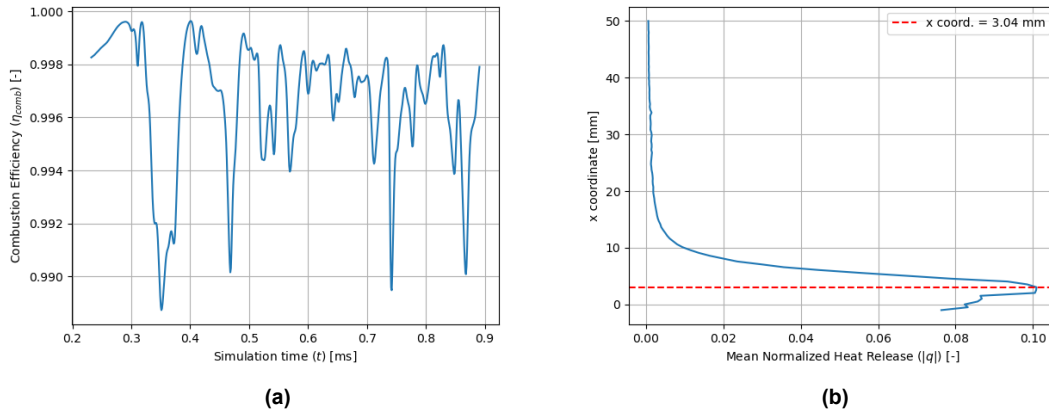
Figure 6.10: a) Combustion efficiency during the simulation. b) Mean normalized heat released along the combustion chamber.

A key parameter connected to the RDE flow field is the detonation velocity. As seen in this section, there are four detonation waves within the combustion chamber, and there is no clear periodicity when looking at the static pressure measurements within the combustion chamber (see figure 6.5a). Thus, a spectral analysis of the signal has been conducted, as seen in figure 6.11a. It shows the power spectrum density of the static pressure signal, before and after filtering. Regarding the original result, it can be seen how the peak is clear, but not much higher than other close local maxima. The signal has very high frequency

oscillations. To ensure that the low frequencies are not influenced by an aliasing problem, a low-pass filter with a cut-off frequency of 50 kHz is applied. It is clear that after suppressing the high frequencies, the peak at the low frequencies remains in exactly the same position. This implies that the frequency sampling of the simulation is enough to reconstruct the signal, thus avoiding the aliasing problem.

The maximum frequency obtained from the PSD plot is 28.8 kHz. To compute the detonation velocity, the following equation is employed:

$$V_D = \frac{f_w}{n_w} L_{cc} \tag{6.7}$$

where f_w is the frequency associated with the periodicity of the detonation displacement, n_w is the number of waves, and L_{cc} is the length of the combustion chamber.
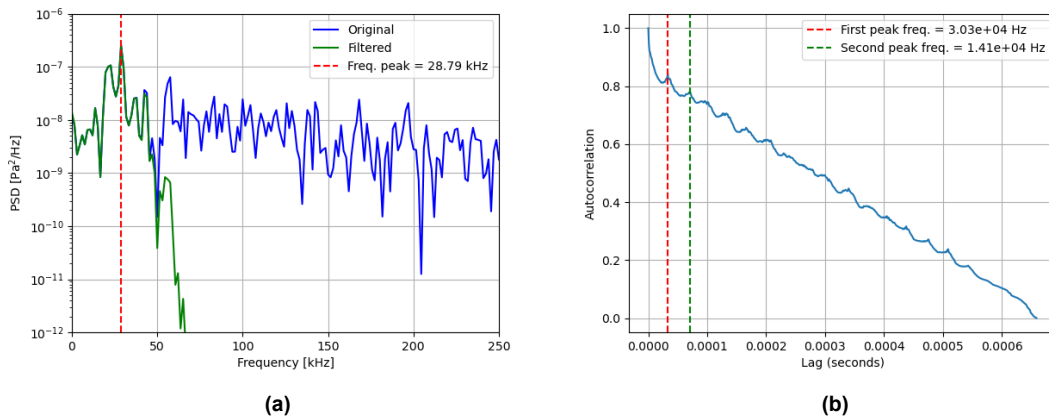
Figure 6.11: a) Power Spectrum Density (PSD) of the static pressure signal measured at the mid-span of the combustion chamber compared with the PSD of the filtered static pressure signal. b) Autocorrelation of the static pressure signal measured at the mid-span of the combustion chamber.

On top of the PSD, another method has been employed to compute the detonation velocity. Figure 6.11b shows the results when applying an autocorrelation function to the pressure signal. The first peak at zero lag corresponds to the comparison with the signal with itself at time $t = 0$ s, hence it is not considered. The first two local maxima after this first maximum have been recorded, and the associated frequencies computed, being 30.3 and 14.1 kHz, respectively. The first maximum is close to the value obtained from the PSD plot, as expected. The second maximum is, approximately, half of the first. This is because there are four detonation waves running within the combustion chamber. Therefore, the associated frequencies are multiples of 2. Nevertheless, is the first peak the frequency associated with one detonation period.

Employing equation 6.7 to compute the detonation velocity, the results are as shown in table 6.2. It can be seen how the autocorrelation function provides a better result than the PSD approximation. However, both results are very close to the experimental value for the detonation velocity.

Table 6.2: Detonation velocity computed from the frequency analysis of the static pressure signal within the combustion chamber employing different methods and compared with the experimental result from Wolfgang et al. [4].

Method	No. of Waves	Velocity [m/s]	Error [%]
Experiment	5	1600	-
PSD	4	1538	3.87
Autocorrelation	4	1618	1.12

Nevertheless, there is an important difference with respect to the experiment, which is the number of detonation waves. Considering equation 2.38, which offers a simple model on the main parameters

influencing the number of detonation waves, it can be theorized that the difference is probably due to the mass flux. The geometry of the combustion chamber Δ is the same, and the detonation velocity u_d, as well as the inlet gases properties ρ, is very similar. There could be a difference in the height of the detonation h_z or the blockage factor ε. However, there is no data available from those parameters. Moreover, as mentioned in the literature review section, the mass flux has a major impact on the number of detonation waves [49].

Table 6.3: Mass fluxes measured in the simulation compared to the experimental values from Wolfgang et al. [4].

Case	Total Mass Flow [g/s]	Hydrogen Mass Flow [g/s]	Oxygen Mass Flow [g/s]
Experiment	44.0	-	-
TAU	63.9	6.21	55.7

From table 6.3 it can be seen how the measured mass flux in the simulation is higher than the one recorded in the experiment. It is interesting to note that in the experimental campaign, two different points were tested: a mass flux of 28 g/s resulting in 3 detonation waves, and the 44 g/s case with 5 detonation waves. It can be seen how, in the simulation, as the mass flux increased, the number of waves decreased instead. This could be due to different factors. Perhaps the ignition strategy had an influence. It could also be due to the mixing process not being properly resolved, either due to the turbulence model employed, or a lack of mesh resolution. It is also important to mention that the reservoir-pressure boundary condition does not prescribe the mass flux through the inlet, but it is influenced by the pressure waves from the detonations. Hence, the difference with the experimental case could be found in the interaction between injection and detonation dynamics. Moreover, when computing the simulation equivalence ratio ϕ from the measured mass fluxes, the value obtained is 0.8907, which is not the desired stoichiometric value. This is also influencing the strength of the detonations and overall engine behavior.

An interesting process captured in the simulation is the transition from an initial detonation wave originated at the ignition, to several detonation waves and the generation of secondary waves. Figure 6.12a shows the initial detonation wave originated from the hot spot. The wave is traveling upwards. As time progresses, it can be seen in figure 6.12b how the pressure front starts wrinkling and changing its shape. Moreover, behind the wave near the injectors, some perturbations are present. These perturbations lead to the formation of a weak pressure wave, as seen in figure 6.12c. There is an interaction between the passing pressure waves and the injected reactants, which causes oscillations that generate the new waves. This process continues as seen in figures 6.12d and 6.12e. These figures show that the initial detonation wave has broken up into four different waves of varying intensity, all of them moving upwards. After this point, the interaction with the inlet gases leads to the formation of counter-rotating pressure waves, as seen in figure 6.12f. After this point, these downwards-running waves gain in strength equal to the previous upwards-running waves. No clear mode of operation can be determined in figures 6.12g and 6.12h. As the simulation continues, the downwards-running pressure waves gain more strength and start dominating, as it can be seen in figure 6.12i, where the downward running pressure wave fronts are stronger. This trend continues with varying levels of strength of the pressure waves (see figures 6.12j and 6.12k) until the final stable operation mode of four downward running detonations is achieved, as seen in figure 6.12l. The exact mechanism behind the generation of the secondary waves is not fully understood. It seems to be related to the interaction of the pressure waves with the injection and to the inlet mass flux of fresh reactants. However, further investigations are required.

In addition, it is interesting to note that, even if there is no clear mode of operation until past $t = 0.7$ ms, the outlet properties seen before (e.g. figure 6.5b), seem to converge after $t = 0.5$ ms. This implies that the presence of secondary waves and multiple competing modes does not lead to unstable outlet properties. Moreover, when looking at the autocorrelation function (figure 6.11b), the peaks are at multiples of 2, which is in agreement with the four pressure waves seen. However, the secondary waves are also identified by the pressure probe, and they are also contributing to the dominant frequency. This implies that there are as many secondary waves as detonation waves, and that they move at similar velocities and in phase. It could also be the case that their contribution to the dominant frequency is small compared to the main pressure waves. Nevertheless, further results are required to arrive to a definite conclusion.

(a) $t = t_0$ **(b)** $t = t_0 + 0.054$ ms   **(c)** $t = t_0 + 0.118$ ms   **(d)** $t = t_0 + 0.160$ ms

(e) $t = t_0 + 0.213$ ms   **(f)** $t = t_0 + 0.280$ ms   **(g)** $t = t_0 + 0.311$ ms   **(h)** $t = t_0 + 0.343$ ms

(i) $t = t_0 + 0.383$ ms   **(j)** $t = t_0 + 0.440$ ms   **(k)** $t = t_0 + 0.466$ ms   **(l)** $t = t_0 + 0.521$ ms
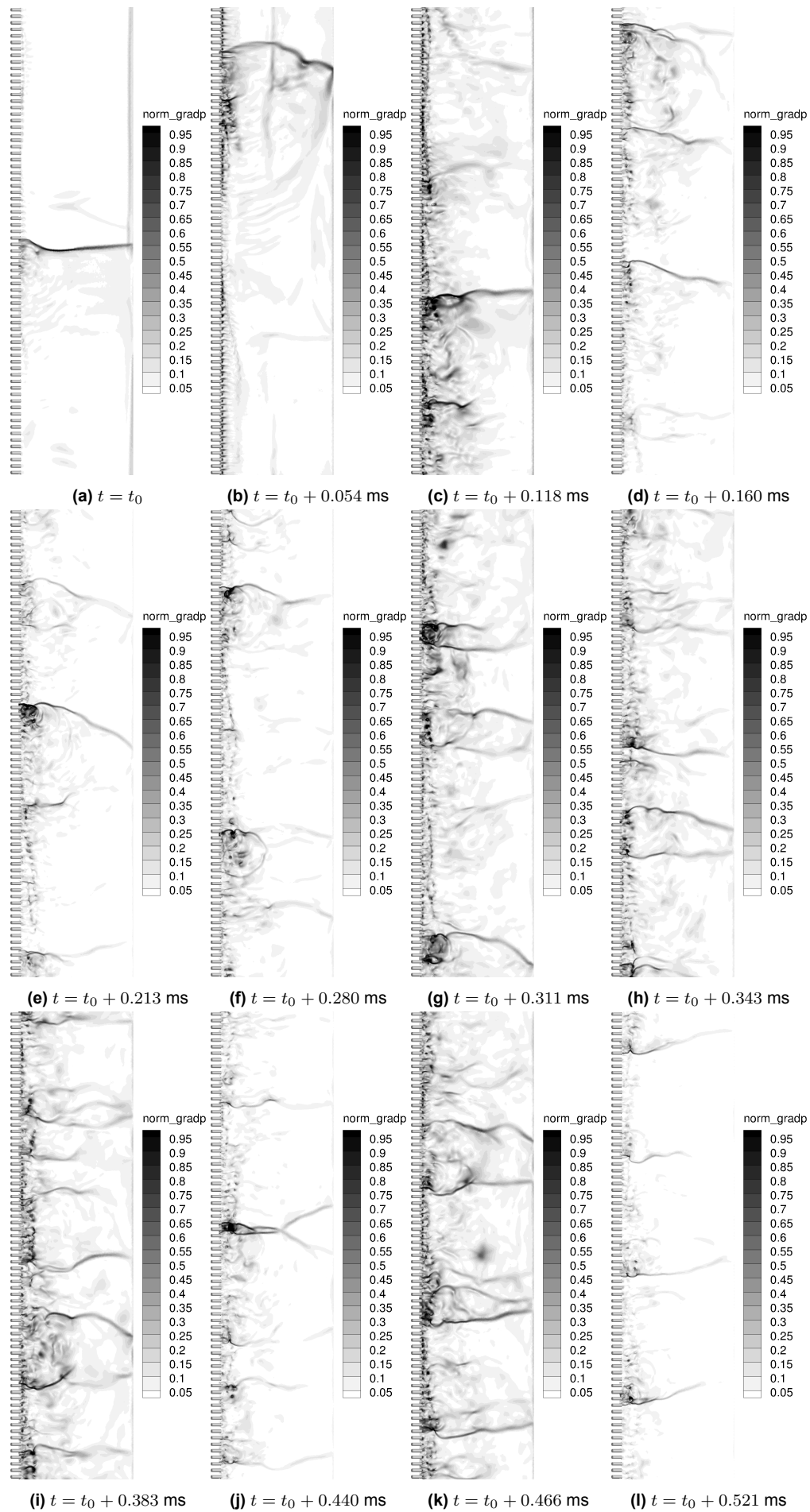
Figure 6.12: Normalized pressure gradient flow field evolution during the simulation.

TU Berlin RDE Experimental Case

This chapter presents the simulations results of the experiment conducted by Bluenmer et al. [5] at the Technische Universität Berlin (TUB). The results are later compared with the simulations performed by Strempfl et al. [122]. Before running the simulation of the 3D engine geometry, a preliminary 2D simulation has been conducted to test the set up presented in Chapter 5. Moreover, the 2D solution is later employed to ignite the 3D simulation.

7.1. Experiment Description

The RDE investigated by Bluenmer et al. [5] employed a radially-inward injector design. Air was injected through a continuous hole at the bottom of the combustion chamber, while hydrogen was injected through 100 injector pipes located on the bottom plate. A cross section of the geometry can be seen in figure 7.1. The engine outer diameter is $D = 90$ mm, the annulus width is $\Delta = 7.6$ mm, and the length of the combustion chamber is $L = 112.6$ mm.

The objective of the experiment was to study the impact on different inlet and outlet boundary conditions on the mode of operation of the engine. In order to do that, two different air inlet slot heights g were employed: 1.6 mm (A16) and 1.0 mm (A10). Moreover, different diameters were tested for the hydrogen inlet pipe: 0.5 mm (F05) and 0.7 mm (F07). The range of the equivalence ratios tested was between $\phi = 0.7$ to $\phi = 1.3$. Regarding the outlet, two cases were tested: an open outlet imposing no restrictions (R100), and a uniform outlet restriction with a throat area to annulus width ratio of 0.75 (R075). The restriction to the outlet can be seen in figure 7.1 in the detailed view of the outlet geometry [5].

To capture the mode dynamics, a total of six high-temperature piezoelectric pressure sensors were mounted in the outer wall of the combustion chamber. A first set of sensors was placed non-uniformly on the annulus close to the base plate. A second set of three sensors was placed along the combustion chamber to capture longitudinal modes. Moreover, a high-speed camera was employed to measure the number of waves and their speed. The total test time was 320 ms to prevent hardware damage, being the relevant data obtained after 200 ms into the run [5].
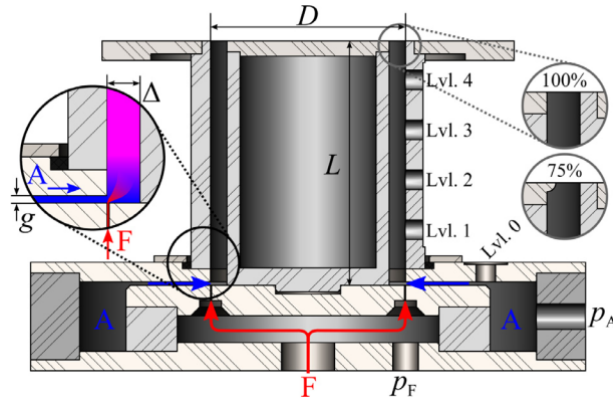
Figure 7.1: Cross section of the experimental set up employed by Bluenmer et al. [5].

Different modes of operation were identified, with counter-rotating waves with different strengths in addition to the single-wave mode [5]. The presence of counter-rotating waves hindered detonation wave speed, most probably due to parasitic combustion ahead of the detonation. Moreover, the best performance was achieved for A10 and F07 injection cases. However, this combination still suffered from unexpected behaviors in lean conditions. The results lead to the conclusion that the balance between fuel and air injection pressures is a key factor to the stability of the single-wave detonation mode [5]. Regarding the outlet restriction, it was seen that the injector pressure ratios were lower due to higher combustion chamber pressure, and that the single-wave mode of operation was more stable. However, certain combinations of parameters suffered a change in operating mode from rotating to longitudinal. The results highlight the importance of considering the longitudinal modes when designing an RDE, since they could hinder its performance [5].

7.2. Reference Simulation Description

The objective of the simulations ran by Strempfl et al. [122] was to evaluate the impact of different mixing assumptions and sub-grid scale models on the flow field within an RDE employing an LES approach. A section of the simulation domain and mesh employed can be seen in figure 7.2a. Both the air and H_2 plenums were included into the simulation domain. The only difference compared to the geometry from the experiment in figure 7.1 is the hydrogen plenum. To save computational power, the hydrogen plenum has a hole in the center, having an annular inlet. Moreover, the geometry configuration of the simulation was A16 for the air inlet, F05 for the hydrogen inlet, and R100 for the outlet.

The total temperature of both plenums was 287 K, while the total pressures were 5.2 and 11.2 bar for the H_2 and air plenums respectively. The H_2 mass flow was set to 13.7 g/s and the air mass flow to 517.7 g/s, which is equivalent to an equivalence ratio of $\phi = 0.9$. Moreover, three cases were considered: CASE 1 assuming a premixed inlet and employing the WALE model as sub-grid scale model, CASE 2 assuming a non-premixed inlet and employing the WALE model as sub-grid scale model, and CASE 3 assuming a non-premixed inlet and employing the SIGMA model as sub-grid scale model [122].

The code employed was the cell-vertex finite-volume AVBP 7.12 code of CERFACS [122]. The numerical scheme was a 2nd-order Lax-Wendroff scheme. A one-reaction reaction mechanism was employed. It considered four species and its parameters were optimized to match CJ results for an H_2-air mixture with an equivalence ratio of 0.9 at ambient conditions. In addition, the simulation was ignited by prescribing in the annulus of a converged cold flow simulation an ideal 1D ZND detonation wave obtained with CANTERA [123], and computing the expansion of the post-combustion gases and inlet of the fresh mixture behind it.
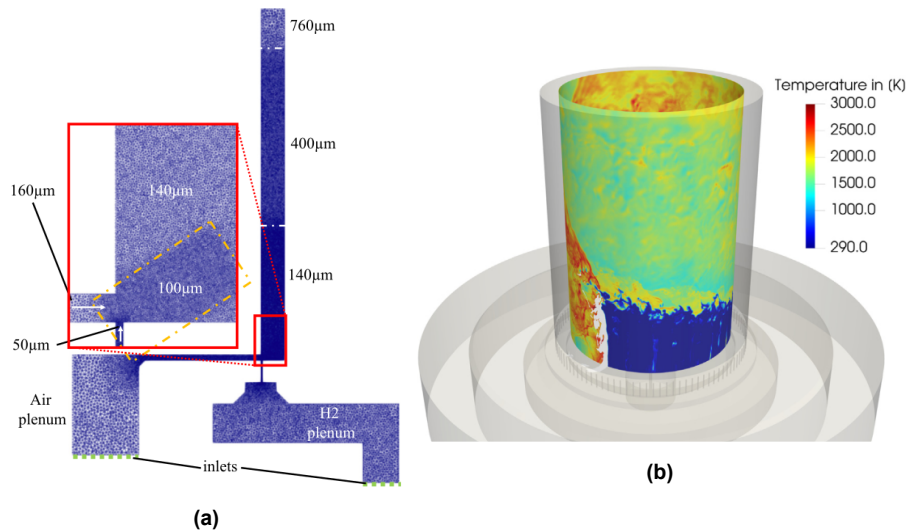
Figure 7.2: (a) Section of the domain and mesh with target grid sizes employed by Strempfl et al. [122]. (b) Instantaneous solution of CASE 1 showing the temperature field and the detonation index iso contour $I_{det} = 1$ coloured in white [122].

The results for the three cases showed a stable single-wave mode dominating. However, the detonation wave speeds obtained were higher than the ideal CJ speed and the experimental value. The highest value was obtained for the premixed inlet case, as expected. The results for both WALE and SIGMA models were very similar regarding the detonation velocity. Moreover, the main factor hindering the efficiency of the combustor was the injection design. The radial inward injector created a re-circulation zone in the outer wall that resulted in mixing losses. Between 30 to 35% of the inlet gases were burnt to deflagration.

7.3. Preliminary 2D Study

The 2D simulation domain schematic is the same as shown in figure 5.9. The simulation is ignited by artificially defining a hot spot in the lower-left corner. The prescribed pressure and temperature are 15 bar and 2900 K respectively. Moreover, a rectangular fresh gas mixture is placed right next to the hot spot to generate a detonation moving to the right (positive x direction). The domain size is 258.8x112.6 mm. The height of the combustion chamber is the same as in the 3D model. On the other hand, the length of the combustion chamber has been computed by taking the radius of the mid-width circumference. The hot spot size is 10x10 mm, and the fresh gases layer is 100x10 mm. Regarding the fresh gases mixture composition, it is an H_2-Air mixture with an equivalence ratio of $\phi = 0.9$, being the mass fractions: $Y_{H_2} = 0.025744$, $Y_{O_2} = 0.227$, and $Y_{N_2} = 0.747256$.

The 2D simulation set up employed is very similar to the one described in the beginning of section 5.2. The inlet boundary condition is a Dirichlet inlet boundary. The expansion of the gases has been computed assuming a total reservoir temperature of 287 K, and a total pressure of 5.2 bar. The 3D experiment has two different total pressures for the fuel and the oxidizer. In this case, since the mixture is premixed, the fuel total pressure from the experiment has been chosen. The outlet is defined as a pressure-outlet boundary condition with an ambient pressure of 1 bar. On the sides, periodic boundary conditions have been defined.

Regarding the solver parameters, the Euler equations with chemical reactions are solved. The time step is 2×10^8 s, with a global CFL of 0.2 and 0.1 in regions with high pressure gradients. For time integration, a third-order Runge-Kutta scheme is employed, paired with a dual-time stepping approach. The chemical reaction mechanism chosen has been Ó Conaire [1], and the AUSMDV upwind flux [2] has been employed. The mesh resolution is of 200 μm.

Figure 7.3a shows the static pressure measured at a probe located in the combustion chamber mid-span. It can be seen how the maximum pressure varies significantly throughout the simulation time. This variation can be explained due to the unsteady nature of the flow and spatial errors in the pressure measurement. Nevertheless, the shape of the signal shows a clear periodicity of the results, as well as a similar expansion pattern after the detonation wave has passed. On the other hand, figure 7.3b shows the power spectral density of the pressure signal. There is a clear highest peak at 7400 Hz, related to the detonation wave speed. As expected, as the frequency increases, the peaks start becoming smaller.

(a)   (b)
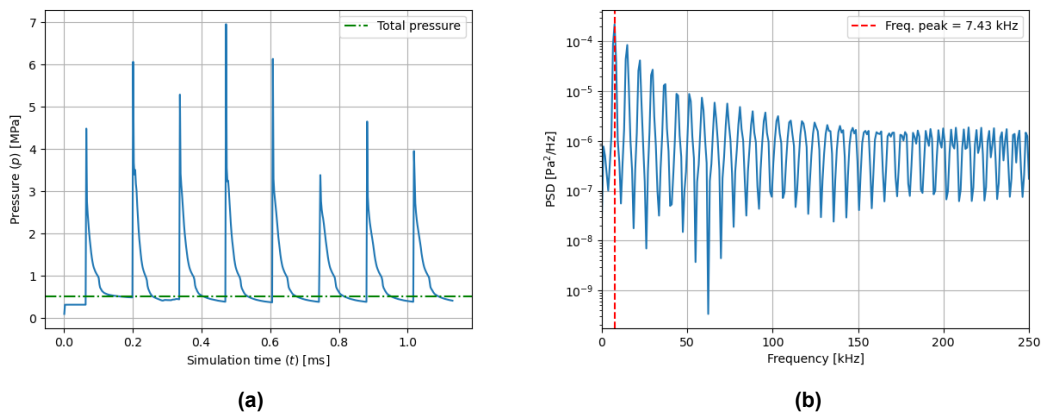
Figure 7.3: a) Static pressure measured at a probe in the combustion chamber mid-span, and b) power spectral density of the static pressure signal.

Different methods were employed to compute the detonation velocity. The methods and the results are presented in table 7.1. The period method is the same as described in chapter 5. It takes the time difference between the pressure peaks of the pressure signal and computes the detonation velocity based on the combustion chamber length. The tracker method computes the distance and time difference between two consecutive solutions. These two methods have associated errors, thus a third method based on the PSD plot (figure 7.3b) has been employed. In this case, since there is only one detonation wave running, the detonation velocity can be computed as: $V_D = f_w L_{cc}$, being f_w the peak detonation frequency and L_{cc} the length of the combustion chamber for the 2D case. The ideal CJ velocity is the highest since it assumes a perfectly premixed mixture. The experimental value has the highest error due to the inhomogeneous mixing present in a realistic RDE setting, where turbulent mixing plays an important role. The 2D simulation presented in this section assumes a perfectly premixed mixture being burned, thus it was expected to obtain a result much closer to the ideal CJ than to a realistic experimental set up. The results show that the 2D simulation predicts with accuracy the ideal CJ results.

Table 7.1: Detonation velocity computed with different methods: pressure signal period (Period), tracking the detonation wave (Tracker), and from the static pressure PSD (PSD), compared with the experimental result from Bluenmer et al. [5] and the theoretical CJ detonation velocity.

Case	Velocity [m/s]	Error [%]
CJ	1925	-
Experiment	1640	14.81
Period	1903	1.137
Tracker	1909	0.825
PSD	1922	0.156

Figure 7.4a shows the static temperature flow field at time $t = 0.878$ ms. The main elements of an RDE flow field can be easily identified, such as the detonation wave, the fresh gases layer, the oblique shock, and the slip line. It can be seen how the slip line grows unstable as it moves downstream the combustion chamber, presenting structures similar to Kelvin-Helmholtz instabilities.

(a)

(b)

(c)
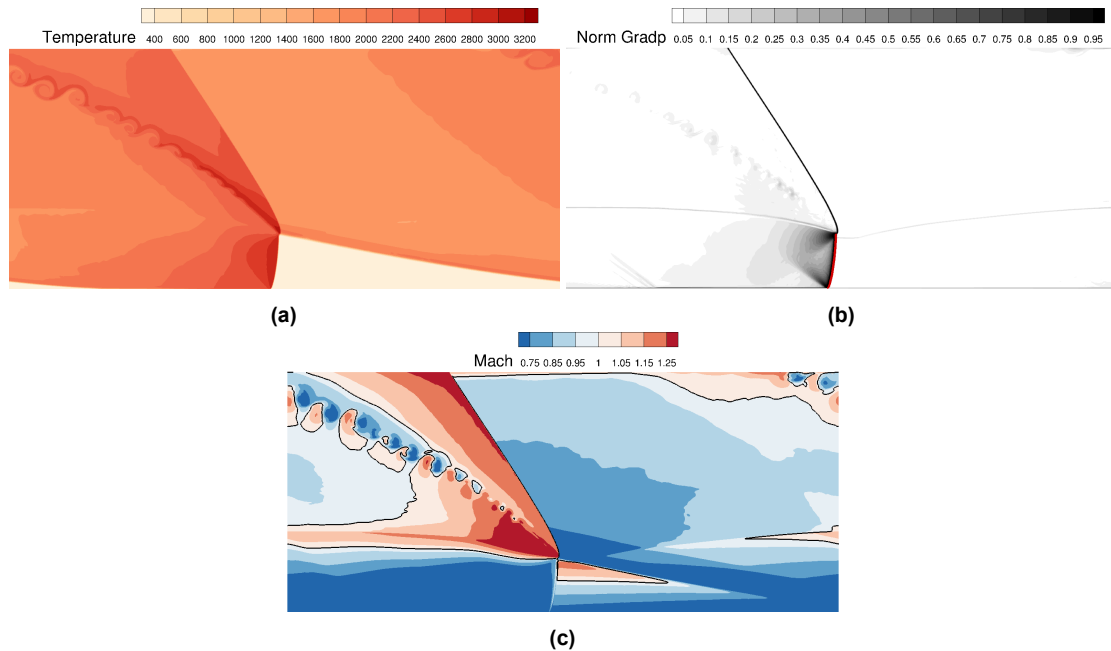
Figure 7.4: Flow field snapshots taken at $t = 0.878$ ms of the: a) static temperature, b) normalized pressure gradient, and c) Mach number.

Figure 7.4b shows a snapshot of the normalized pressure gradient field, as described in equation 6.1. The detonation wave and the expansion fans emanating from both its ends are very well defined. Moreover, the influence of the instabilities in the contact discontinuity behind the oblique shock can also be seen. It is also important to mention that the highest chemical heat release is found at the detonation front, as expected.

Looking at the third figure 7.4c, it shows a snapshot of the Mach number flow field. The main difference with the results shown in figure 5.51a is the presence of the Kelvin-Helmholtz instabilities captured by a mesh with a $200\ \mu$m resolution. In the previous case, a resolution of $100\ \mu$m was required. This is related to the size of domain, being bigger in this case and having larger structures, requiring a less fine resolution to capture them.

Figure 7.5a shows the detonation height as a function of the simulation time. It can be seen before $t = 0.6$ ms how the simulation is still in a transient state with large variations in the detonation height. After this time and closer to the end of the simulation, the height of the detonation seems to be slightly above 25 mm, with oscillations present due to the unsteady nature of the flow.

On the right side, figure 7.5b shows the mean inlet mass flux as a function of simulation time. As seen in the detonation height figure 7.5a after $t = 0.4$ ms the results tends to stabilize around a certain value, leading to the conclusion that the engine has arrived to a stable mode of operation.
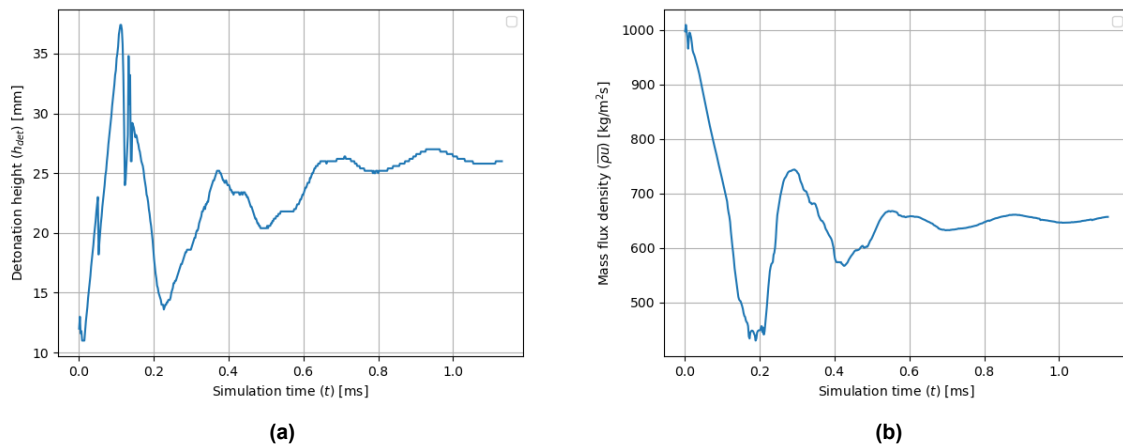
Figure 7.5: a) Detonation height, and b) mean inlet mass flux during the simulation time.

The results presented in this section allow to verify the robustness of the set up presented in chapter 5. No variations on the workflow had to be done to obtain the results for this new case. It is important to note the accuracy of the detonation velocity when compared to the ideal CJ result, being the maximum error close to 1%. Moreover, the 2D flow field solution will be employed to ignite the 3D simulation.

7.4. Simulation Set Up

The 3D simulation domain can be seen in figure 7.6a, and a slice of the combustion chamber is shown in figure 7.6b. To save computational resources, the domain was simplified compared to the geometry employed by Strempfl et al. [122] in figure 7.2a. The authors include in their model the air and H_2 plenums, setting there the inlet boundary conditions. On the other hand, as seen in figure 7.6, this work only considers the pipe section. There are 100 H_2 inlet pipes equally spaced at the bottom plate of the engine with a diameter of 0.5 mm. The air inlet is a continuous cylindrical gap of 1.76 mm height. The combustion chamber width is 7.6 mm, and the outer diameter is 90 mm. The length of the H_2 inlet pipe is 7.6 mm, and the length of the cylindrical air inlet is 35 mm. Lastly, the height of the combustion chamber measured from the bottom plate to the outlet is 112.6 mm. All the relevant geometry parameters are summarized in table 7.2.

Regarding the boundary conditions, the air and H_2 inlets are defined as reservoir-pressure inflow boundaries. The total temperature is set to 287 K, and the total pressure to 5.2 and 11.2 bar respectively.
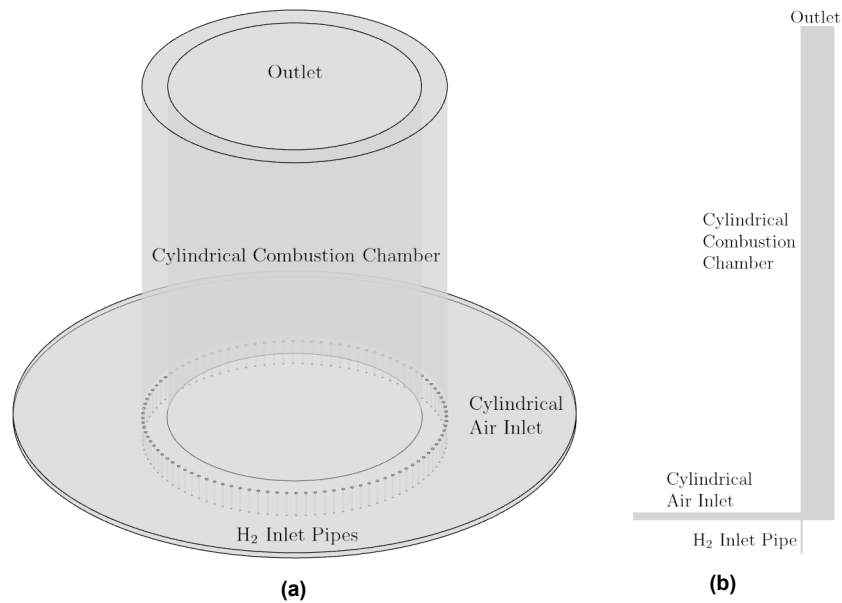
Figure 7.6: a) Isometric view of the 3D simulation domain and b) domain section geometry, based on the experiment from Bluenmer et al. [5].

The injectors are designed to be choked at the exit, having a total H_2 mass flow of 13.7 g/s, and an air mass flow of 517.7 g/s, being the global equivalence ratio of $\phi = 0.9$. The outlet is defined as an exit-pressure outflow with a static pressure of 1 bar. Moreover, the walls are defined as viscous, adiabatic walls.

The Spalart-Allmaras RANS model was employed to solve the Navier-Stokes equations. However, due to numerical instability problems, the laminar Navier-Stokes equations are solved instead. For time integration, a 3rd-order Runge-Kutta scheme is employed combined with a dual-time stepping approach. The time step employed is 5×10^{-8} s, with a CFL of 0.05 for the entire domain, and 0.02 for regions with high pressure gradients. The AUSMDV upwind flux [2] has been employed. In addition, the Ó Conaire chemical reaction mechanism [1] has been chosen.

Table 7.2: Simulation domain geometry parameters.

Name	Dimensions	Value
Number of H_2 injectors	-	100
H_2 pipe diameter	mm	0.5
H_2 pipe length	mm	7.6
Cylindrical air injector height	mm	1.76
Combustion chamber height	mm	112.6
Combustion chamber width	mm	7.6
Combustion chamber diameter	mm	90

7.4.1. Mesh Definition

The mesh employed for the 3D simulations is shown in figure 7.7. It can be seen how it is divided into four regions with different mesh resolutions. The finest region is found where the mixing of the fuel and oxidizer takes place, as well as in the injectors. The detonation wave front is also contained within this region. Therefore, a fine mesh is required to properly resolve the high gradients present in this section of the combustion chamber. The maximum length scale within the mixing region is 170 μm. Moreover, the air inlet close to the mixing region is set to have a maximum length scale of 250 μm. The second mesh resolution region goes from the mixing zone up to half the combustion chamber height. The maximum length scale in this section is 500 μm. Lastly, the global maximum length scale is set to 1000 μm, being the

size of the cells also limited by the growth from the wall cells towards the inner cells of the combustion chamber.
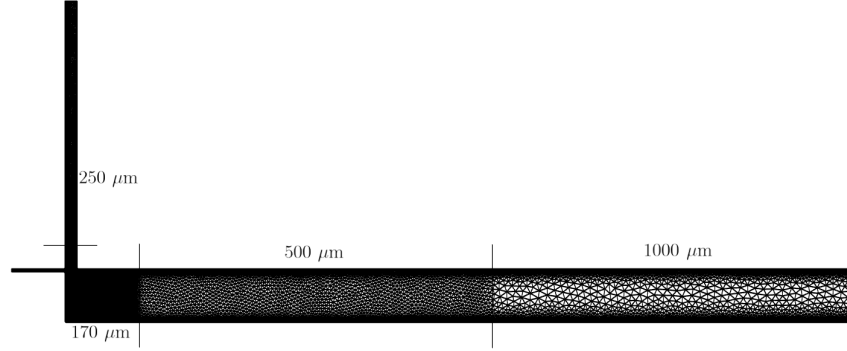
Figure 7.7: 3D simulation domain mesh.

The first layer thickness is set to 10 μm. However, this parameter does not have a relevant impact for the laminar Navier-Stokes case. Lastly, the mesh has a total of 47.846 million points.

7.5. Ignition Strategy

The ignition of the 3D domain is a crucial step of the simulation as it has an influence on the transient and final equilibrium solution. In their work, Strempfl et al. [122] employed a 1D detonation approximation using CANTERA [123]. Then, they computed the expansion of the gases behind the wave and guessed the shape of the refill region. The idea was to start the simulation with only one detonation wave to lock it in that mode of operation. In this work a similar approach has been employed.

The objective is to use the 2D simulation solution presented at the beginning of the chapter to ignite the 3D simulation. The first step is to adapt the 2D solution to the 3D domain. In order to do this, a transformation from cartesian to cylindrical coordinates of the 2D mesh has to be conducted. The new cylindrical coordinates are computed as follows:

$$x_{cyl} = R_{cyl} \cdot \cos\left(\frac{2\pi x}{L_{cc}}\right) \tag{7.1}$$

$$y_{cyl} = R_{cyl} \cdot \sin\left(\frac{2\pi x}{L_{cc}}\right) \tag{7.2}$$

where R_{cyl} is the radius of the new cylindrical mesh, x is the cartesian coordinate of the original 2D mesh, and L_{cc} the length of the combustion chamber in the 2D case. The height coordinate z_{cyl} is the same as in the 2D case.

Once the cylindrical mesh is defined, the values of the 2D solution are interpolated onto the 3D mesh. The cylindrical mesh is defined so that its radius is equal to the mid-width radius of the combustion chamber. In addition, the height of the cylindrical mesh coincides with the height of the 3D combustion chamber measured from the bottom plate. The interpolation method employed is an inverse distance weighting considering 10 neighbours. The interpolated solution is shown in figure 7.8.

As it can be seen in figure 7.8b, the inlet region is taking its values from the geometrically closest points of the interpolated cylindrical mesh. Moreover, figure 7.8a shows how the inlets have a mixture of hydrogen and air in both pipes. This is not physically correct since each inlet should only have hydrogen or air, respectively. In addition, it would lead to numerical stability problems. Thus, the last step is to combine the interpolated solution with a developed cold flow simulation, combining the detonation wave and the resolved flow at the injectors.

Starting from a cold flow simulation solution, the static pressure p, static temperature T, density ρ, species mass fractions Y_k and species partial densities ρ_k are overwritten in a specified region of the

(a) Hydrogen mass fraction flow field.

(b) Temperature flow field.
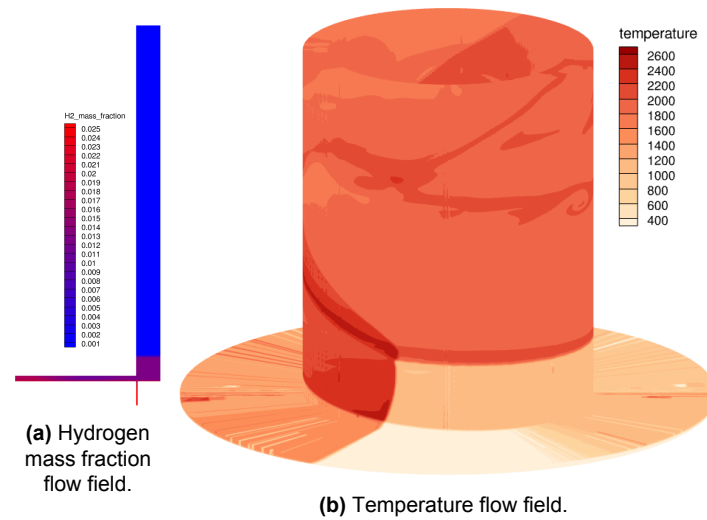
Figure 7.8: Interpolated solution of the 2D results onto the 3D geometry.

(a) Hydrogen mass fraction flow field.

(b) Temperature flow field.
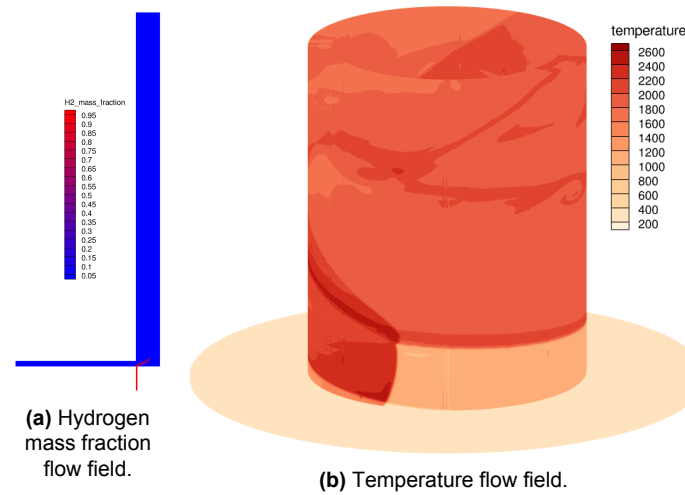
Figure 7.9: Ignition flow field for the TUB [5] simulation.

domain. Two regions were tested. Region A was defined as the entire combustion chamber except for the last 3 mm closest to the bottom plate. This was done to avoid overwriting the cross-flow jet at the mixing region. On the other hand, region B was similar to region A, but also covering the lower right corner of the combustion chamber up to the bottom plate, still not overwriting the mixing of the two injector jets. When running the simulation, the region B case was unable to provide any solutions. However, region A proved to be a stable case. The final ignition solution is shown in figure 7.9.

Figure 7.9b shows how the inlet temperature is of the order of 200 K, as expected by the defined boundary conditions. It can also be seen that the solution within the combustion chamber is still the same as shown in figure 7.8b. On the other hand, figure 7.9a clearly shows the differences in hydrogen mass fraction between the air and the fuel injectors, as well as the developed mixing region flow.

7.6. Simulation Results

Figure 7.10a shows the static pressure measured at the mid-span of an unrolled cylindrical mesh located at the mid-width of the 3D combustion chamber with a resolution of 200 μm. The 3D solution is interpolated on said cylindrical mesh. The pressure plots shows the static pressure measured at different heights, as well as at the outlet and the outlet mean, compared with the total pressures from the hydrogen and air inlets. It can be seen how the highest peak is found at $z = 5$ mm at the beginning, related to the initial

ignition solution. Afterwards, the pressure drops considerably, showing only small peaks. It is after $t = 0.4$ ms that regular high local pressure peaks start appearing, which indicates that there is a periodic pressure wave traveling through the combustion chamber. It is interesting to note that only one of the peaks, marked as t_C, is above the air inlet total pressure. In addition, the regularity of the peaks and pressure signal shape indicates that there is a single detonation wave within the combustion chamber.

On the right figure 7.10b, the outlet static pressure standard deviation is shown. The plot could be separated into three different sections: before $t = 0.4$ ms, between 0.4 and 0.8 ms, and after $t = 0.8$ ms. The first section shows very large amplitudes in the oscillations. This could be associated with a transient state from the ignition to a more stable operation. The second section still shows an oscillatory behavior, but the amplitudes remain similar and around a constant value. Lastly, after $t = 0.8$ ms, the amplitude of the oscillations seems to increase. However, after the first peak the amplitude remains very similar and the curve oscillates around a constant value. This could indicate a change in the operational mode.
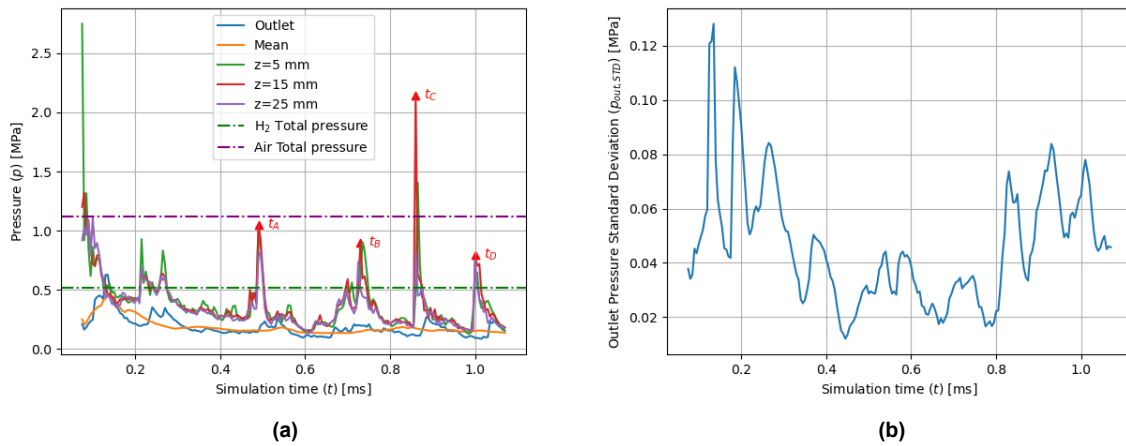
Figure 7.10: a) Static pressure measured at a probe located in the mid-span of the unrolled combustion chamber at different heights during the simulation time compared with outlet, reservoir, and mean exit pressures. b) Standard deviation of the outlet static pressure measured at the mid-span of the unrolled combustion chamber during the simulation time.

A first approximation of the detonation velocity can be obtained from the static pressure plot seen in figure 7.10a. By recording the time at which the pressure peak is registered, the average detonation velocity over one period can be computed as the length of the combustion chamber divided by the time difference between two pressure peaks. Since the measurements were taken at the mid-width of the combustion chamber, the length is $L_{cc} = 258.8$ mm. Taking the time difference from the different peaks, the computed average detonation velocity for each period is shown in table 7.3.

Table 7.3: Detonation velocity computed from the static pressure plot shown in figure 7.10a by taking the time difference between the pressure peaks.

Section	A-B	B-C	C-D	Average
Δt [ms]	0.239	0.130	0.140	0.169
V_D [m/s]	1082	1990	1848	1640

The results in table 7.3 show how the detonation velocity increases in the last two periods, meaning that the detonation wave has become stronger. Moreover, taking the average between the three periods, the mean detonation velocity over the entire simulation time is $\overline{V_D} = 1640.7$ m/s, which is very close to the velocity recorded in the experiment conducted by Bluenmer et al. [5]. However, a longer simulation time would be required to conclude the detonation velocity associated with the stable operational mode.

Figure 7.11a shows the power spectral density (PSD) of the pressure signal at $z = 15$ mm height. As in chapter 6, a low-pass filter with a cut-off frequency of 20 kHz was applied to avoid aliasing. After the

filtering, the low frequencies do not suffer any changes, hence the sampling frequency was high enough. The dominant frequency is found to be $f_w = 5.93$ kHz. The associated detonation velocity is $V_D = 1676$ m/s, which is very similar to the velocity obtained by Bluenmer et al. [5].

The autocorrelation function was also computed from the static pressure signal at $z = 15$ mm, as shown in figure 7.11b. The first peak has an associated frequency of 7.14 kHz and the second peak a frequency of 4.26 kHz. Their associated detonation velocities are 1847 and 1102 m/s, respectively. When comparing these results to the detonation velocities from table 7.3, it can be seen how the first peak of the autocorrelation function is related to the detonation velocity from sections **B-C** and **C-D**, while the second peak is related to the velocity in section **A-B**. On the other hand, the PSD result is related to the mean detonation velocity over the entire simulation time.

(a)   **(b)**
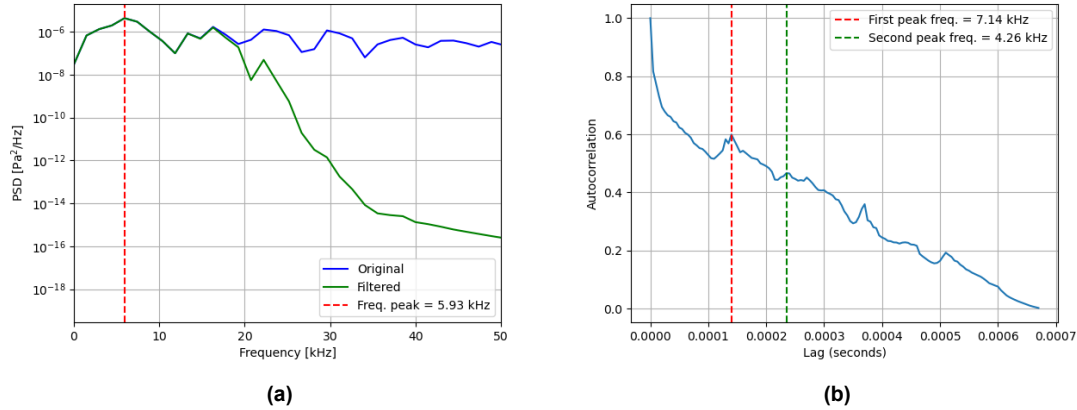
Figure 7.11: a) Power Spectral Density (PSD) of the static pressure signal measured by the probe located at $z = 15$ mm. b) Autocorrelation function of the static pressure signal measured by the probe located at $z = 15$ mm showing only the positive lag values.

The frequencies and associated detonation velocities obtained from the PSD and autocorrelation function are shown in table 7.4. These values are also compared with the ideal CJ solution, the experimental detonation velocity from Bluenmer et al. [5] and the simulation from Strempfl et al. [122]. The detonation velocity obtained in the experiment is lower than the ideal CJ value due to inhomogeneous mixing. On the other hand, the detonation velocity from Strempfl et al. is above this quantity. However, the author does not have a definite conclusion that explains the result. Regarding the PSD result, it is very close to the experimental value. The autocorrelation function is higher and related to the faster periods of the simulation. Letting the simulation run for a longer physical time would help to arrive to more definitive results about the detonation velocity and frequency.

Table 7.4: Detonation velocity computed with different methods: with the PSD (PSD) and with the autocorrelation function (Autocorrelation) from the static pressure measured within the combustion chamber at a height of $z = 15$ mm, the detonation velocity from Strempfl et al. [122], and the result from Bluenmer et al. [5] compared to the ideal CJ detonation velocity.

Case	No. Waves	Detonation Frequency [Hz]	Velocity [m/s]	Error [%]
Ideal CJ	1	6808	1925	-
Bluenmer	1	5800	1640	14.05
Strempfl (CASE 2)	1	7630	2157	12.05
PSD	1	5930	1676	12.93
Autocorrelation	1	7140	1847	4.051

Regarding the number of waves, the dominant mode is a single-detonation wave for all the different cases. This is in agreement with the results from the experiment and the simulation from Strempfl et

al. [122]. Nevertheless, this mode of operation is achieved after a transient state with a complex wave structure system.

Figure 7.12b shows two 2D flow field plots of the 3D combustion chamber at time $t = 0.55$ ms. To obtain this solution, the 3D simulation results were interpolated into a 2D cylindrical mesh located at the mid-width of the combustion chamber. Afterwards, the cylinder is unrolled, obtaining the 2D plot seen below. The resolution of the cylindrical mesh is 200 μm. The fine resolution was employed to minimize the errors of the interpolation.

Figure 7.12: Interpolated 2D flow fields from a circular 2D mesh along the mid-width of the combustion chamber with a resolution of 200 μm at time $t = 0.55$ ms. a) Static temperature with the detonation index outlined in blue. b) Normalized pressure gradient with the detonation index outlined in red.

On the left side, figure 7.12a shows the static temperature flow field with the detonation index marked in blue. The threshold parameters employed to define this quantity are the same in the previous chapter: $\Gamma_w = 10^{-2}$ and $\Gamma_p = 0.4$, for the normalized chemical heat release and normalized pressure gradient, respectively. It can be seen how there is no clear triangular shape of the fresh inlet gases. This is because of the complex wave structure system present within the combustion chamber. In some regions, pockets of unburnt fresh reactants at low temperatures can be seen, as well moving downstream the combustion chamber. Moreover, the detonation index pockets show that there is no clear detonation wave front. Instead, it seems like there are several weak detonations traveling within the combustion chamber.

On the right side, figure 7.12b shows the normalized pressure gradient flow field with the detonation index marked in red. In this case, towards the right side of the figure, a weak detonation could be identified, as the detonation index and the normalized pressure gradient form a small detonation front. The other detonation index pockets are not clearly associated with any pressure waves. In addition, it could be argued that only one weak detonation wave is traveling around the combustion chamber with weak pressure waves present as well. This is in agreement with the single-detonation mode of operation development.

Figure 7.13: Detailed view of the static temperature (a), detonation index (b) and mixing index (c) flow fields at time $t = 0.55$ ms located at the position of the weak detonation from figure 7.4b.

To further inspect the weak detonation in figure 7.12b, figure 7.13 shows a detailed view of the

combustion chamber section at the same position. From the temperature flow field in figure 7.13a, it can be seen how the turbulent mixing influences the detonation dynamics. There are pockets of low-temperature fresh reactants right next to high-temperature burning gases. It is interesting to note how the inner wall shows lower temperatures than the outer wall. The fresh reactants tend to move towards the inner wall, probably pushed by the mass flow of air, and then start moving downstream the combustion chamber. In this process, there is a mixing with the hot post-combustion gases creating a vortical-like structure, leading to a rather stratified flow field.

Figure 7.13b shows the detonation index. There is a correlation between the temperature and the detonation index fields through the chemical heat release. These results show that the turbulent mixing and combustion process leads to inhomogeneous detonation waves. Moreover, the mixture index in figure 7.13c also shows how that the H_2 jet is pushed towards the lower plate and inner wall by the passing detonation wave, having an influence on the mixing process and how the post-combustion products mix with the fresh reactants. It is also interesting to note how the regions where the mixing index is unity (black line border), corresponding to stoichiometric conditions for the defined equivalence ratio, are correlated with the high-temperature regions.

Once the solution arrives to a stable single-wave mode, the flow field changes considerably. Figure 7.14a shows the static temperature field along the mid-width of the combustion chamber at time $t = 1.00$ ms. It can be seen how, compared to figure 7.12a, a clear single-detonation wave structure can be identified. However, the detonation index is very low. Thus, it is not visible in the field. This implies that the detonation wave is very weak. Moreover, the inlet fresh gases layer is still developing since it does not resemble the ideal triangular shape.

Figure 7.14b shows the normalized pressure gradient field at time $t = 1.00$ ms. The color scheme was changed with respect to figure 7.13c to enhance the visibility of the results. It can be seen how the pressure wave is very weak as the pressure gradient is very faint.

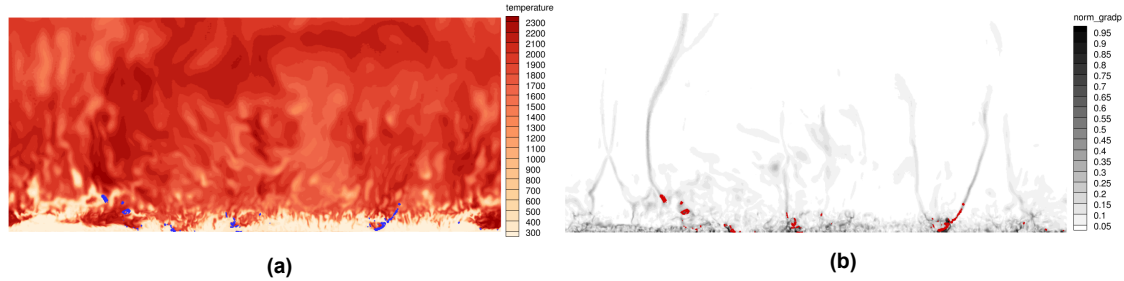**(a)**   **(b)**
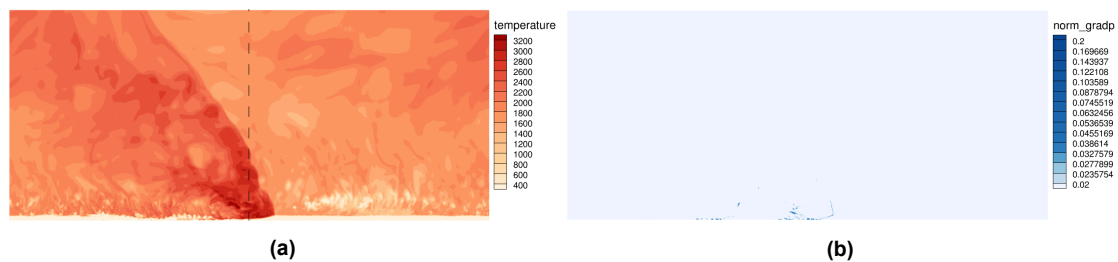
Figure 7.14: Interpolated 2D flow fields from a circular 2D mesh along the mid-width of the combustion chamber with a resolution of $200\ \mu$m at time $t = 1.00$ ms. a) Static temperature. b) Normalized pressure gradient.

Figure 7.15a shows the static temperature field at a slice located where the black dashed line is in figure 7.14a. Compared to the results shown in figure 7.13a, it can be seen how the field is more homogeneous. The highest temperatures are found on the outer wall. In addition, the high temperature region seems to go slightly inside the air inlet and the fresh reactants are pushed towards the lower plate. This can also be seen in figure 7.15c showing the mixture index, where the stoichiometric conditions region (black iso-line) is close to the lower wall and there are no pockets of unburnt reactants downstream the combustion chamber.

Figure 7.15b shows the detonation index field. It can be seen how there is no strong detonation front, and only in the lower corner of the slice there is a pocket of detonation index above 0.9. This confirms that the pressure wave traveling around the combustion chamber is a very weak detonation. This is probably because the layer of mixed fresh reactants is not properly developed, which affects the detonation properties.

Figure 7.16 shows the mean normalized heat release along the combustion chamber length. It was computed employing the interpolated cylindrical mesh at the mid-width of the combustion chamber, recording the maximum heat release at each height for each solution, and then calculating the mean. It can be seen how the region of maximum heat release is very close to the lower plate. When moving downstream the combustion chamber, the mean normalized heat release drops one order of magnitude when reaching $z = 20$ mm, approximately. This implies that the detonations present in the flow field are
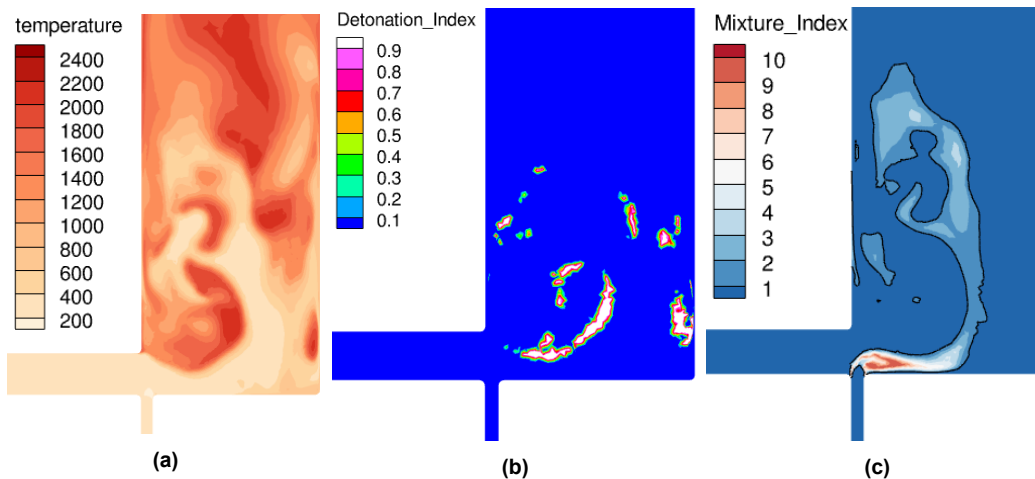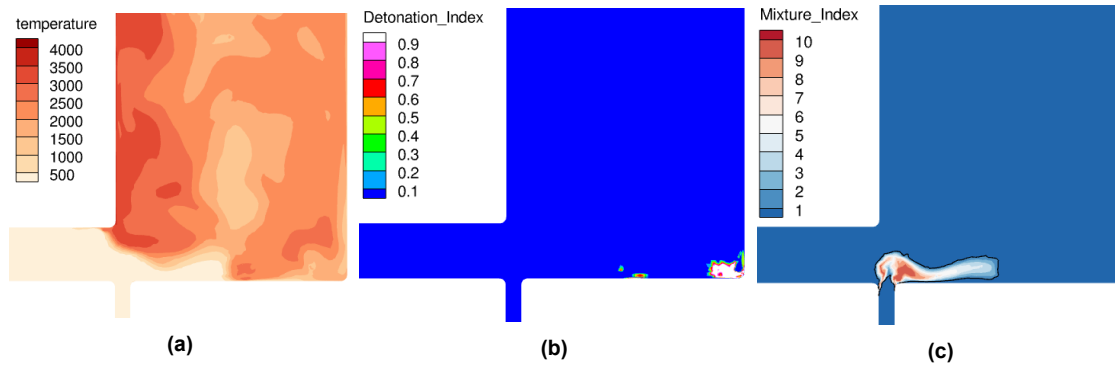
Figure 7.15: Detailed view of the static temperature (a), detonation index (b) and mixing index (c) flow fields at time $t = 1.00$ ms located at the position of the dashed black line from figure 7.14a.

weak, which is in agreement with the previously shown results. Moreover, it also leads to the conclusion that a non-negligible amount of fresh reactants are burned by deflagrations and not detonations, since there is still heat release until around $z = 60$ mm.
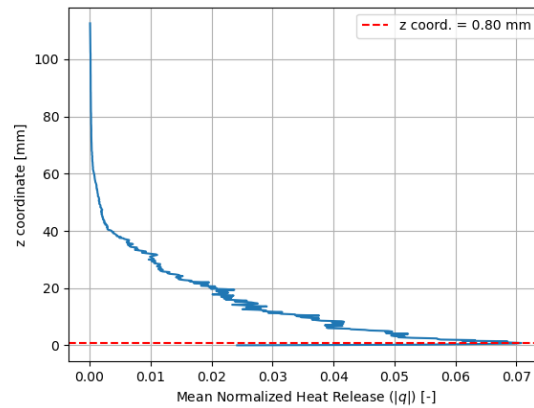
Figure 7.16: Mean normalized heat release along the combustion chamber length calculated at the mid-width circumferential plane.

The mass flux is an important parameter directly connected to the detonation dynamics and the stable mode of operation. Table 7.5 shows the mass flux defined by Strempfl et al. [122] and the measured mass flux at different times during the simulation. Within the early transient state, the mass flux suffers drastic changes in its value, specially the air inlet. As the simulation progresses towards stable operation, the mass flux tends to a constant value, as it can be seen when comparing the mass fluxes at times $t = 0.55$ and $t = 1.00$ ms. At the beginning of the simulation the equivalence ratio reaches very high values due to a blockage in the air inlet. As the simulation advances, the mass fluxes get closer to Strempfl et al. values. As the reservoir-pressure inflow does not prescribe the mass flux and is influenced by the pressure gradient, the value oscillates, having an impact on detonation stability and strength.

To study the evolution of the flow field, figure 7.17 shows the normalized pressure gradient on the lower plate at different simulation times with the detonation index marked in red. Figure 7.17a has a clearly defined detonation front advancing counter-clockwise which was ignited from the 2D solution. However, it can be seen how there are some pressure oscillations behind the detonation wave. These oscillations turn into a clockwise rotating detonation as seen in figure 7.17b. Both detonations collide, leading to a more complex flow field in figure 7.17c. At this time step, the counter-clockwise moving detonation is stronger than the clockwise rotating wave. Moreover, it can be seen how the pressure waves are traveling upstream in the air inlet. This has an impact on the inlet mass flow, thus influencing the detonation dynamics afterwards. The pressure oscillations lead to the formation of a third wave, as shown in figure 7.17d.

Table 7.5: Hydrogen and air mass fluxes comparison between Strempfl et al. [122] and TAU simulations at different simulation times.

Case	Hydrogen Mass Flow [g/s]	Air Mass Flow [g/s]	Equivalence Ratio [-]
Strempfl	13.7	517.7	0.9
TAU ($t = 0.25$ ms)	12.19	146.6	2.828
TAU ($t = 0.50$ ms)	11.51	450.1	0.869
TAU ($t = 0.55$ ms)	12.43	406.4	1.039
TAU ($t = 1.00$ ms)	12.29	406.5	1.028

However, it can be seen how the detonations are weaker since the detonation index is hard to identify in this case. Figures 7.17e and 7.17f show how the three waves co-exist in the combustion chamber with oscillating strength. It is also interesting to note how in figures 7.17g and 7.17h the counter-clockwise detonation wave seems to have an angle with respect to the walls as it is propagated. The wave structure collapses again into a single-wave mode as seen in figure 7.17i. In this case, the counter-clockwise detonation dominates. Due to the presence of pressure oscillations secondary waves are still present, as seen in figure 7.17j, but the counter-clockwise detonation still dominates in figure 7.17k. Nevertheless, the mode is not stable since, as it can be seen in figure 7.17l, many other waves appear, and a single dominant detonation cannot be identified. Later in the simulation, this complex wave structure system collapses into two counter-rotating detonation waves as shown in figure 7.17m. Afterwards, only one detonation wave survives and remains as the only wave traveling within the combustion chamber, as seen in figures 7.17n and 7.17o. However, the detonation is weak since the detonation index value is very low and cannot be seen.

These results show that during the early stages of the simulation, due to pressure and mass flux oscillations, the flow field within the engine is unstable. It is the coupling between and the detonation dynamics and the injection of the inlet gases what leads to this behavior. After enough time has passed, the simulation arrives to a single-wave mode, which coincides with the experimental results in number of waves, and with the simulation of Strempfl et al. [122] in wave direction. Moreover, the mean detonation velocity computed is very similar too. Nevertheless, more simulation time would be required to evaluate the evolution of the detonation wave and to arrive to more definite conclusions about the engine performance and detonation dynamics. In addition, it was proved that a 2D solution can be employed to start a 3D simulation.

(a) $t = t_0$ ms

(b) $t = t_0 + 0.045$ ms

(c) $t = t_0 + 0.1$ ms

(d) $t = t_0 + 0.135$ ms

(e) $t = t_0 + 0.16$ ms

(f) $t = t_0 + 0.19$ ms

(g) $t = t_0 + 0.23$ ms

(h) $t = t_0 + 0.275$ ms

(i) $t = t_0 + 0.34$ ms

(j) $t = t_0 + 0.375$ ms

(k) $t = t_0 + 0.415$ ms

(l) $t = t_0 + 0.465$ ms

(m) $t = t_0 + 0.66$ ms

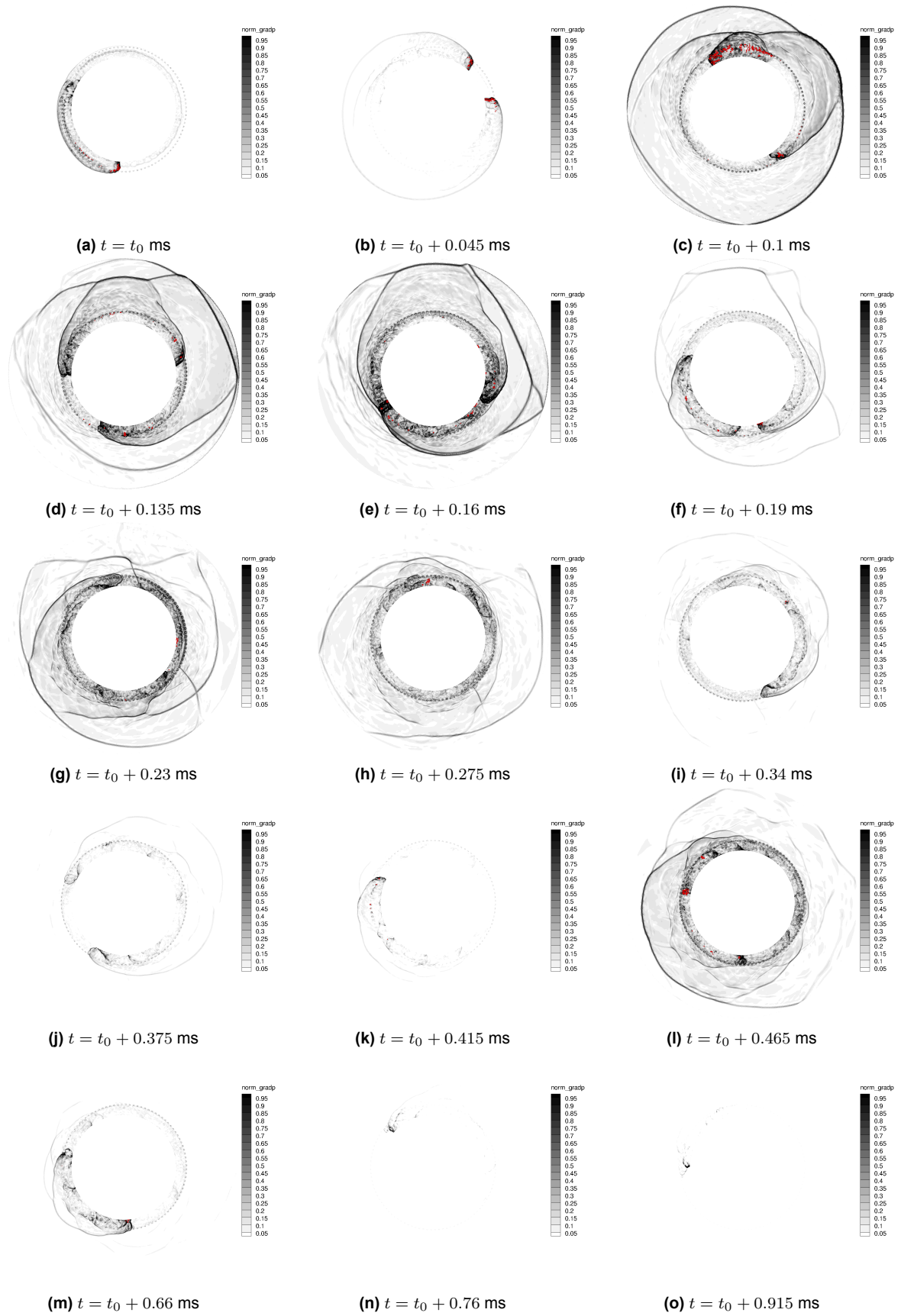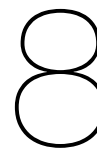**(n)** $t = t_0 + 0.76$ ms

(o) $t = t_0 + 0.915$ ms

Figure 7.17: Normalized pressure gradient flow field on the lower plate at different time steps with the detonation index marked in red.

8

Conclusions

The present thesis introduced a robust work flow to simulate rotating detonation engines (RDEs) employing the DLR TAU code [3]. The different simulation capabilities available in TAU were studied in a systematic manner conducting 1D shock tube detonations, 2D RDE simulations compared with the literature case from Sheng et al. [120], and 3D simulations comparing the results with different experiments and simulations from the literature (see Armbruster et al. [4], Bluenmer et al. [5], and Strempfl et al. [122]). The main objective was to find the best set up to study the flow field within an RDE employing the DLR TAU code, as well as evaluating the impact of different modeling decisions on the results. In order to achieve this objective, a set of research questions were presented in section 1.2, which were answered during the course of this thesis. A summary of the answers is provided in this section.

What is the best available chemical reaction mechanism for this application?

Different chemical reactions available in TAU were tested. The chemical reaction mechanisms studied were: Gaffney [29], Gerlinger [35], Ó Conaire [1], Hong [32], and Boivin [37]. First, a set of 1D simulations were conducted to evaluate how well they captured detonation wave properties compared to ideal Chapman-Jouguet (CJ) theory results obtained with the CEA software [96]. The results lead to the conclusion that the Gerlinger mechanism predicted with the highest accuracy the detonation velocity. However, the Ó Conaire mechanism offered better results for both static temperature and pressure after the detonation wave, while also having a good approximation of the detonation speed. The Hong mechanism also offered good results. These three reaction mechanisms were then studied for a 2D case. When comparing the flow fields, the results were very similar for the three different cases, with slightly more different results for the Gerlinger case due to its pressure independent reaction rates. There were also some differences in the detonation height and other quantities. The Gerlinger mechanism showed higher amplitude oscillations, while the Hong mechanism seemed less sensitive to the changes in the flow field. Lastly, when comparing the detonation velocity with the literature case from Sheng et al. [120], the best approximation was found with the Gerlinger mechanism. However, the Ó Conaire mechanism was also close, and was finally chosen as the chemical reaction mechanism to use for the upcoming RDE simulations due to its overall satisfactory results in both 1D and 2D simulations.

What meshing strategy is suitable to adequately resolve the main flow features?

Regarding the meshing strategy, different grid resolutions were evaluated for the 2D simulation case. In previous studies, as shown in appendix B, the maximum acceptable mesh resolution for 1D shock tube cases was found to be $200 \ \mu$m before the results started to deteriorate. This mesh resolution was employed as the baseline for the 2D cases to save computational costs. It was later compared with a mesh resolution of $100 \ \mu$m for the same case in section 5.2.5. The baseline resolution provides a good trade-off between accuracy of the results and computational costs. The finer resolution showed some flow structures that were previously not present, as well as better results when compared with the literature case from Sheng et al. [120]. However, it is also important to mention that for a bigger 2D domain, such as the case studied in section 7.3, the ideal mesh resolution can change. In this case, the $200 \ \mu$m resolution was able to capture Kelvin-Helmholtz instabilities. It also proved to be sufficient to capture all the main features from an RDE flow field. On the other hand, considering now the 3D mesh definition, the strategies from the literature were employed. Moreover, due to a time constraint, different mesh resolutions were

not evaluated. Nevertheless, the chosen meshes have proven to provide physical results similar to the experiments, as seen in chapter 6.

What solver parameters are most suitable for this application?

Some key solver parameters such as the time step size and numerical stability limits of the simulations were studied previously (see appendix B). The time step of 2×10^{-8} s chosen for the 2D simulations is a trade-off between numerical stability and computational costs. Later, for the different 3D simulations conducted in chapters 6 and 7, the time step was slightly changed, but still of order 10^{-8} seconds. Furthermore, another aspect studied in this thesis is th influence of the chosen upwind flux solver. TAU offers a variety of upwind fluxes, however, based on the state of the art findings in chapter 3, only the AUSM family of upwind fluxes was considered. The results for the 1D shock tube simulation showed that the AUSMDV performed the best. However, when evaluating their differences in 2D the results were similar between the AUSMDV, AUSMP, AUSMPWP, and AUSM van Leer. The AUSMDV was chosen as the baseline option for the upcoming simulations due to the overall better behavior and results.

What inlet boundary condition is most suitable for this application?

Another important aspect of the numerical set up is the inlet boundary condition. In the literature, many authors use a boundary condition similar to the one proposed in section 4.7.8 [17][120]. However, TAU does not have that type of boundary condition available. Two different boundary conditions were studied with the 2D simulations: reservoir-pressure inflow, and a Dirichlet-type inlet. The reservoir-pressure inflow computes the inlet variables based on the velocity field from the inner domain. It computes an isentropic expansion from a specified total reservoir conditions that would match the inner domain velocity field. It could be said that this boundary condition is sensitive to the pressure gradients within the inner domain. On the other hand, the Dirichlet boundary condition prescribes the values of the variables at the inlet. To do so, a code was implemented. Starting from a specified mixture and total reservoir conditions, an isentropic expansion that expands the gases to $M = 1$ is computed. A more detailed explanation can be found in section 5.2.1. After computing the expansion, the inlet variables are prescribed at the boundary. Hence, this inlet boundary is not affected by the inner domain flow. Therefore, the results show that the Dirichlet-type boundary is independent of the detonation dynamics. This decoupling between the injection and the detonation is very clear when comparing the results between the two boundary conditions, having the reservoir-inlet high-frequency oscillations associated with this phenomena. The Dirichlet boundary was chosen as the baseline for the 2D simulations to study the effect on the flow field of other parameters. However, the reservoir-pressure inflow was chosen for the 3D simulations. The Dirichlet inlet is an idealized case were the injection is not affected by the high detonation wave pressures, thus not suffering from blockage. Nevertheless, this interaction is a key factor that determines the dynamic behavior of the engine and the transition from ignition to the stable mode of operation. The inlet boundary conditions plays a major role in the correct modeling of RDE physics. Therefore, as the reservoir-pressure inlet is sensitive to the pressure gradient, it was employed for the 3D simulations, providing satisfactory results when compared to the experiments.

What is the most reliable ignition method to start the simulations?

The ignition of an RDE is still a topic of discussion since it can lead to numerical stability problems or non-physical solutions. In section 5.2.2 three different approaches to ignite a 2D simulation were tested. The results showed that the three cases arrived to the same results at similar simulation times. It is important to note that the main difference was found during the early transient state between the oblique and rectangular strategy. When adding more energy into the domain, the transient state evolution remained the same and the final detonation velocity was slightly higher than the baseline case. On the other hand, different ignition methods were employed for the 3D simulations. The case studied in chapter 6 employed a hot pocket with high temperature and pressure, which is relatively similar to the ignition method with a laser employed by Wolfgang et al. [4]. For the case in chapter 7, a 2D simulation solution was employed. The ignition procedure was successful and a stable simulation was obtained. However, there was not enough time to achieve a stable mode of operation, nor to test different ignition approaches.

To what extent are the main flow features represented in the TAU simulation?

Considering now the accuracy of the results obtained in the simulations, it can be concluded that the presented set ups for 2D and 3D RDE simulations provide physical results. The flow fields shown in chapter 5 present the key features of an RDE flow field: detonation wave, layer of fresh reactants, oblique

shock, and the slip line. Some solutions with enough accuracy even show Kelvin-Helmholtz instabilities developing in the slip line, as in section 7.3. Moreover, the results in chapters 6 and 7 show that, with the current capabilities, the interaction between injection and detonation dynamics can be captured even in 3D simulations, arriving to results similar to experiments. The complexity of the 3D flow field within RDEs is computationally expensive and has different challenges from the modeling perspective. The results presented in this thesis prove that the developed set up is capable of reproducing the complexity of the transient state after ignition, as well as the dominant frequency of the stable operational mode.

To what extent does the TAU simulation predict the results from the literature?

The results obtained with TAU are also very close to those from the literature. In chapter 5 the results for the 1D simulations are close to the values obtained with CEA [96] software, and the 2D simulation results are close to those obtained by Sheng et al. [120]. In addition, 3D results can also be positively correlated to experimental and to other simulations results.

To what extent is the set up stable and robust when running a different case?

It is also important to note the robustness of the set up. The 2D simulations set up can be easily adapted to any case, as seen by the results obtained in chapters 5 and 7. Moreover, there were no major stability problems when running the 3D simulations with the solver parameters defined in chapter 5.

To what extent are the injection and detonation dynamics coupled?

Focusing now more on the results, the 2D simulation results presented in section 5.2.1 show how much of an impact the coupling between injection and detonation can have in the results. This can also be seen when going into 3D simulations, where the blockage of the injectors and the reflection of the pressure waves has an influence in the inlet mass flux. In chapter 7, when evaluating the evolution of the detonation during the simulation time, it is interesting to note how the air mass flow decrement is correlated to the pressure waves traveling upstream the air inlet, having an impact on the total mass flow, and hence on the equivalence ratio and strength of the detonations.

To what extent is the mixing process during injection impacting the results?

Related to this interaction is the mixing process itself. The design of the injector device is what determines the efficiency of the mixing. A bad mixing hinders the detonation properties and leads to inhomogeneous detonation fronts, as seen in the results of both chapters 6 and 7. Moreover, it is interesting to make the comparison between an ideal 2D solution and a 3D simulation from the same case as in chapter 7. It is clear that the mixing of the reactants, as well as other unsteady processes, are playing a major role. The difference in stability and multiple wave system in the 3D case clearly shows the impact of the mixing of the reactants.

To what extent there is a correlation between the operating conditions and multiple wave formation?

It can be concluded that the interaction between the injection and detonation dynamics, the mixing process, and the mode of operation are tightly coupled. From the results of chapter 6, it can be seen that the transient behavior and the number of waves once stability has been achieved is related to the total inlet mass flux, as it was already suggested early in the literature by Wolański et al. [49].

Summary

This thesis presents a robust workflow to study the flow field within a RDE. The results shown provide information about the most suitable chemical reaction mechanism available in TAU to study detonation dynamics. Moreover, an in-depth study about the available upwind flux solvers from the AUSM family and their behavior in these type of problems is presented. The effects of different solver parameters such as time step size and grid resolution were evaluated when defining the set up. Moreover, regarding the validation of the workflow and its comparison with other works from the literature, it has been proven that the results can be reproduced with accuracy. The set up for the 2D simulations is robust and can provide an insight into the main features of an RDE flow. Furthermore, the results obtained for the 3D simulations are very close to the experimental results, capturing the complex interaction between the detonation and injection dynamics. In addition, different ignition strategies were successfully tested, such as igniting the mixture from a hot pocket and starting a 3D simulation from a 2D simulation. On top of that, different diagnostics tools have been developed to extract meaningful data from the simulations and to present it in an insightful manner.

8.1. Future Developments

The present thesis has fulfilled its objective and has answered all the research questions in a satisfactory manner. However, there are many paths to explore further. For example, future works could focus on the implementation and study of the proposed pressure-driven boundary condition, in both 2D and 3D cases. It would be interesting to study how different boundary conditions impact the results of 3D simulations, mainly in the injection-detonation interaction. Moreover, further investigations about the inlet conditions shall be carried out. It would be relevant to evaluate the influence of including the plena geometry in the simulation domain. The geometry of the injector and the plena could be interacting with the pressure waves coming from the combustion chamber, thus having an impact on the detonation dynamics. Supporting these studies with experimental data, it could provide more information about the transient state after ignition and the development of stable modes of operation.

The ignition procedure with 2D simulations has to be further investigated. Due to a time constraint, no more tests could be carried out within the framework of this thesis. Ideally, it should be reliable, robust, and end in the correct mode of operation. It would be interesting not only to be able to lock the mode from the beginning, but also to start a simulation with operating conditions for a different mode and to study its evolution. This is related to the transition from the initial ignited flow field to a stable state. Furthermore, a better ignition modeling would provide better testing conditions for experimental set ups, giving more precise information about the behavior of the engine and the expected results. It is also important to note that the ignition process is a complex wave system of emerging weak pressure waves that transition into detonation waves. Further investigation into deflagration-to-detonation transition (DDT) phenomena within curved combustion chambers shall be conducted. This transitory state is also heavily impacted by the inlet boundary condition. Close collaboration between numerical and experimental works could lead to a repeatable, reliable, and robust ignition method for RDEs.

Regarding the operating conditions, future works could focus on different inlet mixtures and outlet conditions. For example, it would be interesting to study the behavior of methane-oxygen mixtures. The first step would be to study the detonation dynamics and find a suitable chemical reaction mechanism for carbon species which is not too computationally expensive. The transition from ignition to the stable mode of operation and injection-detonation dynamics could also be evaluated. Moreover, cryogenic mixtures could also be further investigated due to their relevance for space applications. Again, injection modeling and detonation-injection interaction could be studied, as well as reliable and repeatable ignition methods. On the other hand, new outlet conditions such as aerospike nozzles could be evaluated. These simulations could provide information about the engine performance, and compared with experiments could lead to more realistic performance predictions to help with the development of the engine as a propulsion subsystem of a space vehicle.

Lastly, the diagnostics shall be improved. On one hand, the data acquisition algorithm for the 3D cases relies on the interpolation of the flow field onto simplified geometries. This algorithm could be tuned to reduce the error associated with it. On the other hand, better data visualization methods could be developed, to study and track where detonation and deflagration waves are. This would help with the study of the transient state and the detonation-injection dynamics. In addition, new visualization parameters could be implemented in the simulations, such as OH^* chemistry. It would be interesting to evaluate how good OH^* chemiluminescence predicts the position of the detonation wave and its inclination with respect to the inlet fresh gases. Experimental efforts would benefit from this study. Moreover, it would be interesting to evaluate the heat loads for different geometries and operating conditions. Experiments are limited by the heat loading due to hardware damage. An in-depth study of the heat distribution and development of cooling systems would potentially solve the time constraint of experimental set ups. Longer firing times ensuring hardware safety would also increase the technology readiness level of RDEs towards real applications.

A
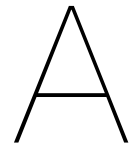
Algorithms

Algorithm 2: Determine CJ state

Init: $i = 0$, $\|q\|_i = \|q\|_{max}$
Result: T_{CJ}, p_{CJ}
for *convergence towards CJ state* **do**

> *compute the difference between two consecutive points downstream the detonation*
> diff $\leftarrow |\|q\|_{i-1} - \|q\|_i|$
> **if** *diff* $<$ *tolerance* **then**
>> $T_{CJ} \leftarrow T_i$
>> $p_{CJ} \leftarrow p_i$
>> *CJ state achieved, exit loop*
>
> **end**
> *If CJ state has not been achieved, update loop index*
> $i \leftarrow i - 1$

end

B

Internship Results

The results presented in this appendix were obtained during the internship period prior to starting the Master Thesis. They serve as the foundation from where the Master Thesis work started. Thus, this early work is presented in this chapter to understand better the learning process.

B.1. 1D Simulations

B.1.1. Set Up

The domain employed for the 1D simulations is a tube of dimensions $500x1$ mm. Different mesh sizes were employed, going from 1 to 400 μm. The shock tube is initially filled with the premixed combustible mix of $H_2 + O_2$ at ambient conditions (1 bar, 295 K). Figure B.1 shows the 100 μm mesh and the ignition region. The numerical ignition region is set to 5 bar and 3000 K to ensure a detonation is formed. It is placed at one of the extremes of the domain.

Figure B.1: 1D shock tube mesh and ignition region.

The Euler equations are employed for this simulation since the objective is to perform a sensitivity analysis of different parameters, thus there is no interest in introducing turbulence. Moreover, the boundaries of the tube are defined as non-viscous walls, and the other extreme of the tube is an outflow boundary with an ambient pressure prescribed of 1 bar.

B.1.2. Results

Mesh Influence

Figure B.2 shows the results for temperature and pressure centered around the shock for different mesh sizes. The dashed line corresponds to the CEA results for the Chapman-Jouguet theoretical solution of the post-combustion state. It is important to mention that for all these simulations the chemical kinetics mechanism is the same, and it is named after his author Gerlinger [35]. Moreover, the solution shown was taken at $t = 2.0e - 5$ seconds.

It can be seen that the finest mesh with a size of 1 μm is not arriving to good results. It had convergence and stability issues. This is thought to happen because the cells are too small to be valid for the mathematical model being employed. As the length scale is very small, and the chemical processes require not only a certain time but also a certain time scale to occur, that is causing the stability problems. When going to coarser meshes the solution is physically reasonable. It can be seen how the spike at the detonation is even higher. However, the solution presents small oscillations around the shock. This spurious oscillations are probably due to numerical error when performing computations in regions with such pronounced
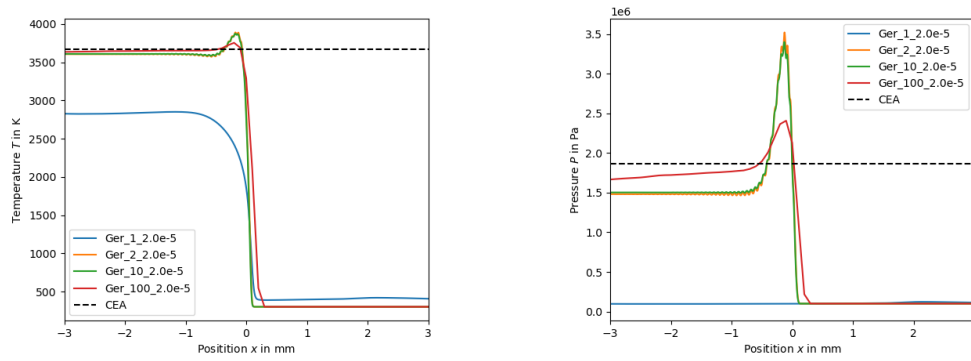
Figure B.2: Temperature (left) and pressure (right) profiles around the shock for different mesh sizes.

gradients. Lastly, the $100 \ \mu$m mesh has a less pronounced spike, but the post-combustion state matches even better with the CEA results. From these results $100 \ \mu$m was selected as the baseline mesh, as a trade-off between results quality and computational costs.
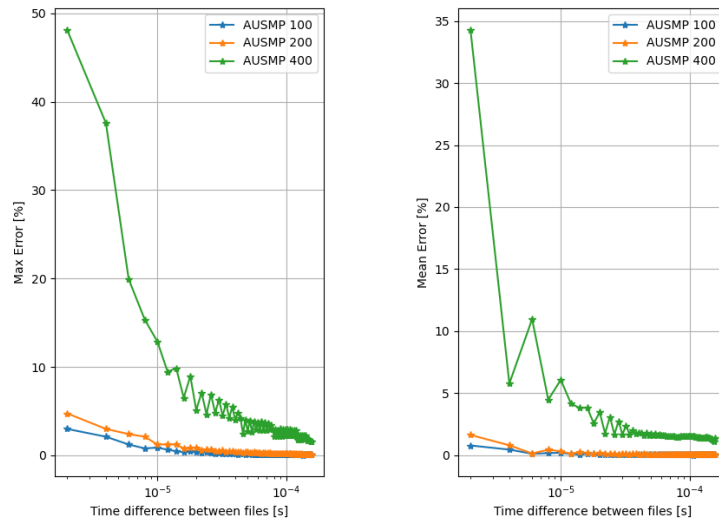

Figure B.3: Max (left) and mean (right) error when computing detonation velocity for different mesh sizes.

Figure B.3 shows the error when computing the detonation velocity taking the time difference between two moving shocks. In this case coarser meshes were evaluated to see the difference with the now baseline mesh. It is interesting to see how the error becomes much higher when computing the velocity employing shocks being too close (small time difference). This is probably because of the small order of magnitude of the time and displacement, converting small numerical errors into big differences when computing velocity. From the results it is clear that there is not a relevant difference between $100 \ \mu$m and $200 \ \mu$m, which is interesting to know to design less computationally expensive meshes.

Time Step Influence

Figure B.4 shows the pressure and temperature profiles centered around the shock for different time step sizes. The time steps are numbered from *Dt0* to *Dt8*. *Dt0* is the baseline time step for which, employing theoretical detonation velocity, half a cell is covered. *Dt1* is the time step required for the detonation to move one cell, and it goes up to moving eight cells with *Dt8*. It can be seen how, as the time step increases, the profile starts to lag. The baseline solution is also the one which achieves the best post-combustion state, and it is clear that very high time steps give very wrong solutions.

Figure B.5 shows the error when computing the detonation velocity for different time steps. As expected, the lowest error is given by the baseline solution. However, there is an interesting behavior of one of the high time steps getting a very low error value. This behavior is probably not because of a good results, but
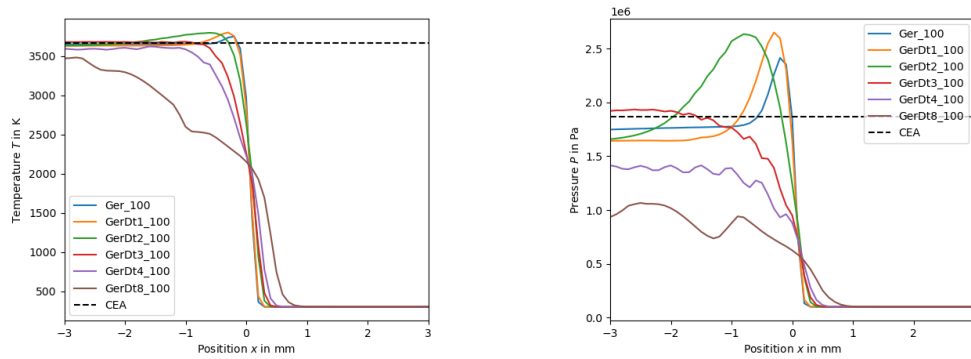
Figure B.4: Temperature (left) and pressure (right) profiles around the shock for different time steps.

rather because of a coincidence in error cancellation due to different sources, since the previous figure clearly showed how the solution was not very accurate.
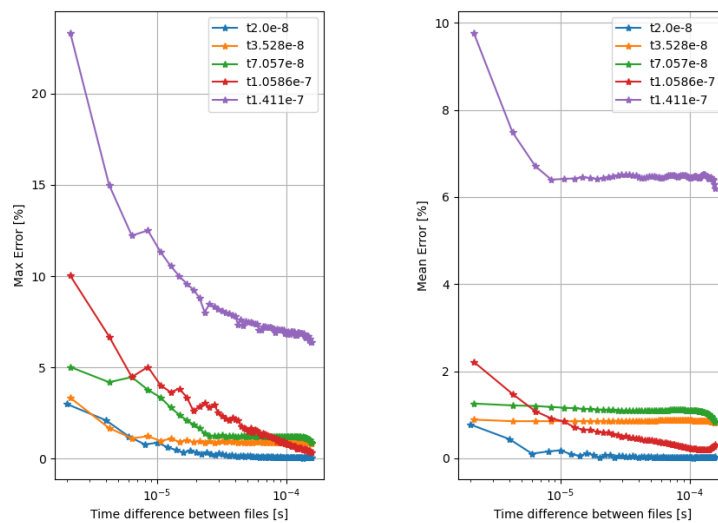

Figure B.5: Max (left) and mean (right) error when computing detonation velocity for different time steps.

Chemical Kinetics Mechanism Influence

Figure B.6 shows the instantaneous temperature (left) and pressure (right) profiles centered around the shock at the time $t = 1.0e - 4$ seconds for different chemical reaction mechanisms. The different mechanisms are referred as Gerlinger [35], Gaffney [29], Boivin [37] and Stanford [32], according to their author or research team who proposed it. Choosing an adequate chemical reaction mechanism is key to a proper representation of the physics since it models all the reaction happening in your mixture. They define the number of species present and the number of chemical reactions happening, as well as the time of reaction. They also determine the auto-ignition time delay.

It can be seen how Gerlinger is the fastest reaction mechanism, while having the smallest spike in the pressure profile. It has been used in the literature in scramjet applications for supersonic H_2-O_2 combustion, where it is key to properly capture auto-ignition delay time (see Sebastian [3]). Similar reaction mechanisms are Stanford and Boivin, having all three of them 9 species considered. Lastly, Gaffney shows the worst behavior among the three. This is probably because it only considers 6 species. It takes longer after the shock to arrive to the expected post-combustion state.

Figure B.7 shows the error committed when computing the detonation velocity. In this case Gaffney was not considered since it was already clear from the previous results that it was not suitable for the simulations. It is clear that Gerlinger shows the lowest errors, although it is closely followed by Stanford. Therefore, the baseline chemicals kinetics mechanism will be Gerlinger.
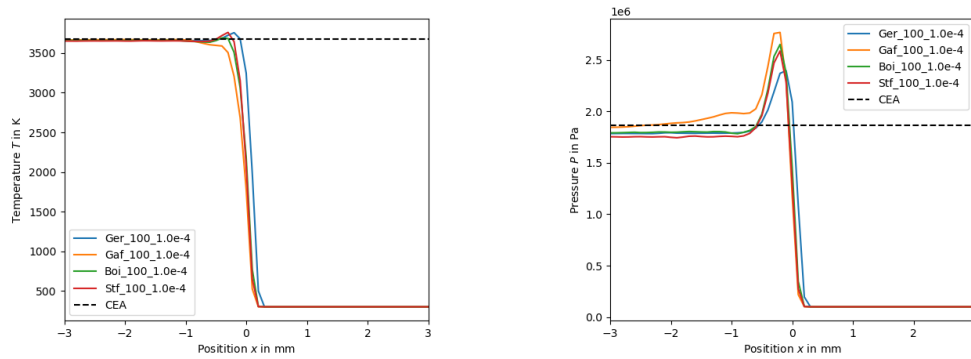
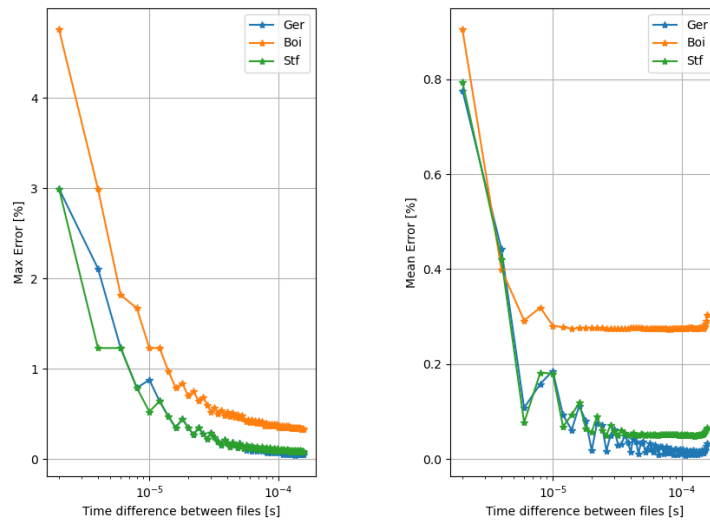**Figure B.6:** Temperature (left) and pressure (right) profiles around the shock for different chemical schemes.

Figure B.7: Max (left) and mean (right) error when computing detonation velocity for different chemical schemes.

Flux Order

Figure B.8 shows the temperature (left) and pressure (right) profiles centered around the shock for different flux order at time $t = 1.0e - 4$ seconds. It is clear that the first order fluxes damp the detonation spike and takes longer to arrive to the post combustion state. This is as expected when going to a less accurate settings. However, it is relevant to know the effects since first order fluxes are more numerically stable. TAU allows the user to set first order fluxes around shocks, to deal with numerical stability. Thus, it is relevant to know the effect it will have on the solution.

Figure B.9 shows the error when computing the detonation velocity. As expected, the error due to having first-order fluxes is higher. However, overall the error is very low, which indicates that even if the detonation front is poorly resolved, the detonation velocity is properly captured.

B.2. 2D Simulations

B.2.1. Set Up

For the 2D simulations the geometry from the DLR Lampoldshausen's experiments has been taken (see Wolfgang et al. [4]). The domain is 213.6x50 mm in size. The mesh sizes employed have been 100 and 200 μm. An example of the mesh can be seen in figure B.10.

For the 2D cases different ignition strategies have been tested. Figure B.11 shows an ignition scheme where all the chamber is filled with premixed combustible mixture, and at the bottom left corner higher pressure and temperature are defined. As before, the numerical ignition values are 5 bar and 3000 K. Other tested ignition strategies employed inert gases as well to fill part of the domain to control the expansion of the detonation wave.
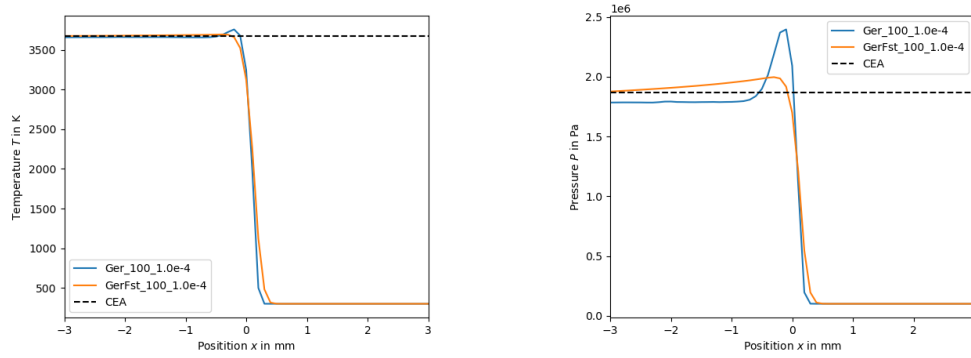
Figure B.8: Temperature (left) and pressure (right) profiles around the shock for different flux order.
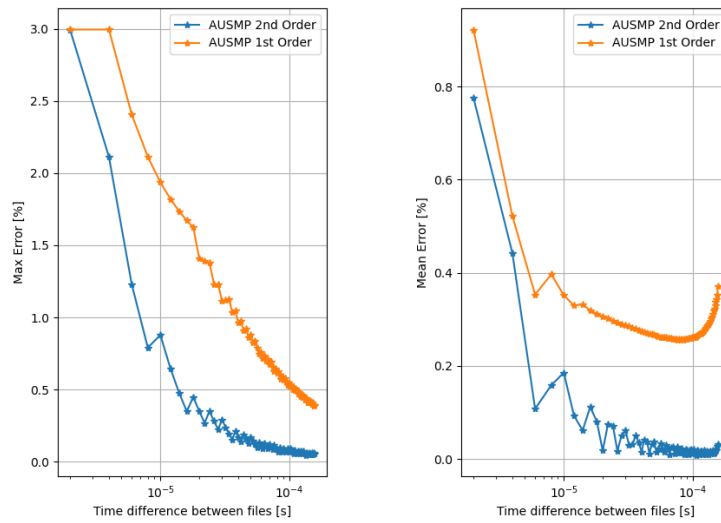

Figure B.9: Max (left) and mean (right) error when computing detonation velocity for different flux order.

For these simulations the Euler equations are employed as well. The left boundary is the inlet boundary, where different inlets have been tested. A reservoir-type inlet has been tested, which allows the user to define a total pressure and total temperature, or a mass flux and a static temperature. It then computes an isentropic expansion taking into account the properties within the domain to compute the inlet properties. Other inlets that have been tested are a supersonic inlet, which for a subsonic case would be overspecified, but in this case provided reasonable results. The right boundary is the outlet boundary, which has the ambient pressure specified at 1 bar. Lastly, the down and upper boundaries are defined as non-viscous walls during the ignition of the detonation, to avoid counter-rotating waves. Once the detonation wave is close to the upper wall, these boundaries are changed to periodic boundary conditions.

Apart from the Lampoldshausen's simulations, some setup validation simulations have been conducted. Based on the set up from Li et al. [17], simulations with the TAU code have been conducted with the exact same conditions.

B.2.2. Results

Lampoldshausen's Case

As described in Wolfgang et al. [4], the experiment at Lampoldshausen is conducted with an H_2-O_2 mixture in stoichiometric conditions. The objective was to simulate an ideal 2D case of this setting, however, it has not been possible. Due to the stiffness of the chemical reactions, the simulations were very unstable during the ignition phase. Moreover, the detonation waves disappeared after setting the upper and lower boundaries to periodic boundary conditions. This occurred due to the lack of a fresh layer of gases at the inlet.
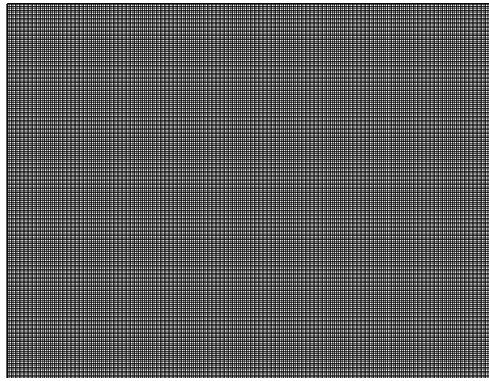
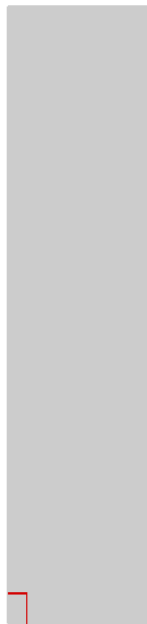**Figure B.10:** Close up of the 2D mesh employed.

Figure B.11: Ignition scheme of the 2D mesh.

To have a stable running detonation, a fresh layer of gases in front of it is required. It is the combustion of these fresh gases what sustains the detonation wave. The problem with the H_2-O_2 mixture was mainly that this layer was not developed after the first detonation period. The expected behavior would be to have a recovery of the injection once the pressure is lowered and the post-combustion gases expand towards the outlet. This problem is most probably related to how the inlet conditions are defined, and due to the chemistry of H_2-O_2 mixtures. The laminar flame speed is very high for hydrogen flames, and it autoignites the moment it gets in contact with the post-combustion gases at high temperatures. Most probably is due to this combination of properties that the fresh layer disappears.

Different strategies were applied to try and solve this problem. The ignition strategy was changed to better control the detonation development. Inert gases were employed to fill in the domain, which altered the first detonation wave, and was used to help the recovery of the injection process. Other strategies were based on changing the inlet conditions, either increasing the total reservoir pressure, change the inlet density or fix a mass flux. The idea was to ensure a mixture flux getting into the domain fast enough to counter the autoignition time and laminar flame speed of the mixture. These tests were not successful.

Starting the simulation directly from an H_2-O_2 mixture was not possible, however, a H_2-Air mixture in stoichiometric conditions proved to be stable and arrived to a stable solution. Figure B.12 shows the evolution of the solution for different nitrogen mass fractions. The idea was to start from a stable solution,

and gradually change towards a pure H_2-O_2 mixture. However, this was not possible. When making small changes to the inlet's mixture, either stability problems appeared, or the fresh layer of gases ended up disappearing, as it is happening in figure B.12.

Figure B.12: Evolution of the temperature (K) for a mixture of H_2 and Air. Nitrogen mass fraction is: $Y_{N_2} = 0.74$ (left), $Y_{N_2} = 0.6$ (middle), $Y_{N_2} = 0.5$ (right).

Figure B.13 shows the heat release for the same conditions as before. Most of the fresh products are consumed in the detonative combustion, however, there is also deflagration in the contact surface between the fresh gases and the post-combustion products. This can be clearly seen in figure B.13, where the highest heat release takes place at the detonation region, but there is still some visible heat release separating the regions of the fresh gases and the post-combustion products. This hinders performance and combustion efficiency. It was expected that, as the nitrogen mass fraction decreased, this deflagration heat release would increase due to Hydrogen's fast chemistry. However, that does not seem to occur. This leads to the conclusion that the problem regarding the instability of H_2-O_2 mixtures comes from the inlet condition definition rather than due to the fresh mixture properties. Nevertheless, is a topic still open to discussion.
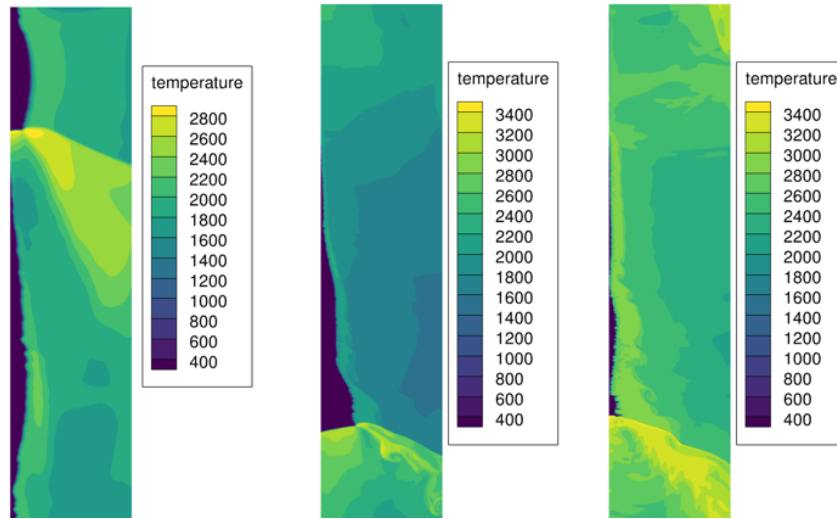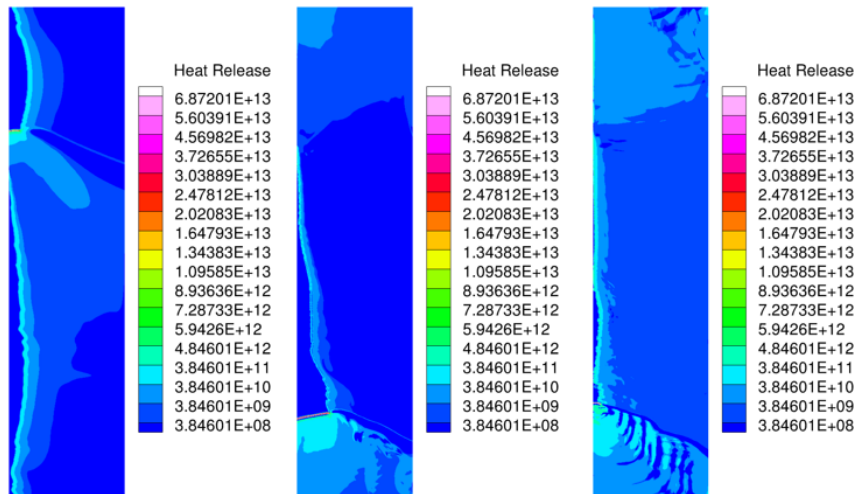

Figure B.13: Evolution of the heat release for a mixture of H_2 and Air. Nitrogen mass fraction is: $Y_{N_2} = 0.74$ (left), $Y_{N_2} = 0.6$ (middle), $Y_{N_2} = 0.5$ (right).

Literature Validation Case

The results obtained from the Lampoldshausen's case were not enough to confirm that the setup proposed was good for this application. Therefore, the set up was tested with a different literature work (see Li et al. [17]), which employs a H_2-Air mixture, which proved to be stable.

The inlet total reservoir pressure is 3.5 bar, and the inlet total reservoir temperature is 300 K. At the outlet an ambient pressure of 1 bar is defined. A probe for taking measurements was placed at the inlet, in the middle of the domain ($z = 50$ mm). Figure B.14 shows the pressure measured at this point for the total physical simulation time. The detonation ran for 5 periods. The detonation velocity was computed from the pressure peaks on the figure. Taking the time between them and averaging, the detonation velocity computed as of 1923 m/s. The CEA [96] theoretical detonation velocity for the given conditions is 1989 m/s. Thus, the absolute error is of 3.31%.
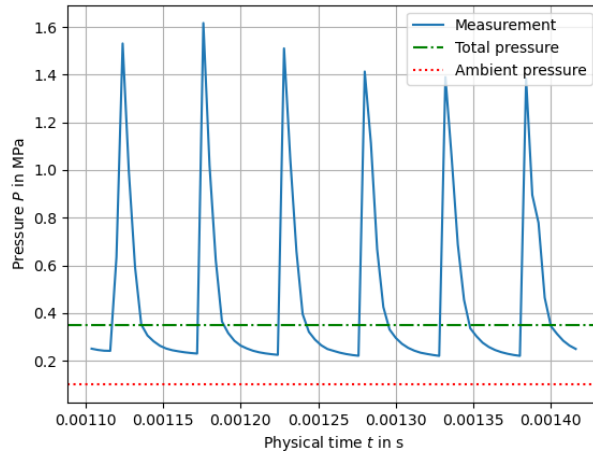
Figure B.14: Pressure measured at $z = 50$ mm during the total simulation physical time.

Figure B.15 shows the instantaneous pressure within the combustion chamber from Li et al. [17] (left) and TAU code (right). It can be seen how the results match very well. The pressure spike is on the same order of magnitude, and the transition to the post-combustion state at the inlet shows a very similar behavior. Moreover, the outlet pressure has approximately the same shape.
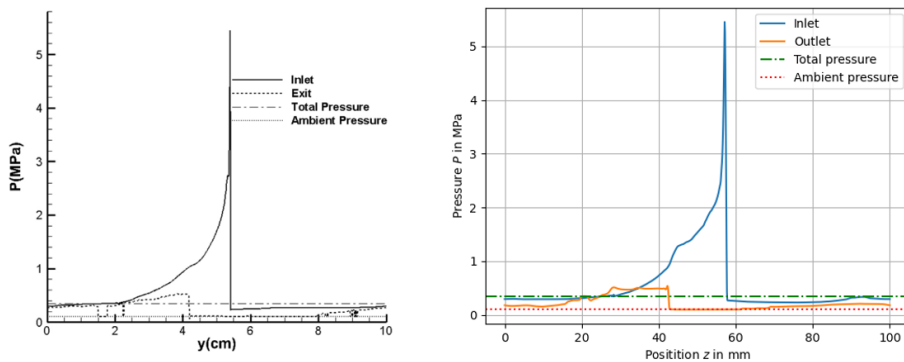
Figure B.15: Comparison between instantaneous pressure profiles from Li et al. [17] (left) and TAU results (right).

Figure B.16 shows the inlet velocity profiles both inlet and outlet from Li et al. [17] (left) and TAU code (right). The inlet velocity profile is very similar in both cases, being the biggest difference the shape and minimum of the negative velocity. On the other hand, the outlet velocity behavior is similar, although there are some differences in the shape of the curve in some sections.

Figure B.17 shows the temperature flow field results from Li et al. [17] (left) and TAU results (right). The literature results show three different solutions since they tested three different mesh resolutions, being the coarsest solution on the left. The results are qualitatively similar, however, there are some clear differences. The layer of fresh gases is not exactly the same, being the TAU results more curved than they

Figure B.16: Comparison between instantaneous inlet velocity profiles from Li et al. [17] (left) and TAU results (right).

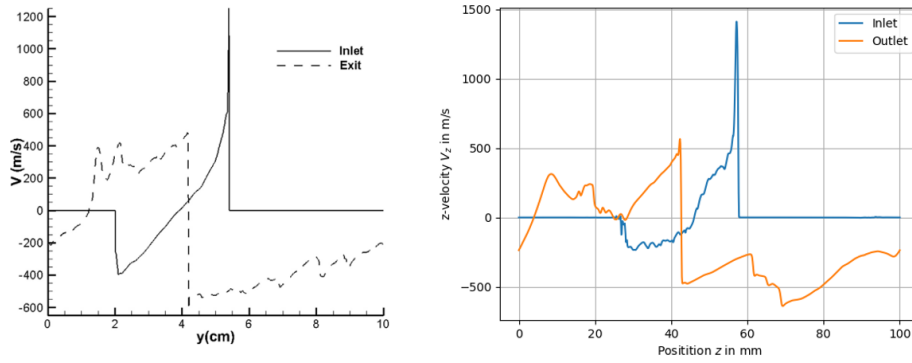should in some regions. Moreover, the geometry around the triple point where the detonation ends and the oblique shock starts is different. While in the literature the oblique shock directly goes backward, in the TAU results the oblique shock is curved to the front in the beginning. Lastly, some of the vortical structures formed after the oblique shock visible in the literature can also be seen in the TAU results.

(a) Case 1.   (a) Case 2.   (a) Case 3.
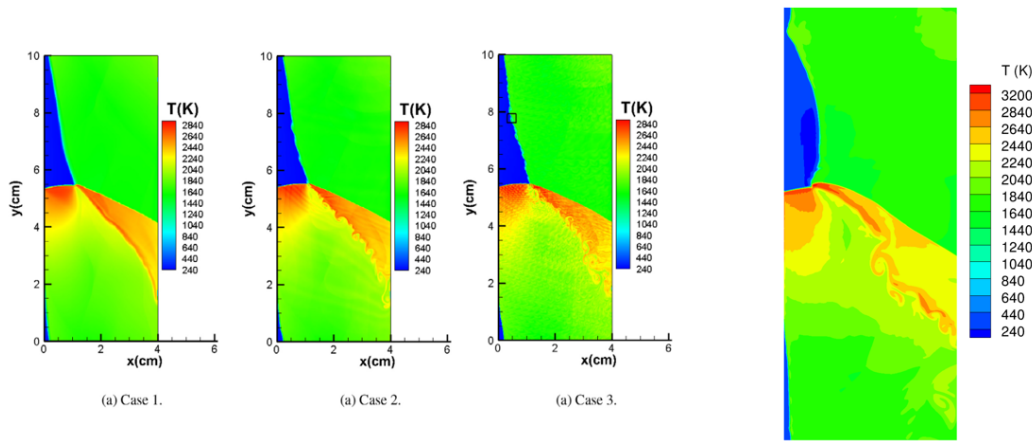
Figure B.17: Comparison between temperature flow fields from Li et al. [17] (left) and TAU results (right).

B.3. 3D Simulations

B.3.1. Set Up

The 3D simulations model geometry is based as well on Lampoldshausen's geometry (see Wolfgang et al. [4]). Figure B.18 shows the geometry of a single injector element (left) and of 24 injector elements (right), which account for a third of the combustion chamber length. The size of the domain has been chosen this way due to the experimental results about the number of co-rotating waves. It was stated that at the equilibrium operational point three detonation waves were running around the chamber, which means one detonation could run continuously in a third of the length. This reduces simulation time.

For these simulations the Spalart-Allmaras (SA) [89] RANS model has been employed. The injector element not only puts the different reactants into the chamber, but is also in charge of mixing them. Turbulence plays an important role in this process, hence why a turbulence model was employed in this case. The model was chosen due to its flexibility for different applications, however, a better study analyzing the influence of different models should be conducted.

Figure B.19 shows the side view of the mesh employed for the simulations. The mesh in the pipes was fine enough to properly resolve the flow at the walls. Moreover, care was taken when meshing the rounded region connecting the pipes with the combustion chamber. The chamber has been divided into three sections of different refinements. The section closest to the injector pipes impingement has the finest resolution to properly capture the mixing process. Downstream, towards, the outlet, the mesh is gradually

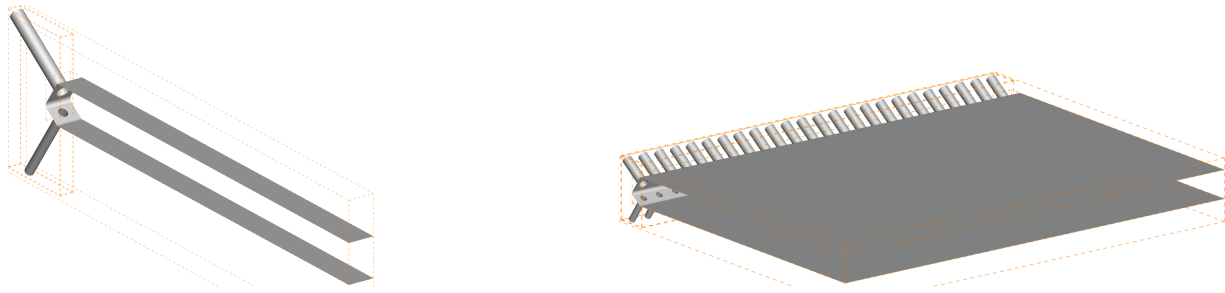**Figure B.18:** Single injector element (left) and 24 injector elements (right) CAD models.

coarser. The size is around 100 μm in the fine region, and around 1000 μm in the coarse region.
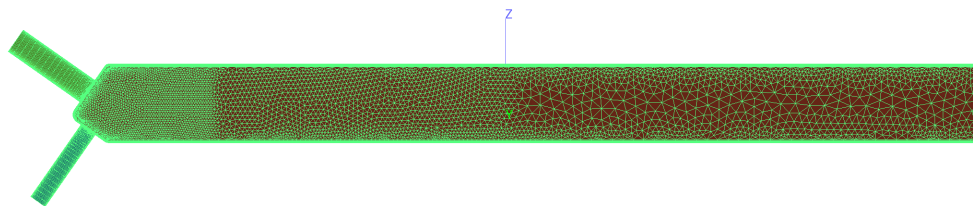

Figure B.19: Side view of the mesh employed for the 3D models.

The inlet boundaries are defined at the pipe inlets. Reservoir conditions for total pressure and total temperature are defined. The upper pipe is the oxidizer pipe, and the lower pipe is the fuel pipe. The injector is designed to have choked flow on both injectors for the given reservoir conditions and to not have any momentum in the parallel plane to the outflow when the two streams collide. Each injector has a total inlet temperature of 295 K, and a total inlet pressure of 2.5 bar.

The outflow is defined at the end of the combustion chamber with a prescribed ambient pressure of 1 bar, and the walls are defined as viscous walls. The side walls are defined as non-viscous walls during the ignition, and as periodic walls for the rest of the simulation.

B.3.2. Results

Single Injector

The first step before running the 3D simulations of the full combustion chamber is to check the quality of the mesh to be employed. Now the fuel and oxidizer enter from different pipes, thus, the mixing process plays an important role in detonation stability. Figure B.20 shows the mixture fraction along the combustion chamber. The stoichiometric mixture fraction is 0.126, which is one of the levels showed in the plot. It can be seen how the stoichiometric line moves towards the fuel side of the combustion chamber. This results also show how much should the refined region of the mesh be extended, to properly capture the most turbulent region where the mixing happens.
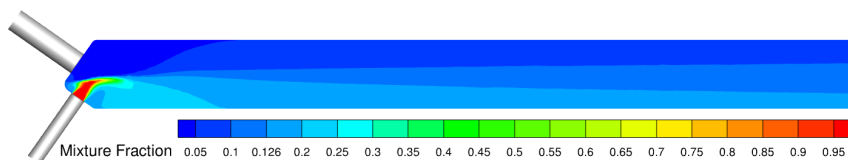
Figure B.20: Mixture fraction along a single injector element.

Figure B.21 shows the y^+ [124] value for the single injector model. Since the 24 injector model is constructed by duplicating the single injector mesh, evaluating the mesh quality of a single injector is enough. The y^+ value is evaluated to check is the flow right next to the wall is properly resolved. It can be seen how the value is below 1 for all the domain, except for the entrance of the pipe, where the pipe flow has not yet been developed and it is expected to find a worse value.
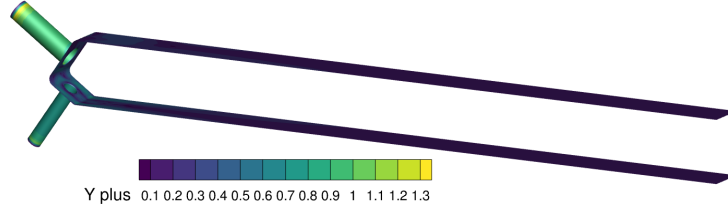
Figure B.21: y^+ value at the walls of a single injector element.

Lastly, figure B.22 shows the mixing efficiency along the combustion chamber, which is a measure of how well are the fuel and oxidizer mixed with each other. The definition of the mixing efficiency is as follows:

$$\eta_{mix} = 1 - \sqrt{\frac{\sigma^2}{\sigma_0^2}} \tag{B.1}$$

where σ is the variance of the oxidizer molar fraction on a cross-section of the combustion chamber, and it is defined in the following manner:

$$\sigma^2 = \frac{1}{A} \int_A (X_O - \langle X_O \rangle)^2 dA \tag{B.2}$$

where $\langle \cdot \rangle$ refers to the average over a cross-section. Moreover, σ_0 is the maximum variance, and is defined as:

$$\sigma_0^2 = \langle X_O \rangle (X_O - \langle X_O \rangle) \tag{B.3}$$
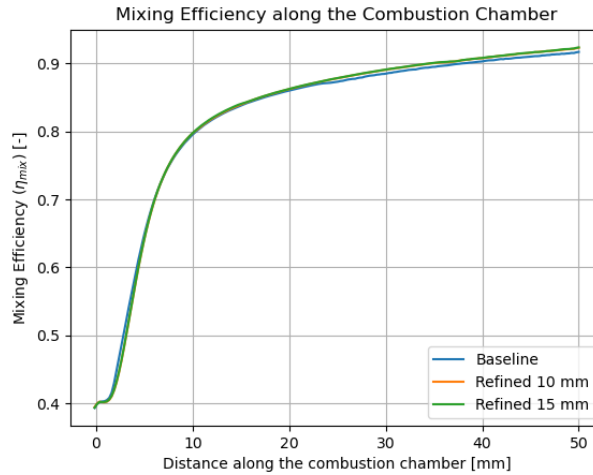
Figure B.22: Mixing efficiency along the combustion chamber.

The results shown in figure B.22 are very similar to the results shown in the literature [51]. This ensures that the baseline mesh is good enough to perform the simulations. Furthermore, two more simulations were performed to evaluate the impact of extending the refined region further downstream in the combustion chamber. The results show that this meshes do not offer a significative improvement of the results.

24 Injector Elements

The last set of simulations performed during the internship were the 24 injector elements domain. The boundary conditions were chosen according to the experimental set up described in Wolfgang et al. [4], as defined in the previous chapter.

Figure B.23 shows the temperature flow field for the 24 injector element case for different iterations. The figure on the left shows a detonation running through the fresh mixture. This situation corresponds to a recently initialized detonation on its first period. It can be seen how there is no proper recovery of the injectors since there is not a clear layer of fresh gases. As there are no fresh gases entering the domain, when the detonation goes through the periodic boundary it vanishes, since there are not enough reactants to sustain it.
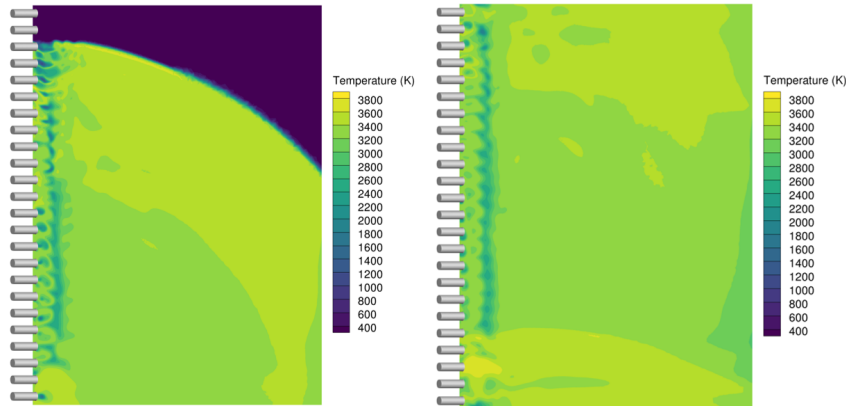
Figure B.23: Temperature flow field at $z = -2.5$ mm for the iteration 1800 (left) and 2000 (right).

Figure B.24 shows the heat release flow field on the same plane as the previous figure. It is interesting to see that for the 3D case the heat release is not only confined to the detonation or the boundary separating the fresh and the post-combustion gases, but it is distributed over the domain. Moreover, due to the finite number of injectors and the mixing process, there is a pattern of high heat release regions combined with no heat release regions.
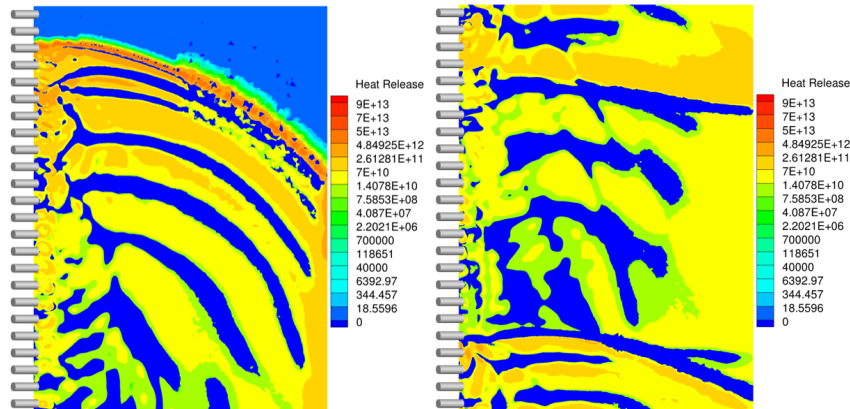
Figure B.24: Heat release flow field at $z = -2.5$ mm for the iteration 1800 (left) and 2000 (right).

By the end of the internship period it has not been possible to get a stable running detonation with the experimental settings. The boundary conditions and initial conditions shall be thoroughly evaluated to find out the problem and achieve a stable operation point comparable to the experimental results.

B.4. Conclusions

The objective of the internship was to develop a consistent and repeatable setup for RDEs simulation employing the TAU DLR code, to validate the data gathered in the experiment from Wolfgang et al. [4]. In order to achieve this a series of steps were taken.

First, a literature review of the topic was conducted. The aim of this first step was to get a better understanding of the RDE working principles and its main features. Moreover, a special focus was put

onto the setup employed by other authors. A good understanding of the problems and limitations of RDE simulations was achieved, as well as general trends. Currently there are both 2D and 3D studies of RDEs, depending on the main objective of the work. The mesh resolution for the finest regions is around $100~\mu$m, being the coarsest regions around $1000~\mu$m. Codes employed to run these simulations use finite volumes schemes with second order Runge-Kutta schemes for time integration and tailored numerical fluxes for these applications. Regarding turbulence modeling, Euler equations have been used for certain works, but most authors employ an LES approach with Smagorinsky subgrid viscosity to study the coupling between the small and the large scale dynamics. On the other hand, each author employs its own tailored chemical kinetics scheme validated for this type of simulations. Moreover, the initialization of the detonations has been done employing both numerical ignitions and by interpolation from other solutions.

Secondly, a set of 1D simulations were performed to evaluate the best setup to capture detonation physics. Different setup parameters were evaluated and a baseline setup for detonation simulations was defined. The baseline mesh was defined to be $100~\mu$m. The baseline time step chosen was $2\text{e-}8$ seconds, however, $5\text{e-}8$ seconds also provided a good trade-off between computational cost and accuracy of the results. Moreover, the chemical kinetics mechanism chosen was the Gerlinger mechanism [35], already validated for similar applications. The numerical flux chosen was the AUSMDV [2], and setting a flux order of one damps the solution, but still provides accurate enough results.

The third step consisted of a series of 2D simulations to test the defined setup. The idea was to simulate an ideal case with a distributed premixed inlet employing Euler equations of the experimental case. However, it was not possible to perform premixed simulations of H_2-O_2 in stoichiometric conditions. Different strategies were tested, nevertheless stability was never achieved. There was no layer of fresh gases to sustain the running detonation. Instead, a case from the literature (see Li et al. [17]) employing a H_2-Air mixture was reproduced. The results were satisfactory, although not identical, thus leaving some room for improvement.

The last step was performing different 3D simulations trying to replicate the results from the Lampold-shausen's experiment. Prior to the combustion simulations, steady-state frozen flow simulations were carried out. The mixing efficiency of the injector element was tested against the literature results, getting a very good match. Moreover, the y^+ value over the walls i below or around 1 for all the domain, indicating a properly resolved boundary layer. However, when running the 3D combustion detonations the results were not satisfactory since a stable running detonation was not achieved. This was probably because of the dynamic behavior of the injectors coupled with the detonation dynamics.

References

[1] M. O Conaire et al. "A Comprehensive Modeling Study of Hydrogen Oxidation". In: *Wiley Inter-Science (www.interscience.wiley.com)* (2004).

[2] Y. Wada et al. "A Flux Splitting Scheme with High-Reslution and Robustness for Discontinuities". In: *ICOMP-93-50; AIAA-94-0083* (1994).

[3] S. Karl. "Numerical investigation of a generic Scramjet Configuration". In: *Ph.D. Thesis, Fakultät für Maschinenwesen der Technischen Universität Dresden, Dresden, Germany, 2011* (2011).

[4] W. Armbruster et al. "Experimental Investigation of a Small-Scale Oxygen-Hydrogen Rotating Detonation Combustor". In: *AIAA SciTech 2024 Forum 10.2514/6.2024-2612* (2024).

[5] R. Bluenmer et al. "Effect of inlet and outlet boundary conditions on rotating detonation combustion". In: *Combustion and Flame 216, 300-315* (2020).

[6] T. Gaillard et al. "Numerical simulation of a rotating detonation with a realistic injector design for separate supply of gaseous hydrogen and oxygen". In: *HAL Id: hal-01558902* (2017).

[7] B.V. Voitsekhovskii. "Stationary Spin Detonation". In: *Soviet Journal of Applied Mechanics and Technical Physics 3 (1960) 157-164* (1960).

[8] R. Cullen et al. "Feasibility Studies of a Rotating Detonation Wave Rocket Motor". In: *J. Spacecr. Rockets 3(6):893-98* (1966).

[9] F.A. Bykovskii et al. "Continuous spin detonations". In: *J. Propul. Power 22(6):1204-16* (2006).

[10] K. Kailasanath. "Recent developments in the research on pulse detonation engines". In: *AIAA J. 41(2):145-59* (2003).

[11] V. Raman et al. "Nonidealities in Rotating Detonation Engines". In: *Annu. Rev. Fluid Mech. 2023. 55:639-74* (2023).

[12] P. Wolański. "Detonative propulsion". In: *Proceedings of the Combustion Institute 34 (2013) 125-158* (2013).

[13] S.D. Heiser et al. "Rotating Detonation Combustion for Advanced Liquid Propellant Space Engines". In: *Aerospace 2022, 9, 581* (2022).

[14] F.A. Zhdan S.A.and Bykovskii et al. "Mathematical Modeling of a Rotating Detonation Wave in a Hydrogen-Oxygen Mixture". In: *Combustion, Explosion, and Shock Waves, Vol. 43, No. 4, pp. 449-459* (2007).

[15] A. Okinski et al. "Rocket rotating detonation engine flight demonstrator". In: *Aircraft Engineering and Aerospace Technology: An International Journal 88/4 (2016) 480–491* (2015).

[16] K. Goto et al. "Space Flight Demonstration of Rotating Detonation Engine Using Sounding Rocket S-520-31". In: *Journal of Spacecraft and Rockets. Vol. 60, No. 1, January–February 2023* (2022).

[17] Q. Li et al. "Further invertigations on the interface instability between fresh injections and burnt products in 2-D rotating detonation". In: *Computers and Fluids 170 (2018) 261-272* (2018).

[18] B. Le Naour et al. "Rotating detonation combustors for propulsion: Some fundamental, numerical and experimental aspects". In: *Front. Aerosp. Eng. 2:1152429* (2023).

[19] P. Hellard et al. "Quasi-CJ rotating detonation with partially premixed methane-oxygen injection: Numerical simulation and experimental validation". In: *Applications in Energy and Combustion Science 19 (2024) 100278* (2024).

[20] S. Nakagami et al. "Experimental Visualization of the Structure of Rotating Detonation Waves in a Disk-shaped Combustor". In: *J. Propul. Power 33(1):80-88* (2017).

[21] R. Huff et al. "Design and Operation of a Radial Rotating Detonation Engine". In: *J. Propul. Power 35(6):1143-50* (2019).

[22] M. Zhao et al. "Simulation of a Rotating Detonation Ramjet Model in Mach 4 Flow". In: *21st Australasian Fluid Mechanics Conference. Adelaide, Australia. 10-13 December 2018* (2018).

[23] F.A. Williams. *Combustion Theory*. Princeton University, 1985.

[24] M.A. Liberman. *Combustion Physics. FLames, Detonations, Explosions, Astrophysical Combustion and Intertial Confinement Fusion*. Springer, 2021.

[25] C.J. Barfuß. "Efficient Multi-Scale Simulation of Deflagration-to-Detonation Transition in Stratified H_2-CO-Air Mixtures". In: *Technische Universität München. TUM School of Engineering and Design* (2023).

[26] S. Kao et al. "SDToolbox: Numerical Tools for Schock and Detonation Wave Modeling". In: *GALCIT Report FM2018.001. Revised April 18, 2023* (2023).

[27] J.M. Justin. "The Role of Instability in Gaseous Detonation". In: *PhD thesis. California Institute of Technology* (2003).

[28] S. Prakash et al. "High Fidelity Simulations of a Methane-Oxygen Rotating Detonation Rocket Engine". In: *AIAA 2020-0689* (2020).

[29] R.L.Jr. Gaffney et al. "Modeling Turbulent/Chemistry Interactions Using Assumed PDF Methods". In: *AIAA/SAE/ASME/ASEE 28th Joint Propulsion Conference and Exhibit. July 6-8, Nashville, TN* (1992).

[30] T. Horchler. "Skalenauflösende Simulation der Flammen-Akustik-Wechselwirkung bei resonanter und nicht-resonanter Anregung in einer Experimental-Raketenbrennkammer". In: *Ph.D. Thesis, Justus-Liebig-Universitäat Gießen, Fachbereich 07, I. Physikalisches Institut* (2022).

[31] Jachimowski C.J. "An Analytical Study of the Hydrogen-Air Reaction Mechanism With Application to Scramjet Combustion". In: *NASA Technical Paper 2791* (1988).

[32] Z. Hong et al. "An improved H2/O2 mechanism based on recent shock tube/laser absorption measurements". In: *Combustion and Flame 158 (2011) 633–644* (2010).

[33] ANSYS. "Chemkin Theory Manual 17.0 (15151)". In: *Reaction Design: San Diego 2015* (2016).

[34] J.S. Evans et al. "Influence of Chemical Kinetics and Unmixedness on Burning in Supersonic Hydrogen Flames". In: *AIAA* 18, NO. 2.79 (1980).

[35] P. Gerlinger et al. "An Implicit Multigrid Method for Turbulent Combustion". In: *Journal of Computational Physics 167, 247–276 (2001)* (2000).

[36] M. Mueller et al. "Flow reactor studies and kinetic modeling of the H2/O2 reaction". In: *Int. J. Chem. Kinet. 31, 113-125* (1999).

[37] P. Boivin. "Reduced-Kinetic Mechanisms for Hydrogen and Syngas Combustion Including Autoignition". In: *PhD Thesis. Departamento de Ingeniería Térmica y de Fluidos. Universidad Carlos III* (2011).

[38] E. Winterberger et al. "Thermodynamic Cycle Analysis for Propagating Detonations". In: *J. Propul. Power 22.3 (2006), pp.694-698* (2006).

[39] Q. Xie et al. "Review on the Rotating Detonation Engine and its Typicl Problems". In: *Transactions on Aerospace Research 4(261) 2020, pp. 107-163* (2020).

[40] V. Anand et al. "Investigation of rotating detonation combustor operation with H2-Air mixtures". In: *International Journal of Hydrogen Energy 41, 1281-1292* (2016).

[41] D. Schwer et al. "Numerical Investigation of the Physics of rotating-detonation-engines". In: *Proceedings of the Combustion Institute 33, 2195-2202* (2011).

[42] S.M. Frolov et al. "Three-Dimensional Numerical Simulation of Operation Process in Rotating Detonation Engine". In: *Progress in Propulsion Physics 4, 467-488* (2013).

[43] S.M. Frolov et al. "Three-Dimensional Numerical Simulation of Operation of a Rotating-Detonation CHamber with Separate Supply of Fuel and Oxidizer". In: *Russian Journal of Physical Chemistry B, Vol. 7, No. 1, pp. 35-43* (2013).

[44] S. Yao et al. "Numerical Investigation of Spontaneous Formation of Multiple Detonation Wave Fronts in Rotating Detonation Engine". In: *Combustion Science and Technology, 187: 1867-1878* (2015).

[45] W. Lin et al. "Experimental study on propagation mode of H2/Air continuously rotating detonation wave". In: *International Journal of Hydrogen Energy 40, 1980-1993* (2015).

[46] S.M. Frolov et al. "Large-scale hydrogen-air continuous detonation combustion". In: *International Journal of Hydrogen Energy 40, 1616-1623* (2015).

[47] D. Wu et al. "Numerical Investigation of the Stability of Rotating Detonation Engines". In: *Combustion Science and Technology, 186:10-11, 1699-1715* (2014).

[48] B.A. Rankin et al. "Periodic Exhaust Flow through a Converging-Diverging Nozzle Downstream of a Rotating Detonation Engine". In: *AIAA 2014-2015. Session: Detonations and PDEs I* (2014).

[49] P. Wolański. "Rotating Detonation Wave Stability". In: *23rd ICDERS. July 24-29* (2011).

[50] S. Connolly-Boutin et al. "Small-size rotating detonation engine: scaling and minimum mass flow rate". In: *Shock Waves 31: 655-674* (2021).

[51] B.S. Hermannsson. "Development and Analysis of a Gaseous Hydrogen-Oxygen Rotating Detonation Combustor". In: *KTH Royal Institute of Technology, MSc Aerospace Engineering.* (2022).

[52] M. Kaneshige et al. "Detonation Database. Explosion Dynamics Laboratory Report FM97-8". In: *Pasadena, California* (1999).

[53] K. Goto et al. "Investigation into the efective injector area of a rotating detonation engine with impact of backfow". In: *Shock Waves 31:753–762* (2021).

[54] H.F. Celebi et al. "Response of angled and tapered liquid injectors to passing detonation fronts at high operating pressures". In: *Shock Waves 31:717–726* (2021).

[55] S. Prakash et al. "Numerical simulation of a methane-oxygen rotating detonation rocket engine". In: *Proceedings of the Combustion Institute 38, 3777-3786* (2021).

[56] T. Sato et al. "Mixing and detonation structure in a rotating detonation engine with an axial air inlet". In: *Proceedings of the Combustion Institute 38, 3769-3776* (2021).

[57] S. Prakash et al. "Analysis of the Detonation Wave Structure in a Linearized Rotating Detonation Engine". In: *AIAA Journal, Vol. 58, No. 12* (2020).

[58] F. Chacon. "Non-Ideal Phenomena in Rotating Detonation Combustors". In: *Ph.D. Thesis, University of Michigan* (2021).

[59] F. Chacon et al. "Secondary waves dynamics and their impact on detonation structure in rotating detonation combustors". In: *Shock Waves 31:675-702* (2021).

[60] A.K. Hayashi et al. "Experimental and numerical study on disc-RDE: flow structure and its performances". In: *2021 AIAA Scitech Forum, AIAA pap. 2021-1253* (2021).

[61] F. Ettner et al. "Mach reflection in detonations propagating through a gas with a concentration gradient". In: *Shock Waves 23:201-206* (2013).

[62] W. Han et al. "Flame acceleration and deflagration-to-detonation transition in micro- and macro-channels: An integrated mechanistic study". In: *Combustion and Flame 176, 285-298* (2017).

[63] Gaillard T. et al. "Numerical Optimisation in Non Reacting Conditions of the Injector Geometry for a Continuous Detonation Wave Rocket Engine". In: *Acta Astronautica 111, 334-344* (2015).

[64] Computational Study of Reactants Mixing in a Rotating Detonation Combustor Using Compressible RANS. "Computational Study of Reactants Mixing in a Rotating Detonation Combustor Using Compressible RANS". In: *Flow, Turbulence and Combustion (2020) 105:267-295* (2019).

[65] J. Melguizo-Gavilanes et al. "Dynamics of detonation transmission and propagation in a curved chamber: a numerical and experimental analysis". In: *Combustion and Flame 223 (2021) 460-473* (2020).

[66] M. Hishida et al. "Fundamentals of rotating detonations". In: *Shock Waves (2009) 19:1-10* (2009).

[67] D.E. Paxson. "Numerical Analysis of a Rotating Detonation Engine in the Relative Reference Frame". In: *AIAA-2014-0284* (2014).

[68] J. Fujii et al. "Numerical investigation on detonation velocity in rotating detonation engine chamber". In: *Proceedings of the Combustion Institute 36 (2017) 2665-2672* (2017).

[69] W. Fang et al. "On the feasibility and performance of the ammonia/hydrogen/air rotating detonation engines". In: *Physics of Fluids 35, 066133* (2023).

[70] Y. Wang et al. "Effect of the inlet spatial fluctuation on the gas–solid continuous rotating detonation flow field characteristics". In: *Physics of Fluids 36, 076107* (2024).

[71] L. Deng et al. "The feasibility of mode control in rotating detonation engine". In: *Applied Thermal Engineering 129 (2018) 1538-1550* (2018).

[72] M. Cheng et al. "BYCFoam: An Improved Solver for Rotating Detonation Engines Based on OpenFOAM". In: *Energies 2024, 17, 769* (2024).

[73] OpenCFD Ltd. *OpenFOAM*. 2016. URL: `https://www.openfoam.com/` (visited on 01/30/2025).

[74] K. Kailasanath et al. "Rotating Detonation Engine Research at NRL". In: *International Worksop on Detonation Propulsion. July 26-28, 2013* (2013).

[75] P. Hellard et al. "A modeling strategy for transitory injection simulation in Rotating Detonation Engines". In: *Joint Meeting of International Workshop on Detonation for Propulsion (IWDP) and International Constant Volume and Detonation Combustion Workshop (ICVDCW), Aug 2022, Berlin, Germany. hal-03826954* (2022).

[76] P. Hellard et al. "Transitory injection simulation to study injector performance of an experimental Rotating Detonation Engine". In: *IWDP and ICVDCW 2022, Aug 2022, Berlin, Germany. hal-03826979* (2022).

[77] V. Athmanathan et al. "On the effects of reactant stratification and wall curvature in non-premixed rotating detonation combustors". In: *Combustion and Flame 240 (2022) 112013* (2022).

[78] S. Yao et al. "The Effect of the Inlet Total Pressure and the Number of Detonation Waves on Rotating Detonation Engines". In: *2014 Asia-Pacific International Symposium on Aerospace Technology (APISAT2014)* (2015).

[79] T. Sato et al. "Mass flow rate effect on a rotating detonation combustor with an axial air injection". In: *Shock Waves (2021) 31:741-751* (2021).

[80] P. Pal et al. "Numerical Analysis of Combustion Dynamics in a Full-Scale Rotating Detonation Rocket Engine Using Large Eddy Simulations". In: *Journal of Energy Resources Technology, Vol. 145, 021702-1* (2023).

[81] P. Hellard et al. "Evaluation of a computational strategy to model transitory injection in rotating detonation combustors". In: *Front. Aerosp. Eng. 2:1127671* (2023).

[82] P. Hellard et al. "Numerical investigation of the effects of friction and heat transfer on a non-premixed Rotating Detonation Combustor operation". In: *European Combustion Meeting (ECM2023), CORIA UMR 6614; French section Combustion institute, Apr 2023, Rouen, France. hal-04591653* (2023).

[83] T. Sato et al. "Numerical and boundary condition effects on the prediction of detonation engine behavior using detailed numerical simulations". In: *Front. Aerosp. Eng. 2:1123249* (2023).

[84]   P. Pal et al. "Multidimensional Numerical Modeling of Combustion Dynamics in a Non-Premixed Rotating Detonation Engine With Adaptive Mesh Refinement". In: *Journal of Energy Resources Technology, Vol. 143, 112308-1* (2021).

[85]   P. K. Senecal et al. "A New Parallel Cut-Cell CFD Code for Rapid Grid Generation Applied to In-Cylinder Diesel Engine Simulations". In: *SAE Technical Paper, Detroit, MI, Apr. 9–11, p. 0159* (2007).

[86]   C. Laurent. "Low-order modeling and high-fidelity simulations for the prediciton of combustion instabilities in liquid rocket engines and gas turbines". In: *(Ph.D. Thesis) Toulouse, INPT* (2020).

[87]   K. Nordin-Bates et al. "Understanding Scramjet Combustion Using LES of the HyShot II Combustor". In: *Proceedings of the Combustion Institute 36, 2893-2900* (2017).

[88]   A. Jameson. "Time dependent calculations using multigrid, with application to unsteady flows past airfoils and wings". In: *AIAA paper 91-1596* (1991).

[89]   P.R. Spalart et al. "A One-Equation Turbulence Model for Aerodynamic Flows". In: *AIAA Paper 92-0439* (1992).

[90]   D.C. Wilcox. "Turbulence Modelling for CFD". In: *DCW Industries, La Canada, California* (1998).

[91]   F. Menter. "Two-Equation Eddy-Viscosity Turbulence Models for Engineering Applications". In: *AIAA-Journal, Vol. 32, No. 8* (1994).

[92]   D. Schwamborn et al. "The DLR TAU-Code: Recent Applications in Research and Industry". In: *European Conference on Computational Fluid Dynamics* (2006).

[93]   National Institute of Standards and Technology. *NIST Computational Chemistry Comparison and Benchmark Database*. Ed. by Russell D. Johnson III. `http://cccbdb.nist.gov/`. NIST Standard Reference Database Number 101, Release 22. May 2022. DOI: `10.18434/T47C7Z`.

[94]   L.V. Gurvich. "Thermodynamic Properties of Individual Species". In: *Hemisphere* (1989).

[95]   R.N. Gupta et al. "A Review of Reaction Rates and Thermodynamic and Transport Properties for an 11-Species Air Model for Chemical and Thermal Nonequilibrium Calculations to 30000 K". In: *NASA Reference Publication, No. 1232* (1990).

[96]   NASA. *Chemical Equilibrium with Applications*. 2002. URL: `https://www1.grc.nasa.gov/research-and-engineering/ceaweb/` (visited on 10/24/2024).

[97]   C.R. Wilke. "A Viscosity Equation for Gas Mixtures". In: *Journal of Chemical Physics, Vol. 18(4)* (1960).

[98]   G.E. Palmer et al. "Comparison of Methods to Compute High-Temperature Gas Viscosity". In: *Journal of Thermophysics and Heat Transfer, Vol. 17* (2003).

[99]   Eucken. "Über das Wärmeleitvermögen, die spezifische Wärme und die innere Reibung der Gase". In: *Physik. Zeitschrift XIV* (1913).

[100] J.O. Hirschdelder. "Generalization of the Eucken Approximation fort he Heat Conductivity of Polyatoomic or Chemically Reacting Gas Mixtures". In: *Conference on Thermodynamics and Transport Properties of Fluids* (1957).

[101] L. Zipperer et al. "Beitrag zur Berechnung der Zähigkeit technischer Gasgemische aus den Zähigkeitswerten der Einzelbestandteile". In: *Das Gas- und Wasserfach, Vol. 4* (1936).

[102] T.J. Barth et al. "The Design and Application of Upwind Schemes on Unstructured Meshes". In: *AIAA-89-0366, AIAA 27th AIAA Aerospace Sciences Meeting, Reno* (1989).

[103] W.K. Anderson et al. "An Implicit Upwind Algorithm for Computing Turbulent Flows on Unstructured Grids". In: *Computers Fluids Vol. 23, No. 1, pp 1-21* (1994).

[104] A. Haselbacher et al. "On the Accurate and Efficient Discretisation of the Navier-Stokes Equations on Mixed Grids". In: *AIAA Journal Vol. 38(11)* (1994).

[105] E.F. Toro. "Riemann Solvers and Numerical Methods for Fluid Dynamics: A Practical Introduction". In: *2nd Edition, Springer* (1999).

[106] A. Jameson et al. "Numerical Solution of the Euler Equations by Finite Volume Methods Using Runge-Kutta Time-Stepping Schemes". In: *AIAA 81-1259, AIAA 14th Fluid and Plasma Dynamic Conference, Palo Alto* (1981).

[107] S.G. Sheffer et al. "An Efficient Multigrid Algorithm for Compressible Reacting Flows". In: *Journal of Computational Physics Vol. 144:484-516* (1998).

[108] M. Liou et al. "A New Flux Splitting Scheme". In: *NASA Technical Memorandum 104404* (1991).

[109] P.L. Roe. "Approximate Riemann Solvers, Parameter Vectors and Difference Schemes". In: *J. Comput. Phys., 43, 257-72* (1981).

[110] B. van Leer. "Flux-Vector Splitting for the Euler Equations". In: *8th International Conference on Numerical Methods in Fluid Dynamics. Springer Berlin Heidelberg. p.507-512* (1982).

[111] D Hänel et al. "On the accuracy of upwind schemes for the solution of the Navier-Stokes equations". In: *8th Computational Fluid Dynamics Conference*. 1987, p. 1105.

[112] M. Liou. "The Evolution of AUSM Schemes". In: *Defence Science Journal, Vol. 60, No.6, November 2010, pp. 606-613* (2003).

[113] J.R. Edwards. "On the Development of 'All Speed' Flux Formulae based on the AUSM Framework". In: *ICCFD10-337* (2018).

[114] M. Liou. "A Sequel to AUSM: AUSM+". In: *J. Comput. Phys., 129, 364-82* (1996).

[115] M. Liou. "A Further Development of the AUSM+ Scheme towards Robust and Accurate Solutions for All Speeds". In: *AIAA 2003-4116* (2003).

[116] M. Liou. "A Sequel to AUSM, Part II: AUSMP+-up for All Speeds". In: *Journal of Computational Physics 214 (2006) 137-170* (2006).

[117] K.H. Kim et al. "An Improvement of AUSM Schemes by Introducing the Pressure-Based Weight Functions". In: *Computer and Fluids Vol. 27, No. 3, pp. 311-346* (1998).

[118] K.H. Kim et al. "Methods for the Accurate Compuations of Hypersonic Flows". In: *Journal of Computational Physics 174, 38-80* (2001).

[119] K.H. Kim et al. "Accurate, Efficient and Monotonic Numerical Methods for Multi-Dimensional Compressible Flows Part I: Spatial Discretization". In: *Journal of Computational Physics 208, 527-569* (2005).

[120] Z. Sheng et al. "Multi-wave effects on stability and performance in rotating detonation combustors". In: *Physics of Fluids 35, 076119* (2023).

[121] J.M. Tizón et al. *Introducción a los Motores Cohete*. Garceta, 2019.

[122] P. Strempfl et al. "Effects of mixing assumptions and models for LES of Hydrogen-fueled Rotating Detonation Engines". In: *International Journal of Hydrogen Energy 62, 1-16* (2024).

[123] David G. Goodwin et al. *Cantera: An Object-oriented Software Toolkit for Chemical Kinetics, Thermodynamics, and Transport Processes*. `https://www.cantera.org`. Version 3.1.0. 2024. DOI: `10.5281/zenodo.14455267`.

[124] Simscale. *What is y+ (yplus)?* 2020. URL: `https://www.simscale.com/forum/t/what-is-y-yplus/82394` (visited on 12/06/2024).